Cavitation in Lubricating Films

Nicholas Letchford
Christ Church
University of Oxford

A thesis submitted for the degree of
Doctor of Philosophy
Michaelmas Term, 2016

To my parents for their unrelenting belief in me and my abilities. To my grandparents for the love and kindness they have shown me, and to my amazing and supportive girlfriend who has always buoyed me through the toughest and most challenging times.

Acknowledgements

I would like to thank my supervisors, Professor Chris Breward, Professor Dominic Vella, and Professor Peter Howell for their invaluable direction, insightful comments, encouragement and support throughout the last four years. I am very grateful to have such excellent supervisors who believe in me. I would also like to thank my sponsors BP and in particular Dr. Ben Leach, for the assistance and collaboration they provided over this time. Their sponsorship of my D.Phil. made this research possible.

I would like to thank my Oxford friends, both near and far. You have provided with an invaluable source of support and friendship with many of you having a lasting impact on my life.

I would like to thank my delightful and amazing girlfriend, and partner for life, Lakshmi Neelakantan. Your support, encouragement and motivation enable me to survive this year. You have always been available to talk and help me through the most difficult times when I needed it (including having superhuman abilities like proof-reading 200 pages in less than an hour). I hope I'll see you go through this same process in a few years time, as it will be an opportunity for me to support and encourage you as you have done for me!

I would like to thank my brothers, Isaac and Nathanael. You of all people know the chaos that it is to be apart of this family. To my grandparents, Grandma, Poppy, and Nana: you have always been so reassuring and comforting, even in the worse times. My parents Mum and Dad: Over the last four years, I have relied heavily on Dad for his guidance and support as to how to manage my supervisors and listening to the nostalgia of Oxford from 30 years ago. Lastly, I would like to thank my Mum, who helped me believe in myself and achieve my dreams. Without her teaching, I would not have attained a university degree (let alone three) and return to Oxford, where my learning all began so long ago.

Statement of Originality

I confirm that this thesis is wholly my own original work, and that no part of my thesis has been accepted or is currently being submitted for and degree, diploma, certificate or other qualification at the University of Oxford or elsewhere. All methods and techniques used in this thesis that have been developed by other authors have been acknowledged by citation of the relevant publication.

Cavitation in Lubricating Films

Nicholas Letchford

Christ Church

University of Oxford

A thesis submitted for the degree of

Doctor of Philosophy

Michaelmas Term, 2016

Wear and friction are significant problems in machinery. A particularly harsh environment is the space between the piston ring and cylinder wall of a combustion engine. Lubricant films are commonly used to mitigate these effects, separating metal to metal contact.

The experiments of Zhu and Granick (Langmuir, **18**, 2002) attempt to understand how surfactants change the behaviour of lubricating films. They claim surfactants that have adsorbed onto a solid surface cause the fluid to slip past the surface. We hypothesize that their observations could instead be caused by the liquid cavitating. We develop a mushy region model, based on the work of Ockendon, Howison, and Lacey (Q J Mech Appl Math, **56**, 2003), to represent the cavitated region which we assume is composed of liquid, vapour, and gas. We show that the normal force predicted by the model gives a good fit to experimental observations.

We also model experiments of Professor J. Nouri, who investigated the formation of gaseous cavities in a slider bearing, again using a mushy region model. We present a detailed asymptotic analysis of the model and show how the solution changes from being quasi-steady to dynamic as the velocity of the bottom surface changes sign. We show that numerical solutions of the model are in good qualitative agreement with experimental measurements, yet several persistent discrepancies remain. We suggest possible causes of these discrepancies, and estimate the effects that various physical phenomena might have on the experiments. By modifying the mushy region model to study the impact of various additional processes on the film, we attempt to explain specific differences between the model and the experimental results. We also extend the model to include other effects so it is more representative of the operating conditions experienced by lubricants in engines.

Contents

1 Introduction 1

1.1 Lubricant Films in Engines . . . 4

1.1.1 Literature review of lubricant films . . . 6

1.2 Cavitation . . . 8

1.2.1 The Process of Gaseous Cavitation on a Molecular Level . . . 10

1.2.2 Evolution of Cavitation Models in Slider and Journal Bearings . . . 11

1.2.3 Cavitation in Negative Squeeze Films . . . 22

1.3 Thesis layout . . . 23

2 Cavitation and Effective Slip in Squeeze Films 26

2.1 Introduction . . . 26

2.2 Zhu and Granick Experiment . . . 27

2.3 The Bubble Model . . . 31

2.3.1 Thin film model . . . 31

2.3.2 Cavitation . . . 35

2.3.3 Pressure profile in bubble model . . . 45

2.4 Mushy Region Model . . . 47

2.5 Comparison with Experimental Results . . . 53

2.6 Conclusions . . . 58

3 Cavitation in Slider Bearings 61

3.1 Introduction . . . 61

3.2 City University of London Experiment . . . 64

3.3 Model for the opening of the Cavitated Region . . . 67

3.3.1 Problem Setup . . . 67

3.3.2 Solution of the Model Problem . . . 71

3.3.3 Steady State Solution 78
3.3.4 Linear Stability of the Steady State 83
3.4 Closing of the Mushy Region 85
3.4.1 Numerical Solutions 85
3.4.2 Quasi-Steady Solution 88
3.4.3 Summary 89
3.5 Mushy Region Model with an Oscillatory Velocity 90
3.5.1 Solutions 95
3.5.2 Discussion 101
3.6 Conclusions 109

4 Asymptotic Analysis of the Mushy Region Problem 111
4.1 Introduction 111
4.2 Quasi-Steady Solution 114
4.2.1 Upstream Region 115
4.2.2 Downstream Region 117
4.3 Unsteady Downstream Region 118
4.4 Unsteady Upstream Region 123
4.4.1 Outward-Travelling Characteristics 124
4.4.2 Inward-Travelling Characteristics 133
4.5 Secondary Cavitation 136
4.6 Interaction Between The Mushy Regions 142
4.6.1 Time When First Mushy Region Closes 148
4.7 Change in Causality for the Upstream Boundary of the Mushy Region . . . 149
4.8 Summary 158
4.9 Comparison with Experiments 160
4.10 Conclusions 165

5 Real-World Applications of the Mushy Region Model 167
5.1 Additional Physical Effects 168
5.1.1 Elastic Deformation of the Surfaces 168
5.1.2 Inertia of the Top Surface 169
5.1.3 Piezo-Viscous Effect 170
5.1.4 Viscous Heating 170

5.1.5 Liquid Compressibility . . . 171

5.1.6 Surface Roughness . . . 172

5.1.7 Summary . . . 172

5.2 Finite Width Slider . . . 173

5.2.1 Influence of Finite Width of the Ring . . . 174

5.2.2 Comparison with Experiment . . . 177

5.2.3 Summary . . . 179

5.3 Sources of Asymmetry . . . 179

5.3.1 Asymmetry of Ring Profile . . . 179

5.3.2 Asymmetry in the Velocity of the Bottom Surface . . . 184

5.3.3 Asymmetry of Oil Supply . . . 189

5.3.4 Summary . . . 190

5.4 Applications to Operating Engine Environments . . . 190

5.5 Conclusions . . . 193

6 Conclusions 196

6.1 Review of Thesis . . . 196

6.2 Future Work . . . 200

6.3 Executive Summary . . . 202

A ode15s Algebraic Differential Equation Solver 204

B Equation for the Linear Stability of the Steady State 206

C Closing Mushy Region Model Differential Equations 209

D Expansion of the Mushy Region Model when x_L Changes Causality 212

E Mushy Region Model Differential Equations 215

List of Figures

1.1 The Stribeck Curve, as shown in Heshmat (2010). On the horizontal axis is the 'Stribeck Number' which is the product of the speed of the moving surface U, and viscosity of the liquid μ, over the applied normal force F, and on the vertical axis is the Coefficient of Friction, the ratio between the friction force and the applied normal force. 3

1.2 A schematic of an internal combustion engine. 3

1.3 A schematic of a piston ring sliding against the cylinder wall. 4

1.4 The two types of piston rings typically found in an internal combustion engine: compression rings, (a,b,c), and oil control rings, (d). The object to the left is the piston head. 5

1.5 Schematic of a journal bearing. 6

1.6 Pressure-specific volume (P-V) diagram of a material. The blue and red curves are the liquid and vapour saturation curves respectively, the black line is the line of constant temperature, and the large dot between the blue and red lines is the critical point. Liquid at pressure equal to the critical point or higher will instantly change to a vapour when the specific volume is increased. The space between the blue and red lines is the region where liquid and vapour can exist simultaneously. The point $2'$ represents the point where the material changes from a saturated liquid to a liquid-vapour mixture in the presence of impurities. 9

1.7 A plan view of a cavitated film, showing the Swift-Stieber Condition. The Swift-Stieber model requires the pressure, and the pressure gradient, to both equal zero on the cavity boundary. 12

1.8 A side-view schematic the model proposed by Mori et al. (1968). In their model, they seek the location where the shear rate relative to the flat stationary surface is zero, $\partial u / \partial y = 0$ and the pressure reduces to zero. They take this point, $x = x_s$, to be the upstream boundary of the bubble. The liquid is carried underneath the bubble by the moving surface. 13

1.9 Two types of cavitation observed by Taylor (1961, 1963). From their experiments, they hypothesise that for small capillary numbers the upstream boundary of the cavitation region forms a sharp point, and as the capillary number increases the upstream boundary forms a blunt point. 14

1.10 An $x - z$ cross-section of flow approaching an infinitely straight cavity-liquid interface with the point (c, z) is displaced to $(c + \epsilon, z)$. 16

1.11 A side view of the model proposed by Coyne and Elrod Jr. (1970). Here, liquid flows underneath a gas bubble. However, unlike Mori et al. (1968), they assume the stagnation point of the liquid, c, is not at the same location where the liquid separates from the stationary surface. 17

1.12 A plan view of the JFO model, as proposed separately by Jakobsson and Floberg (1957), Olsson (1965) and Floberg (1974). They study an infinitely wide liquid film with the upstream boundary u and downstream boundary d. 18

2.1 Sketch showing the experiment set up used by Zhu and Granick (2002c). . . 27

2.2 The maximum normal force in dimensional form vs the shear rate. The red dots are the experimental data taken from Figure 4 in Zhu and Granick (2002c) where the base fluid is tetradecane, and the green curve is the theoretical maximum of the normal force, (2.1), provided by Vinogradova (1995). 28

2.3 The slip length shown as a function of the shear rate, taken from Figure 5 from Zhu and Granick (2002c) where the base fluid is tetradecane. 29

2.4 Schematic of the model: a paraboloid radius of curvature R_c oscillates above a horizontal plane. 32

2.5 Schematic of the bubble model: after cavitation a single bubble, radius $R(t)$, of vapour forms. Inside the vapour bubble the pressure $p = p_b$, a constant. . 36

2.6 The radius of the bubble, $R(t)$, for various values of p_c. The solid curves show the numerical solution to (2.41) and the thin dashed curves show the asymptotic solution (2.52). The time of formation, t_f, the time the radius is maximum, t_{max}, and the time the bubble closes t_c are also shown. Curves show results for $p_c = 2.99$, (red); $p_c = 2.95$, (blue); $p_c = 2.9$, (black); and $p_c = 2.85$, (green). The inset shows that the maximum error between the numerical and asymptotic solutions for $R(t)$ decreases linearly as $\Delta \to 0$. . 40

2.7 The numerical values, (red dots), and asymptotic prediction equation (2.66), (blue line), of the time at which the bubble collapses. The constant A was evaluated by matching the asymptotic expression to the numerical values; this procedure suggests $A = 2.9$. 44

2.8 The radius of the vapour bubble as a function of time for strongly cavitating films. The numerical solutions of (2.39) and (2.41) are shown for various cavitation pressures (solid curves). The corresponding asymptotic predictions for when the bubble is opening, (2.63), and when the bubble is closing, (2.73), are shown as dashed curves with the parameter values $p_c = 10^{-4}$ (green), $p_c = 10^{-3}$ (blue), and $p_c = 10^{-2}$ (red). 46

2.9 Pressure profiles for the bubble model with $p_c = 1$ (red curve) and non-cavitated fluid (blue curve), at time $t_f = 2.4$. The results of the classical lubrication model, (2.27), are valid for $p_c > 3$. Note immediately outside the bubble, the pressure reduces below the cavitation pressure for $r > R(t)$. . . 47

2.10 Schematic of the mushy region model in which the volume fraction of the liquid in the cavitated region, $\theta(r,t)$, varies. 48

2.11 The radius of the mushy region, $R(t)$, for weakly cavitating films. The solid curves show the numerical solution to (2.87) and the thin dashed curves show the asymptotic solution (2.89). The time of formation, t_f, the time the radius is maximum, t_{max}, and the time the bubble closes t_c are also shown. The results of the computations are shown for $p_c = 2.99$, (red); $p_c = 2.95$, (blue); $p_c = 2.9$, (black); and $p_c = 2.85$, (green). 52

2.12 The radius of the mushy region as a function of time for various values of the cavitation pressure, $p_c \simeq 0$, (the strong cavitation regime). The solid curves are numerical solutions to (2.87), while the dashed curves show the asymptotic solutions, (2.90) as $t \to t_f$, and (2.91) as $t \to t_c$. The time of formation, t_f, the time the radius is maximum, $t = t_{max}$, and the time the mushy region closes, t_c, are indicated for $p_c = 2.99$. The red curves show $p_c = 1$, the blue curves $p_c = 0.75$, the black curves $p_c = 0.5$, and the green curves $p_c = 0.25$. 53

2.13 The dimensionless normal force F_n/π as a function of time. The green curve shows the force found with the classical lubrication model, (2.28), the red curve shows the force given by the bubble model, (2.40), and the blue curve shows the force given by the mushy region model, (2.86). The later two used a cavitation pressure of $p_c = 1$. The normal force is only affected around the times $t \approx \pi$, when there is a cavitation region. 54

2.14 Results of the control test performed by Zhu and Granick (2002c) (red dots) compared to the absolute values of the most negative normal force from the bubble model (red curve) and the mushy region model (blue curve). In this experiment they hold the mean film height fixed, (which, from the data provided, we calculated to be 20 nm) and varied the velocity between 10 and 1000 nm/s. Zhu and Granick (2002c) note it is not until the change in pressure experienced in the film approaches atmospheric pressure that they start to notice a deviation in the normal force from classical lubrication theory. 55

2.15 Results of experiments involving tetradecane and the surfactant, 1-hexadecylamine (Zhu and Granick, 2002c), (dots), compared with our models for cavitation: the bubble model and the mushy region model. We present the absolute value of the most negative normal force from the bubble model (red curves), the mushy region model (blue curves), and the maximum dimensionless normal force taken from Figure 4 in Zhu and Granick (2002c). The solid curves show the solutions with physical parameters reported by Zhu and Granick (2002c): vapour pressure, $p_{vap} = 1.5$ Pa and the amplitude of oscillation $A = 2$ nm. The dashed curves show solutions with $(p_{atm} - p_{vap})\,\omega A = 0.0018$ N/m s, thus equating the point where Zhu and Granick (2002c) first notice a deviation in their results with the point where we expect cavities to first form in the film. 56

3.1 A schematic of an engine, showing a close up view of the piston head, piston ring and cylinder wall, taken from Gilles (1996). 61

3.2 Engine cycle geometry. 62

3.3 City University of London experimental apparatus. 63

3.4 Film thickness, $H(t)$, varying with crank angle for 4 different applied normal forces (977 N/m, 1868 N/m, 2354 N/m, 2841 N/m). The frequency of oscillation in this test is 300 rpm. The film thickness was measured using the capacitance method. (Reproduced with permission from Prof. J. Nouri, 15 Jan. 2015). 64

3.5 The liquid film in the experiment at a crank angle of 40^o. The light intensity is proportional to the volume fraction of liquid in the film, i.e., the lightest areas contain only liquid and the darker areas contain a combination of liquid, gas, and vapour. The moving surface travels to the right, drawing liquid in through the upstream edge of the cavitated region, emitting it through the downstream edge. (Reproduced with permission from Prof. J. Nouri, 15, Jan., 2015). 65

3.6 The blue line shows the thickness of the liquid in a given column in the film and the red line shows the pressure profile. Both were measured relative to a fixed point on the moving glass surface. The blue dashed line shows the ring profile where the cavitated region exists in the film. The liquid separates from the ring profile at approximately 85^o, referred to as the upstream edge, and reattaches to it at approximately 93^o, referred to as the downstream edge. In this image, the moving surface is travelling to the right. (Reproduced with permission from Prof. J. Nouri, 15, Jan., 2015). 66

3.7 Schematic for the mushy region model. The bottom surface moves to the right with speed U_0. The upstream region of the liquid is to the left of the mushy region and the downstream region is to the right. 68

3.8 Schematic characteristic diagram for the mushy region model. The up- and downstream boundaries are denoted by $x = x_u(t)$ (blue curve) and $x = x_d(t)$ (red curve). The mushy region first forms at $t = 0$, with $x_u(0) = x_d(0) = x_c$. The green lines show the characteristics $x + U_0 t/2$ = constant, with the limiting characteristic $x = x_c + U_0 t/2$ marked with a dashed line. The characteristics propagate out of the upstream boundary for all time. The characteristics propagate out of the downstream boundary while $dx_d/dt > U_0/2$ (corresponding to $t < t_*$ in this schematic), and propagate into the downstream boundary while $dx_d/dt < U_0/2$ (corresponding to $t > t_*$). In the scenario depicted here, the downstream boundary is parallel to the characteristics at the critical point $(x, t) = (x_*, t_*)$. 75

3.9 The minimum film thickness as a function of time, $H(t)$ when $U_0 = 1$. The steady state asymptote (3.50)-(3.52), is shown as the thick dashed line, and the thin dashed line is the initial behaviour, (3.43)-(3.46). 78

3.10 The boundaries of the mushy region as functions of time, the red curve shows $x_d(t)$ and the blue curve shows $x_u(t)$ when $U_0 = 1$. The steady state asymptote (3.50)-(3.52), is shown as the thick dashed line, and the thin dashed line is the initial behaviour, (3.43)-(3.46). 79

3.11 Steady state solutions x_d and x_u as functions of U_0. The asymptotic expressions in the limits $U_0 \to 0$ and $U_0 \to \infty$, (3.53a), (3.53b) and (3.60a), (3.60b) are shown as dashed lines. 80

3.12 Steady state film thickness, H, as a function of U_0. The asymptotic expressions in the limits $U_0 \to 0$ and $U_0 \to \infty$, (3.53c) and (3.60c) are shown as dashed lines. 81

3.13 The linear decay rate λ as functions of U_0. For $U_0 > 49.5$, there are three real decay rates, and for $U_0 < 49.5$ two of those become complex. We observed that for all values of U_0, the real parts of all the linear decay rates are positive, showing that the solution is stable. The dashed line shows the asymptotic for the largest rate of decay, expressed in (3.71). 84

3.14 Graph showning the positions of x_u and x_d versus $1 - U_0(t)/\hat{U}_0 = 2\alpha t$, for four values of α. The parameters used in the computation are $\hat{U}_0 = 1$ and $\alpha = 10^{-4}$, 10^{-3}, 10^{-2} and 10^{-1}. The quasi-steady solution, shown as a dashed line, closely resembles the closing of the mushy region model in the limit $\alpha \to 0$ when $U_0(t)/\hat{U}_0 \approx 1$, but the similarity no longer holds as $U_0(t) \to 0$. 87

3.15 Graph showing the minimum film thickness H for the dynamic model and the quasi-steady model, plotted against $1 - U_0(t)/\hat{U}_0$ $(= 2\alpha t)$. The parameters used in the computation are $\hat{U}_0 = 1$ and $\alpha = 10^{-4}$, 10^{-3}, 10^{-2} and 10^{-1}. The quasi-steady solution closely resembles the dynamic model in the limit $\alpha \to 0$ when $U_0(t)/\hat{U}_0 \approx 1$. 88

3.16 Experimental data showing the film thickness, $H(t)$, against time in dimensionless form. All sixteen tests are shown, varying with the frequency: $\omega = 300$ rpm, (black data point); 400 rpm, (red data points); 500 rpm, (blue data points); and 600 rpm, (green data points); and with the normal force: $F = 977$ N/m, (dots, ·); 1868 N/m, (crosses, +); 2354 N/m, (circles, o); and 2841 N/m, (asterisks, *). 91

3.17 Pressure profile of the film when the second mushy region forms, $t = t_{2c}$. The green dot shows the location of the minimum pressure, $x = x_{2c}$. Parameters used in this computation are $\delta = 10^{-2}$ and $\Omega = 1$. 97

3.18 Schematic of the model showing the two mushy regions, 1 and 2, and the liquid regions u, M and d. 98

3.19 Film thickness during the first half of the period of oscillation, $0 < t < \pi$, solved using equations (3.89)-(3.91), (3.100)-(3.103), and (3.126)-(3.129), with different initial film thicknesses: red line, $H_0 = 0.01$; blue line, $H_0 = 0.1$; black line, $H_0 = 1$; brown line, $H_0 = 10$; and green line, $H_0 = 100$. Regardless of the initial film thickness, the film thickness at $t = \pi$ is the same for all. In this computation we used the parameters $\delta = 0.01$ and $\Omega = 1$. 102

3.20 $x - t$ diagram showing the boundaries of the mushy region over the time, $0 < t < 2\pi$, solved using equations (3.89)-(3.91), (3.100)-(3.103), and (3.126)-(3.129). The blue curves show the 'inside' boundaries, $x_u(t)$, $x_{2d}(t)$ and $x_{1u}(t)$, and the red curves show the 'outer' boundaries, $x_d(t)$, $x_{1d}(t)$ and $x_{2u}(t)$. Three solutions are shown with varying values of δ: $\delta = 10^{-1}$, (thin line), $\delta = 10^{-2}$, (medium line), and $\delta = 10^{-3}$, (thick line); Ω was kept constant at $\Omega = 1$. 103

3.21 the film thickness $H(t)$ varying with time, $0 < t < 2\pi$, solved using equations (3.89)-(3.91), (3.100)-(3.103), and (3.126)-(3.129). Three solutions are shown with varying values of δ: $\delta = 10^{-1}$, (thin line), $\delta = 10^{-2}$, (medium line), and $\delta = 10^{-3}$, (thick line); Ω was kept constant at $\Omega = 1$. The dashed curve shows the quasi-steady solution, (4.19). 104

3.22 $x - t$ diagram showing the boundaries of the mushy region over the time, $0 < t < 2\pi$, solved using equations (3.89)-(3.91), (3.100)-(3.103), and (3.126)-(3.129). The blue curves show the 'inside' boundaries, $x_u(t)$, $x_{2d}(t)$ and $x_{1u}(t)$, and the red curves show the 'outer' boundaries, $x_d(t)$, $x_{1d}(t)$ and $x_{2u}(t)$. Three solutions are shown with varying values of Ω: $\Omega = 10$, (thin line), $\Omega = 1$, (medium line), and $\delta = 0.1$, (thick line); δ was kept constant at $\delta = 10^{-2}$. 105

3.23 the film thickness $H(t)$ varying with time, $0 < t < 2\pi$, solved using equations (3.89)-(3.91), (3.100)-(3.103), and (3.126)-(3.129). Three solutions are shown with varying values of Ω: $\Omega = 10$, (thin line), $\Omega = 1$, (medium line), and $\delta = 0.1$, (thick line); δ was kept constant at $\delta = 10^{-2}$. 106

3.24 The volume fraction plotted against x at three times throughout the lifetime of the first mushy region, $t = 0.14$, $t = 1.7$, and $t = 3.2$. The final image was taken immediately prior to the closure of the first mushy region, and hence has reduced to a single point. Parameters in this figure are those from test number 1 with parameters: $\delta = 10^{-2}$ and $\Omega = 1$. 107

3.25 The pressure profile in the film, the red curve is shown immediately before the first mushy region closes, $t = t_f^-$, and the blue curve shows it immediately afterwards, $t = t_f^+$. The black line shows the pressure inside the mushy region, and the boundaries of the mushy region are also noted, $x_{2u}(t_f)$, $x_{2d}(t_f^-)$, $x_{1u}(t_f)$, $x_{1d}(t_f)$, and $x_u(t_f^+)$. Parameters used in this figure are: $\delta = 10^{-2}$ and $\Omega = 1$. 108

4.1 The right hand panel shows the $x - t$ diagram of the asymptotic solutions discussed in this chapter. Each section is represented by a different colour: the quasi-steady solution in Section 4.2 is shown as dark blue; the unsteady downstream boundary in Section 4.3 as light green; the unsteady upstream boundary in Section 4.4 as light blue; the secondary cavitation in Section 4.5 as red; the interaction between the mushy regions in Section 4.6 as black; and the change in causality for the upstream boundary of the mushy region in Section 4.7 as dark green. Asymptotic solutions shown here were calculated with parameter values $\Omega = 1$ and $\delta = 10^{-3}$. The left hand panel is the velocity profile, $u = \sin(t)$. 112

4.2 The maximum film thickness, determined numerically (blue dots), converges to the asymptotic prediction (4.21) (red line). In Section 4.2.2, we shall see that the first order correction to the maximum film thickness is at $O(\delta^{2/3})$; motivated by this we use $\delta^{2/3}$ as the abscissa. 116

4.3 Solution $X(T)$ of the problem (4.46). The thick dashed curve shows the leading-order behaviour (4.47) as $T \to -\infty$; and the thin dashed curve shows (4.50), which is valid as $T \to T_f$. 121

4.4 The time the mushy region closes, t_f plotted against δ, with $\Omega = 1$. The black curve shows the asymptote (4.49), and the blue dots show the time at which the the mushy region closes, as calculated from the numerical solution. The inset shows the error between the numerical solution and the asymptote reduces as $\delta \to 0$; we shall also provide a second order correction to (4.49) in Section 4.6. 122

4.5 Plot of $X(T) + 3T^2/10$ against T, where $X(T)$ is the solution of the problem (4.46). The quantity remains positive for all $T < T_f = 1.10$. 122

4.6 Numerical solution of the problem (4.79) for $X(T)$. The thin, blue, dashed curves show (4.80) as $T \to \infty$ and (4.81) as $T \to 0$. The thick, black, dashed lines indicate $X = X_c \approx 1.0928$ at $T = T_c \approx 2.0695$, which is the time when the characteristics are tangent to the upstream boundary. The inset shows $X(T)T$ against T as $T \to 0$, and extrapolating this to the y-axis we find $X(T)T \to 1.43$. 127

4.7 The function $R(T)$ defined by equation (4.82). The dashed lines show $R(T_c) = 0$, at which point the characteristics no longer travel outwards from the upstream boundary. 128

4.8 At time $t = t_2$, the upstream boundary is tangent to the characteristics. We show this physically with the numerical solutions to (3.89)-(3.91), (3.100)-(3.103), and (3.126)-(3.129) with parameters $\delta = 10^{-2}$ and $\Omega = 1$, as the red and blue curves. The green curves are the characteristics from equation (3.31).128

4.9 The time when the characteristics start to intersect the upstream boundary. The numerics are shown as the blue dots, (calculated with $\Omega = 1$), and the red curve is the asymptote, $-t_2 = T_c\delta^{2/3}$. 129

4.10 The scaled minimum thickness $\bar{H}(T)$ plotted versus $T = -\bar{t}$. The solid curve shows the numerical solution (4.79), and the dashed line shows the far-field behaviour (4.83). 129

4.11 The scaled upstream free boundary $\bar{x}_u(T)$ plotted versus $T = -\bar{t}$. The dashed curve shows the far-field behaviour (4.83). The minimum $\bar{x}_u(T)$ is $\bar{x}_{um} \approx 3.93$, which is attained at $T = T_{xm} \approx 5.77$. 131

4.12 The function F defined by (4.89) against $\xi = \sqrt{6TY\big(X(T)\big)\,X(T) + T^2/4}$. The dashed line shows the far-field behaviour (4.92); the dashed line in the inset shows the behaviour (4.95) of $F(\xi)$ close to the critical value $\xi_c \approx 6.00$. 132

4.13 The solutions $X(T)$ and $\bar{H}(T)$ to the problem (4.101)-(4.102) with the initial value (4.107), and the position of the free boundary $\bar{x}_u = (2\bar{H})^{1/2}\, X$, with $\epsilon = 10^{-4}$. 135

4.14 The film thickness, $\bar{H}$, evaluated at $T = 0$ varying with changes in ϵ. For $\epsilon \approx 10^{-4}$, no change in $\bar{H}(0)$ was observed, indicating the solution is insensitive for values of ϵ approximately less than this. 136

4.15 The pressure profile of liquid in the film when $t = \delta\acute{t}_{2c}$, the time when the pressure equals the cavitation pressure on the other side of the film and a second mushy region forms. The parameters used in the computation are $\delta = 10^{-2}$ and $\Omega = 1$. The position of the newly cavitated region is shown as the green dot. 138

4.16 The time the second mushy region opens, t_{2c} plotted against δ, with $\Omega = 1$. The red line shows the asymptote $t_{2c} = \delta\acute{t}_{2c}$, with $\acute{t}_{2c}$ given by (4.117); the blue dots show the numerically determined time at which the mushy region forms. 139

4.17 The numerically determined evolution of $X_1\,(\bar{t})$ and $-X_2\,(\bar{t})$ (obtained by solving the system (4.147)-(4.148) subject to the initial condition (4.149) and (4.150). The dashed lines show the small-$\bar{t}$ behaviour (4.149) and (4.150) and the large-$\bar{t}$ asymptotic behaviour (4.160) and (4.155). 145

4.18 The normalized position $\bar{x}_{1u}$ of the upstream boundary of the first mushy region, plotted versus normalized time $\bar{t}$. The dashed line shows the large-$\bar{t}$ behaviour, (4.161). 145

4.19 The normalized position $-\bar{x}_{2d}$ of the downstream boundary of the second mushy region, plotted versus normalized time $\bar{t}$. The dashed lines show the small-t behaviour (4.153) and the large-$\bar{t}$ behaviour (4.161). 146

4.20 The normalized film thickness $\bar{H}$ versus normalized time $\bar{t}$ as determined numerically. The dashed line shows the large-$\bar{t}$ behaviour (4.161). The minimum film thickness is $\bar{H}_m \approx 4.698$ and is attained at $\bar{t} = \bar{t}_{Hm} \approx 2.435$. . . . 146

4.21 The minimum film thickness computed in the numerical solution, (blue dots), recovers the asymptotic result $H \sim \bar{H}_m \delta^{2/3}$ (red line), as $\delta \to 0$. Here, $\Omega = 1$. 147

4.22 The time at which the mushy region closes, t_f, plotted against δ, with $\Omega = 1$. Main Figure: the numerically determined value for t_f are shown (dots) together with the leading order asymptotic result (4.49) (black curve). The second order asymptotic result (4.163), (red curve), agrees much better with the numerical results. The inset shows the error between the numerical solution and the two asymptotic results (4.49) (black dots), and (4.163) (red dots). 149

4.23 At time $t = t_1$, the upstream boundary is tangent to the characteristics. We show this physically with the numerical solutions to (3.89)-(3.91), (3.100)-(3.103), and (3.126)-(3.129) with parameters $\delta = 10^{-2}$ and $\Omega = 1$, as the red and blue curves. The green curves are the characteristics from equation (3.31).151

4.24 The time at which the characteristics start to intersect the upstream boundary of the second mushy region, t_1, when $\Omega = 1$. Numerical results are shown as the blue dots while the red line shows the asymptote $t_1 = \delta^{2/5}\hat{t}_1$, and $\hat{t}_1$ comes from (4.176). 152

4.25 The function $\Phi(\zeta)$ defined by equation (4.187). The solution exhibits a square root behaviour at $\zeta = -5/6$ which corresponds to the tangency of the characteristics to the free boundary at $\hat{t} = \hat{t}_c$. 154

4.26 Numerical solution $\Phi(T)$ of the ODE (4.197) subject to the initial condition (4.199) with $\epsilon = 10^{-4}$. 156

4.27 normalized free-boundary position $X(T) = \hat{x}_{2u}/\hat{x}_{2u1}$. The dashed curve shows the large-T behaviour (4.203). For $1 < T \leq T_s$, $X(T)$ is given by equation (4.195), where $\Phi(T)$ is the function plotted in Figure 4.26 (and determined numerically); for $T > T_s$, $X(T)$ is found by solving equations (4.201)-(4.202) numerically. 157

4.28 The film thickness $H(t)$ of a periodic solution calculated with $\delta = 10^{-3}$ and $\Omega = 1$. The numerical solution approximates the asymptotic solution so closely it is difficult to differentiate between them. The thick solid curve shows the numerical solution, (3.89)-(3.91), (3.100)-(3.103), and (3.126)-(3.129) the thin solid curve shows the quasi-steady solution, (4.19), and the thin dashed curve shows the dynamic solution, (4.79), (4.101) and (4.102), (4.147) and (4.148), with their respective scaling. 158

4.29 The $x-t$ diagram of a periodic solution calculated with $\delta = 10^{-3}$ and $\Omega = 1$. The numerical solution approximates the asymptotic solution so closely it is difficult to differentiate between them. The blue curves show the upstream boundaries, $x_u(t)$, $x_{2d}(t)$ and $x_{1u}(t)$, and the red curves show the downstream boundaries, $x_d(t)$, $x_{1d}(t)$ and $x_{2u}(t)$. The thick solid curves show the numerical solution,(3.89)-(3.91), (3.100)-(3.103), and (3.126)-(3.129), the thin solid curves show the quasi-steady solution, (4.19) and (4.29), and the thin dashed curves are the dynamic solution, (4.46), (4.79), (4.101) and (4.102), (4.122), (4.129), (4.147) and (4.148), (4.197) and (4.201), with their respective scaling. 159

4.30 The quantity $H_{max}F/\left[3(1-\beta^2)UR_c\right]$ calculated for each of the 16 experimental runs performed by Nouri (2016), plotted as a function of $\omega^{1/3}/F$. Runs varied the oscillation frequency: $\omega = 300$ rpm, (black data points); 400 rpm, (red data points); 500 rpm, (blue data points); and 600 rpm, (green data points); and the normal force: $F = 977$ N/m, (dots, $\cdot$); 1868 N/m, (crosses, +); 2354 N/m, (circles, o); and 2841 N/m, (asterisks, *). The black solid line is the line of best fit to the data, $y = -13.963x + 0.0366$. 161

4.31 Comparison between four experimental sets of data and the numerical and quasi-steady solutions of our model. The thick solid curves are the numerical solution, (3.89)-(3.91), (3.100)-(3.103), and (3.126)-(3.129), the thin solid curves are the quasi-steady solution, (4.19) and (4.29), and black dots are the experimental data. 162

4.32 The friction force, F_{fric}, in the oscillatory solution against time, $0 < t < 2\pi$, solved using equations (4.207). The black curve shows the numerical solution, while the black dots show the experimental data. Parameters in this figure are those from test number 1 with parameters: $\delta = 0.028$ and $\Omega = 1.74$. . . 164

5.1 Schematic of the mushy region model with boundary conditions located at $x = \pm a$. 173

5.2 Ring profile used in the City Experiments, shown in red, and the parabola $y = x^2/(2R_c)$, shown in blue. 174

5.3 Comparison of the boundaries of the mushy region, x_d (red curves), and x_u (blue curves), when the ring boundaries are at $x = \pm a$. Four computations are shown with $a = 1$, 2, 5, and 10. The solid curves show the numerical solutions to the mushy region model with the edges of the top surface located symmetrically about the origin, $x = \pm a$, solved using equations (3.89), (3.91), (3.92), (3.100)-(3.105), (3.126)-(3.131), and (5.13), and dashed curves show the infinite boundary case, $a \to \pm\infty$, solved with equations: (3.89)-(3.92), (3.100)-(3.105), (3.126)-(3.131). In each of the solutions, the parameters used are $\delta = 0.01$ and $\Omega = 1$. 175

5.4 The effect of a finite ring width on the evolution of the film thickness, H. The solid curves show the numerical solutions to the model with the pressure boundary conditions located symmetrically about the origin, $x = \pm a$, solved using equations (3.89), (3.91), (3.92), (3.100)-(3.105), (3.126)-(3.131), and (5.13), and dashed curves show the infinite boundary case, $a \to \pm\infty$, solved with equations: (3.89)-(3.92), (3.100)-(3.105), (3.126)-(3.131). In each of the solutions, the parameters used are $\delta = 0.01$ and $\Omega = 1$. 176

5.5 Comparing the film thickness for four sets of data from the City Experiments (black dots) and the numerical solutions for the mushy region with the pressure boundary conditions implemented at infinity, (dashed curves), (solved using equations (3.89)-(3.92), (3.100)-(3.105), (3.126)-(3.131)), and $x = \pm a$, (solid curves), (solved using equations (3.89), (3.91), (3.92), (3.100)-(3.105), (3.126)-(3.131), and (5.13)). The position at which the pressure boundary condition is implemented corresponds to the edges of the ring profile. 177

5.6 The boundaries of the mushy region as a function of time over the period of oscillation with x_d (red curve), and x_u (blue curve). Solid curves show the numerical solution with the pressure boundaries implemented at $x = \pm a$, (solved using equations (3.89), (3.91), (3.92), (3.100)-(3.105), (3.126)-(3.131), and (5.13)); dashed curves show the numerical solutions when $a \to \pm\infty$, (solved using equations (3.89)-(3.92), (3.100)-(3.105), (3.126)-(3.131)). We only show how x_u and x_d for a single solution, (test 1, $a = 7.91$, $\delta = 0.028$, $\Omega = 1.74$), because each solution shows qualitatively similar. 178

5.7 The effect of ring asymmetry on the film thickness. To obtain these solutions, we solved equations (3.89), (3.91), (3.92), (3.100)-(3.105), (3.126)-(3.131), (5.13), and (5.14) with parameters: $a = 10$, $\delta = 10^{-2}$, $\Omega = 1$ and four values of $\epsilon = 1$, 2, 5, and 8. The thinnest curve shows $\epsilon = 1$, the thickest curve shows $\epsilon = 8$, and the dashed curve shows the symmetric case $\epsilon = 0$. 180

5.8 We study the effect of asymmetry on the boundaries of the mushy region, shown as a function of time with x_d (red curve), and x_u (blue curve). The asymmetric model, shown as the solid curves, solved equations (3.89), (3.91), (3.92), (3.100)-(3.105), (3.126)-(3.131), (5.13), and (5.14) with parameters: $a = 10$, $\delta = 10^{-2}$, $\Omega = 1$, and four values of ϵ. 181

5.9 Pressure in the film with an increasing degree of asymmetry at two different times in the period of oscillation. Numerical solutions solve equations (3.89), (3.91), (3.92), (3.100)-(3.105), (3.126)-(3.131), (5.13), and (5.14) with parameters: $a = 10$, $\delta = 10^{-2}$, $\Omega = 1$, and four values of ϵ (1, 2, 5, and 8). The thinnest curve shows $\epsilon = 1$, the thickest curve shows $\epsilon = 8$, and the dashed curve shows the symmetric case $\epsilon = 0$. The blue curves show the pressure upstream of the mushy region, the red curves show the pressure downstream of the mushy region, and the black curve shows the pressure in the mushy region. 182

5.10 The upper and lower maximum film thickness, shown as red and blue dots respectively, over the range $0 < \epsilon < 8$. We note for small values of ϵ, the asymmetry between these two beaks increases in proportion to the asymmetry in the ring profile. Equations used to produce these solutions are (3.89), (3.91), (3.92), (3.100)-(3.105), (3.126)-(3.131), (5.13), and (5.14), with parameters: $a = 10$, $\delta = 10^{-2}$, and $\Omega = 1$. 183

5.11 Ring profile used in the City Experiments, shown in red, the parabola with the offset, $y = (x + \epsilon)^2/2$, shown in blue, and the parabola $y = x^2/2$ without the offset, shown as a black dashed curve. In order to explain the asymmetry of the experimental results, ϵ would have to be of the order $\epsilon \approx 3.5$. We conclude the ring profile does not exhibit this degree of asymmetry, and so the asymmetry included in this model cannot fully explain the asymmetry in the experimental results. The ring profile was non-dimensionalized using parameters from test 1, $F = 977$ N/m and $\omega = 300$ rpm. 184

5.12 A diagram of a Scotch Yoke mechanism, as used in the City Experiments. A circular disk rotates in the clockwise direction which causes the horizontal movement of the mass M. 185

5.13 The velocity of the bottom surface against t for different values of ϵ: $\epsilon = 0$ case is the dashed curve, and the solid curves show $\epsilon = 0.1$ (thin curve), 0.2 (middle curve), and 0.3 (thick curve). 185

5.14 The boundaries of the mushy region as functions of time over the period of oscillation with x_d (red curve), and x_u (blue curve). Solutions were computed for four values of ϵ: 0, (dashed curve), and the solid curves show $\epsilon = 0.1$ (thin curve), 0.2 (middle curve), and 0.3 (thick curve). These solutions were obtained by solving equations (3.89)-(3.91), (3.100)-(3.103), (3.126)-(3.129), and (5.15) numerically with parameters $\delta = 10^{-2}$ and $\Omega = 1$. 186

5.15 The film thickness against t for different values of ϵ: $\epsilon = 0$ case is the dashed curve, and the solid curves show $\epsilon = 0.1$ (thin curve), 0.2 (middle curve), and 0.3 (thick curve). These solutions were obtained by solving equations (3.89)-(3.91), (3.100)-(3.103), (3.126)-(3.129), and (5.15) numerically, with parameters $\delta = 10^{-2}$ and $\Omega = 1$. 187

5.16 Schematic diagram showing the rotation of the crankshaft in relation to the motion of and piston head along the bore centre-line of an engine. 188

5.17 On the right-hand axis we show how the gas pressure, p_{ch}, in the combustion chamber varies as the fuel is ignited. The gas may flow between the piston head and piston ring, causing an additional normal force on the liquid film separating the piston ring and cylinder wall (a schematic of the piston head geometry is shown in Figure 1.3). The magnitude of this additional force could be as large as 10 times that of the diametral tension of the ring, motivating us to investigate the effect it has on the liquid film. On the left-hand axis, we show the normal force exerted on the liquid film used to develop the numerical solutions for this model, as described in (5.23). Three values of ΔF are shown: 5, (thin curve); 10, (middle curve); and 15, (thick curve). We chose the offset $T = 0.436$, so the peak in the normal force occurs at the same time as the peak in the gas pressure. 191

5.18 The film thickness as a function of time with variable applied force. We show four solutions, varying with the size of the non-uniformity in F, ΔF : 0, (dashed curve); 5, (thin solid curve); 10, (middle solid curve); and 15, (thick solid curve). Solutions are plotted from the numerical solutions to equations (3.89)-(3.91), (3.100)-(3.103), (3.126)-(3.129), and (5.23) with parameters $\delta = 10^{-2}$, $\Omega = 1$, and $T = 0.436$. 192

5.19 Boundaries of the mushy region, as functions of time with x_d (red curves) and x_u (blue curves). We show four solutions, varying with the size of the non-uniformity in the normal force, $\Delta F : \Delta F = 0$, (dashed curve); $\Delta F = 5$, (thin solid curve); $\Delta F = 10$, (middle solid curve); and $\Delta F = 15$, (thick solid curve). Solutions are plotted from the numerical solutions to equations (3.89)-(3.91), (3.100)-(3.103), (3.126)-(3.129), and (5.23) with parameters $\delta = 10^{-2}$, $\Omega = 1$, and $T = 0.436$ 193

List of Tables

4.1 Parameter values for each of the 4 tests. 162

4.2 The relaxation time-scale, $\check{T}_S$, calculated using equation (3.74), and the period of oscillation for each of the four tests. 163

Chapter 1

Introduction

Wear is a key consideration when designing an engine[1]. It determines the life expectancy of the engine, and by studying the wear rates of various parts of the engine it is possible to estimate those which need to be replaced the most frequently. Replacing broken or disabled components can be time consuming, costly, and dangerous, risking the chances of engine failure. Several categories of wear exist, and can be broadly categorised into seven types (Stachowiak and Batchelor, 2013):

- adhesive wear: which is generally found between surfaces during frictional contact,
- abrasive wear: which occurs when a hard, rough surface slides against a softer surface, analogous to ploughing a field,
- surface fatigue: which occurs where the surface of a material is weakened by cyclic loading,
- fretting wear: which is the process of repeated rubbing of two solid surfaces against each other, and fretting wear typically occurs in bearings,
- erosive wear: which involves the direct impact of solid or liquid particles against a surface, analogous to asteroids hitting the earth,
- cavitation wear: which involves the sudden collapse of cavitation bubbles in bearings, turbines, and propeller blades impacting the solid surfaces,
- corrosive and oxidation wear: which is the process of a chemical reaction that corrodes a surface, forming a surface film of a new material which is removed through another

---

[1] http://academica-e.unavarra.es/bitstream/handle/2454/3885/577521.pdf?sequence=4, accessed 21-March-2016

type of wear.

Friction is another area of concern for engine manufacturers. Modern petrol internal combustion engines typically operate at only 15% efficiency, with energy being lost though many different avenues; a large component of that being through friction[2].

Engine manufacturers use lubricants to mitigate the risk of failure. A lubricant is any substance that reduces either the wear or friction, or both, between two solid surfaces sliding relative to each other. Lubricants reduce wear by separating the solid surfaces, preventing contact (Fusaro, 1981). The thickness of the gap separating the solid surfaces is related to the viscosity of the liquid; a liquid with a larger viscosity results in a larger separation gap and hence less wear[3]. Conversely, friction between two sliding solid surfaces can be reduced by lowering the viscosity of the separating lubricant. BP, who are the CASE collaborators on this study, are interested in finding a solution that minimizes both wear and friction, and thus are presented with a dilemma: a lubricant with a smaller viscosity will reduce the friction inside an engine, but may increase the wear. Conversely a liquid with a larger viscosity will increase the friction in the engine, but will generally decrease the wear of surfaces[4].

The balance between friction and wear is often aided by a graph referred to as the Stribeck Curve, shown in Figure 1.1, as shown in Heshmat (2010). In this graph, the coefficient of friction (the ratio of the friction force to the applied normal force) is plotted against the 'Stribeck Number' which is defined to be the product of the speed of the moving surface U and the viscosity of the liquid separating the solids μ, over the applied normal force F. The Stribeck Curve is generally divided into three sections, characterised by the roughness on both of the surfaces relative to the mean film thickness that separates them. We describe the different regimes of the Stribeck Curve below.

The first section is the 'full film regime', shown as the inset to the right in Figure 1.1. The solid surfaces are rough, with many asperities, but the surfaces are separated by a sufficiently large thickness. Due to the lack of contact between the surfaces, one would expect a low degree of wear on the surfaces bounding the film. However, the friction caused by the liquid in this regime is considerable. At the other extreme of the Stribeck Curve is the 'boundary regime', shown in the inset to the left in Figure 1.1. In this regime, the lubricant has very little effect since the two solid surfaces are in nearly complete contact,

---

[2] http://www.consumerenergycenter.org/transportation.html, accessed 21-March-2016.

[3] http://www.machinerylubrication.com/Read/586/viscosity-coefficient-bearing

[4] https://www.princeton.edu/ asmits/Bicycleweb/frictionflows.html

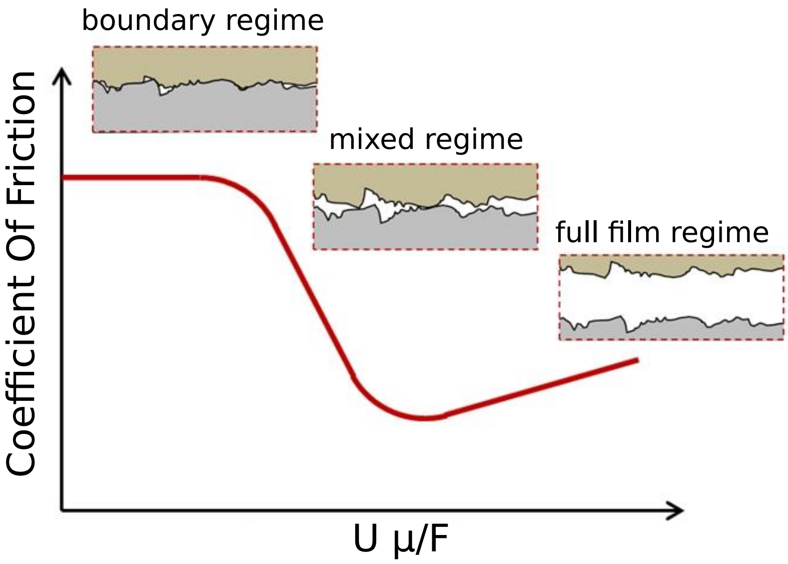

Figure 1.1: The Stribeck Curve, as shown in Heshmat (2010). On the horizontal axis is the 'Stribeck Number' which is the product of the speed of the moving surface U, and viscosity of the liquid μ, over the applied normal force F, and on the vertical axis is the Coefficient of Friction, the ratio between the friction force and the applied normal force.

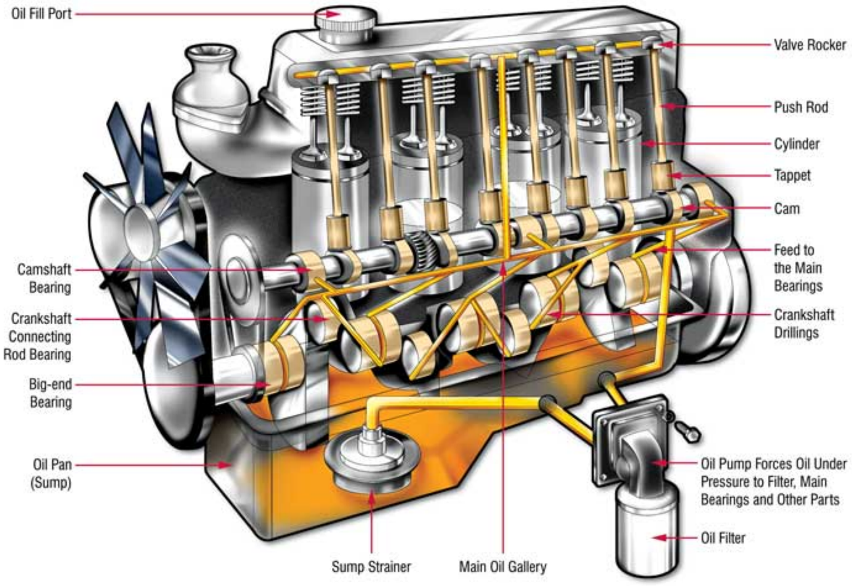

Figure 1.2: A schematic of an internal combustion engine.

i.e. the film thickness is significantly smaller than the asperity height of the surfaces. As the Stribeck Number approaches zero, i.e. $U\mu/F \to 0$, the moving surfaces experience dry friction, and the coefficient of friction approaches a constant, often referred to as the coefficient of kinetic friction. Between these regimes of friction there is a minimum in the coefficient of friction which occurs in the 'mixed regime'. We see from the inset, shown in the middle of Figure 1.1, that the height of the asperities is comparable with the film

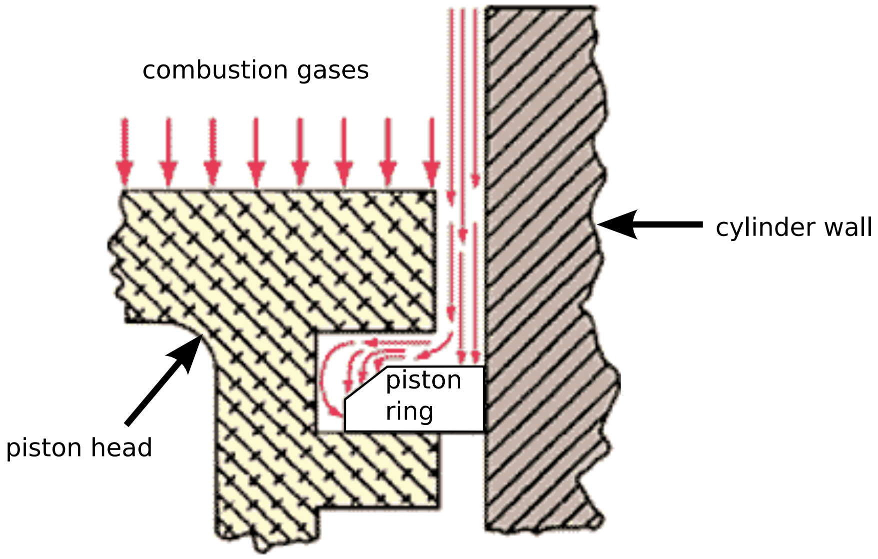

Figure 1.3: A schematic of a piston ring sliding against the cylinder wall.

thickness that separates them, but the liquid separates the solid surfaces sufficiently, so that the wear of the surfaces is reduced[5].

We now briefly describe the historical background of lubricant films, discussing the relevant academic literature currently available.

1.1 Lubricant Films in Engines

Lubricant films are used in many different locations within an engine. Areas that are of particular interest to BP include the space between the camshaft and tappet, inside bearings, and between the piston rings and cylinder wall, to name a few. In Figure 1.2[6] we show a schematic of an engine and various locations where lubricants exist in it. The lubricant is circulated throughout all of these components; it is first pumped up to the top of the engine near the camshaft and through gravity it is supplied to the different parts of the engine, finally reaching the oil pan where it is filtered. Lubricants are generally composed of two components: a base oil and various additives. In general, lubricant additives are designed to act as either a dispersant, a substance that prevents foreign bodies from clumping together and forming larger pieces, or a detergent, a substance that prevents foreign bodies from settling in a film by holding them in suspension and transporting them through the liquid. Additives may be designed to operate in specific parts of the engine, or under extreme conditions such as high or low pressures or ambient temperatures.

---

[5] http://www.stle.org/files/Whatistribology/Tribology.aspx, accessed 21-March-2016.

[6] http://www.lubrita.com/news/78/671/How-The-Lubrication-System-Works-In-An-Engine/, accessed 17-March-2016.

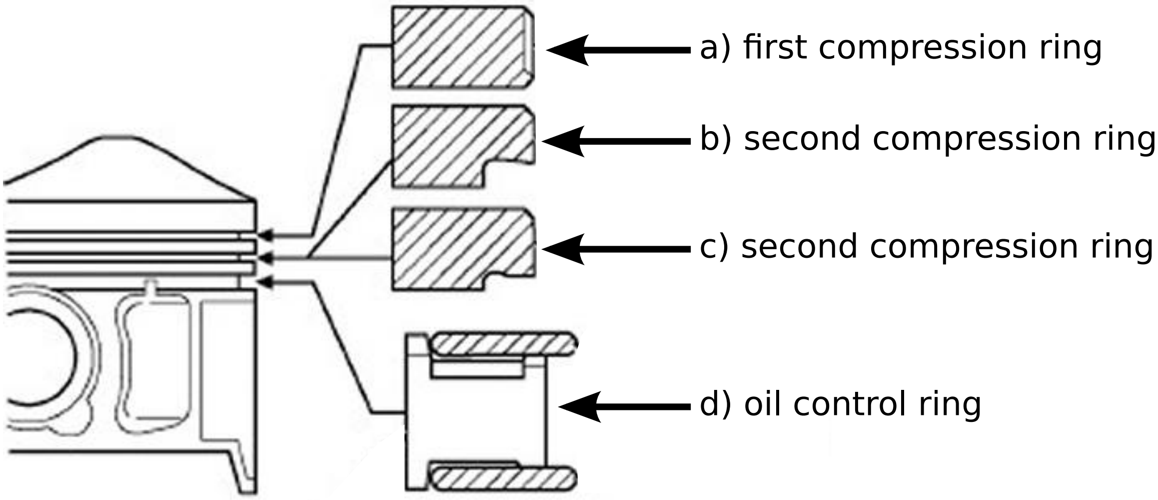

Figure 1.4: The two types of piston rings typically found in an internal combustion engine: compression rings, (a,b,c), and oil control rings, (d). The object to the left is the piston head.

In this thesis, we mainly focus on the liquid film between the piston ring and cylinder wall of a combustion chamber of an internal combustion engine. An example of a slider bearing is shown in Figure 1.3[7]. This situation is considered to be one of the harshest environments in which lubricants are used as it contains gases and other products of combustion from the combustion chamber. The rapid rise in heat in the chamber causes the thermal expansion of the piston head and ring, squeezing the lubricant out. High pressures in the film cause the liquid to thicken and at the same time the liquid experiences high degrees of shear from the oscillatory movement of the piston head. As the piston head moves, the piston rings may vibrate in the grooves which they are fitted into and may cause an unintended disturbance to the liquid film.

To clarify, piston rings are categorized into two main types: compression rings and oil control rings, and depending on the type of engine, there are usually between 2-5 rings in each piston (Andersson et al., 2002). Compression rings are primarily designed to seal off the combustion chamber, preventing the combustion gases and lubricant from mixing. They do this by ‘scraping’ the lubricant off the cylinder wall on the down stroke of the engine, and in some cases using the high chamber pressure to eliminate gaps which the fluids may be able to pass through. In contrast to a compression ring, an oil control ring is designed to ensure the space between the cylinder wall and piston head is well lubricated. Here, the

---

[7] http://jobspapa.com/diesel-engine-diagram.html, accessed 17-March-2016

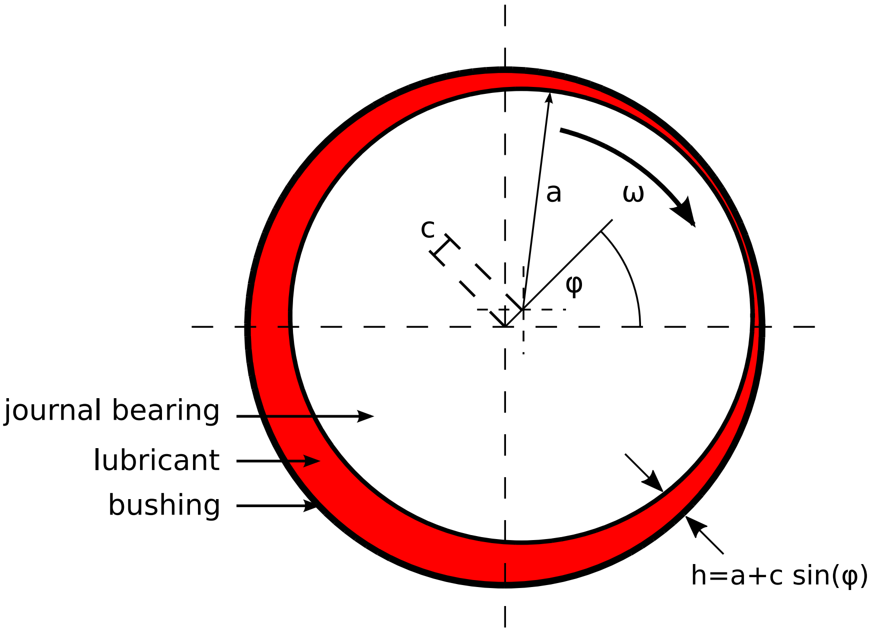

Figure 1.5: Schematic of a journal bearing.

lubricant film helps prevent the piston head from vibrating uncontrollably and causing wear to other parts of the engine. Typical designs of a compression ring and oil control rings are shown in Figure 1.4[8].

1.1.1 Literature review of lubricant films

Hamrock et al. (2004) provides a detailed analysis of liquid lubricant films in engines. The first person to describe the flow of a lubricant was Osborne Reynolds (Reynolds, 1886). Reynolds attempts to understand the flow around a journal bearing which is a cylindrical mass with radius a, rotating at speed ω, and is housed inside a bushing, as shown in Figure 1.5. Reynolds assumes the film thickness, h, is sufficiently thin compared to the length of the film, such that the inertial forces and body forces of the liquid can be neglected. Choosing to balance the pressure gradient with the viscous term in the Navier-Stokes equation, Reynolds finds that the pressure gradient can be described as a function of a single variable, ϕ, the angular displacement in the bearing, by solving

$$\frac{1}{a^2}\frac{d}{d\phi}\left(\frac{h^3}{6\mu}\frac{dp}{d\phi}\right) = \omega\frac{dh}{d\phi}. \tag{1.1}$$

Equation (1.1) is the "Reynolds Equation", where μ is the viscosity of the liquid, the film thickness has the form $h = a + c\sin(\phi)$, and c is the displacement of the journal from the centre of the bushing, which is also referred to as the eccentricity. In deriving the Reynolds

---

[8] http://www.marineinsight.com/tech/proceduresmaintenance/, accessed 17-March-2016

equation, Reynolds (1886) assumed the liquid on the solid surface was moving with the surface and so used the no slip boundary conditions,

$$u_\phi = \omega a \text{ and } u_r = 0 \text{ on } r = a, \tag{1.2}$$

on the journal bearing surface and

$$u_\phi = 0 \text{ and } u_r = 0 \text{ on } r = h, \tag{1.3}$$

on the bushing surface, where u_ϕ and u_r are the tangential and radial velocities of the liquid respectively. In certain situations, these conditions do not accurately represent the physics at the solid boundary (such as a rough surface), in which case it is common to introduce a slip length so the liquid can 'slip' past the solid surface.

More recently, Myers et al. (1991) present a study of the elastohydrodynamic domain of a lubricant film. Their model includes two dimensionless parameters: the pressure-viscosity coefficient, c_{p-v}, that determines the influence the pressure has on the viscosity, and the elastic deformation coefficient, c_E, which determines the ratio between the modulus of elasticity and the applied pressure. They partition the solution space into five main regions: rigid-isoviscous region (small c_{p-v} and c_E), rigid-piezoviscous region (small c_E and large c_{p-v}), elastic-isoviscous region (small c_{p-v} and large c_E), the transition region between the rigid-piezoviscous and elastic-isoviscous regions (moderate levels of c_{p-v} and c_E), and finally the elastic-piezoviscous region (large c_{p-v} and c_E). They also show how the minimum film thickness varies with the coefficients c_{p-v} and c_E in each of the respective regions.

Hsu et al. (1988) consider how a lubricant film affects various processes of wear from solid surfaces. Linking complex chemical phenomena to mechanical and material properties, they propose a statistical calculation to determine the effectiveness of a lubricant operating between two moving solid surfaces. They suggest, that by determining the density and distribution of asperities on two given surfaces, it would be theoretically possible to predict the force required to shear off asperities when they collide. Based on the surface asperity properties, the asperity friction force could also be determined and compared to an experimentally measured frictional force. They state that by understanding the distribution of all asperity friction forces and contacts, it would be possible to determine the average temperature distribution throughout the contact area, the statistical distribution of flash temperatures near the contact area, and the chemical reaction rates between the various components involved, including metal-metal, metal-base oil, and metal-additive interactions. The calculation proposed by Hsu et al. (1988) has been proved to be effective in specific circumstances noted in Hsu (1991); Hsu et al. (1997); Hsu and Gates (2005); however it currently remains very difficult to predict the wear characteristics for the majority of surfaces due to the complex physical, chemical and thermo-elasto-hydrodynamic interactions that takes place on micro scales of time and space.

The environments which engine lubricants are designed to be used in are typically extremely harsh. Given (i) the large negative pressures typically generated in lubricant films, (ii) the presence of dissolved gas, and (iii) the presence of foreign bodies in the film, the lubricant is prone to cavitation (Mang and Dresel, 2007) and this is of significant concern to BP. Reynolds (1886) identifies the influence cavitation had on the load capacity of journal bearings. Understanding the process and effects of cavitation in liquid films is of significant importance to lubricant and bearing manufacturers alike.

1.2 Cavitation

Cavitation is the process of gaseous or vapourous cavities forming in a liquid resulting from large negative pressures. In gaseous cavitation, dissolved gas diffuses out from the liquid, filling the void, whereas vapourous cavitation represents a change in phase of the same substance.

The process of gaseous cavitation is determined by the liquid-gas solubility. Solubility is the property of a substance, in this instance a gas, dissolving into another substance, usually a liquid medium (Atkins and De Paula, 2013). As the solubility of a gas decreases, more of the gas will come out of the solution and form a secondary phase. As the pressure in a liquid reduces, the solubility of a gas in the liquid also reduces, until the liquid is saturated with gas. We refer to this pressure as the saturation pressure, p_{sat}. As the liquid pressure is reduced below the saturation pressure, negative stresses cause the gas to diffuse of the liquid, causing it to cavitate. There are many examples of dissolved gas diffusing out of a liquid; divers breathing in compressed air must be careful not to rise too quickly as the dissolved nitrogen in their blood will form bubbles, potentially resulting in death, and when opening a carbonated drink the liquid will foam from the sudden release of carbon dioxide dissolved in the liquid.

The processes of vapourous cavitation and evaporation are considered to be similar

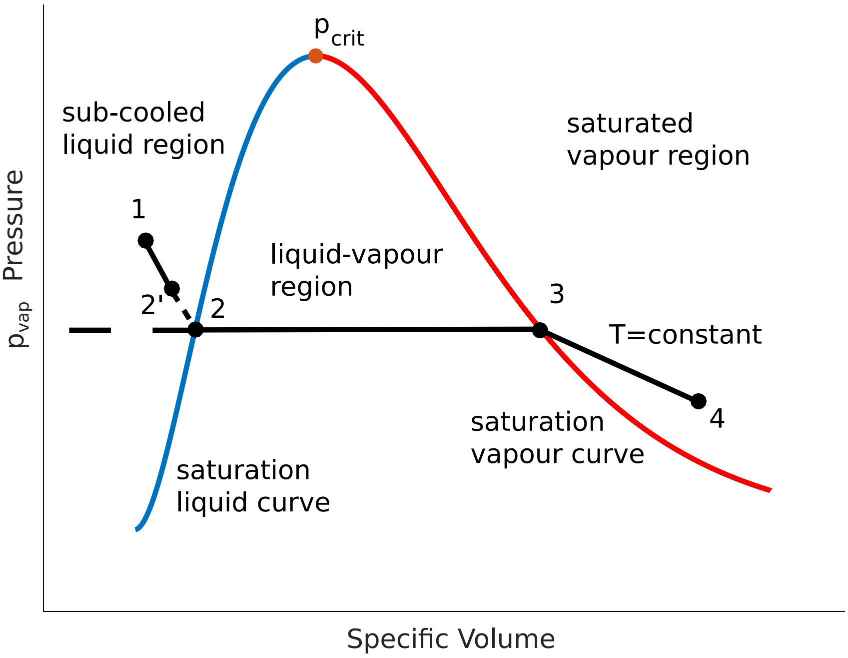

Figure 1.6: Pressure-specific volume (P-V) diagram of a material. The blue and red curves are the liquid and vapour saturation curves respectively, the black line is the line of constant temperature, and the large dot between the blue and red lines is the critical point. Liquid at pressure equal to the critical point or higher will instantly change to a vapour when the specific volume is increased. The space between the blue and red lines is the region where liquid and vapour can exist simultaneously. The point $2'$ represents the point where the material changes from a saturated liquid to a liquid-vapour mixture in the presence of impurities.

(Brennen, 1995). Batchelor (1967) relates the process of boiling to cavitation: a liquid boils when the temperature exceeds the boiling temperature, and vapourous cavitation occurs in a liquid when the pressure reduces below the vapour pressure. To describe this further, consider the pressure-specific volume diagram of a material, as shown in Figure 1.6. The blue and red curves are the saturation liquid and vapour curves, respectively, which bound the liquid-vapour region. The black lines are the lines of constant temperature, and the dot between the blue and red lines is the critical point. Assuming the material is a sub-cooled liquid, it is located at state 1 in the P-V diagram. Reducing the pressure (while holding the temperature constant) to the vapour pressure p_{vap}, the substance reaches the saturation liquid curve at state 2. As the substance crosses the liquid saturation curve, it changes phase from being entirely composed of liquid to a combination of liquid and vapour, the ratio of which is now independent of the pressure and temperature of the mixture. Impurities in the liquid will cause this transition to take place at a higher absolute pressure, state 2'. The amount of energy required to add to the system in order to complete the phase change (transition from state 2 to 3) is the latent heat of vaporization. If the pressure is higher than the critical pressure, p_{crit}, the material will transition from a liquid to a vapour instantaneously. Decreasing the pressure further will cause the material to transition from state 3 to 4 where it is entirely vapour. Braun and Hannon (2010) suggest a common example of vapourous cavitation is in high vibratory journal bearings where, due to its inertia, the liquid cannot remain attached to the moving surface. Consequently, the local pressure in the liquid rapidly decreases, exceeding the yield tensile stresses and causing flash evaporation of the liquid.

We now briefly describe the historical background of cavitation in lubricant films, to best understand the context of this thesis. We first discuss the process of gaseous cavitation on a molecular level. We then discuss the evolution of mathematical models for cavitation in slider bearings and journal bearings. Lastly, we briefly discuss experiments that consider cavitation in negative squeeze films and the models they inspire.

1.2.1 The Process of Gaseous Cavitation on a Molecular Level

Frenkel (1955) draws an analogy between a crack developing in a solid as it being stretched to gaseous cavitation in a liquid. Using classical nucleation theory described by Volmer (1939), Fisher (1948) proposes a formula to estimate the 'fracture pressure' of a liquid. For water, Fisher estimates the 'fracture pressure' to be 132 MPa, at least two orders of magnitude greater than the experimentally observed value for gassed water near an irregular surface (Temperley and Chambers, 1946; Temperley, 1946). Hendricks et al. (1983) attribute this difference to impurities in the liquid, again drawing comparisons to a crack forming in a solid to the first bubble forming in a liquid and the expansion of the cavitated region.

Floberg (1973) considers a single gas bubble of fixed mass, ($R^3\rho = R_0^3\rho_0$), existing in a liquid with which it is in equilibrium and stretches to infinity in all directions. He shows that the fluid pressure on the bubble interface q and the bubble pressure p, (the initial conditions are represented with a subscript zero), are related through the expressions

$$q = p\left(\frac{R_0}{R}\right)^{3k} - \frac{2T}{R}, \text{ where } \frac{p_0}{\rho_0^k} = \frac{p}{\rho^k}, \tag{1.4}$$

where ρ is gas density, R is the bubble radius, T is the surface tension, and k is the adiabatic coefficient which under isothermal conditions is $k = 1$. Equation (1.4) shows that as p decreases, the gas bubble increases in volume by pure expansion; a process called pseudo-cavitation because no additional gas diffuses into the bubble. Pseudo-cavitation is akin to a balloon of fixed mass expanding as the outside pressure decreases (Braun and Hannon, 2010). It is different from gaseous cavitation, in that gases may desorb from the liquid in the bubble, contributing to its growth. Inside an engine, it is common to have a mixture of gases dissolved in the liquid. In this instance, the saturation pressure of the mixture, $p_{\mathrm{sat}_{mix}}$, is determined by Dalton's Law,

$$p_{\mathrm{sat}_{mix}} = \sum_{i=1}^{n} p_{\mathrm{sat}_{gas,i}} \tag{1.5}$$

where $p_{\mathrm{sat}_{gas,i}}$ is the gas saturation pressure of the individual gas and n is the total number of gases in the mixture.

Sun and Brewe (1991b) estimate the time required for a sufficient volume of vapour to evaporate and fill the void for a typical lubricant to be $t = 1.67 \times 10^{-3}$ s, and for air to diffuse from squalene, a common lubricant oil, into the same volume was $t = 3.24 \times 10^{5}$ s. The eight orders of magnitude in difference is due to the extremely low rate of diffusion of air from the liquid compared to the rate of evaporation.

Sun and Brewe (1991b) conclude cavitation bubbles that have formed in low pressure areas in liquid films are most likely to be filled with vapour. However, their analysis does not include the fact that air saturation pressures are usually significantly higher than liquid vapour pressures, suggesting gas will separate from the liquid well before the pressure is low enough for the liquid to evaporate. They also assume the volume of the bubble is constant, and already filled with an anonymous and immiscible fluid.

We have considered how vapour and gaseous bubbles form in an infinite medium; now we focus on mathematical models that describe their formation in slider and journal bearings.

1.2.2 Evolution of Cavitation Models in Slider and Journal Bearings

We now discuss models of cavitation inside lubricant films and journal bearings. The review articles of Dowson and Taylor (1979), Priest et al. (2000) and Braun and Hannon (2010) provide a comprehensive description of current models for cavitation in thin films.

Early Cavitation Models in Lubricant Films

Research on cavitation inside lubricant films has taken place for over one hundred years. A subject of considerable debate is the boundary conditions imposed on the bubble inter-

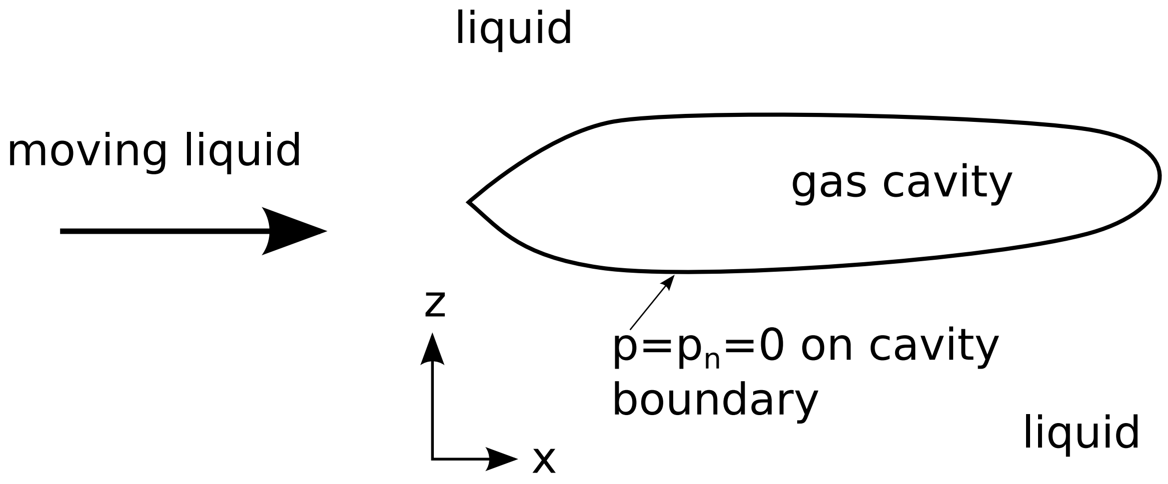

Figure 1.7: A plan view of a cavitated film, showing the Swift-Stieber Condition. The Swift-Stieber model requires the pressure, and the pressure gradient, to both equal zero on the cavity boundary.

face, and its location in the film. Sommerfeld (1904) was one of the earliest researchers to consider the topic, choosing to neglect the regions of sub-atmospheric pressure (regions where the liquid pressure reduces below the atmospheric pressure and hence is under tension). However, this requires the fluid to sustain periods of large tensile stresses. Gumbel (1921) modifies the model of Sommerfeld (1904) by replacing the regions of sub-atmospheric pressure with zero gauge pressure,

$$p = 0, \tag{1.6}$$

inside the cavitated region. Sommerfeld (1904) and Gumbel (1921) represent the earliest attempts to model the rupture of a thin liquid film, but these models do not conserve mass across the boundaries of the cavitated region.

Working independently, Swift (1932) and Stieber (1933) conclude that to satisfy mass conservation across the cavitation boundary, the pressure gradient normal to the boundary must equal zero, so that

$$\frac{\partial p}{\partial \mathbf{n}} = p = 0. \tag{1.7}$$

Swift (1932) considers (1.7) to be a ‘stability condition’, while Stieber (1933) describes it as a condition on the continuity of the liquid mass across the cavitated region boundaries. In Figure 1.7, we show a plan view of a cavitated film where the liquid passes between the gas cavities, illustrating the Swift-Stieber condition. According to Brewe et al. (1988),

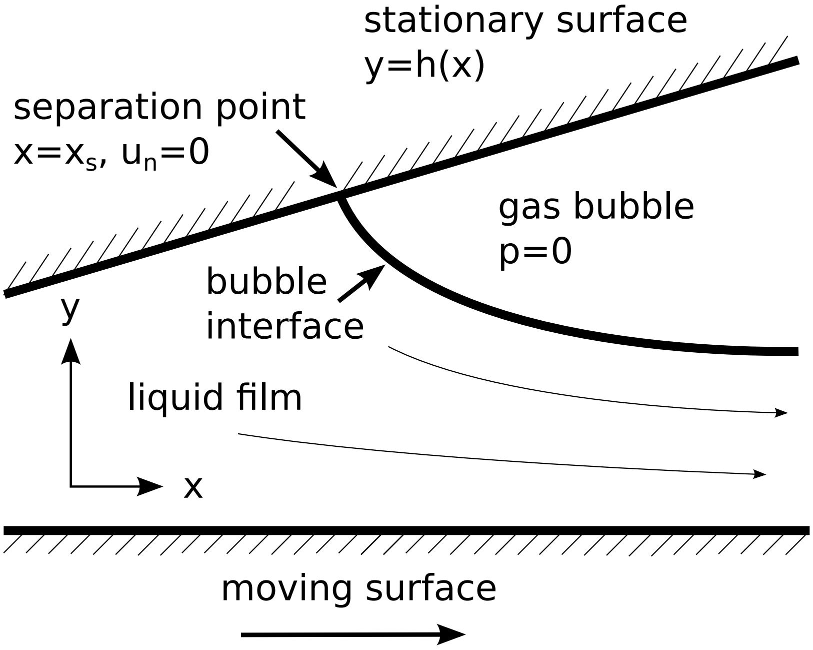

Figure 1.8: A side-view schematic the model proposed by Mori et al. (1968). In their model, they seek the location where the shear rate relative to the flat stationary surface is zero, $\partial u/\partial y = 0$ and the pressure reduces to zero. They take this point, $x = x_s$, to be the upstream boundary of the bubble. The liquid is carried underneath the bubble by the moving surface.

the Swift-Stieber condition accurately represents the establishment of the bubble interface, however it fails to predict the closure of the bubble, or situations where the liquid film is time-dependent (Brewe, 1986). Regardless of this, it is a well-recognized theoretical description of cavitation, and is sometimes referred to as the Reynolds boundary condition (Cope, 1949; Taylor, 1964; Khonsari, 1986).

Flow Separation Models

Mori et al. (1968) consider a different approach: they suggest that the rupture of the film is caused by the separation of the flow from the solid surface in the film. They describe a static bubble, attached to the stationary solid surface, while a film of liquid flows underneath the bubble carried by the motion of the moving solid surface, as shown in Figure 1.8. They theorize that the location where the shear rate relative to the flat stationary surface is zero, the separation point $x = x_s$, is the upstream boundary of the bubble interface. Assuming the liquid is unable to withstand negative pressures, they also require the pressure in the gas to be zero. With this information, they apply the conditions

$$\left.\frac{\partial u}{\partial \mathbf{n}}\right|_{y=h} = 0 \text{ and } p = 0, \text{ at } x = x_s, \tag{1.8}$$

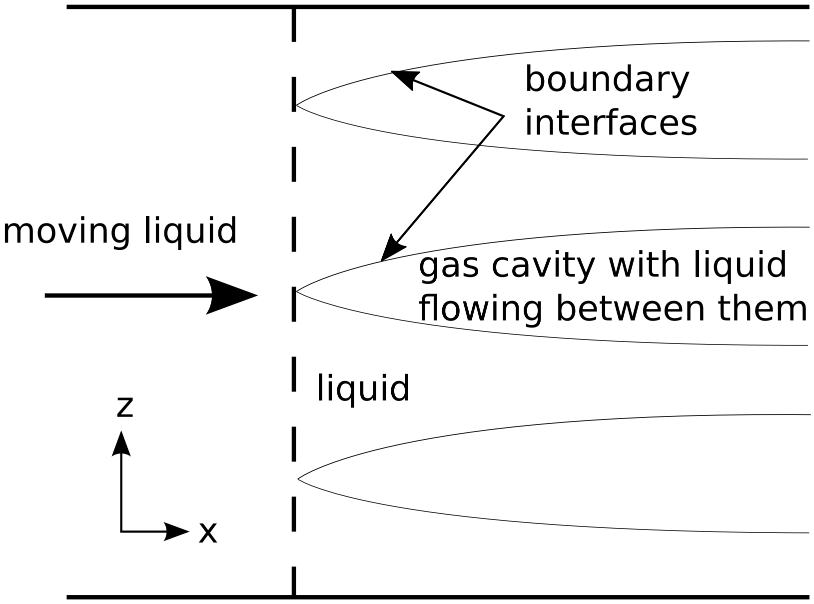

(a) A plan view of observations made by Taylor (1961, 1963) with small capillary numbers, $\mu U/T \ll 1$.

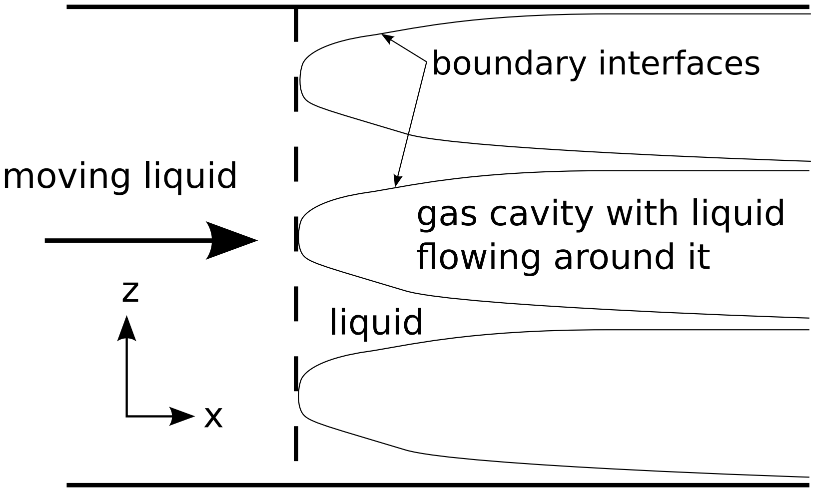

(b) A plan view of observations made by Taylor (1961, 1963) with large capillary numbers, $\mu U/T \gg 1$.

Figure 1.9: Two types of cavitation observed by Taylor (1961, 1963). From their experiments, they hypothesise that for small capillary numbers the upstream boundary of the cavitation region forms a sharp point, and as the capillary number increases the upstream boundary forms a blunt point.

where $\mathbf{n}$ here is the unit normal vector to the top surface, $y = h$. Hopkins (1957) and Birkhoff and Hays (1963) go further to conclude that the pressure gradient at the upstream boundary of the cavitated region is

$$\frac{\partial p}{\partial x} = \frac{2\mu U}{h^2}, \tag{1.9}$$

where U is the velocity of the moving surface and μ is the viscosity of the liquid.

Bretherton (1961) was the first to recognize the effect of surface tension, T, on the shape of a bubble interface as liquid is being swept above it, in the context of a moving bubble inside a capillary tube. Taylor (1961, 1963) have shown experimental evidence of the effect surface tension has on cavity formation.

At low capillary numbers, $\mu U/T \ll 1$, Taylor identifies cavities that form a sharp point at the upstream boundary, and theorizes that the liquid passes between the cavitated region in long, thin streams that span the height of the gap separating the solid surfaces, resembling the flow between the gas regions in Figure 1.9(a).

The second type of cavity Taylor identifies is with large capillary numbers, and forms a blunt point at the upstream boundary as shown in the plan view in Figure 1.9(b). He suggests that the majority of flow separates from the stationary solid surface and passes underneath the gas region.

Savage (1974, 1977) derives a stability condition for a steady, uniform, and infinitely wide boundary at the upstream edge of the cavity-liquid interface. A schematic, in plain view, of the cavitated region in their model is shown in Figure 1.10. At the upstream boundary of the cavity-liquid interface that is in equilibrium, the liquid pressure and surface tension balance the gas pressure, which they assume to be zero, so that

$$p + \frac{T}{R_0} = 0, \tag{1.10}$$

where R_0 is the radius of curvature in the $x - y$ plane as shown in side view in Figure 1.11. Savage (1974, 1977) considers a small perturbation to the interface $x = c$. Calculating the new force per unit area, F, on the interface, while ignoring the effect of surface tension in the $x - z$ plane, leads to

$$F = p(c + \epsilon) + \frac{T}{R_0(c + \epsilon)}. \tag{1.11}$$

Linearizing about $x = c$, using (1.10), the first order term may be written as

$$F = \epsilon \frac{d}{dx}\left(p + \frac{T}{R_0}\right). \tag{1.12}$$

Assuming the interface is stable to small perturbations, F and ϵ must be of opposite signs. Savage (1974, 1977) concludes that the stability criterion for the upstream boundary of an

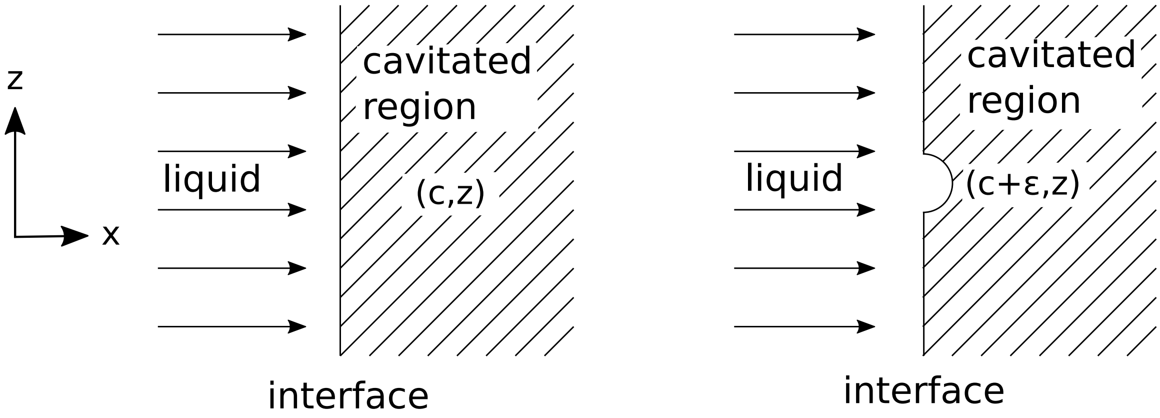

Figure 1.10: An $x - z$ cross-section of flow approaching an infinitely straight cavity-liquid interface with the point (c, z) is displaced to $(c + \epsilon, z)$.

infinitely straight, cavity-liquid interface is

$$\frac{d}{dx}\left(p + \frac{T}{R_0}\right) < 0. \tag{1.13}$$

Coyne and Elrod Jr. (1970) extend the models of Hopkins (1957) and Birkhoff and Hays (1963), by including the effects of surface tension, gravity and inertia. A schematic of their model is shown in Figure 1.11. However, they make a key assumption that a stagnation point exists on the nose of the bubble and is at a different location from the separation point. In their model, the liquid separates from the solid surface creating a small region where the fluid circulates in front of the head of the bubble. For a fixed plate separation, h_0 = constant, they show that the asymptotic film height, h_∞, is a function of three parameters: R_0 the radius of curvature at the head of the bubble, c the height of the stagnation point on the bubble interface above the moving surface, and $\phi < \pi/2$ the surface wetting angle. Coyne and Elrod Jr. (1971) study the case of low capillary number and conduct experiments validating their model. Taylor (1974) further validates the work of Coyne and Elrod Jr. (1970, 1971), comparing it to the experimental studies of Floberg (1965). However, Taylor (1974) concludes that though the model proposed by Coyne and Elrod Jr. (1970, 1971) compares well with experimental data, it would be unreasonable to expect a single cavitation model to be appropriate for all circumstances.

The Mass Conservation Models

The mathematical models discussed so far have shown varying degrees of success when compared to experimental data. However, none of these models satisfy the mass conserva-

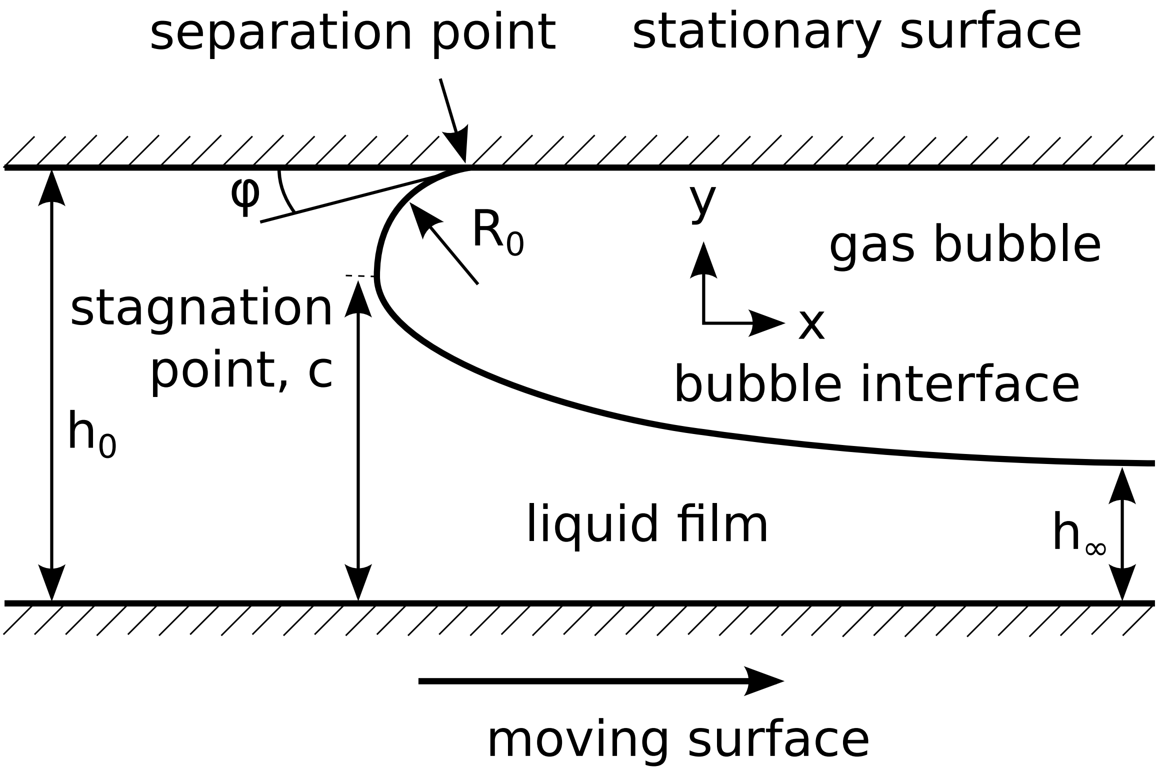

Figure 1.11: A side view of the model proposed by Coyne and Elrod Jr. (1970). Here, liquid flows underneath a gas bubble. However, unlike Mori et al. (1968), they assume the stagnation point of the liquid, c, is not at the same location where the liquid separates from the stationary surface.

tion rule at the downstream boundary of the cavitated region. Nor do they consider the liquid film to be capable of sustaining pressures below the atmospheric pressure, a concept that was proven to be false in experiments conducted by Floberg (1965, 1968). Working independently, Jakobsson and Floberg (1957), Olsson (1965) and Floberg (1974) consider similar models to Swift (1932) and Stieber (1933). The model in these papers is collectively referred to as the Jakobsson, Floberg, Olsson (JFO) model of cavitation theory, (Elrod and Adams, 1974). The JFO model describes the cavitated region in the film as having constant pressure and containing long finger-like bubbles separated by streams of liquid. At the upstream boundary $x = u$, they apply the Swift-Stieber condition, and assuming the film is infinitely wide, this reduces to

$$\left.\frac{dp}{dx}\right|_{x=u} = 0, \tag{1.14}$$

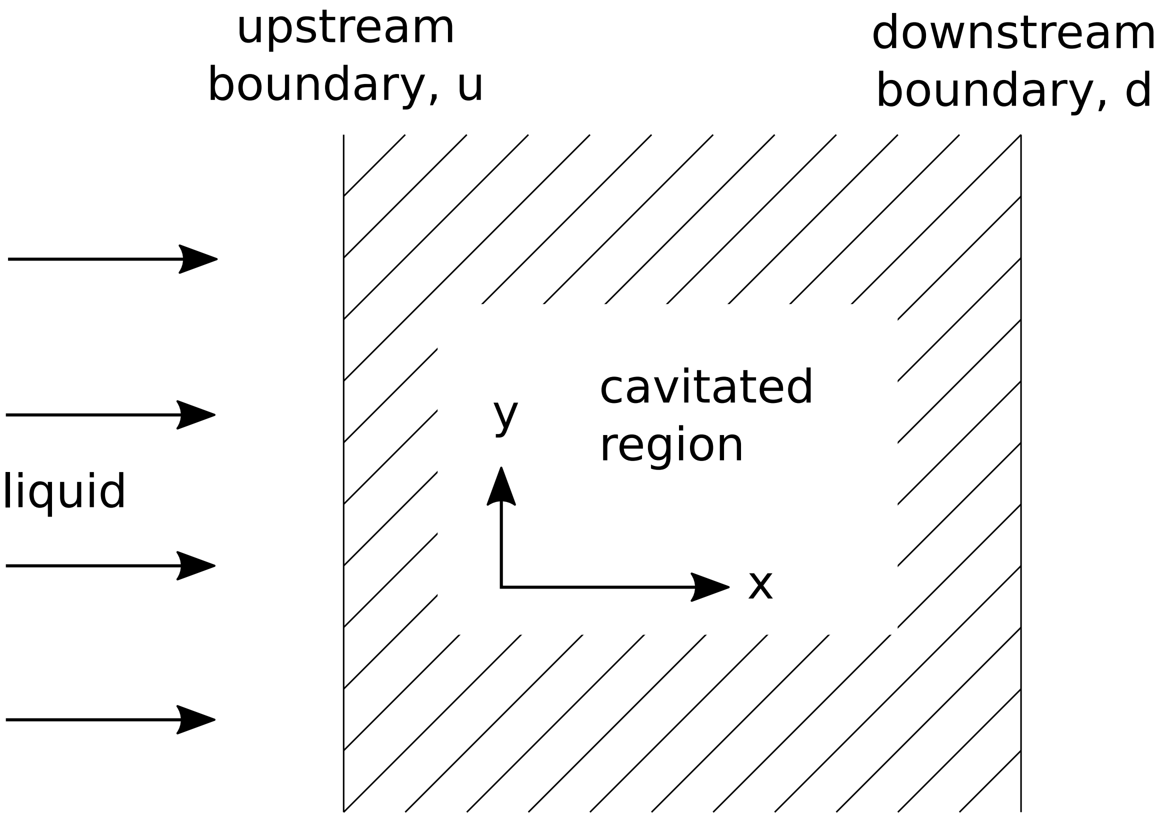

Figure 1.12: A plan view of the JFO model, as proposed separately by Jakobsson and Floberg (1957), Olsson (1965) and Floberg (1974). They study an infinitely wide liquid film with the upstream boundary u and downstream boundary d.

which was derived from the conservation equation. Considering the conservation of mass across the downstream boundary, they derive the equation

$$\left[-\frac{h^3}{12\mu}\left(\frac{\partial p}{\partial x}\right)+\frac{Uh}{2}\right]_{x=d}=\left[\frac{Uh}{2}\right]_{x=u}. \tag{1.15}$$

The term $Uh/2$ is the thickness-averaged volume flux of liquid evaluated at a given location in the film. The experimental data from a static journal bearing provided by Floberg (1974) compare well to the theoretical predictions of JFO theory, successfully validating the model.

JFO theory was modified by Elrod and Adams (1974) so that the governing equations can be written as a single equation over the entire film. They assume the liquid in the film is compressible, relating the density of the liquid ρ to the pressure and bulk modulus β (assumed to be constant) using

$$\rho\frac{dp}{d\rho}=\beta, \tag{1.16}$$

while neglecting other aspects of liquid compressibility. These approximations allow Elrod and Adams (1974) to write the thin film equation, both inside and outside of the cavitated region, as a single equation,

$$\frac{\partial(\phi h)}{\partial t}+\frac{U}{2}\frac{\partial(\phi h)}{\partial x}=\frac{\partial}{\partial x}\left(\frac{h^3\beta g(\phi)}{12\mu}\frac{\partial \phi}{\partial x}\right) \tag{1.17}$$

where $\phi = \rho/\rho_c$, and ρ is the density of the liquid in the full film regions, and ρ_c is the density of the liquid when it cavitates. They define the switch function $g(\phi)$ as

$$g(\phi)=\begin{cases}1, & \phi > 1,\\ 0, & \phi \leq 1.\end{cases} \tag{1.18}$$

Elrod and Adams (1974) solve equation (1.17) using a finite difference algorithm, with Elrod (1981) producing a more easily adaptable and 'user friendly' algorithm employing the same physics.

Numerical Adaptations of the Elrod Cavitation Algorithm

The cavitation model proposed by Elrod and Adams (1974) has been used as the fundamental model in this field of research for the last 40 years, and is referred to as 'the Elrod Cavitation Algorithm' (Braun and Hannon, 2010). A continuing source of debate concerns the type of algorithm used to solve the equations set out in Elrod and Adams (1974). We discuss the benefits and disadvantages of some of these modifications below.

Vijayaraghavan and Keith Jr (1989) develop a numerical scheme to assist the finite difference computation across the cavitation boundaries. The cavitation boundary is an area the computation has particular difficulty with, due to the fundamental difference in the finite difference schemes on either side of the boundary. Inside the cavitation region the fluid motion is described by a hyperbolic differential equation, and so the domain may be discretized using a backwards or forwards difference scheme. However, outside the cavitated region, the fluid motion is governed by a parabolic differential equation, and so the domain may be discretized using a central difference scheme. They circumvent this problem by using methods employed in computations of transonic flow (Pletcher et al., 2012). Vijayaraghavan and Keith Jr (1989) introduce an 'artificial viscosity' term into the shear term so it now has the form

$$\frac{\partial(\phi h)}{\partial x}=\frac{\partial}{\partial x}\left(\phi h-\mu_A\frac{\partial(\phi h)}{\partial x}\frac{\Delta x}{2}\right) \tag{1.19}$$

in (1.17), where μ_A is switched on inside the cavitated region,

$$\mu_A = \begin{cases} 0 & \text{in the liquid region,} \\ 1 & \text{in the cavitated region.} \end{cases} \tag{1.20}$$

They compare their results to the numerical solutions of Elrod and Adams (1974) and the experimental data of Jakobsson and Floberg (1957), with steady state slider bearings and journal bearings. In both instances, they show favourable comparisons.

Vijayaraghavan and Keith Jr (1990) further develop the algorithm in Vijayaraghavan and Keith Jr (1989), comparing a series of modifications to the numerical method, including: Successive Over-Relaxation scheme (SOR), Successive Line Over-Relaxation scheme (SLOR), Alternating Direction Implicit scheme (ADI), and an Approximate Factorization scheme (AF). Comparing these algorithms for a variety of cases, they find SOR and SLOR schemes are the slowest, the ADI scheme being faster and the AF scheme the fastest. However, the ADI scheme was noticed to experience some difficulty towards the downstream edge of the cavitation boundary, a consequence being a limited range of values over which to set the time step to in order to produce an accurate solution.

Woods and Brewe (1989) adapted an iterative multi-grid technique to the Elrod cavitation algorithm. The numerical method performs well prior to the formation of cavities in the film. However, care must be taken near the boundaries of the cavitated region, as high-frequency local error terms become apparent in this area. They note a significantly finer grid is required when the cavitated region is opening and closing than at other times in the computation. Despite this, their results were shown to closely represent the solutions that used a single-grid Gauss-Seidel or direct ADI algorithm while significantly reducing the computational running time.

A review of early finite-element (FE) algorithms and their application to cavitation in lubricant films is provided by Booker (1990). However, despite their popularity, many of these models do not conserve mass at various locations in the film. Later, Kumar and Booker (1991a) proposed a FE solution of the Elrod Cavitation Algorithm, based on the algorithm first developed by Booker and Huebner (1972), and is the counterpart to the finite-difference solution for the same algorithm. Their algorithm was validated by Kumar and Booker (1991b), where the results compared favourably to the experimental analysis of Lundholm (1969) under quasi-static and dynamic environments.

Further Experimental Studies on Cavitation in Liquid Films

There is an extensive volume of literature on the experimental analysis of cavitation in thin films, and the reviews of Swales (1974) and Braun and Hannon (2010) provide detailed descriptions.

Etsion and Ludwig (1982) study the visualization and pressure distribution of the cavitated region under steady state conditions in a journal bearing. They observe a reverse flow of the liquid close to the downstream end of the cavitated region. The oil streamers were also shown to fluctuate in the lateral direction. Etsion and Ludwig (1982) and Braun and Hendricks (1984) note that the pressure varies towards the end of the cavitated region, which is in contrast with many of the mathematical models that assume the pressure to be constant in this region. Etsion and Ludwig (1982) suggest that these observations are related to the instability of the oil streams in the cavitated region, a result predicted by Savage (1974).

Groper and Etsion (2001, 2002) propose two possible mechanisms that describe the non-constant and sub-atmospheric pressure fluctuations observed in Etsion and Ludwig (1982). These mechanisms are:

- the shear of a cavity gas bubble by a thin lubricant film dragged through the cavitated region by the rotating shaft,
- the rate of diffusion of dissolved gas out of and back into the lubricant.

To incorporate the first mechanism, they match the velocity and shear stress of the liquid and the gas at the bubble interface, showing that the rupture and reformation of the cavity bubble correlates well with the mathematical model. However, this model underestimates the pressure towards the end of the cavity by as much as 20%, and they conclude that the shear mechanism in isolation is insufficient to explain the results. For the second mechanism they calculate the diffusion flux of the gas across the bubble interface to be approximately one-thousandth that of the convective flux, concluding it is too slow to be of significant influence on the film dynamics.

Using a high speed camera, Jacobson and Hamrock (1983a,b) have shown a dramatic improvement in the flow visualization of journal bearings. They observe how a liquid film behaves when held between a rotating journal and a stationary transparent cylindrical sleeve made of a hard glass. The journal was able to move away from the sleeve, and allowed the experimenters to study the liquid film in either a static or dynamic environment. These advances in experimental technology confirmed the formation, development, and collapse of a bubble in a journal bearing, concluding the composition of the bubble to be a combination of gas and vapour. Up until then, it was thought bubbles that contain mainly vapour were unable to exist in a liquid medium. However, this study shows they do exist, but dissolve within milliseconds and hence require a high speed camera to capture proof of their existence.

Brewe (1986) compares the Elrod cavitation algorithm favourably to the experimental results of Jacobson and Hamrock (1983a,b). They observe vapour bubbles remaining in the liquid film for 23 μs, while Brewe (1986) calculates they should persist for 32 μs. Brewe (1986) proposes two reasons for this difference: (i) the time required for the vapour bubbles to be large enough to the observer's eye is not known; (ii) apparatus compliance and thermal effects in the liquid. Sun and Brewe (1991a) and Sun et al. (1993) repeat the experiments of Jacobson and Hamrock (1983a,b), but instead use a quartz sleeve which is more rigid than the material used by Jacobson and Hamrock (1983a,b). However, they are unable to visually determine the content of the cavitation bubbles, but note there is no difference in the results when the aerated and degassed lubricant is used.

Ashmore et al. (2005) provides photographic and experimental evidence of the presence of a vapour bubble inside a thin film separating a sphere that is free to rotate but fixed in location inside a rotating cylinder. In their experiment, the film thickness separating the sphere and the cylinder, and the angular velocity of the cylinder, are held constant. Building on the theory of Goldman et al. (1967a,b), they modify the normal force, accounting for the presence of the bubble. They do this by truncating the pressure where it exceeds the vapour pressure of the liquid (the same conditions applied by Gumbel (1921)). In addition to the normal force, they calculate the area of the cavitation bubble and the angular velocity of the sphere. Despite the Gumbel (1921) condition neglecting mass conservation in the cavitated region and across its boundaries, the experimental results of Ashmore et al. (2005) are in close agreement with the theory.

1.2.3 Cavitation in Negative Squeeze Films

We now discuss experiments and models that describe cavitation in negative squeeze films. A negative squeeze film is a layer of liquid that separates two solid surfaces that move vertically apart from each other. A common application of squeeze films is to dampen the motion of a moving object, such as a swaying bridge or moving machinery.

Hays and Feiten (1964) study experimentally the formation and growth of a cavitated region in a negative squeeze film. The parallel plates that bound the film are fixed horizontally, and only allowed to move vertically relative to each other. The liquid, being unable to follow the vertical motion of the surface vapourizes, producing a cavitated region composed of a mixture of vapour and liquid. The results from these experiments are the quintessential example of flash cavitation.

Hays and Feiten (1964) and Haber and Etsion (1985) describe a single cavitation bubble inside a negative squeeze film. In the analysis of Haber and Etsion (1985), they assume an ideal gas fills the bubble entirely, and the pressure inside the bubble changes uniformly according to isothermal conditions. In both models, they observe the pressure in the liquid region reduce below the pressure of the bubble. However, one would expect these models to be unstable in three dimensions because a less viscous fluid will displace a more viscous fluid, causing a Saffman-Taylor instability. Therefore, one would expect the single bubble present in their model to break up into many smaller bubbles, similarly to the model described by Ockendon et al. (2003).

Ockendon et al. (2003) consider the region of cavitated fluid to be a combination of vapour, gas, and liquid, which they call a “mushy region”. However, instead of attempting to model individual phase movements in the cavitated region, they define a volume fraction of liquid inside this region, and apply the Swift-Stieber condition on the mushy region boundary. Boedo and Booker (1996) provide a similar analysis using a finite element implementation.

1.3 Thesis layout

In this thesis, we focus on developing cavitation models specifically for applications in slider bearings and negative squeeze films. The content is divided into five remaining chapters, which we lay out below.

In Chapter 2, we consider cavitation in negative squeeze films. Zhu and Granick (2002c) published a set of results in which they claim to measure the effect of fluid slipping on the solid-liquid interface but fail to provide evidence that this is the case. We hypothesize that their results could be explained with cavitation. We propose two models; the first describes a single bubble that forms in the film when the pressure reduces below the vapour pressure of the liquid. Here, we assume the liquid cannot move through the bubble interface, which leads to a negative pressure outside the bubble and so we expect the bubble to break up into smaller bubbles. This motivates us to consider a second model similar to Ockendon et al. (2003), where fluid passes through the boundary in such a way that there is no change in the pressure. We study two experiments presented in Zhu and Granick (2002c), the first being a control experiment and the second experiment including a surfactant in the liquid and compare them to our mushy region model.

Motivated by experiments conducted at City University of London, hence forth referred to as the City Experiments, in which cavitation is observed inside a liquid film undergoing horizontal movement, in Chapter 3 we describe how a mushy region develops in a slider bearing. We base this model on the theory of Jakobsson and Floberg (1957), Olsson (1965) and Floberg (1974). The chapter is divided into three distinct sections. First, we investigate how a mushy region opens when the dimensionless velocity of the bottom surface is constant, which we use as the only parameter in this model. We show the film thickness reaches a steady state after sufficient time and calculate the linear decay rate of the solution to the model. In the second section, we investigate how the mushy region closes as the velocity decreases to zero and determine whether the motion is quasi-steady. In the final section of this chapter, we investigate how the mushy region evolves as the velocity varies sinusoidally in time. Due to the oscillatory nature of the bottom surface, we non-dimensionalize the problem so the dimensionless frequency and amplitude of oscillation of the bottom surface are of unit magnitude. This results in two dimensionless parameters for this model, δ and Ω, and we investigate how changes in these parameters affect the model.

In Chapter 4 we validate the numerical algorithm that was used to solve the oscillatory case of the mushy region model by taking the asymptotic limit of the model as $\delta \to 0$. In this limit we show that the numerical solution can be approximated as a quasi-steady solution provided the velocity of the bottom surface is large. As the velocity of the bottom surface approaches zero, the quasi-steady solution is no longer valid and the model is now driven by the dynamics in the system. We compare the numerical solution and quasi-steady solution to the experimental data, and infer the viscosity by matching the quasi-steady solution to the maximum film thickness measured in the experiment. We compare the friction calculated from the model to that measured in the experiment, and show the two agree well when the velocity of the bottom surface is large.

In Chapter 5, we consider potential causes that might explain the discrepancy between the mushy region model and the experimental data. We briefly consider the effects of:

surface roughness and elastic deformation of the solid surfaces, inertia of the top surface, Piezo-Viscous effect, the inertia and compressibility of the liquid, viscous heating. From the numerical solutions, we calculate that the finite length of the film may influence the mushy region model. We also consider whether by truncating the bearing to be of finite length, (but keeping it symmetrically located about the origin), the numerical solution better approximates the experimental data. Next, we investigate three candidates for explaining the asymmetry seen in the City Experiments. We first consider whether an asymmetric curved surface could cause the asymmetry. Second, we consider whether the results could be caused by an asymmetry in the velocity of the bottom surface. Third, we speculate whether the asymmetry could be due to an asymmetry in the oil supply to the experimental apparatus. In the final section, we extend the mushy region model to study how it behaves under realistic operating conditions in an engine. We study how the mushy region model behaves when the normal force varies periodically. This model is motivated by periodic changes in the ring tension, caused by the ignition of gases in the combustion chamber, exerting a force on the lubricant film between the piston ring and cylinder wall of an engine.

We draw together all our conclusions, and make recommendations for future work and research, in Chapter 6.

Chapter 2

Cavitation and Effective Slip in Squeeze Films

2.1 Introduction

In fluid mechanics and surface science, the fluid-solid boundary condition is one of considerable debate. This condition is an important topic of research because it is thought that understanding the fluid-solid interaction could lead to significant advances in reducing friction and wear inside engines. On a macroscopic scale, it is common to apply the no-slip boundary condition. However, this boundary condition is questionable at micro- or nano- meter scales, where the fluid is thought to 'slip' past the solid. The exact mechanism that causes slip is poorly understood; many authors think slip is influenced by the adsorption of surfactants onto the solid surface repelling the liquid away, e.g. Zhu and Granick (2002a,b,c); Tretheway and Meinhart (2004); Pit et al. (2000). Others have proposed that small-scale cavities and/or bubbles can cause an effective slip, but that the no-slip boundary conditions remain valid (Lauga and Brenner, 2004).

In this chapter, we focus on the experiments of Zhu and Granick (2002c), who investigated the effect of surfactant on lubrication oil. We describe their experiment and the results they report in detail in Section 2.2. In the final part of the section, we hypothesize that their results could be explained by the fluid cavitating due to large tensile stresses. This motivates us to consider two models that describe cavitation in a lubricant film: the 'bubble model' and the 'mushy region model'. In Section 2.3, we assume that below a critical pressure a single vapour bubble forms in the fluid. On the interface of the bubble, the velocity of the liquid matches the rate of the expansion of the radius of the bubble

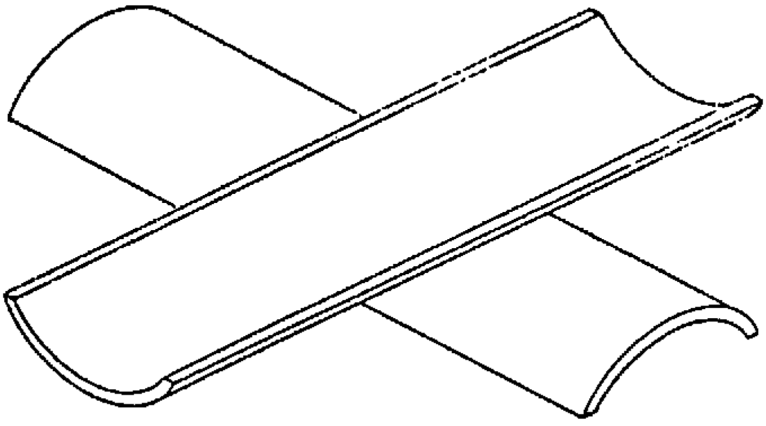

Figure 2.1: Sketch showing the experiment set up used by Zhu and Granick (2002c).

and prevents the mass transfer of liquid into the bubble. We shall see that this model is not self-consistent in the sense that the pressure falls below the vapour pressure outside the bubble. We therefore present a second model of cavitation, in Section 2.4, in which the volume fraction of liquid in the cavitated region varies. The mushy region model extends upon the model proposed by Ockendon et al. (2003), who consider the expansion of a mushy region between two flat, parallel plates moving relative to each other. Both models are dependent on a single parameter; the dimensionless cavitation pressure, which signifies the change in pressure of the film relative to the vapour pressure of the liquid. Lastly, in Section 2.5, we fit the prediction of both our models to the experimental results of Zhu and Granick (2002c), and show that the normal force from the 'mushy region model' closely resembles their observations provided we fit the value of the cavitation pressure. We draw conclusions in Section 2.6.

2.2 Zhu and Granick Experiment

Let us now consider the experiments of Zhu and Granick (2002c). They used a surface force apparatus (SFA) to measure the normal force between two muscovite mica sheets separated by a fluid film. Muscovite mica is a common material in experimental surface science due to its hard, hydrophilic, and atomically smooth nature. The mica sheets were 'glued' to two glass cylinders each with a radius of curvature $R_c = 2$ cm, and were orientated perpendicularly to each other, as shown in Figure 2.1. The geometry of their experiment can be represented mathematically as a liquid separated by an axi-symmetric parabolic surface and a flat plate. If we describe the top surface in their experiment as $\bar{z} = \bar{x}^2/(2R_c)$, the bottom surface as $\bar{z} = -\bar{y}^2/(2R_c)$, and the minimum vertical distance that separates

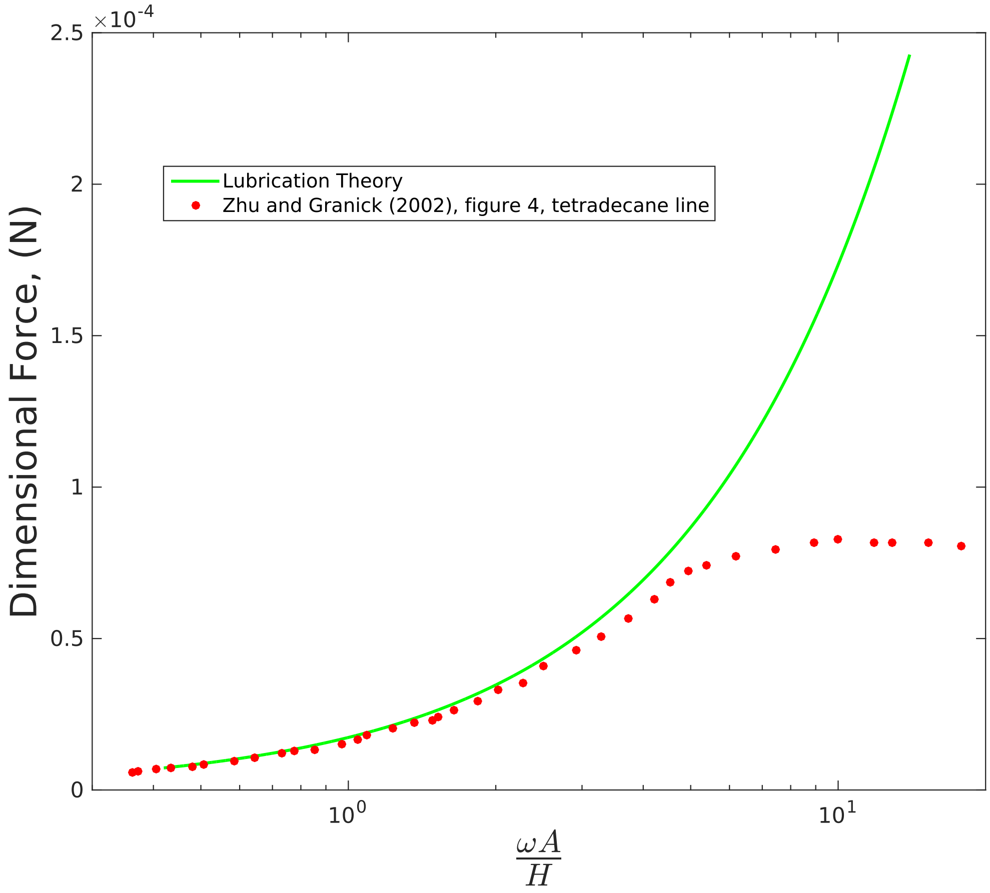

Figure 2.2: The maximum normal force in dimensional form vs the shear rate. The red dots are the experimental data taken from Figure 4 in Zhu and Granick (2002c) where the base fluid is tetradecane, and the green curve is the theoretical maximum of the normal force, (2.1), provided by Vinogradova (1995).

the surfaces as $\bar{H}$, then the thickness of the fluid layer is approximately given by $\bar{h} = \bar{r}^2/(2R_c) + \bar{H}$, where $\bar{r}^2 = \bar{x}^2 + \bar{y}^2$.

Zhu and Granick (2002c) studied three base fluids: tetradecane, decane, and octane, each containing the surfactant 1-hexadecylamine. The bottom cylinder was oscillated in the vertical direction while they measured the normal force. Apparatus compliance was taken into account in their analysis by modelling the glue that attaches the mica sheet to the cylinder as a Voigt cell in a visco-elastic material. However, they specify neither the true oscillatory amplitude the film experiences, nor the parameters they use to calculate this effect. The film thickness was measured using interferometry to a resolution of ±0.5 nm. They state that the shear rates they consider are six orders of magnitude below the limit where Newtonian behaviour breaks down, and conclude that this does not influence their results. Zhu and Granick (2002c) do not explicitly state they degassed their liquid prior to the experiment. However, they note that the surface forces have a negligible effect

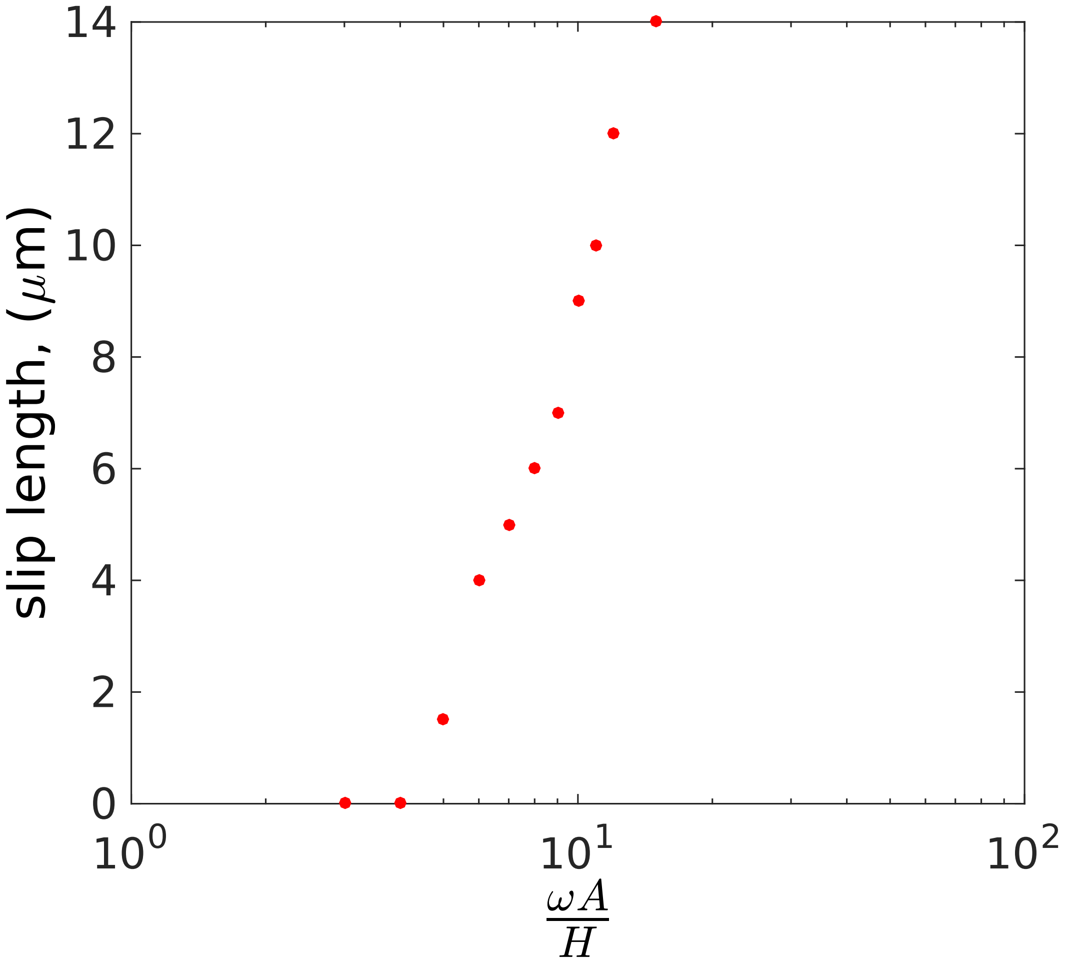

Figure 2.3: The slip length shown as a function of the shear rate, taken from Figure 5 from Zhu and Granick (2002c) where the base fluid is tetradecane.

on the experiment over the range of film thicknesses considered.

The analysis of Vinogradova (1995) provides the following prediction for the relation between the maximal normal force $\bar{F}_n$ and the shear rate $\omega A/H$:

$$\bar{F}_n = 6\pi\mu R_c^2 \left(\frac{A\omega}{H}\right), \tag{2.1}$$

where μ is the liquid viscosity, H is the time-averaged minimum film thickness, and A and ω are the amplitude and frequency of oscillation. Zhu and Granick (2002c) compare their experimental results with the prediction (2.1). As shown in Figure 2.2, the results agree well for small values of $\omega A/H$, but diverge from each other for larger values. The authors attribute this deviation to slip between the fluid and the solid surfaces, though they do not directly observe slip in their experiment. Using an equation derived by Vinogradova (1995), Zhu and Granick (2002c) calculate the slip length for the same set of data (Figure

5 from Zhu and Granick (2002c)), which we show in Figure 2.3. We note two important interpretations from their results. First, in their experiment, they infer that slip suddenly becomes present at a critical shear rate. Second, once the shear rate has exceeded the critical value, the apparent slip length increases with the shear rate. Zhu and Granick (2002c) conclude that the slip length is shear rate dependent.

One explanation of Zhu and Granick's results was suggested by Lauga and Brenner (2004) for a similar experiment by Zhu and Granick (2001) who consider the effect of different contact angles between the liquid and the hydrophobic or hydrophilic surface. Their model describes the dynamic response of nanobubbles to changes in the hydrodynamic pressure. Lauga and Brenner (2004) show that both diffusion and compression of the gas in the bubbles might decrease the normal force in the experiment. They use the analogy that the bubble layer is like a 'leaking mattress', creating an apparent shear-dependent slip. For fitted values of the contact angle, the size, and the surface coverage of the nanobubbles, the model of Lauga and Brenner (2004) predicts a decrease in the force consistent with the experiments of Zhu and Granick (2001). However, the use of three fitting parameters seems somewhat unsatisfactory and provides no explanation of the origin of the bubbles.

An alternative explanation might be that the liquid cavitates. To test this possibility, we begin by estimating the pressure in the film. Zhu and Granick (2002c) do not explicitly state the film thickness observed in their experiment. The frequency and amplitude of the modulations for the test shown in Figure 2.3 were given to be $A = 2$ nm and $\omega = 63$ rad/s, respectively, so that the film thickness at which they first observe slip in their experiment is $H = 31.5$ nm. The magnitude of the change in the pressure in the film relative to ambient pressure, given by Vinogradova (1995), is

$$\Delta\overline{p} = \frac{3\mu A\omega R_c}{H^2}. \tag{2.2}$$

Assuming the viscosity of tetradecane is $\mu = 2.3 \times 10^{-3}$ Pa s, $\Delta\overline{p}$ is of the order 2×10^4 Pa at the point where Zhu and Granick (2002c) first observe slip. Since this is comparable to the atmospheric pressure, we hypothesize that their results were caused by the rupture of the film through the formation of vaporous cavities in the liquid. Cavitation occurs when a liquid experiences extreme tensile stresses that reduce the total pressure below the vapour pressure of the liquid. The vapour pressure of pure tetradecane at room temperature is

$p_{vap} = 1.5$ Pa[1]. However, the vapour pressure of the base oil is likely to increase with the addition of surfactant (Krotov and Rusanov, 1982).

We also note that the sign of the maximal normal force is of significant importance to the cavitation problem. It would be unreasonable to expect gaseous cavities to persist in a liquid when the applied normal force is compressive and hence the pressure in the liquid is far greater than the saturation pressure of the gas-liquid mixture. However, it is possible for cavities to form when the applied normal force is negative, separating the solid surfaces from each other, and hence creating negative tensile pressures in the film. Zhu and Granick (2002c) do not provide a time series of the normal force and so we cannot confirm *when* in the period of oscillation the maximal normal force was measured.

We now describe some models for cavitation in lubricant films, beginning with the simplest model, the 'bubble model'.

2.3 The Bubble Model

2.3.1 Thin film model

We start by assuming that, at $t = 0$, the pressure in the film is above the vapour pressure of the liquid, and therefore no cavitation bubble exists in the film. The space separating the surfaces has a minimum time-averaged thickness H and is completely flooded with fluid. A schematic of the model is shown in Figure 2.4. The bottom surface is flat and located at $\overline{z} = 0$, and the top surface is $\overline{z} = \overline{h}\left(\overline{r}, \overline{t}\right) = H + \overline{r}^2/2R_c - A\sin\left(\omega\overline{t}\right)$. The top surface is a parabola with respect to $\overline{r}$, and undergoes surface modulations with amplitude A and frequency ω. The variables $\overline{u}_r$ and $\overline{u}_z$ are the dimensional radial and vertical velocities, and $\overline{p}$ refers to the dimensional change in pressure in the film relative to atmospheric pressure, p_{atm}. The total pressure we write as $\overline{p}_{tot} = \overline{p} + p_{atm}$.

Taking the precedent of Vinogradova (1995), we choose to represent the complicated geometry of the Zhu and Granick (2002c) experiment simply with a cylindrical coordinate system, $\left(\overline{r}, \overline{z}, \overline{t}\right)$. Assuming the film is sufficiently thin, $\delta = \sqrt{H/R_c} \ll 1$, the motion of the fluid may be described by the dimensional lubrication equations in axisymmetric cylindrical-polar coordinates, Leal (2007)

---

[1] http://www.chemicalbook.com/ProductMSDSDetailCB7854039.html, accessed 24-November-2013

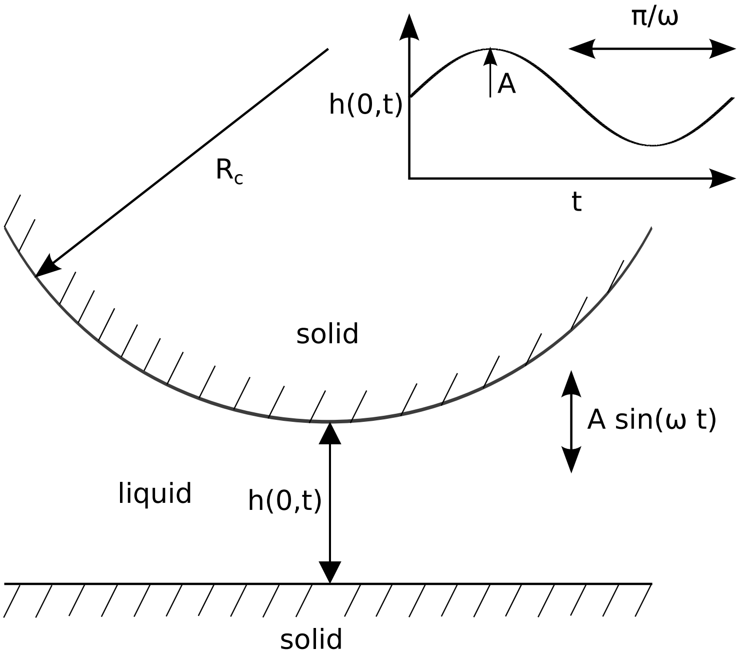

Figure 2.4: Schematic of the model: a paraboloid radius of curvature R_c oscillates above a horizontal plane.

$$\frac{\partial \overline{p}}{\partial \overline{r}} = \mu \frac{\partial^2 \overline{u}_r}{\partial \overline{z}^2}, \tag{2.3}$$

$$\frac{\partial \overline{p}}{\partial \overline{z}} = 0, \tag{2.4}$$

$$\frac{1}{\overline{r}} \frac{\partial \left(\overline{r}\ \overline{u}_r\right)}{\partial \overline{r}} + \frac{\partial \overline{u}_z}{\partial \overline{z}} = 0. \tag{2.5}$$

We apply the no-slip and no penetration boundary conditions on the top and bottom surfaces

$$\overline{u}_r = 0 \text{ on } \overline{z} = \overline{h}\left(\overline{r}, \overline{t}\right), \tag{2.6}$$

$$\overline{u}_z = \frac{\partial \overline{h}}{\partial \overline{t}} \text{ on } \overline{z} = \overline{h}\left(\overline{r}, \overline{t}\right), \tag{2.7}$$

$$\overline{u}_r = 0 \text{ on } \overline{z} = 0, \tag{2.8}$$

$$\overline{u}_z = 0 \text{ on } \overline{z} = 0. \tag{2.9}$$

We assume the total pressure approaches atmospheric pressure as $r \to \infty$, and therefore the change in pressure approaches zero

$$\overline{p} \to 0 \text{ as } \overline{r} \to \infty. \tag{2.10}$$

We also require continuity at $\overline{r}=0$, and therefore apply the boundary condition

$$\frac{\partial \overline{p}}{\partial \overline{r}} = 0 \text{ at } \overline{r} = 0. \tag{2.11}$$

We refer to equations (2.3)-(2.5) and boundary conditions (2.6)-(2.11) as the classic lubrication model to distinguish it from models that involve the formation of a second, cavitated, phase in the film.

We non-dimensionalize the radial coordinate by letting $\overline{r} = \sqrt{R_c H} r$, the vertical coordinate by letting $\overline{z} = Hz$, the velocity vector $\overline{u}_r \mathbf{e}_r + \overline{u}_z \mathbf{e}_z = \sqrt{R_c/H} A\omega u_r \mathbf{e}_r + A\omega u_z \mathbf{e}_z$, the pressure $\overline{p} = (\mu A\omega R/H^2)p$, normal force $\bar{F}_n = (\mu A\omega R_c^2/H)F_n$, and time $\overline{t} = t/\omega$. In dimensionless terms, equations (2.3)-(2.5) take the form

$$\frac{\partial p}{\partial r} = \frac{\partial^2 u_r}{\partial z^2}, \tag{2.12}$$

$$\frac{\partial p}{\partial z} = 0, \tag{2.13}$$

$$\frac{1}{r}\frac{\partial (r u_r)}{\partial r} + \frac{\partial u_z}{\partial z} = 0. \tag{2.14}$$

On the top and bottom surfaces we apply the dimensionless boundary conditions

$$u_r = 0 \text{ on } z = h(r,t), \tag{2.15}$$

$$\epsilon u_z = \frac{\partial h}{\partial t} \text{ on } z = h(r,t), \tag{2.16}$$

$$u_r = 0 \text{ on } z = 0, \tag{2.17}$$

$$u_z = 0 \text{ on } z = 0, \tag{2.18}$$

$$p \to 0 \text{ as } r \to \infty, \tag{2.19}$$

$$\frac{\partial p}{\partial r} = 0 \text{ at } r = 0, \tag{2.20}$$

where $\epsilon = A/H$. We express the top surface as

$$z = h(r,t) = 1 + \frac{r^2}{2} - \epsilon \sin(t) \tag{2.21}$$

Motivated by the experiments of Zhu and Granick (2002c), for which $\epsilon \sim O(10^{-2})$, we assume that $\epsilon \ll 1$; to leading order in ϵ, the change in film thickness with time may be neglected. In what follows, we shall only work to leading order in ϵ. The boundary condition

(2.16) may then be written as

$$u_z = -\cos(t) \ \text{ on } z = h_0(r), \tag{2.22}$$

where

$$h_0(r) = 1 + \frac{r^2}{2}. \tag{2.23}$$

We see from equation (2.13), that the pressure is only a function of r and t. Integrating equation (2.12) twice with respect to z and using the no-slip boundary conditions (2.15) and (2.17) the radial velocity is

$$u_r = \frac{1}{2}\frac{\partial p}{\partial r} z\left(z - h_0\right). \tag{2.24}$$

Integrating the continuity equation (2.14) once with respect to z and using the boundary conditions (2.18) and (2.22) we derive the Reynolds equation

$$\frac{1}{6}\frac{\partial}{\partial r}\left(r\left(1 + \frac{r^2}{2}\right)^3 \frac{\partial p_l}{\partial r}\right) = -\cos(t), \tag{2.25}$$

which may be integrated once with respect to r using the boundary condition (2.20) to solve for the pressure gradient

$$\frac{\partial p}{\partial r} = -\frac{6r\cos(t)}{\left(1 + \frac{r^2}{2}\right)^3}. \tag{2.26}$$

Equation (2.26) may be integrated again with respect to r, subject to the boundary condition (2.19) to give the pressure field

$$p(r,t) = \frac{3}{\left(1 + \frac{r^2}{2}\right)^2}\cos(t). \tag{2.27}$$

The quantity of most interest is the normal force, which we calculate to be

$$F_n(t) = 2\pi \int_0^\infty r p(r,t)\, dr = 6\pi\cos(t), \tag{2.28}$$

which is consistent with (2.1).

An important feature of the pressure field is that it is negative for $\pi/2 < t < 3\pi/2$: as the sphere moves upwards, liquid moves in by mass conservation leading to a suction. If this negative pressure is large enough then the total pressure, $\overline{p}_{tot} = \overline{p} + p_{atm}$, reduces below the vapour pressure, p_{vap}, i.e. the liquid is in tension and so may cavitate. In dimensional terms, this will occur when,

$$p_{atm} + \frac{3\mu A\omega R_c}{H^2} \frac{\cos(t)}{\left(1 + \frac{r^2}{2}\right)^2} \leq p_{vap}. \tag{2.29}$$

At any instant in time, the magnitude of the pressure is largest where the film thickness is minimum, i.e. at $r = 0$. We may therefore rewrite (2.29) as a cavitation condition

$$\cos(t) \leq -\frac{p_c}{3} \tag{2.30}$$

where

$$p_c = (p_{atm} - p_{vap}) \frac{H^2}{\mu A\omega R_c}. \tag{2.31}$$

By definition $p_c > 0$. If $p_c > 3$, the pressure never becomes sufficiently negative for cavitation to occur. When $p_c = 3$, the minimum total pressure in the film is equal to the vapour pressure of the fluid only at the centre of the film, $r = 0$, and only at the instant $t = \pi$. For $0 < p_c < 3$ cavitation occurs when $t = t_f = \cos^{-1}(-p_c/3)$. The pressure described by the classic lubrication model then rises above the cavitation pressure everywhere in the film at $t_2 = 2\pi - \cos^{-1}(-p_c/3)$. The range within which t_f and t_2 may vary between is $\pi/2 < t_f < \pi$ and $\pi < t_2 < 3\pi/2$, respectively.

2.3.2 Cavitation

As a first attempt to model what happens when the liquid goes into tension we assume that, once the pressure falls below the cavitation pressure, the fluid may be partitioned into two regions: the liquid region and the bubble, as shown in Figure 2.5. We denote the pressure in each region using subscripts l and b, while the radius of the bubble is denoted by $R(t)$. We write the pressure in the film as a piecewise continuous function

$$\hat{p}(r,t) = \begin{cases} p_b(r,t), & 0 < r < R(t), \\ p_l(r,t), & r > R(t). \end{cases} \tag{2.32}$$

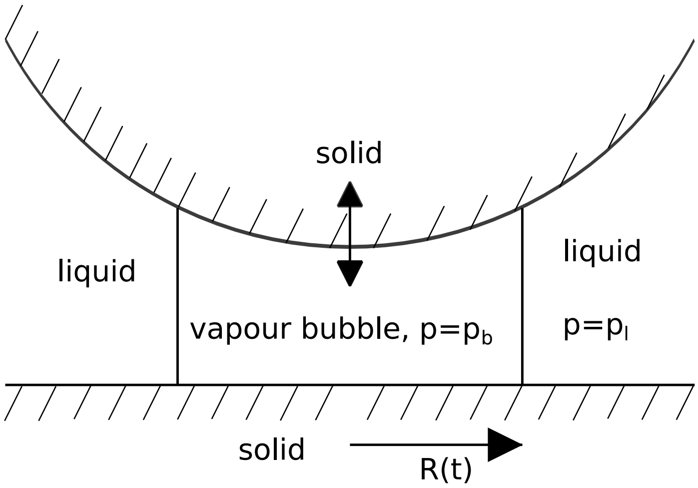

Figure 2.5: Schematic of the bubble model: after cavitation a single bubble, radius $R(t)$, of vapour forms. Inside the vapour bubble the pressure $p = p_b$, a constant.

The classic lubrication equations (2.12)-(2.14) and the boundary conditions (2.15), (2.17)-(2.18), and (2.22) apply in the liquid region. We assume the bubble is purely composed of vapour, and the rate of the growth of the bubble is significantly less than the speed of sound in the bubble. We also assume the system is at thermal equilibrium so that the pressure inside the bubble may assumed to be constant, and equal to the cavitation pressure:

$$p_b \equiv -p_c. \tag{2.33}$$

Requiring the pressure to be continuous at the bubble-vapour interface, we write

$$p_l = -p_c \text{ on } r = R\left(t\right). \tag{2.34}$$

Finally we note that the radius of the bubble is unknown, $R\left(t\right)$, and has to be determined as part of the solution. We assume the bubble surface moves with the average speed of the liquid there, and thus write

$$\dot{R}\left(t\right) = \frac{1}{1+\frac{R(t)^2}{2}} \int_0^{1+\frac{R(t)^2}{2}} u_r\left[R\left(t\right), z, t\right] dz. \tag{2.35}$$

Integrating the Reynolds equation (2.25), once with respect to r we find pressure gradient has the form

$$\frac{\partial p_l}{\partial r} = 6\left(\frac{C\left(t\right) - r^2\cos\left(t\right)}{r\left(1+\frac{r^2}{2}\right)^3}\right), \tag{2.36}$$

which has the solution

$$p_l\left(r,t\right) = A + 6\int_{R(t)}^{r}\frac{C\left(t\right) - r^2\cos\left(t\right)}{r\left(1+\frac{r^2}{2}\right)^3}dr \tag{2.37}$$

where the function of integration $C(t) \neq 0$ is, in general, non-zero since the liquid region does not extend to $r = 0$. The integral in equation (2.37) may be calculated analytically to give,

$$\begin{aligned} p_l\left(r,t\right) = A &+ 3\cos\left(t\right)\left(\frac{4}{\left(2+r^2\right)^2} - \frac{4}{\left(2+R\left(t\right)^2\right)^2}\right) \\ &- 3C\left(t\right)\left[\log\left(\frac{R\left(t\right)^2}{r^2}\frac{2+r^2}{2+R\left(t\right)^2}\right) + 2\left(\frac{4+R\left(t\right)^2}{\left(2+R\left(t\right)^2\right)^2} - \frac{4+r^2}{\left(2+r^2\right)^2}\right)\right]. \end{aligned} \tag{2.38}$$

We apply the boundary conditions and (2.19) and (2.34) to evaluate expressions for the coefficients A and $C\left(t\right)$,

$$\begin{aligned} A &= -p_c, \\ C(t) &= \frac{4\cos\left(t\right) + \frac{p_c}{3}\left(2+R\left(t\right)^2\right)}{3\left(2+R\left(t\right)^2\right)\log\left(1+\frac{2}{R(t)^2}\right) - 6}. \end{aligned} \tag{2.39}$$

The normal force is given by

$$\begin{aligned} F_n\left(t\right) &= 2\pi\int_0^\infty r\hat{p}\left(r,t\right)dr \\ &= \frac{-4\pi p_c + 24\pi\cos\left(t\right)\left[-2+\left(1+R\left(t\right)^2\right)\log\left(1+\frac{2}{R(t)^2}\right)\right]}{-2\left(3+R\left(t\right)^2\right) + \left(2+R\left(t\right)^2\right)^2\log\left(1+\frac{2}{R(t)^2}\right)}. \end{aligned} \tag{2.40}$$

The equation for the bubble radius (2.35) may be expressed as

$$\dot{R}\left(t\right) = -\frac{C\left(t\right) - R\left(t\right)^2\cos\left(t\right)}{R\left(t\right)\left(2+R\left(t\right)^2\right)}. \tag{2.41}$$

In the limit when the bubble is small, $R \ll 1$, equation (2.41) reduces to

$$R(t)\left[3+2\log\left(\frac{R(t)^2}{2}\right)\right]\dot{R}(t)=\frac{3\cos(t)+p_c}{3}+O\left(R(t)^2\log(R(t))\right) \tag{2.42}$$

as $R(t)\to 0$. Equation (2.42) governs the local behaviour when the bubble is opening or closing. We now consider two limiting cases of (2.42): the first when $p_c \simeq 3$ (so that the total pressure decreases only slightly below the vapour pressure), and the second when $p_c \simeq 0$ (when the film is extremely cavitated).

Weak cavitation, $p_c \simeq 3$

For $p_c \simeq 3$, the right hand side of (2.42) shows that either $R=0$ or $\dot{R}=0$ when $t=\cos^{-1}(-p_c/3)\simeq \pi$, i.e. this is either the time of formation of the bubble, t_f, or the time, t_{max}, at which the bubble reaches its maximum radius. Letting $\Delta = 3-p_c \ll 1$, we use the following ansatz for R and t

$$\left.\begin{aligned} R(t) &= \Delta^{\alpha}R_1(t)+o(\Delta^{\alpha}) \\ t &= \pi+\Delta^{\beta}t_1+o\left(\Delta^{\beta}\right)\end{aligned}\right\}\text{ as }\Delta\to 0,$$

where R_1 and t_1 are of order $O(1)$, and we are free to choose α and β. Expanding (2.41) out in powers of Δ around $t=\pi$, and rearranging for $R(t)$, we derive the equation

$$\Delta^{(2\alpha-\beta)}R_1(t_1)\left[3-2\log(2)+4\log\left(\Delta^{\alpha}R_1(t_1)\right)\right]\frac{dR_1}{dt_1}=-\frac{\Delta}{3}+\frac{1}{2}\Delta^{2\beta}t_1^2+O\left(\Delta^{2\beta}\right)$$

$$\text{as }\Delta\to 0. \tag{2.43}$$

For a dominant balance in (2.43), we require $\beta=1/2$ and $\alpha=3/4$, i.e.

$$R_1(t_1)\left[3-2\log(2)+4\log\left(\Delta^{\frac{3}{4}}R_1(t_1)\right)\right]\frac{dR}{dt_1}=-\frac{1}{3}\left(1-\frac{3t_1^2}{2}\right)+O\left(\Delta^{\frac{1}{2}}\right) \tag{2.44}$$

$$\text{as }\Delta\to 0. \tag{2.45}$$

We note that the right hand side of equation (2.45) is zero to $O(\Delta^{3/2})$ when $t_1=\pm\sqrt{2/3}$, which is equivalent to $t=\pi\pm\sqrt{2\Delta/3}$. The earlier time must correspond to the time at which the bubble forms $t_f\simeq\pi-\sqrt{2\Delta/3}$, while the later time corresponds to the time when $\dot{R}=0$ since the radius of the bubble is greater than zero here. From this we conclude the time, t_{max}, at which the bubble has maximum extent is $t_{max}\simeq\pi+\sqrt{2\Delta/3}$. Integrating

(2.45) with respect to t_1 from t_f (the time the bubble forms) to $\hat{t}$ yields

$$\Delta^{\frac{3}{2}} R_1^2\left(\hat{t}\right)\left(\frac{1}{2}-2\log\left(2\right)+2\log\left(\Delta^{\frac{3}{4}}R_1\left(\hat{t}\right)\right)\right)=-\frac{\Delta^{\frac{3}{2}}}{6}\left(\hat{t}+\sqrt{\frac{2}{3}}\right)^2\left(2\sqrt{\frac{2}{3}}-\hat{t}\right)$$
$$+O\left(\Delta^2\right) \text{ as } \Delta\to 0. \qquad (2.46)$$

We note the right hand side of equation (2.46) is zero when $\hat{t}=2\sqrt{2/3},-\sqrt{2/3}$. We recognize $\hat{t}=2\sqrt{2/3}$ corresponds to the time at which the bubble closes, ($t_c\simeq\pi+2\sqrt{2\Delta/3}$), and $\hat{t}=-\sqrt{2/3}$ corresponds to the time when the bubble forms.

To obtain an approximation for $R\left(t\right)$, we make the substitution

$$R_1=\left(\hat{t}+\sqrt{\frac{2}{3}}\right)\sqrt{\frac{1}{6}\left(2\sqrt{\frac{2}{3}}-\hat{t}\right)}X, \qquad (2.47)$$

where $X=O\left(1\right)$. Dividing both sides by the common factor $\Delta^{3/2}$, equation (2.46) may now be written as

$$X^2\left(\frac{1}{2}-2\log\left(2\right)+2\log\left(X\right)+\log\left(\frac{\Delta^{\frac{3}{2}}}{6}\left(\hat{t}+\sqrt{\frac{2}{3}}\right)^2\left(2\sqrt{\frac{2}{3}}-\hat{t}\right)\right)\right)$$
$$=-1+O\left(\sqrt{\Delta}\right) \text{ as } \Delta\to 0. \qquad (2.48)$$

Making the assumption

$$\log\left(\Delta^{\frac{3}{2}}\left(\hat{t}+\sqrt{2/3}\right)^2\left(2\sqrt{2/3}-\hat{t}\right)/6\right)\gg 1/2-2\log\left(2\right)+2\log\left(X\right) \qquad (2.49)$$

we derive the approximation

$$X\sim\frac{1}{\left[-\log\left(\frac{\Delta^{\frac{3}{2}}}{6}\left(\hat{t}+\sqrt{\frac{2}{3}}\right)^2\left(2\sqrt{\frac{2}{3}}-\hat{t}\right)\right)\right]^{\frac{1}{2}}}. \qquad (2.50)$$

The ratio of the left hand side of (2.49) to the right hand side of (2.49) is

$$\frac{\log\left[\frac{\Delta^{\frac{3}{2}}}{6}\left(\hat{t}+\sqrt{2/3}\right)^2\left(2\sqrt{2/3}-\hat{t}\right)\right]}{1/2-2\log\left(2\right)-\log\left[-\log\left[\frac{\Delta^{\frac{3}{2}}}{6}\left(\hat{t}+\sqrt{\frac{2}{3}}\right)^2\left(2\sqrt{\frac{2}{3}}-\hat{t}\right)\right]\right]}\gg 1. \qquad (2.51)$$

This verifies *a posteriori* that the assumption (2.49) is valid in the limit $\Delta\to 0$. Combining

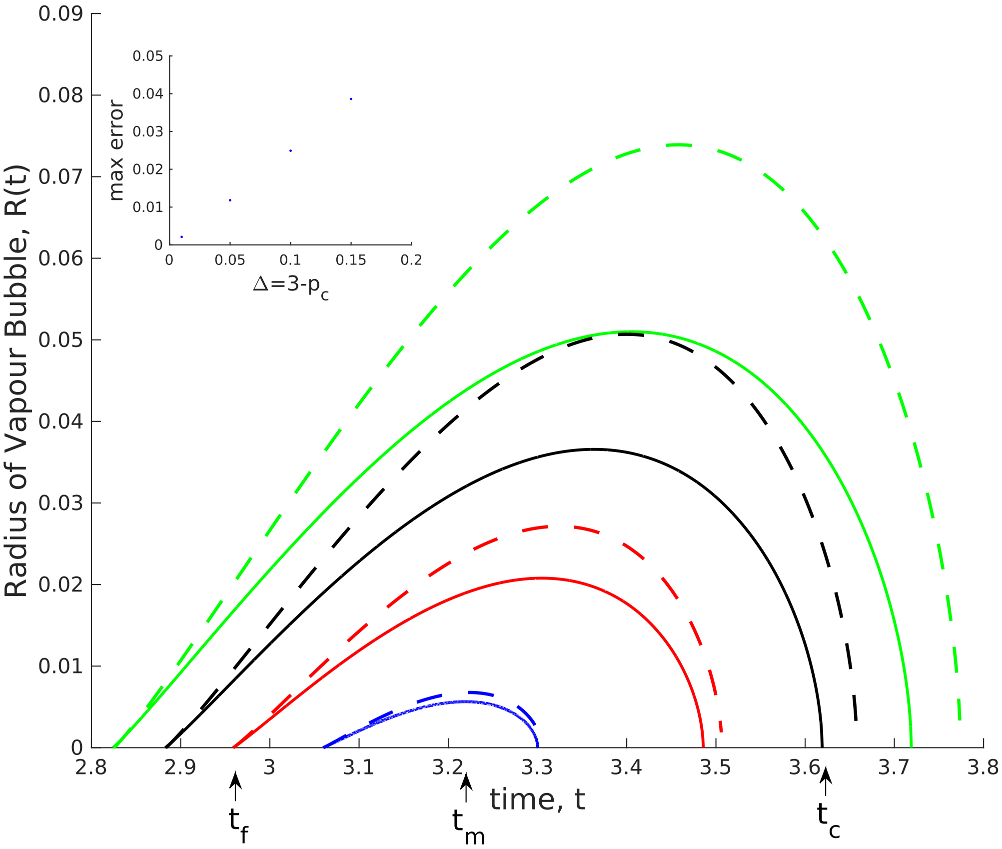

Figure 2.6: The radius of the bubble, $R(t)$, for various values of p_c. The solid curves show the numerical solution to (2.41) and the thin dashed curves show the asymptotic solution (2.52). The time of formation, t_f, the time the radius is maximum, t_{max}, and the time the bubble closes t_c are also shown. Curves show results for $p_c = 2.99$, (red); $p_c = 2.95$, (blue); $p_c = 2.9$, (black); and $p_c = 2.85$, (green). The inset shows that the maximum error between the numerical and asymptotic solutions for $R\,(t)$ decreases linearly as $\Delta \to 0$.

(2.47) and (2.50), we derive an asymptotic expression[2] for $R\,(t)$, namely

$$R\,(t) \sim \frac{\left(t-\pi+\sqrt{\frac{2\Delta}{3}}\right)\left[\frac{1}{6}\left(2\sqrt{\frac{2\Delta}{3}}+\pi-t\right)\right]^{\frac{1}{2}}}{\left[-\log\left(\frac{1}{6}\left(\left(t-\pi+\sqrt{\frac{2\Delta}{3}}\right)^{2}\left(2\sqrt{\frac{2\Delta}{3}}+\pi-t\right)\right)\right)\right]^{\frac{1}{2}}}+O\left(\left[\frac{\Delta^{3}}{-\log\left(\Delta\right)}\right]^{\frac{1}{2}}\right) \quad \text{as } \Delta \to 0. \tag{2.52}$$

Figure 2.6 shows as solid curves the numerical solutions to equation (2.41) which were obtained using Matlab's numerical integration package, ode45. To complete the numerical calculation, the initial radius $R_0 = 0$ was required. However, in this limit (2.41) is singular, and instead we approximated R_0 with (2.52) evaluated at $t = t_f$. The dashed curves show

---

[2] Expression (2.52) is approximate because we made the approximation that $X = O(1)$, which was verified *a posteriori* by (2.51)

the asymptotic solutions (2.52). The inset shown in Figure 2.6 shows that the maximum error between the numerical and the asymptotic solutions for $R(t)$ decreases monotonically to zero as $\Delta \to 0$.

Taking the derivative of (2.52), the velocity of the interface as $t \to t_c$ is found to be given by

$$\frac{dR}{dt} \sim \frac{1}{2\left[\sqrt{\frac{3\Delta}{2}}\left(t_c - t\right)\log\left(\sqrt{\frac{3\Delta}{2}}\left(t_c - t\right)\right)\right]^{\frac{1}{2}}} + O\left(\frac{1}{\left[-\log\left(\sqrt{\frac{3\Delta}{2}}t_c\right)\right]^{\frac{1}{2}}}\right) \quad \text{as } \Delta \to 0, \tag{2.53}$$

and we conclude that the bubble closing speed diverges as $t \to t_c$. Eventually the velocity of the interface will exceed the speed of sound in the medium, producing high frequency pressure waves inside the bubble. We choose to ignore the complex physics in the final stages of the bubble collapse.

Strong Cavitation, $p_c \simeq 0$

To study the effect of strong cavitation, with $p_c \approx 0$, we begin by considering the limiting case $p_c = 0$. Equation (2.41) then takes the form

$$\dot{R} = I\left[R(t)\right]\cos\left(t\right) \tag{2.54}$$

where

$$I\left(R\right) = \frac{-4 + R^2\left(\left(2 + R^2\right)^2 \log\left(1 + 2R^{-2}\right) - 2\left(3 + R^2\right)\right)}{R\left(2 + R^2\right)\left(\left(2 + R^2\right)^2 \log\left(1 + 2R^{-2}\right) - 2\left(3 + R^2\right)\right)}. \tag{2.55}$$

In this case, the bubble forms at $t_f = \pi/2$, and so rearranging equation (2.54) and integrating from $t = \pi/2$, to t we have

$$\int_0^{R_0(t)} \frac{1}{I\left(R\right)} dR = \sin\left(t\right) - 1. \tag{2.56}$$

Because the right hand side of equation (2.56) is symmetric about $3\pi/2$, we can expect in this limit, the radius of the bubble to be symmetric about $t = 3\pi/2$, and the lifetime of the bubble in the film to approach 2π as $p_c \to 0$. This defines $R_0(t)$, the radius of the bubble with $p_c = 0$.

We now derive an asymptotic expression for $R(t)$ in the limit $p_c \ll 1$. In this limit, we observe that the right hand side of (2.42) is zero when $t = \cos^{-1}(-p_c/3) \approx (2n-1)\pi/2$ for $n \in \mathbb{N}$. We use the following ansatz for R and t:

$$\left.\begin{aligned} R(t) &= p_c^{\alpha} R_1(t) + o\left(p_c^{\alpha}\right) \\ t &= \frac{\pi}{2} + p_c^{\beta} t_1 + o\left(p_c^{\beta}\right) \end{aligned}\right\} \text{ as } p_c \to 0,$$

where R_1 and t_1 are $O(1)$, and we choose α and β to maintain a consistent balance. Expanding (2.41) out in powers of p_c around $t = \pi/2$, we find that

$$p_c^{(2\alpha-\beta)} R_1(t_1)\left(3 - 2\log(2) + 4\log\left(p_c^{\alpha} R_1(t_1)\right)\right)\frac{R_1}{dt_1} = \frac{p_c}{3} - p_c^{\beta} t_1 + o\left(p_c^{\beta}\right) \text{ as } p_c \to 0. \tag{2.57}$$

For a dominant balance in (2.57) we thus require $2\alpha - \beta = \beta = 1$, i.e., $\beta = \alpha = 1$. We therefore have

$$R_1(t_1)\left[3 - 2\log(2) + 4\log\left(p_c R_1(t_1)\right)\right]\frac{dR_1}{dt_1} = -\left(t_1 - \frac{1}{3}\right) + O(p_c) \text{ as } p_c \to 0. \tag{2.58}$$

We note that the right hand side of (2.58) is zero when $t_1 = 1/3$, which corresponds to the time the bubble forms $t_f \sim \pi/2 + p_c/3$. Integrating (2.58) with respect to t_1 from t_f to $\hat{t}$, we obtain

$$R_1^2\left(\hat{t}\right)\left(\frac{1}{2} - 2\log(2) + 2\log\left(p_c R_1\left(\hat{t}\right)\right)\right) = -\frac{1}{2}\left(\hat{t} - \frac{1}{3}\right)^2 + O(p_c) \text{ as } p_c \to 0. \tag{2.59}$$

To obtain an asymptotic expression for $R(t)$ as $t \to t_f$, we make the substitution

$$R_1 = \frac{X}{\sqrt{2}}\left(\hat{t} - \frac{1}{3}\right) \tag{2.60}$$

where $X = O(1)$. Making the assumption

$$\log\left[p_c^2\left(\hat{t} - 1/3\right)^2/2\right] \gg 1/2 - 2\log(2) + 2\log(X) \tag{2.61}$$

we derive the asymptotic expression[3]

$$X \sim \frac{1}{\sqrt{-\log\left(\frac{p_c^2}{2}\left(\hat{t}-\frac{1}{3}\right)^2\right)}}, \tag{2.62}$$

so that

$$R\left(t\right) \sim \frac{t-\frac{\pi}{2}-\frac{p_c}{3}}{\sqrt{2\left(\log\left(2\right)-\log\left(t-\frac{\pi}{2}-\frac{p_c}{3}\right)\right)}} + O\left(\frac{p_c^2}{\sqrt{-\log\left(p_c\right)}}\right) \text{ as } p_c \to 0. \tag{2.63}$$

The ratio of the left hand side of (2.61) to the right hand side of (2.61) is

$$\frac{\log\left[\frac{p_c^2}{2}\left(\hat{t}-1/3\right)^2\right]}{1/2-2\log\left(2\right)-\log\left[-\log\left[\frac{p_c^2}{2}\left(\hat{t}-\frac{1}{3}\right)^2\right]\right]} \gg 1. \tag{2.64}$$

This verifies *a posteriori* that the assumption (2.61) is valid in the limit $p_c \to 0$.

To analyse the behaviour when bubble is closing, we use the following ansatz for R and t

$$\left.\begin{aligned} R\left(t\right) &= p_c^{\alpha} R_1\left(t\right) + o\left(p_c^{\alpha}\right) \\ t &= \frac{5\pi}{2} - \left(A+t_1\right)p_c^{\beta} + o\left(p_c^{\beta}\right) \end{aligned}\right\} \text{ as } p_c \to 0, \tag{2.65}$$

where R_1 and t_1 are $O\left(1\right)$, and we are free to choose α, A, and β. Substituting these expansions into equation (2.41), and equating the leading order terms in p_c, we find $\alpha = \beta = 1/2$. We note

$$t_c = 5\pi/2 - A\sqrt{p_c} \tag{2.66}$$

is the asymptotic expression for the time at which the bubble closes. The constant A may be determined by matching the asymptotic expansion for t_c, (2.66), with the numerical value for t_c, shown as red dots in Figure 2.7, in the limit $p_c \to 0$. By calculating the slope of the straight line that best fit the red dots against $\sqrt{p_c}$ in the range $10^{-5} < p_c < 10^{-2}$, we found $A \simeq 2.9$.

With these substitutions, the leading order terms of equation (2.41) may be expressed

---

[3] Expression (2.63) is approximate because we made the approximation that $X = O(1)$, which was verified *a posteriori* by (2.64).

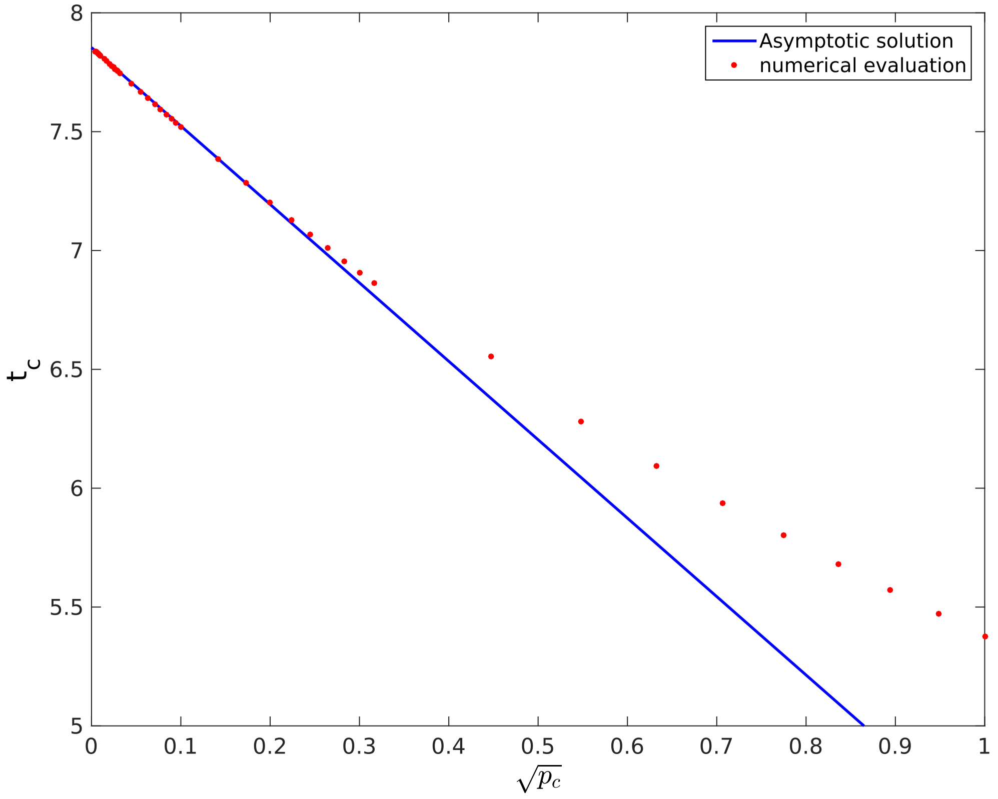

Figure 2.7: The numerical values, (red dots), and asymptotic prediction equation (2.66), (blue line), of the time at which the bubble collapses. The constant A was evaluated by matching the asymptotic expression to the numerical values; this procedure suggests $A = 2.9$.

as

$$-\left[3 - \log\left(2\right)\right] R_1 \frac{dR_1}{dt_1} = A + t_1 + O\left(\sqrt{p_c}\right) \tag{2.67}$$

which may be integrated to give

$$R_1^2 \left[1 - \log\left(2\right)\right] = -t_1 \left(A + \frac{t_1}{2}\right) + O\left(\sqrt{p_c}\right). \tag{2.68}$$

Using the following substitution

$$R_1 = \sqrt{t_1 \left(A + \frac{t_1}{2}\right)} X, \tag{2.69}$$

where X is assumed to be $O\left(1\right)$, equation (2.68) may now be expressed as

$$X^2 \{\log\left[p_c t_1 \left(A + t_1/2\right)\right] + 2 \log X + 1 - \log 2\} = -1 + O\left(\sqrt{p_c}\right). \tag{2.70}$$

Making the assumption

$$\log\left[p_c t_1\left(A + t_1/2\right)\right] \gg 2\log X + 1 - \log 2, \tag{2.71}$$

we find that

$$X \sim \left[-\log\left(p_c t_1\left(A + \frac{t_1}{2}\right)\right)\right]^{-\frac{1}{2}}, \tag{2.72}$$

i.e.

$$R\left(t\right) \sim \frac{1}{2}\left[\frac{\left(\frac{5\pi}{2} - t\right)^2 - A^2 p_c}{-\log\left(\frac{\sqrt{\left(\frac{5\pi}{2} - t\right) - A^2 p_c}}{2}\right)}\right]^{\frac{1}{2}} + O\left(\frac{p_c}{\sqrt{-\log\left(p_c\right)}}\right) \text{ as } p_c \to 0. \tag{2.73}$$

The ratio of the left hand side of (2.71) to the right hand side of (2.71) is

$$\frac{\log\left[p_c t_1\left(A + t_1/2\right)\right]}{1 - \log 2 - \log\left[-\log\left[p_c t_1\left(A + \frac{t_1}{2}\right)\right]\right]} \gg 1. \tag{2.74}$$

This verifies *a posteriori* that the assumption (2.71) is valid in the limit $p_c \to 0$.

A comparison between the asymptotic expressions (2.63) and (2.73)[4] and the numerical solution to equation (2.41) is shown in Figure 2.8. The numerical solutions were obtained using the ODE solver ODE45 in MATLAB. We generally observe good agreement between the numerical solution and the asymptotic solutions; the asymptotic solution valid near the bubble formation shows a better agreement to the numerical solutions than that valid near the closure of the bubble. This is because the error in the asymptotic solution near closure (2.73), is an order in p_c lower than that in the asymptotic solution near the bubble opening (2.63).

2.3.3 Pressure profile in bubble model

We now consider the pressure profile in the bubble model and compare it to the pressure profile predicted by the classical lubrication model. Figure 2.9 shows pressure profiles, in the cases of cavitation described by equation (2.38) (red line), and no cavitation described by equation (2.27) (blue line), at time $t_f = 2.4$. For the cavitated case ($p_c = 1$), the

---

[4] Expression (2.73) is approximate because we made the approximation that $X = O(1)$, which was verified *a posteriori* by (2.74).

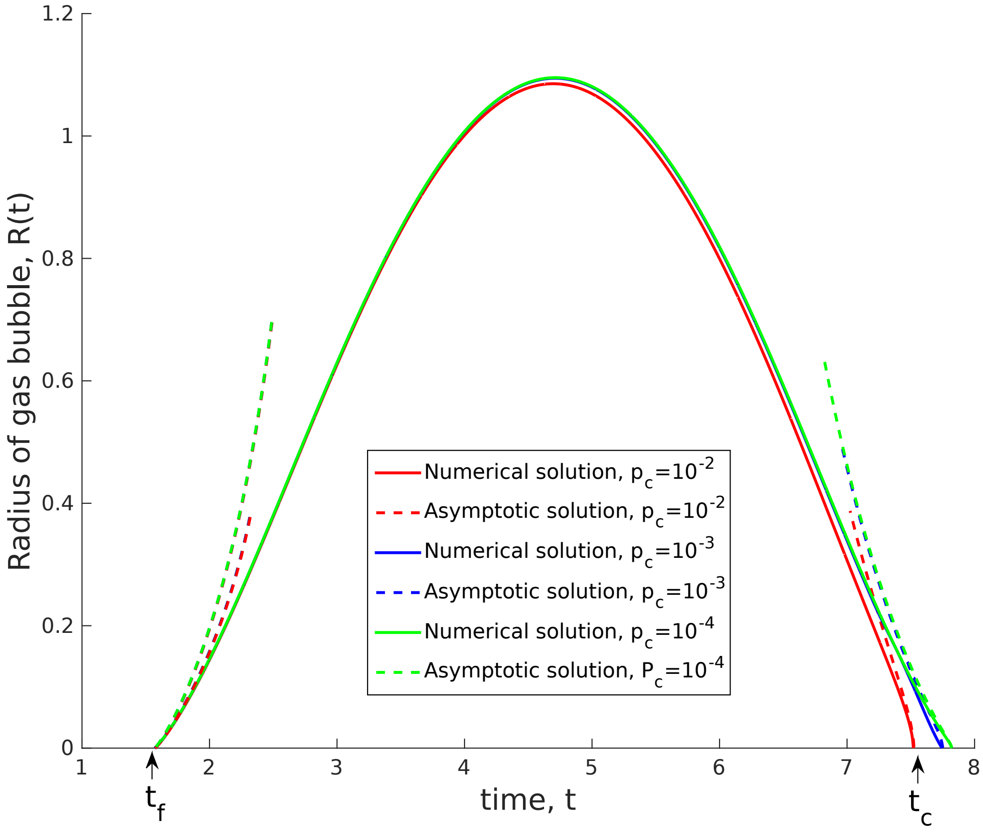

Figure 2.8: The radius of the vapour bubble as a function of time for strongly cavitating films. The numerical solutions of (2.39) and (2.41) are shown for various cavitation pressures (solid curves). The corresponding asymptotic predictions for when the bubble is opening, (2.63), and when the bubble is closing, (2.73), are shown as dashed curves with the parameter values $p_c = 10^{-4}$ (green), $p_c = 10^{-3}$ (blue), and $p_c = 10^{-2}$ (red).

bubble forms at $t_f = 1.9$ and shortly after, the bubble model predicts that the pressure immediately outside the bubble reduces below the cavitation pressure. In fact, the pressure gradient on the liquid side of the bubble interface must be negative while the bubble radius is still increasing.

We relate the bubble model to Lacey and Shillor (1983), who discuss a one-phase Stefan problem which considers a liquid metal cooling and solidifying into a solid over a sharp interface. They show that in a sharp solid-liquid interface model, the temperature in a region of the solid will increase above the solidification temperature, causing the solid to be superheated. Lacey and Shillor (1983) show the interface to be linearly unstable when the heat flux towards the free boundary from the superheated solid is greater than the heat flux from the liquid. In this instance, one would expect the superheated region to break up into a mixture of liquid and solid particles with a uniform temperature. The equivalent situation in fluid mechanics is a less viscous fluid flowing into a more viscous fluid which

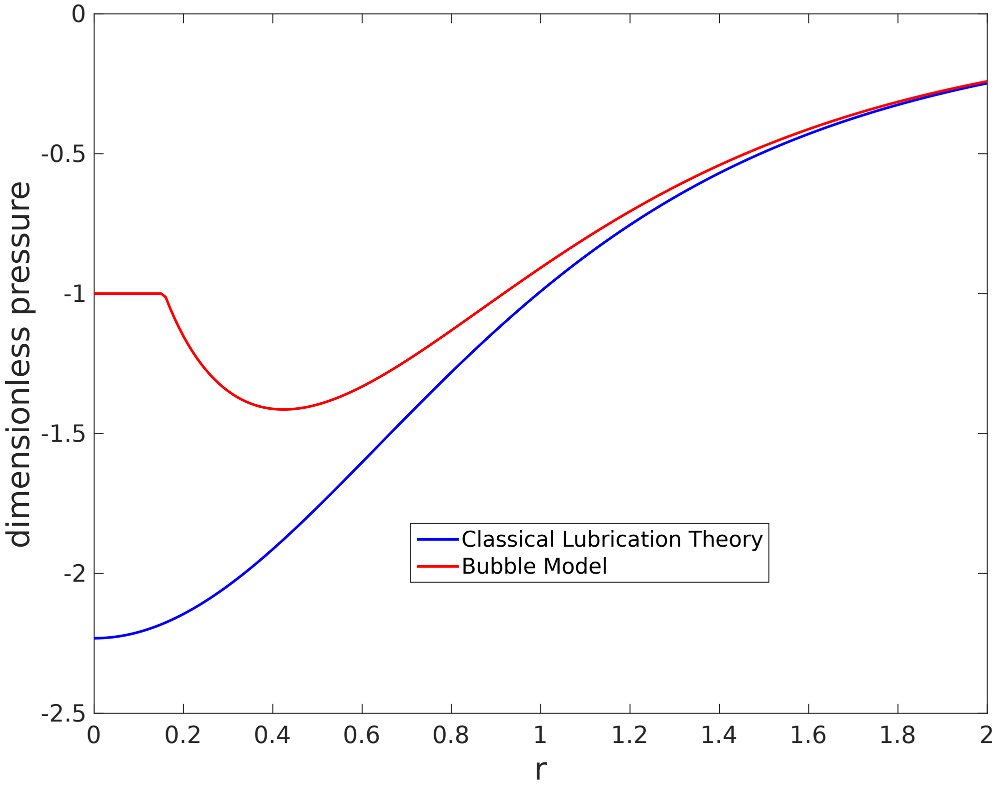

Figure 2.9: Pressure profiles for the bubble model with $p_c = 1$ (red curve) and non-cavitated fluid (blue curve), at time $t_f = 2.4$. The results of the classical lubrication model, (2.27), are valid for $p_c > 3$. Note immediately outside the bubble, the pressure reduces below the cavitation pressure for $r > R(t)$.

is well known to lead to the Saffman-Taylor instability (Saffman, 1991). In the bubble model considered here, the region of negative pressure outside the bubble should therefore be expected to break up into many smaller bubbles almost as soon as it forms. This leads us to consider a model where liquid is able to pass through the boundary of the cavitated region forming a mixture of vapour and liquid.

2.4 Mushy Region Model

Here we describe the mushy region model for a cavitating fluid, based on the work of Ockendon et al. (2003), who consider the expansion of a mushy region in a fluid bounded by two flat parallel plates moving apart from each other. Similarly to the treatment in the previous section, when the fluid cavitates we partition the fluid domain in two regions: a region composed entirely of liquid, $(r > R\,(t))$, and a mushy region consisting of liquid and vapour, $(r < R\,(t))$. A schematic of the model is shown in Figure 2.10. The pressure is thus

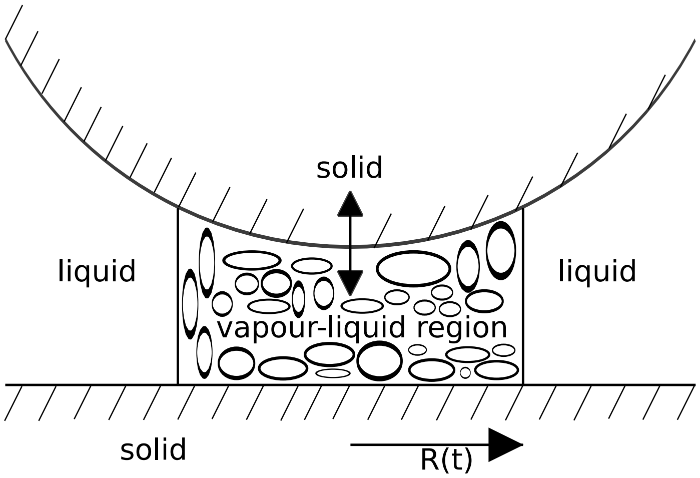

Figure 2.10: Schematic of the mushy region model in which the volume fraction of the liquid in the cavitated region, $\theta(r,t)$, varies.

$$\hat{p}\,(r,t) = \begin{cases} p_m\,(r,t)\,, & 0 < r < R\,(t)\,, \\ p_l\,(r,t)\,, & r > R\,(t)\,. \end{cases} \tag{2.75}$$

We define θ to be the volume fraction of liquid in the mushy region. Since in lubrication theory the pressure in the film is independent of z, it is reasonable to assume that the volume fraction of liquid is also independent of z. We also assume, that due to the presence of the bubbles in the film, the pressure within the mushy region is constant with respect to r and t and equal to the cavitation pressure:

$$p_m \equiv -p_c, \tag{2.76}$$

as in Ockendon et al. (2003). However, the volume fraction of liquid $\theta = \theta(r,t)$. Assuming the viscosity of the vapour is significantly less than that of the liquid, applying the no-slip boundary conditions on the top and bottom surfaces (2.15) and (2.17), and since the pressure gradient in the mushy region is zero, we see the radial velocity of the liquid must be zero. The thickness-averaged conservation of liquid mass in the mushy region then reads

$$\frac{\partial}{\partial t}\left(\theta(r,t)h_0(r)\right) = 0 \tag{2.77}$$

which may be integrated with respect to t to yield

$$\theta(r)h_0(r) = f(r) \tag{2.78}$$

with $f\left(r\right)$ to be determined. We note that $h_0(r)$ and $f(r)$ are only dependent on r, and so θ must be approximately independent of t. The continuity of flux across the mushy region boundary may be expressed as

$$-\frac{h_0^3}{12}\frac{\partial p}{\partial r}\bigg|_{r=R^+(t)} = h_0\left(1-\theta\right)\frac{dR}{dt}\bigg|_{r=R^-(t)}. \tag{2.79}$$

We require the pressure to be above the cavitation pressure everywhere in the film, and hence require

$$\frac{\partial p}{\partial r} > 0 \quad \text{at} \quad r = R(t) \quad \text{while} \quad \frac{dR}{dt} > 0. \tag{2.80}$$

To satisfy this criteria we place the following condition on θ:

$$\theta = 1 \quad \text{on} \quad r = R(t) \quad \text{while} \quad \frac{dR}{dt} > 0. \tag{2.81}$$

Since θ is approximately independent of t, we conclude that $\theta = 1 + O(\epsilon)$ everywhere inside the mushy region, $r < R(t)$. Our model differs from the analysis of Ockendon et al. (2003), who consider a film thickness that varies as a function of time at leading order (so that θ must also depend on t). This difference arises because we have assumed that the amplitude of the oscillations of the paraboloid are small compared to the film thickness, $\epsilon \ll 1$.

We conclude that the boundary condition on the interface $r = R\left(t\right)$ for the pressure in the liquid region is simply

$$\frac{\partial p}{\partial r} = 0 \text{ at } r = R\left(t\right) \tag{2.82}$$

for all time the mushy region exists in the film. We also require the pressure to be continuous over across the interface,

$$p_l = -p_c \text{ at } r = R\left(t\right). \tag{2.83}$$

Substituting the equation for the velocity (2.24) into the continuity equation (2.14), integrating with respect to z, and applying the boundary conditions (2.18), (2.22), and

(2.82) yields the Reynolds equation in the liquid region

$$\frac{\partial p_l}{\partial r} = 6\left(\frac{R(t)^2 - r^2}{r\left(1+\frac{r^2}{2}\right)^3}\right)\cos(t). \tag{2.84}$$

Equation (2.84) may be integrated with respect to r, and applying the boundary condition at $r = \infty$, (2.19), yields the pressure within the liquid, namely

$$p_l(r,t) = 6\left[\frac{R(t)^2}{2}\log\left(\frac{r^2}{2+r^2}\right) + \frac{2+R(t)^2\left(3+r^2\right)}{\left(2+r^2\right)^2}\right]\cos(t). \tag{2.85}$$

The normal force is given by

$$F_n(t) = -\pi p_c R(t)^2 + 6\pi\left(1 - R(t)^2 - \frac{1}{2}R(t)^4\log\left(\frac{R(t)^2}{2+R(t)^2}\right)\right)\cos(t). \tag{2.86}$$

The radius of the mushy region is determined by solving (2.76), i.e.

$$p_l(R(t),t) = -p_c,$$

which leads to

$$R(t)^2\log\left(\frac{R(t)^2}{2+R(t)^2}\right) + \frac{2\left(1+R(t)^2\right)}{2+R(t)^2} = -\frac{p_c}{3\cos(t)}. \tag{2.87}$$

The transcendental equation (2.87) determines R implicitly in terms of p_c and t.

We now determine the asymptotic results in the limiting cases of $p_c \simeq 3$ and $p_c \ll 0$. To estimate the time at which the bubble forms, we expand equation (2.87) as a series around $R(t) = 0$, giving

$$\left(\frac{1}{2} - \log 2 + 2\log R(t)\right)R(t)^2 = -\frac{p_c + 3\cos(t)}{3\cos(t)} + O\left(R(t)^3\right) \text{ as } R(t) \to 0. \tag{2.88}$$

Weak cavitation, $p_c \simeq 3$

From the right hand side of (2.88), it is clear that the cavitation first occurs when $t = \cos^{-1}(-p_c/3)$; for $p_c \simeq 3$, this occurs at $t \simeq \pi$. Letting $\Delta = 3 - p_c \ll 1$, we use the following ansatz for R and t:

$$\left.\begin{aligned} R\left(t\right) &= \Delta^{\alpha} R_1\left(t\right) + o\left(\Delta^{\alpha}\right) \\ t &= \pi + \Delta^{\beta} t_1 + o\left(\Delta^{\beta}\right) \end{aligned}\right\} \text{as } \Delta \to 0$$

where R_1 and t_1 are $O\left(1\right)$, and we are free to choose α, and β. We find that $\alpha = 1/2$ and $\beta = 1/2$ and that

$$R\left(t\right) \sim \frac{1}{2}\sqrt{\frac{\frac{2\Delta}{3} - \left(t-\pi\right)^2}{\log\left(2\right) - \log\left(\frac{2\Delta}{3} - \left(t-\pi\right)^2\right)}} + O\left(\frac{\Delta}{\sqrt{-\log\left(\Delta\right)}}\right) \text{ as } \Delta \to 0. \tag{2.89}$$

The right hand side of (2.89) is zero when $t = \pi \pm \sqrt{2\Delta/3}$. The earlier time must correspond to the time the mushy region forms, $t_f \simeq \pi - \sqrt{2\Delta/3}$, and the later time corresponds to the time at which the mushy region closes $t_c \simeq \pi + \sqrt{2\Delta/3}$. We also note from (2.89) that the radius of the mushy region is maximal at $t = \pi$ and further that $R(t)$ is symmetric about $t = \pi$. The asymptotic prediction[5] is compared to the numerical solution of the full problem in Figure 2.11, demonstrating increasingly good agreement as $\Delta \to 0$.

Strong cavitation, $p_c \simeq 0$

When $p_c \simeq 0$, the right hand side of equation (2.88) vanishes when $t = \cos^{-1}\left(-p_c/3\right) \approx \left(2n-1\right)\pi/2$ for $n \in \mathbb{N}$. We consider only $t > 0$ and so the first relevant instant is $t = \pi/2$. We use the following ansatz for R and t

$$\left.\begin{aligned} R\left(t\right) &= p_c^{\alpha} R_1\left(t\right) + o\left(p_c^{\alpha}\right) \\ t &= \frac{\pi}{2} + p_c^{\beta} t_1 + o\left(p_c^{\beta}\right) \end{aligned}\right\} \text{as } p_c \to 0,$$

where R_1 and t_1 are $O\left(1\right)$, and we are free to choose α, and β. We find that $\alpha = 0$ and $\beta = 1$ and $R(t)$ approaches the limit

$$R\left(t\right) \sim \left[\frac{2\left(t - \frac{\pi}{2} - \frac{p_c}{3}\right)}{\left(\frac{\pi}{2} - t\right)\left[\log\left(t - \frac{\pi}{2} - \frac{p_c}{3}\right) - \log\left(t - \frac{\pi}{2}\right)\right]}\right]^{\frac{1}{2}} + O\left(\frac{1}{\sqrt{-\log\left(p_c\right)}}\right) \text{ as } p_c \to 0. \tag{2.90}$$

We note that the mushy region forms at $t = t_f \sim \pi/2 + p_c/3$.

---

[5] Expression (2.89) is approximate for similar reasons made in the derivation of expression (2.52).

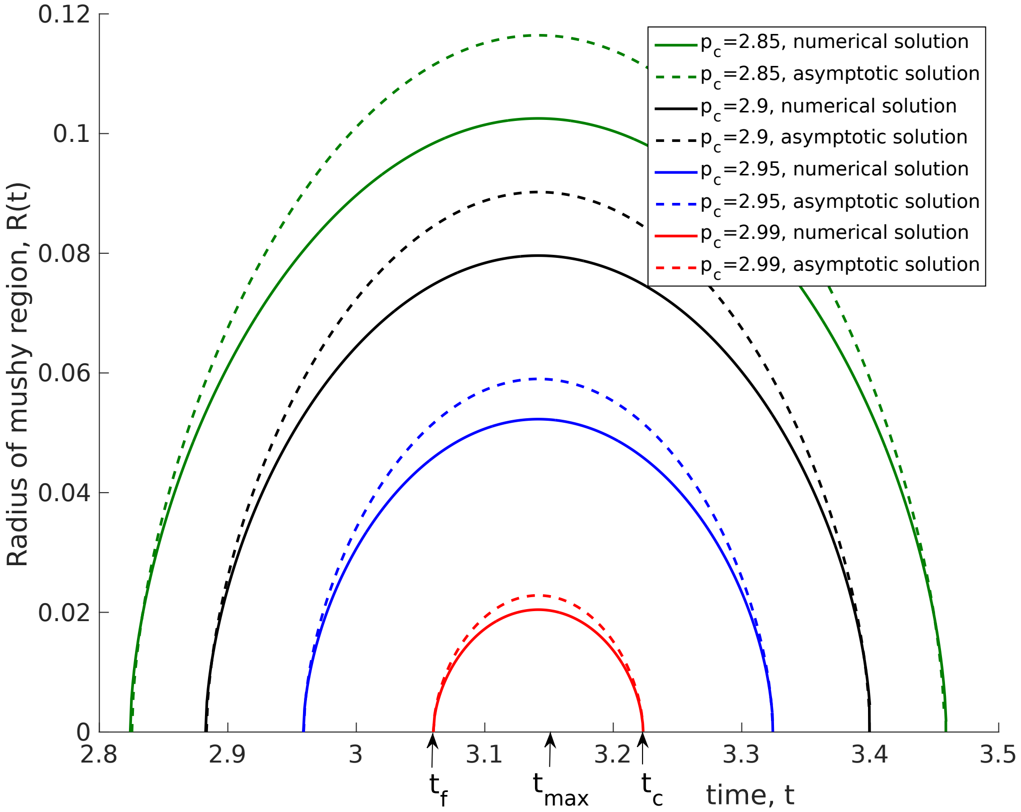

Figure 2.11: The radius of the mushy region, $R(t)$, for weakly cavitating films. The solid curves show the numerical solution to (2.87) and the thin dashed curves show the asymptotic solution (2.89). The time of formation, t_f, the time the radius is maximum, t_{max}, and the time the bubble closes t_c are also shown. The results of the computations are shown for $p_c = 2.99$, (red); $p_c = 2.95$, (blue); $p_c = 2.9$, (black); and $p_c = 2.85$, (green).

The next point in time when equation (2.88) is zero is approximately $t \approx 3\pi/2$ which we expect will correspond to the closing time of the mushy region. Using a similar analysis, the following asymptotic expression[6] for $R\left(t\right)$ around the time $t \approx 3\pi/2$ may be derived

$$R\left(t\right) = \left[\frac{2\left(\frac{3\pi}{2} - \frac{p_c}{3} - t\right)}{\left(t - \frac{3\pi}{2}\right)\left[\log\left(\frac{3\pi}{2} - \frac{p_c}{3} - t\right) - \log\left(\frac{3\pi}{2} - t\right)\right]}\right]^{\frac{1}{2}} + O\left(\frac{1}{\sqrt{-\log\left(p_c\right)}}\right) \quad \text{as } p_c \to 0 \tag{2.91}$$

Figure 2.12 shows the radius of the mushy region as a function of time for various values of p_c. As p_c decreases, the radius of the mushy region increases but always remains bounded within the interval $\pi/2 < t < 3\pi/2$.

---

[6] Expression (2.91) is approximate for similar reasons made in the derivation of expressions (2.63) and (2.73).

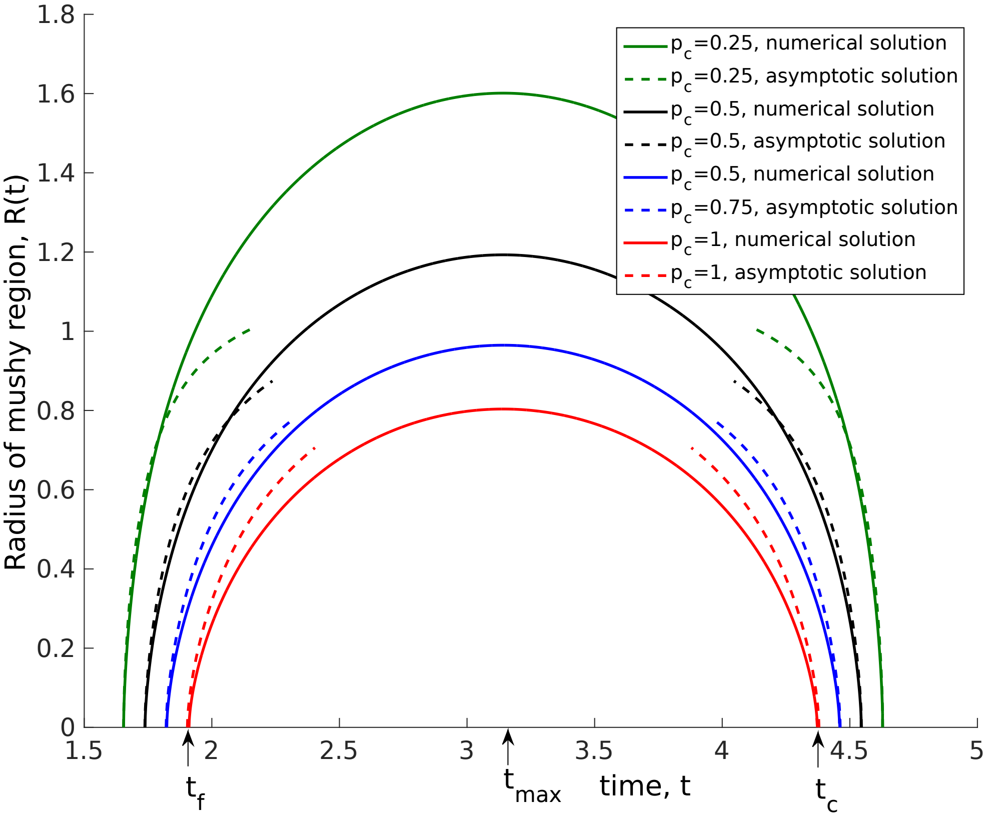

Figure 2.12: The radius of the mushy region as a function of time for various values of the cavitation pressure, $p_c \simeq 0$, (the strong cavitation regime). The solid curves are numerical solutions to (2.87), while the dashed curves show the asymptotic solutions, (2.90) as $t \to t_f$, and (2.91) as $t \to t_c$. The time of formation, t_f, the time the radius is maximum, $t = t_{max}$, and the time the mushy region closes, t_c, are indicated for $p_c = 2.99$. The red curves show $p_c = 1$, the blue curves $p_c = 0.75$, the black curves $p_c = 0.5$, and the green curves $p_c = 0.25$.

2.5 Comparison with Experimental Results

We now consider the experiments of Zhu and Granick (2002c) and consider whether cavitation can explain their measurements of a maximal normal force that is different from what is predicted by classical lubrication theory.

We focus on two test results presented in Figures 2 and 4 of Zhu and Granick (2002c). Both sets of experiments were conducted using tetradecane, with surfactant 1-hexadecylamine. We assume both tests were conducted at room temperature and atmospheric pressure $p_{atm} = 1.01 \times 10^5$ Pa, and that the addition of surfactants did not alter the physical parameters of tetradecane significantly. The vapour pressure and viscosity at room temperature are therefore $p_{vap} = 1.5$ Pa, and $\mu = 2.3 \times 10^{-3}$ Pa s, respectively[7].

However, before we compare their experimental results to our cavitation models, we

---

[7] http://www.chemicalbook.com/ProductMSDSDetailCB7854039.html, accessed 24-November-2013

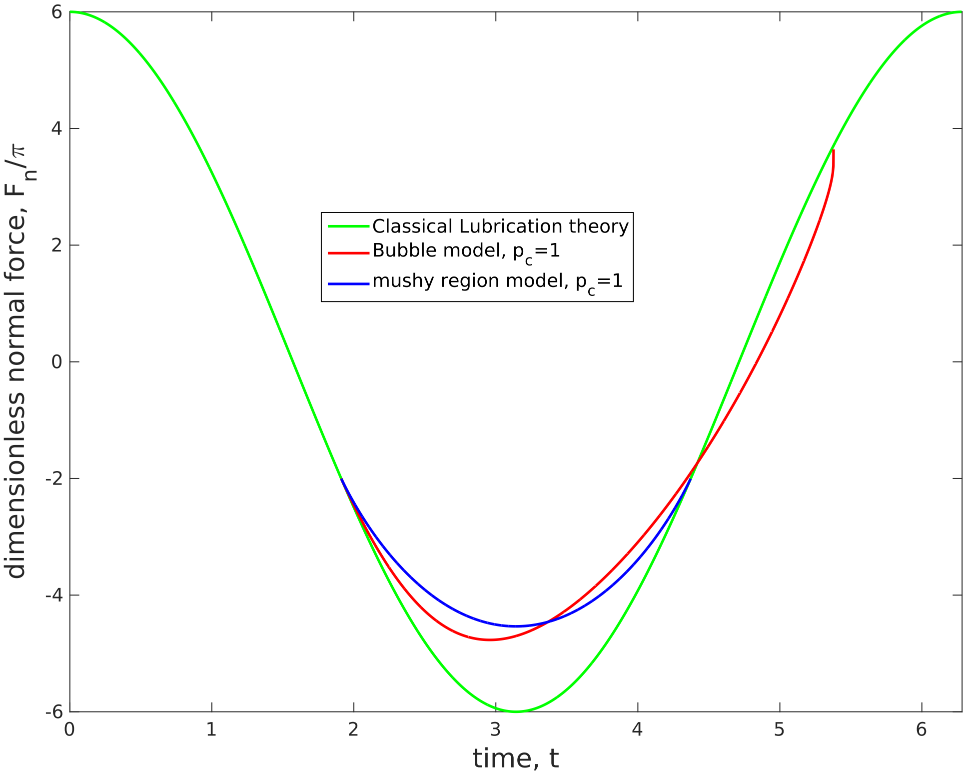

Figure 2.13: The dimensionless normal force F_n/π as a function of time. The green curve shows the force found with the classical lubrication model, (2.28), the red curve shows the force given by the bubble model, (2.40), and the blue curve shows the force given by the mushy region model, (2.86). The later two used a cavitation pressure of $p_c = 1$. The normal force is only affected around the times $t \approx \pi$, when there is a cavitation region.

note that Zhu and Granick (2002c) do not provide a time series of the normal force they measure in the experiment. We therefore do not know the point in the cycle at which they measure the maximum force: it could either be measured when the moving surface is accelerating up or down. In the first instance, the normal force would be compressive, and therefore positive, but in the latter, the normal force would be tensile, and therefore negative and theoretically of equal magnitude to the maximum force if no cavitation had occurred. However, the effects of cavitation would first be noticed when the force is minimum at $t = \pi$. Deviation in the maximum normal force at $t = 0$ or 2π would either be only observed when $p_c \approx 0$, in the bubble model, or not at all in the mushy region model. In Figure 2.13, we show the dimensionless normal force F_n/π as a function of time. We see that the graph has two turning points and note that it is not clear which of them corresponds to the maximum force measured in the experiment. The dimensionless normal force calculated from the bubble model, (2.40), is shown as the red curve and the mushy region model (2.86) is shown as the blue curve, both with a cavitation pressure of $p_c = 1$. The dimensionless normal

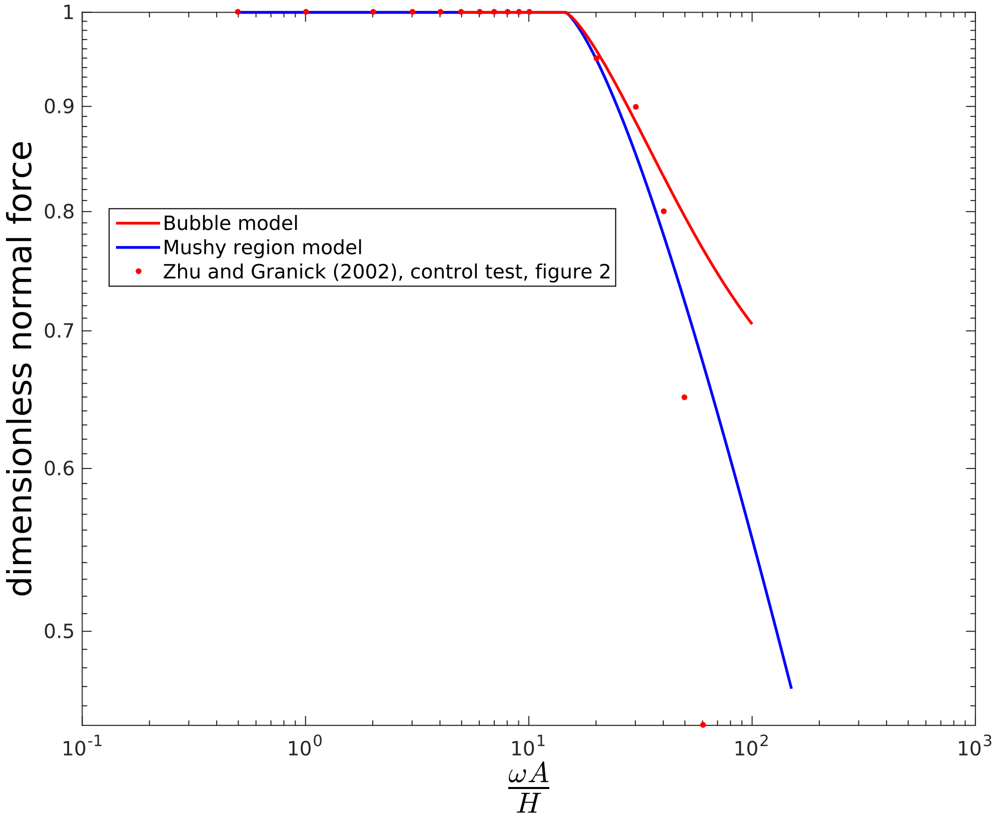

Figure 2.14: Results of the control test performed by Zhu and Granick (2002c) (red dots) compared to the absolute values of the most negative normal force from the bubble model (red curve) and the mushy region model (blue curve). In this experiment they hold the mean film height fixed, (which, from the data provided, we calculated to be 20 nm) and varied the velocity between 10 and 1000 nm/s. Zhu and Granick (2002c) note it is not until the change in pressure experienced in the film approaches atmospheric pressure that they start to notice a deviation in the normal force from classical lubrication theory.

force from the classical lubrication model is the simple sinusodial curve (2.28), shown as the green curve. Due to this reason, for the rest of this chapter, we assume Zhu and Granick (2002c) refer to the most negative, tensile, force measured in their experiment when they describe the maximum normal force.

The red dots in Figure 2.14 show the experimental results of the maximum normal force taken from the control test conducted by Zhu and Granick (2002c), Figure 2, and is plotted against the shear rate $\omega A/H$. The control test contained the surfactant 0.1 % by weight 1-hexadecylamine. In this test, the film height H is held constant, but they do not state what the height of the film is in this test. We were therefore required to calculate it from values of pressure also given on the graph; we found it to be $H \approx 20$ nm. They vary the velocity of the surface between 10 to 1000 nm/s by changing the frequency and amplitude of oscillation. Zhu and Granick (2002c) note that the control test deviates from

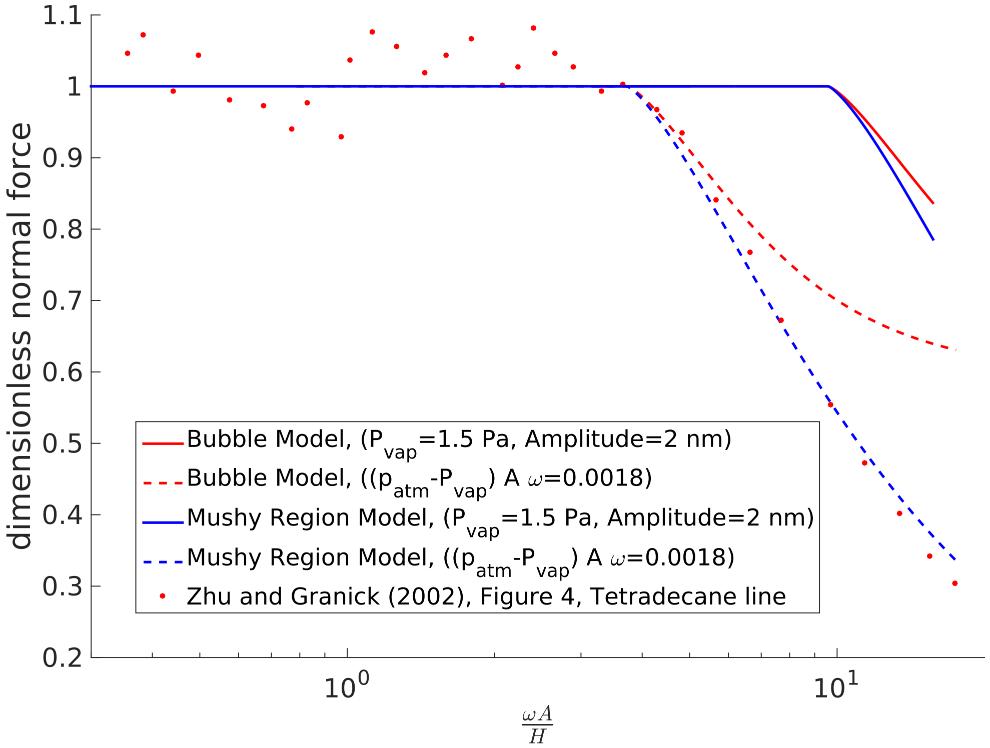

Figure 2.15: Results of experiments involving tetradecane and the surfactant, 1-hexadecylamine (Zhu and Granick, 2002c), (dots), compared with our models for cavitation: the bubble model and the mushy region model. We present the absolute value of the most negative normal force from the bubble model (red curves), the mushy region model (blue curves), and the maximum dimensionless normal force taken from Figure 4 in Zhu and Granick (2002c). The solid curves show the solutions with physical parameters reported by Zhu and Granick (2002c): vapour pressure, $p_{vap} = 1.5$ Pa and the amplitude of oscillation $A = 2$ nm. The dashed curves show solutions with $(p_{atm} - p_{vap})\,\omega A = 0.0018$ N/m s, thus equating the point where Zhu and Granick (2002c) first notice a deviation in their results with the point where we expect cavities to first form in the film.

classical lubrication theory as the magnitude of the change in pressure experienced in the film approaches that of atmospheric pressure. This agrees with our hypothesis that for cavitation to occur, the change in pressure required would have to be of a similar order of magnitude to that of atmospheric pressure, given the vapour pressure of tetradecane is negligible. The red line in Figure 2.14 shows the absolute value of the most negative force experienced in the film for the bubble model (2.40), and the blue line shows the mushy region model (2.86). The mushy region model predicts their control test results better than the bubble model for published physical values of tetradecane.

We now consider a different experiment, one with twice as much surfactant, 0.2 % by weight 1-hexadecylamine, shown in Figure 4 of Zhu and Granick (2002c). In this experiment, the bottom surface was oscillated in a sinusoidal manner with a fixed amplitude and frequency $A = 2$ nm and $\omega = 63$ rad/s respectively. They do not explicitly state the range of film heights H they considered in this experiment. We therefore were required to estimate the film height in their experiment from the shear rate, $A\omega/H$.

Figure 2.15 shows the absolute value of the most negative normal force as a function of shear rate, the bubble model in red (2.40), the mushy region model in blue (2.86), and the results taken from Figure 4 in Zhu and Granick (2002c), as red dots. The solid curves show the results using the parameters reported by Zhu and Granick (2002c), namely $p_{vap} = 1.5$ Pa and $A = 2$ nm. We calculated the film height when cavities first start to form to be $H = 13.1$ nm, and the shear rate $A\omega/H = 9.6$ s^{-1}. Zhu and Granick (2002c) first notice a deviation in their measurements at approximately a shear rate of $A\omega/H \approx 3.7$ s^{-1}. Given the fixed amplitude and frequency, we calculate the film height when this happens in their experiment to be approximately $H \approx 34.1$ nm.

We would like to highlight some features of the Zhu and Granick (2002c) experiments here. First, surfactants in the fluid film are known to lower the local surface energy of a liquid-bubble interface. Krotov and Rusanov (1982) apply chemical potential theory to show that the vapour pressure of a liquid will increase as the surface tension, and hence surface energy, decreases with the adsorption of surfactants. However, the magnitude of the change in vapour pressure in the presence of surfactant is likely to be highly dependent of the type on fluid and surfactant used. We therefore cannot easily estimate the magnitude of the change in vapour pressure in their experiment. We also note that the presence of gas bubbles, foreign bodies such as micelles, and the mica surfaces will provide nucleation sites for cavities in the liquid. We also highlight that the true amplitude of oscillation of the bottom surface in their experiment is not the amplitude they state. Even though they account for apparatus compliance in their experiment, they do not provide an estimate of the true amplitude of oscillation the fluid experiences. Decreasing the amplitude will decrease the magnitude of the change in pressure, but it will also decrease the shear rate, $A\omega/H$. This may reduce the shear rate at which cavitation first occurs. We note that changing the shear rate will change the value we calculated for the film height, H.

With those points in mind, we list the quantities we do know. These are: the magnitude of the dimensionless normal force, the shear rate expressed as $\omega A/H$, and that (assuming the film does experience cavitation) the point where Zhu and Granick (2002c) first observe a deviation in the normal force from the classical lubrication theory requires the dimensionless cavitation pressure to equal

$$p_c = (p_{atm} - p_{vap}) \frac{H^2}{\mu A \omega R_c} = 3. \tag{2.92}$$

Rearranging (2.92), we find

$$p_c = [(p_{atm} - p_{vap}) \, \omega A] \, \frac{1}{\mu R_c} \left(\frac{H}{A\omega} \right)^2 = 3 \tag{2.93}$$

and the quantity $1/(\mu R_c)(H/A\omega)^2$ is known with completely. This leaves us to modify the values of p_{vap} and A such that the expression

$$(p_{atm} - p_{vap}) \, \omega A = 3\mu R_c \left(\frac{\omega A}{H} \right)^2 = 0.0018 \quad \frac{\text{N}}{\text{m s}} \tag{2.94}$$

is satisfied. The range we calculate p_{vap} and A to vary between are 1.5 Pa $< p_{vap} <$ 8.67×10^4 Pa and 0.29 nm $< A <$ 2 nm, however these are not consistent with published values of the vapour pressure and amplitude in their experiment.

By letting $(p_{atm} - p_{vap}) \, \omega A = 0.0018$ N/m s, we calculate the absolute value of the most negative normal force from the bubble model and mushy region model as the shear rate was varied between 0.1 $\text{s}^{-1} < \omega A/H <$ 20 s^{-1}. These are shown as dashed red and blue curves respectively in Figure 2.15. It is clear from Figure 2.15 that the mushy region model for these parameters closely resembles the results presented by Zhu and Granick (2002c). However, if the fluid in the experiments was indeed cavitating, the authors might have been expected to observe its effects in the interferometer they used to measure the film height. However, Zhu and Granick (2002c) make no such remarks.

2.6 Conclusions

In this chapter, we considered the experiments of Zhu and Granick (2002c) who use a surface force apparatus to measure the maximum normal force in a film during the vertical oscillation of a surface bounding the film. We discuss their experiment and results in Section 2.2. They find at a critical shear rate that the normal force deviates from the classical lubrication model. They attribute the deviation they observe to fluid slipping at the liquid-solid interface, but cannot conclusively show this is what is happening in their experiment. We calculate the approximate change in pressure in the film and find it to be of a similar order of magnitude to the atmospheric pressure, leading us to hypothesise that their results may be caused by cavitation.

We show that the formation of cavities in the film is dependent on a single parameter we call the cavitation pressure, p_c. For cavitation to occur in the film, p_c must take a value between $0 < p_c \leq 3$. At $p_c = 3$, the total pressure in the film equals the vapour pressure at a single point in time and location in the film. We consider two models of the fluid cavitating. In Section 2.3, we describe the bubble model, which consists of a single bubble composed entirely of vapour. On the bubble-liquid boundary, we apply the kinematic boundary condition, preventing the liquid from crossing the interface. For larger values of the cavitation pressure, $p_c \approx 3$, the radius of the bubble is shown to be asymmetric about its maximum. Once the bubble has formed, it grows steadily until it reaches a maximum, after which the bubble experiences a rapid collapse. We showed that when $p_c = 0$, the radius of the bubble is symmetric around its maximum, showing no rapid expansion or collapse. As the bubble is radially expanding, we show that the pressure reduces below the cavitation pressure immediately outside the bubble and suspect this would cause the single bubble to break up and disperse into a multitude of many smaller bubbles.

This motivates us to consider a second model for cavitation, described in Section 2.4 and originally considered by Ockendon et al. (2003). We refer to the model as the mushy region model. Here, the cavitated region is a composition of vapour and liquid. Instead of considering the physics of individual bubbles in the film, we describe the macroscopic properties, such as pressure and volume fraction in the region. In contrast to the bubble model, in the mushy region model, we assume the liquid may pass freely through the interface such that there is no change in pressure across the interface. The radius of the mushy region is shown to be symmetric about its maximum, regardless of the value of p_c. However, as $p_c \to 0$, the rate of expansion and collapse of the radius approach infinity.

The lifetime of the cavitation region in the bubble model is shown to approach the period of oscillation of the top surface, leading us to conclude that the bubble may exist in the film even when the pressure described by the classical lubrication model is above the vapour pressure everywhere in the film. This is in contrast with the mushy region model where the lifetime of the mushy region is shown to be bounded by the time the pressure described by the classic lubrication model remained below the vapour pressure. The differences in the models are attributed to the difference in the boundary condition at the liquid-vapour interface; that is, whether or not the liquid can cross the interface into the cavitated region.

In Section 2.5, we compare our cavitation models to two experiments in Zhu and Granick (2002c): a control test that contained a small amount of surfactant, and a second experiment that contained twice as much surfactant as the control test. The results from the control test in Zhu and Granick (2002c) show reasonable agreement with the mushy region model for published physical properties of the base liquid. In this test, Zhu and Granick (2002c) note a deviation in the normal force when the change in pressure in the film approaches atmospheric pressure, supporting the possibility of the film cavitating. In the second set of experimental results found in Figure 4 of Zhu and Granick (2002c), the mushy region model was able to reproduce their experimental results without appealing to slip. However, to do this we had to use parameter values that are not consistent with those reported by Zhu and Granick (2002c). Possibly, inclusion of other physical aspects in these models, such as apparatus compliance or surfactant effects, might account for this discrepancy.

We have proposed a mechanism that reproduces the experimental results of Zhu and Granick (2002c), without appealing to slip. We conclude that it is plausible that the liquid film in their experiments does cavitate, though further experimental evidence is needed to confirm this. We also note that if the fluid in their experiments was indeed cavitating, the authors might have been expected to observe the effects of the vapour bubbles in the interferometer used to measure the film thickness. Since they did not report any bubbles in the film it may, in fact, be consistent with our finding that only a small volume of vapour is required in the mushy region ($\epsilon = 1 + O(\epsilon)$).

In the next chapter, we discuss how a mushy region develops in a liquid film that experiences both sliding pressure from the horizontal movement of the bottom surface and squeezing pressure from the vertical movement of the top surface.

Chapter 3

Cavitation in Slider Bearings

3.1 Introduction

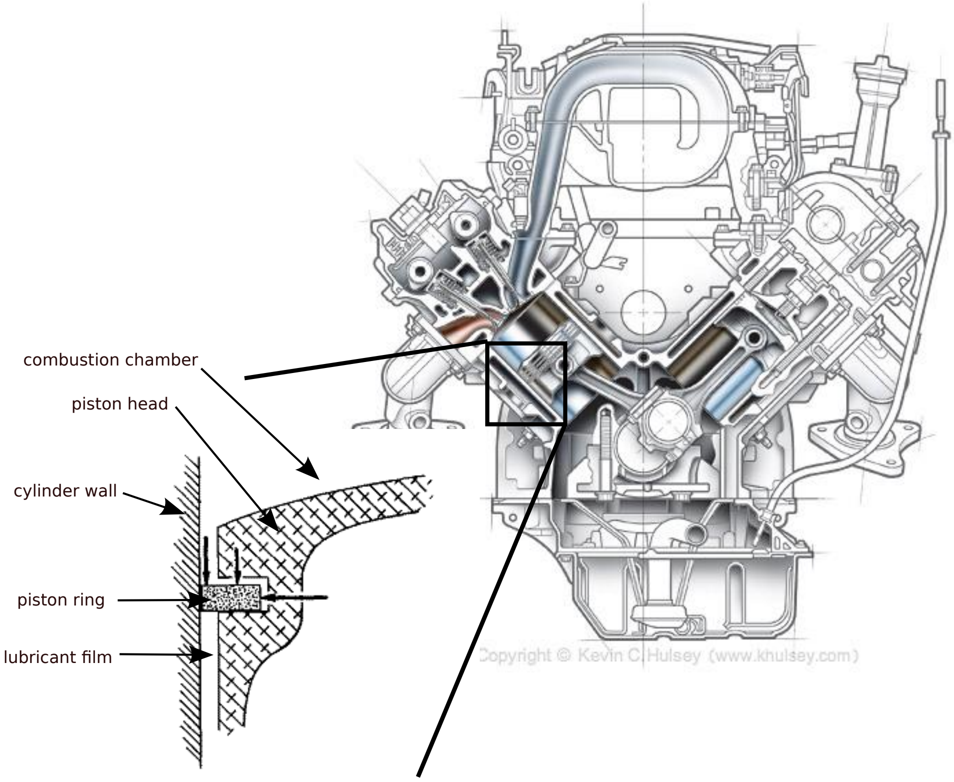

Figure 3.1: A schematic of an engine, showing a close up view of the piston head, piston ring and cylinder wall, taken from Gilles (1996).

In the previous chapter, we considered how cavitation bubbles may form inside a negative squeeze film. We continue to investigate cavitation in thin liquid films, now in a situation where one surface moves horizontally at a known velocity; which is analogous to a film of liquid between the piston ring and cylinder wall inside a car engine, as shown in a schematic

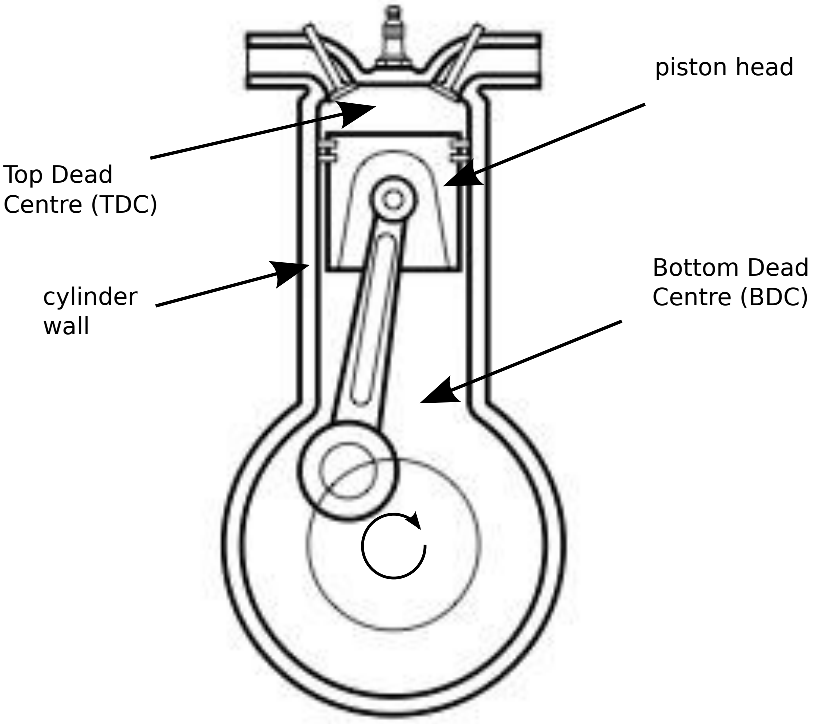

Figure 3.2: Engine cycle geometry.

in Figure 3.1, taken from Gilles (1996).[1] The piston ring is housed inside a groove in the piston head. The piston head slides parallel to the cylinder wall in a sinusoidal motion which, through the connection rod, drives the crank shaft. When the piston head reaches its maximum distance from the crank shaft, it is said to be at Top Dead Centre (TDC), and when it is at its minimum distance from the crank shaft it is said to be at Bottom Dead Centre (BDC). These positions in the cylinder are shown in Figure 3.2[2]. Top Dead Centre and Bottom Dead Centre are the two most extreme environments the lubricant experiences in the engine cycle. At these locations, the film thickness is at its minimum in the cycle, increasing the chance of surface-to-surface contact, as well as high levels of pressure, stress and liquid heating.

In this chapter, we study a series of experiments performed at City University of London, hence forth referred to as the City Experiments, that replicates the flow between the piston ring and cylinder wall of an engine. A description of the experimental setup and the results is provided in Section 3.2. Subsequent sections are devoted towards modelling the cavitation process with a mushy region model, an adaption of the Jakobsson, Floberg, Olsson (JFO) model (Jakobsson and Floberg (1957); Olsson (1965); Floberg (1974)), applied to a

---

[1] http://www.dreamstime.com/royalty-free-stock-image-retro-styled-image-old-classic-car-engine-partly-cutaway-image31587076

[2] http://www.allpar.com/mopar/a-engines.html

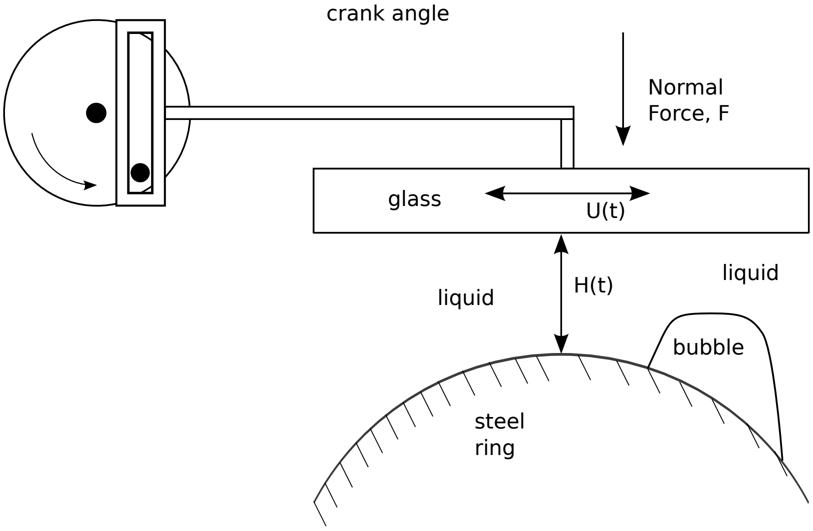

Figure 3.3: City University of London experimental apparatus.

thin liquid film that experiences squeezing pressure from the vertical movement of the top surface, and sliding pressure from the horizontal movement of the bottom surface. We do not appeal to 'the Elrod cavitation algorithm' developed in Elrod and Adams (1974), because we consider the assumption of liquid compressibility is unnecessary in many applications. The theory developed by Jakobsson and Floberg (1957); Olsson (1965); Floberg (1974) has so far mostly been applied to steady journal bearings. This is important to note since in slider bearings, the normal force is usually constant requiring the film thickness to be calculated for; the opposite of a journal bearing.

We study the simplest model first. In Section 3.3, we consider how a mushy region forms under constant velocity, U_0, of the bottom surface which is the only dimensionless parameter in this model. We describe how the steady state film thickness varies with U_0, discuss the stability of the steady state, and estimate the linear decay rate towards the steady state. Using the steady state as an initial condition, we discuss how the mushy region closes as the velocity of the bottom surface decreases to zero. We will show that, if the velocity of the bottom surface is sufficiently large and decreases sufficiently slowly, the numerical solution may be approximated by a quasi-steady solution: a state where the time-scale of decay is significantly larger than the deceleration time-scale of the bottom surface. In section 3.5 we consider the case where the bottom surface undergoes an oscillatory motion. However, we refrain from drawing a comparison to the City Experiments until Section 4.9, when we have a greater understanding of the model. We draw conclusions in section 3.6.

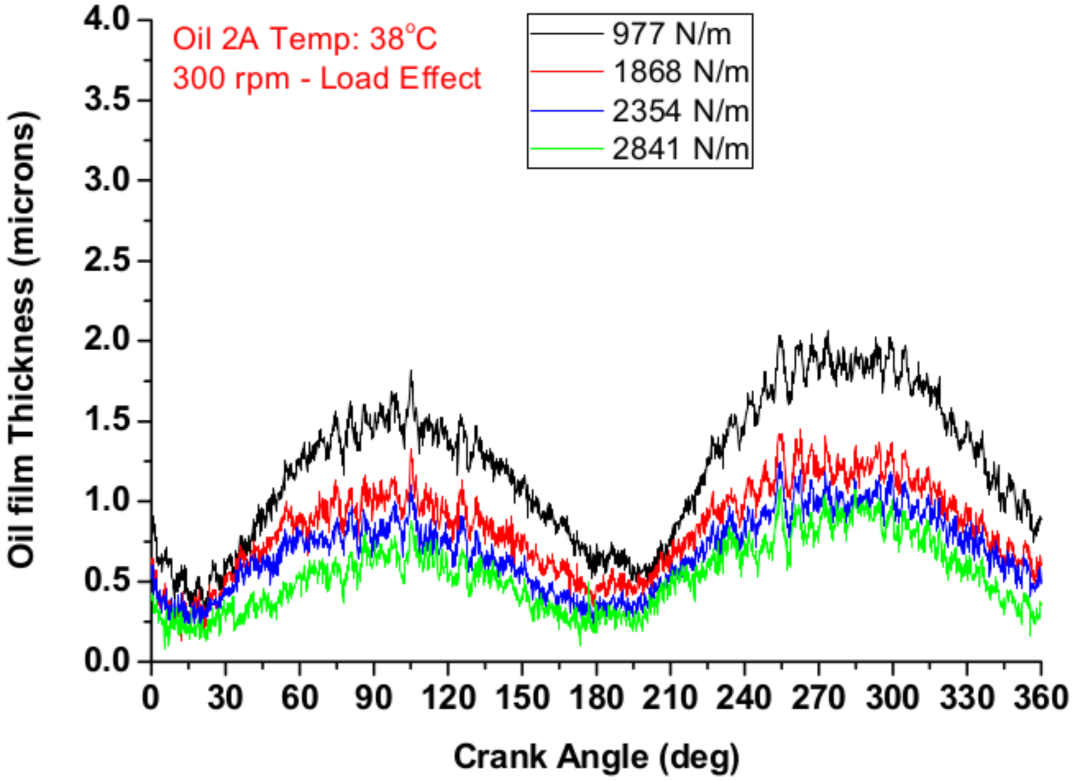

Figure 3.4: Film thickness, $H(t)$, varying with crank angle for 4 different applied normal forces (977 N/m, 1868 N/m, 2354 N/m, 2841 N/m). The frequency of oscillation in this test is 300 rpm. The film thickness was measured using the capacitance method. (Reproduced with permission from Prof. J. Nouri, 15 Jan. 2015).

3.2 City University of London Experiment

In this section, we focus on the City Experiments. No work has been published on this experiment, thus all information has been received through personal communication with Prof. J Nouri. In Figure 3.3 we show a schematic of the apparatus used in the experiment; a circular disk rotates with constant angular speed, which causes the long glass surface to slide horizontally across a liquid film. Beneath the liquid film is a curved steel surface with similar geometry to a piston ring, and the normal force applied to the liquid is the weight of the glass surface pushing down on the liquid film. The aim of this experiment is to determine how lubricants behave when the piston is close to TDC and BDC, since the majority of wear and friction occurs at these locations in the cycle.

In the experiment, the mean temperature of the liquid, the velocity of the glass plate, the normal force applied to the liquid film, and the viscosity of the liquid are all varied. In total, six lubricants were tested in the experiment. We do not know how the test lubricants differed from each other, or their respective viscosities, but all lubricants were standard

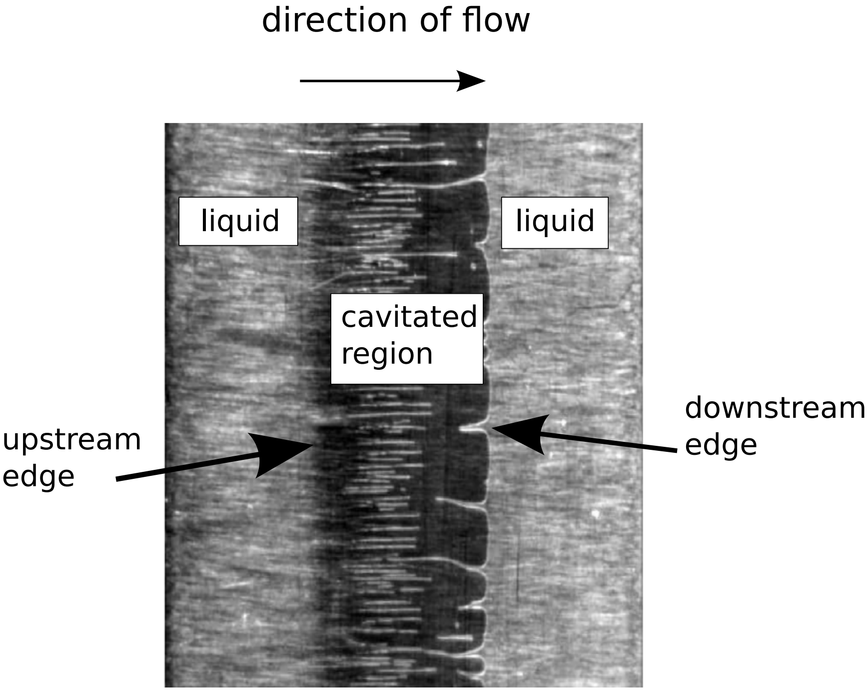

Figure 3.5: The liquid film in the experiment at a crank angle of 40^o. The light intensity is proportional to the volume fraction of liquid in the film, i.e., the lightest areas contain only liquid and the darker areas contain a combination of liquid, gas, and vapour. The moving surface travels to the right, drawing liquid in through the upstream edge of the cavitated region, emitting it through the downstream edge. (Reproduced with permission from Prof. J. Nouri, 15, Jan., 2015).

Grade 5W-40 (an industrial standard for engine lubricants). The shear force, the pressure profile, and the minimum film thickness were measured as outputs of the experiment, and averaged over 20 cycles to eliminate experimental variability.

In Figure 3.4, we show a sample of the experimental results; the minimum film thickness (shown as $H(t)$ in Figure 3.3) was calculated by measuring the voltage drop between two metal sheets on either side of the film, and is shown against the crank angle. A crank angle of 0^o (and 360^o) corresponds to the piston at TDC, and a crank angle of 180^o to BDC. This test was run at constant angular speed $\omega = 300$ rpm, and four variations of the normal force, 977 N/m, 1868 N/m, 2354 N/m, and 2841 N/m. The mean minimum film thickness appears to decrease with increasing normal force.

The main point of interest in Figure 3.4 is that the minimum film thickness does not remain constant, but varies between 0.25-2 μm over the course of the cycle. The reversibility of Stokes flow proves that the sliding pressure in the film makes no contribution to the normal force, leaving the weight of the glass surface to be supported solely by the squeezing pressure, so we would expect the film thickness to monotonically decrease to zero. Because

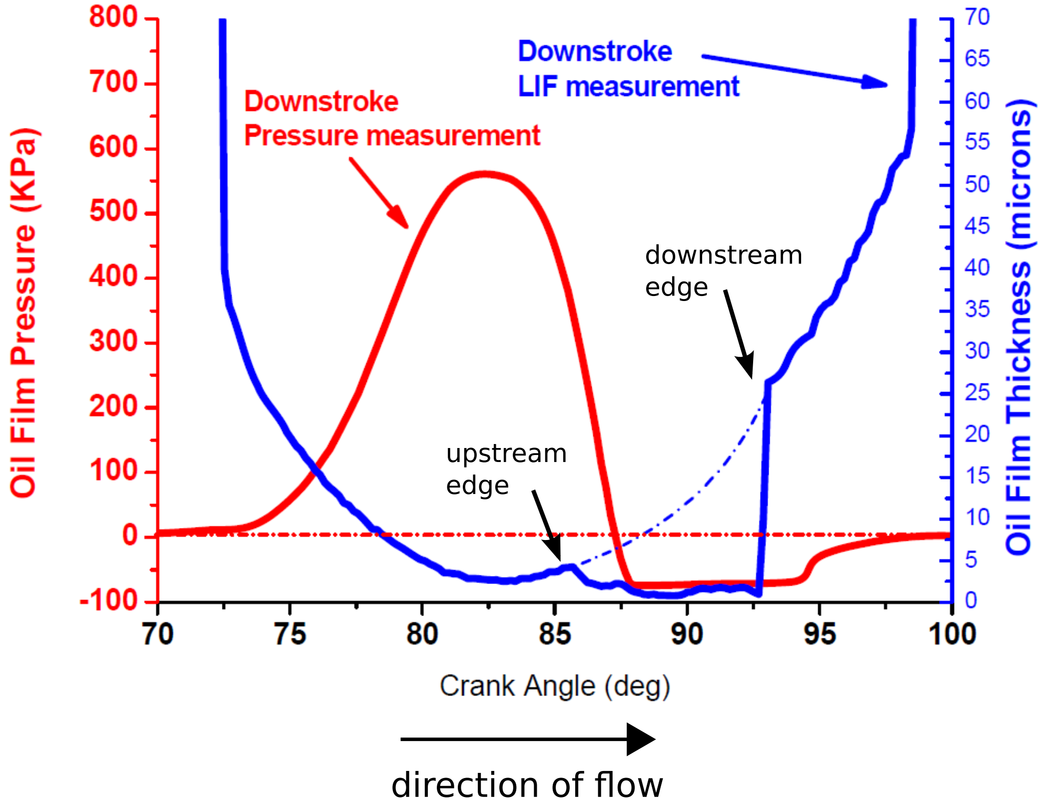

Figure 3.6: The blue line shows the thickness of the liquid in a given column in the film and the red line shows the pressure profile. Both were measured relative to a fixed point on the moving glass surface. The blue dashed line shows the ring profile where the cavitated region exists in the film. The liquid separates from the ring profile at approximately 85^o, referred to as the upstream edge, and reattaches to it at approximately 93^o, referred to as the downstream edge. In this image, the moving surface is travelling to the right. (Reproduced with permission from Prof. J. Nouri, 15, Jan., 2015).

this is not the case, we conclude that a physical event occurs in the liquid which breaks the symmetry of Stokes flow, and causes the film to experience oscillatory behaviour. Images provided by City University of London show cavities forming in the film, leaving us to investigate the process of cavitation in slider bearings.

In Figure 3.5, we show a screen shot of a video recording of a section of the liquid film looking down, through the glass, onto the curved steel surface. The crank angle is at 40^o. The film is divided into three regions, a cavitated region in the middle, and two liquid regions on either side. The glass plate is travelling to the right, drawing liquid in through the upstream edge of the cavitated region and emitting it at the downstream edge. The intensity of light in the image is proportional to the volume fraction of liquid; i.e., the lightest areas show regions that contain only liquid and the darker areas contain a mixture of liquid, gas, and vapour, where long finger-like structures have formed in the film. On the downstream edge of the cavitation region, the volume fraction undergoes a rapid transition where the liquid film reattaches to the curved steel surface.

In Figure 3.6 we show two curves. The blue line shows the thickness of the liquid in a given column in the film, measured using Laser Induced Florescence (LIF), and relative to a fixed point on the moving surface. As in Figure 3.5, the moving surface travels to the right. We see that the liquid film detaches from the curved steel surface at a crank angle of approximately 85◦, referred to as the upstream edge of the cavitated region, and reattaches later at 93◦, referred to as the downstream edge of the cavitated region. In Figure 3.6, we see the thickness undergoes a rapid change across the downstream edge of the cavitated region, showing the liquid film reattaching to the curved steel surface. The red curve in Figure 3.6 is the pressure profile of the liquid in the film, again measured relative to a fixed point on the moving surface. The pressure was measured using a pressure transducer, and was found to be constant inside the bubble for slightly later values of the crank angle than suggested by the LIF measurements. The delay shown in Figure 3.6 between the pressure and liquid thickness measurements, located near crank angles of 85◦ and 93◦ degrees, is because the pressure transducer is at a different location in the film from the LIF.

In the next section, we present the mathematical model describing cavitation in a slider bearing where the bottom surface moves with constant velocity.

3.3 Model for the opening of the Cavitated Region

3.3.1 Problem Setup

In this section, we consider how a cavitated region forms and reaches steady state in the situation where the velocity of the bottom surface is constant. Our key modelling assumption is that we can represent the cavitated region as a mushy mixture of liquid and gas. We later apply these concepts to the model with an oscillating bottom surface.

The model is described using Cartesian coordinates with the origin located on the bottom surface, $\breve{y} = 0$. We suppose that and the top surface is parabolic and symmetric in $\breve{x}$ about the origin,

$$\breve{y} = \breve{h}(\breve{x}, \breve{t}) = \breve{x}^2/(2R_c) + \breve{H}(\breve{t}) \tag{3.1}$$

where $\breve{H}(\breve{t})$ is the minimum vertical distance that separates the two solid surfaces and R_c is the radius of curvature of the top surface. We assume initially that the bottom surface

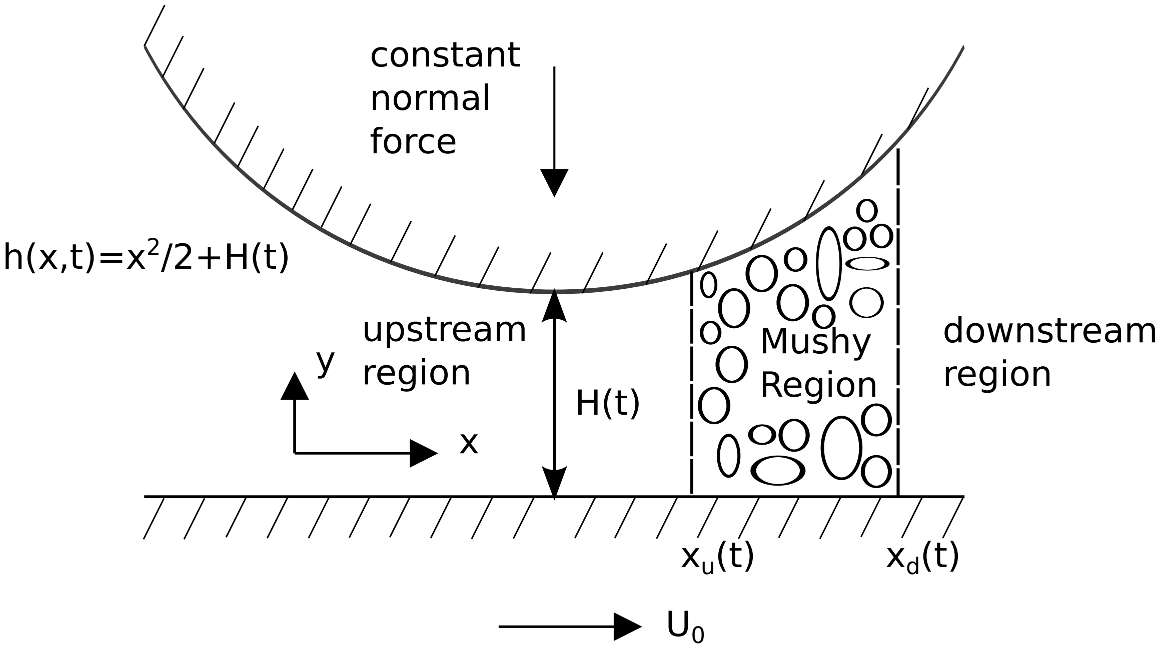

Figure 3.7: Schematic for the mushy region model. The bottom surface moves to the right with speed U_0. The upstream region of the liquid is to the left of the mushy region and the downstream region is to the right.

moves to the right at constant velocity U. In what follows, μ and ρ refer to the dynamic viscosity and density of the liquid, and a constant normal force per unit length F is applied to the top surface.

The liquid domain divided into three regions, separated by two interfacial boundaries, $\breve{x}_u\left(\breve{t}\right)$ and $\breve{x}_d\left(\breve{t}\right)$, as shown in Figure 3.7. We assume that these boundaries have negligible surface tension and curvature. The three regions of liquid in the film are: upstream of the mushy region, ($\breve{x} < \breve{x}_u(\breve{t})$, denoted with subscript u), the mushy region ($\breve{x}_u(\breve{t}) < \breve{x} < \breve{x}_d(\breve{t})$, denoted with subscript 1), and the region downstream of the mushy region, ($\breve{x}_d(\breve{t}) < \breve{x}$, denoted with subscript d). We now calculate the aspect ratio and reduced Reynolds number of the film to ensure lubrication theory is valid. Taking the time scale of the experiments to be $\breve{T} = 1/\omega = O(0.1 \text{ s})$, the viscosity and density of the liquid are of the order $\mu = O(0.01$ Pa s) and $\rho = O(10^3 \text{ kg/m}^3)$ respectively, the radius of curvature to be $R_c = O(0.1 \text{ m})$, and from Figure 3.6, we read the vertical length scale is of the order $\breve{H} = O(10^{-6} \text{ m})$, we calculate the film to be sufficiently thin, i.e. $\sqrt{\breve{H}/R_c} = O(10^{-3})$, and that the reduced Reynolds number is sufficiently small $\rho/\mu\left(\breve{H}^2/\breve{T}\right) = O(10^{-6})$ so that lubrication theory is valid. Thus, the flow is described by the dimensional thin film equation

$$\frac{\partial(\theta\breve{h})}{\partial\breve{t}} + \frac{1}{2}\frac{\partial}{\partial\breve{x}}\left(\left[U - \frac{\breve{h}^2}{6\mu}\frac{\partial\breve{p}}{\partial\breve{x}}\right]\theta\breve{h}\right) = 0, \tag{3.2}$$

where $\breve{p}$ is the pressure in the film and θ is the volume fraction of liquid in the film. Outside of the mushy region, $\breve{x} < \breve{x}_u$ and $\breve{x}_d < \breve{x}$, the film is entirely composed of liquid, so $\theta = 1$. Inside the mushy region, $\breve{x}_u < \breve{x} < \breve{x}_d$, the film is composed of liquid and gas so the volume fraction takes values between $0 < \theta \leq 1$, and we assume the pressure is constant and equal to the vapour pressure of the liquid

$$\breve{p} = p_{vap} \text{ in } \breve{x}_u \leq \breve{x} \leq \breve{x}_d. \tag{3.3}$$

We model the liquid film as extending to infinity in both directions, and in this limit, the dimensional total pressure approaches atmospheric pressure

$$\breve{p} \to p_{atm} \text{ as } \breve{x} \to \pm\infty. \tag{3.4}$$

Continuity of flux across each mushy region boundary gives

$$\left(\frac{U\breve{h}}{2} - \frac{\breve{h}^3}{12\mu}\frac{d\breve{p}}{d\breve{x}} - \breve{h}\frac{d\breve{x}_u}{d\breve{t}}\right)_{\breve{x}_u^-} = \left(\theta\left[\frac{U\breve{h}}{2} - \breve{h}\frac{d\breve{x}_u}{d\breve{t}}\right]\right)_{\breve{x}_u^+}, \tag{3.5}$$

$$\left(\frac{U\breve{h}}{2} - \frac{\breve{h}^3}{12\mu}\frac{d\breve{p}}{d\breve{x}} - \breve{h}\frac{d\breve{x}_d}{d\breve{t}}\right)_{\breve{x}_d^+} = \left(\theta\left[\frac{U\breve{h}}{2} - \breve{h}\frac{d\breve{x}_d}{d\breve{t}}\right]\right)_{\breve{x}_d^-}. \tag{3.6}$$

Assuming the inertia of the moving surface is negligible, (i.e. $MH''(t) \ll F$), where M is the mass per unit length of the glass plate, a force balance relates the normal force, F (in units of N/m), with the integral of the pressure in the liquid,

$$F = \int_{-\infty}^{\infty} \breve{p}\; d\breve{x}. \tag{3.7}$$

We scale the problem using

$$\breve{x} = \sqrt{R_c\check{H}}x, \quad \breve{H} = \check{H}H, \quad \breve{p} = p_{atm} + \frac{F}{\sqrt{R_c\check{H}}}p, \quad \breve{t} = \check{T}t, \quad \breve{\mathbf{u}} = \hat{U}\hat{\mathbf{u}}. \tag{3.8}$$

In this section, we choose to scale the problem so the dimensionless normal force and the cavitation pressure are both of unit magnitude, which requires $\check{H}$, $\check{T}$, and $\hat{U}$ to have the form

$$\check{H} = \frac{F^2}{\left(p_{atm} - p_{vap}\right)^2 R_c}, \quad \check{T} = \frac{\mu R_c^2 \left(p_{atm} - p_{vap}\right)}{F^2}, \quad \hat{U} = \frac{\sqrt{R_c \check{H}}}{\check{T}} = \frac{F^3}{\mu R_c^2 \left(p_{atm} - p_{vap}\right)^2}. \tag{3.9}$$

The problem contains a single dimensionless free parameter, U_0 the normalized velocity of the bottom surface,

$$U_0 = \frac{U \mu R_c^2 \left(p_{atm} - p_{vap}\right)^2}{F^3}. \tag{3.10}$$

The scaling (3.8)-(3.9) reduces equations (3.2)-(3.7) to

$$\frac{\partial(\theta h)}{\partial t} + \frac{\partial}{\partial x}\left(\left[\frac{U_0}{2} - \frac{h^2}{12}\frac{\partial p}{\partial x}\right]\theta h\right) = 0, \tag{3.11}$$

where $h(x,t) = x^2/2 + H(t)$, and p and θ take the form:

$$\begin{cases} x < x_u, & p = p_u \geq -1, & \theta = 1, \\ x_u \leq x \leq x_d, & p \left(= p_1\right) = -1, & 0 < \theta \leq 1, \\ x_d < x, & p = p_d \geq -1, & \theta = 1. \end{cases} \tag{3.12}$$

The flux boundary conditions (3.5)-(3.6) are rewritten as

$$\left(\frac{U_0 h}{2} - \frac{h^3}{12}\frac{\partial p_u}{\partial x} - h\frac{dx_u}{dt}\right)_{x_u^-} = \left(\theta\left[\frac{U_0 h}{2} - h\frac{dx_u}{dt}\right]\right)_{x_u^+}, \tag{3.13}$$

$$\left(\frac{U_0 h}{2} - \frac{h^3}{12}\frac{\partial p_d}{\partial x} - h\frac{dx_d}{dt}\right)_{x_d^+} = \left(\theta\left[\frac{U_0 h}{2} - h\frac{dx_d}{dt}\right]\right)_{x_d^-}. \tag{3.14}$$

The pressure conditions in the far field and on the mushy region boundaries have the forms

$$p_{u,d} \to 0 \text{ as } x \to \pm\infty, \quad p = -1 \text{ at } x = x_{u,d}, \tag{3.15}$$

while the force balance reads

$$1 = \int_{-\infty}^{\infty} p \, dx = \int_{-\infty}^{x_u} p_u \, dx + \int_{x_d}^{\infty} p_d \, dx + \left(x_u - x_d\right). \tag{3.16}$$

Equations (3.11)-(3.16) are the governing equations for the opening of the mushy region with a constant velocity of the bottom surface. In the next section we show asymptotic and numerical solutions to the model problem.

3.3.2 Solution of the Model Problem

Integrating (3.11) with respect x and applying the upstream condition, (3.15), we derive Reynolds equation

$$\frac{\partial p_{u,d}}{\partial x} = 6\frac{U_0 h - q_{u,d} + 2x_{u,d}\frac{dH}{dt}}{h^3}, \tag{3.17}$$

where $q_{u,d}$ are functions of integration that have the form

$$q_u(t) = U_0\theta\left(x_u(t),t\right)h\left(x_u,t\right) + 2x_u(t)\frac{dH}{dt} + 2\left(1-\theta\left(x_u(t),t\right)\right)\frac{dx_u}{dt}, \tag{3.18}$$

$$q_d(t) = U_0\theta\left(x_d(t),t\right)h\left(x_d,t\right) + 2x_d(t)\frac{dH}{dt} + 2\left(1-\theta\left(x_d(t),t\right)\right)\frac{dx_d}{dt}. \tag{3.19}$$

The pressure boundary conditions on the up and downstream boundaries of the mushy region, (3.15), have the form

$$\begin{aligned} p_u\left(x_u,t\right) = &-\frac{6x_u(q_u - 2x_u\frac{dH}{dt})}{H\left(2H+x_u^2\right)^2} + \frac{3x_u\left(4HU_0 - 3q_u\right)}{2H^2\left(2H+x_u^2\right)} \\ &+ 3\left(\pi + 2\tan^{-1}\left(\frac{x_u}{\sqrt{2H}}\right)\right)\frac{\left(4HU_0-3q_u\right)}{4\sqrt{2H^5}} = -1, \end{aligned} \tag{3.20}$$

$$\begin{aligned} p_d\left(x_d,t\right) = &-\frac{6x_d(q_d - 2x_d\frac{dH}{dt})}{8H\left(2H+x_d^2\right)^2} + \frac{3x_d\left(4HU_0 - 3q_d\right)}{2H^2\left(2H+x_d^2\right)} \\ &+ 3\left(\pi - 2\tan^{-1}\left(\frac{x_d}{\sqrt{2H}}\right)\right)\frac{\left(3q_d-4HU_0\right)}{4\sqrt{2H^5}} = -1, \end{aligned} \tag{3.21}$$

and the force balance (3.16),

$$\begin{aligned} &12\left(\frac{q_d - 2x_d\frac{dH}{dt}}{\left(2H+x_d^2\right)^2} - \frac{q_u - 2x_u\frac{dH}{dt}}{\left(2H+x_u^2\right)^2}\right) - 4\left(\frac{4U_0 - x_d}{\left(x_d^2+2H\right)}\right) + 6\left(\frac{2U_0-x_u}{2H+x_u^2}\right) \\ &-\frac{3}{\sqrt{2H^3}}\frac{dH}{dt}\left(2\pi + 2\tan^{-1}\left(\frac{x_u}{\sqrt{2H}}\right) - 2\tan^{-1}\left(\frac{x_d}{\sqrt{2H}}\right)\right) = 1. \end{aligned} \tag{3.22}$$

Equations (3.20), (3.21), and (3.22) provide three equations which we use to solve for three unknown variables: $x_u(t)$, $x_d(t)$, and $H(t)$. However, to close the problem, we need to evaluate the fluxes $q_u(t)$ and $q_d(t)$, and thus need to know the values of the liquid fraction $\theta(x,t)$ at the up- and downstream boundaries $x = x_u(t)$ and $x = x_d(t)$.

Within the mushy region, the pressure gradient is zero, and therefore equation (3.11) reduces to

$$\frac{\partial(\theta h)}{\partial t} + \frac{U_0}{2}\frac{\partial\,(\theta h)}{\partial x} = 0. \tag{3.23}$$

The characteristics of the hyperbolic partial differential equation (3.23) are simply straight lines

$$x - \frac{U_0 t}{2} = \text{ constant}, \tag{3.24}$$

and the general solution for θ is given by

$$\theta\,(x,t)\,h\,(x,t) = f\left(x - \frac{U_0 t}{2}\right), \tag{3.25}$$

where f is an arbitrary integration function. To determine f, we must impose boundary conditions on θ wherever the characteristics of (3.23) propagate into the mushy region through either boundary $x = x_u(t)$ or $x = x_d(t)$.

Appropriate boundary conditions for θ may be inferred by evaluating the pressure gradient at the mushy region boundaries, found from (3.13) and (3.14) to be given by

$$\frac{\partial p_{u,d}}{\partial x} = \left(\frac{6\,(1-\theta)}{h^2}\left[U_0 - 2\frac{dx_{u,d}}{dt}\right]\right)_{x=x_{u,d}}. \tag{3.26}$$

Following Floberg (1961), we require the pressure to be above the cavitation pressure everywhere in the film, and hence require $\partial p_u/\partial x \leq 0$ at $x = x_u(t)$ and $\partial p_d/\partial x \geq 0$ at $x = x_d(t)$. Since $\theta \in (0,1]$, we deduce the two conditions

$$\theta = 1 \text{ on } x = x_u, \text{ while } \frac{dx_u}{dt} < \frac{U_0}{2}, \tag{3.27}$$

$$\theta = 1 \text{ on } x = x_d, \text{ while } \frac{dx_d}{dt} > \frac{U_0}{2}. \tag{3.28}$$

These conditions correspond to specifying θ at any boundary where the characteristics propagate into the mushy region, as anticipated above. At any such point, with $\theta = 1$, equation (3.26) reduces to

$$\frac{\partial p_{u,d}}{\partial x} = 0 \text{ at } x = x_{u,d}(t), \tag{3.29}$$

which is equivalent to the Swift-Stieber condition, see Swift (1932) and Stieber (1933).

A possible characteristic diagram for the problem is illustrated schematically in Figure 3.8, with the mushy region starting from a point $x = x_c$ at $t = 0$. In this model problem, we expect $dx_u/dt < 0 < U_0/2$ and therefore we impose the upstream boundary condition (3.27) for all time. Therefore the solution (3.25) for θ may be expressed as

$$\theta(x,t)h(x,t) = \frac{x_u\left(t_u(x,t)\right)^2}{2} + H\left(t_u(x,t)\right), \tag{3.30}$$

where $t_u(x,t)$ is the time at which the characteristic passing through the point (x,t) left the boundary $x = x_u(t)$, i.e.

$$x - \frac{U_0 t}{2} = x_u\left(t_u(x,t)\right) - \frac{U_0 t_u(x,t)}{2}. \tag{3.31}$$

The solution (3.30) holds in the domain of the mushy region swept out by characteristics emanating from the upstream boundary $x = x_u(t)$ (i.e. the region $x < x_c + U_0 t/2$ to the left of the dividing characteristic indicated by a dashed line in Figure 3.8).

In the scenario depicted in Figure 3.8, the downstream boundary initially moves sufficiently quickly that $dx_d/dt > U_0/2$ for early times. According to (3.28), we must therefore initially specify $\theta = 1$ at the downstream boundary also, leading to the solution

$$\theta(x,t)h(x,t) = \frac{x_d\left(t_d(x,t)\right)^2}{2} + H\left(t_d(x,t)\right), \tag{3.32}$$

where $t_d(x,t)$ is the time at which the characteristic passing through the point (x,t) left the boundary $x = x_d(t)$, i.e.

$$x - \frac{U_0 t}{2} = x_d\left(t_d(x,t)\right) - \frac{U_0 t_d(x,t)}{2}. \tag{3.33}$$

The solution (3.32) holds in the region $x > x_c + U_0 t/2$ to the right of the dashed line in Figure 3.8.

Now suppose that the downstream boundary decelerates, such that, at some critical time t_*, it is moving at the characteristic speed $U_0/2$. Then, for $t > t_*$ the characteristics are propagating out of the mushy region through the downstream boundary, the inequality in (3.28) no longer holds, and we stop imposing a boundary condition on θ at $x = x_d(t)$. Instead, the value of θ is found from the solution on the characteristic exiting the mushy region through $x = x_d(t)$, i.e. either (3.32) (for $x_d(t) > x_c + U_0 t/2$) or (3.30) (for $x_d(t) <$

$x_c + U_0 t/2)$.

In summary, the structure of the problem, and the solution strategy, depends on how many of the inequalities in (3.27) and (3.28) are satisfied. For the scenario illustrated in Figure 3.8, a switch in behaviour occurs at the critical time $t = t_*$ when the causality of the downstream boundary changes.

(i) For $t < t_*$, we impose $\theta = 1$ at both boundaries. We then see from (3.18) and (3.19) that the fluxes $q_{u,d}(t)$ both depend on $H(t)$ and on the free boundary position $x_{u,d}(t)$, but not on the velocity $dx_{u,d}/dt$. Therefore, the governing equations (3.20)-(3.22) reduce to two algebraic equations for $x_u(t)$ and $x_d(t)$, and one first-order differential equation for H(t).

(ii) For $t > t_*$, we no longer impose $\theta = 1$ at the downstream boundary but instead determine θ using (3.30) or (3.32). Thus, from (3.19), we see that now $q_d(t)$ depends on dx_d/dt, as well as dH/dt. Therefore we now have a system of one algebraic equation and two first-order differential equations for $x_u(t)$, $x_d(t)$ and $H(t)$.

The scenario sketched here assumes that $dx_d/dt > U_0/2$ at $t = 0$, and it may alternatively be that $dx_d/dt < U_0/2$ for all t. If so, then case (i) above never occurs, and we go directly to case (ii). It is evidently difficult to initialise the numerical solution without knowing in advance whether we are in case (i), or case (ii). We therefore perform a small-t asymptotic analysis to calculate appropriate initial conditions for the model.

At $t = 0$, we assume the film is entirely liquid, and the film is just about to cavitate. Integrating (3.11) twice with respect to x subject to the far field conditions, (3.15), and integrating it again to satisfy the force balance, (3.16), we can calculate the location of the minimum pressure, $x = x_c$, the film thickness when the film cavitates $H_c = H(0)$, and its derivative, dH/dt, using

$$\left.\frac{dp}{dx}\right|_{x=x_c} = 0, \quad p\left(x_c, 0\right) = -1, \quad \int_{-\infty}^{\infty} p dx = 1. \tag{3.34}$$

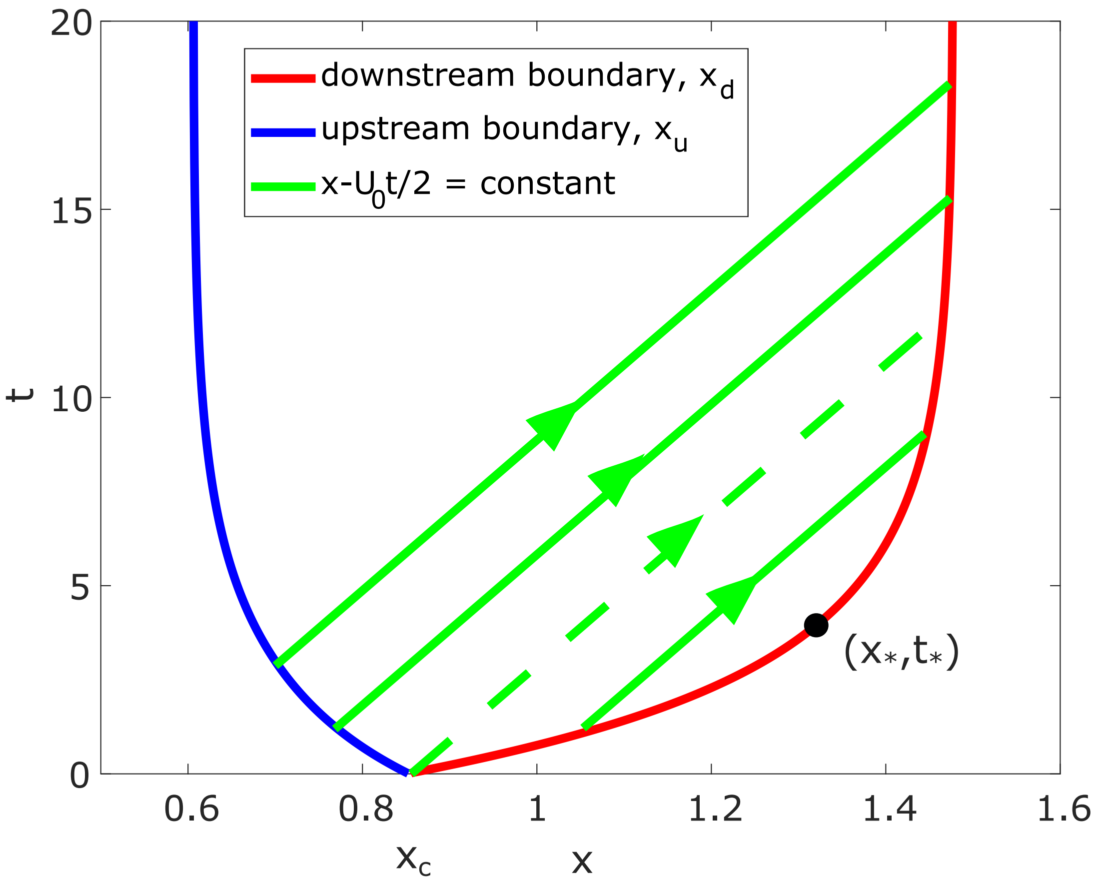

Figure 3.8: Schematic characteristic diagram for the mushy region model. The up- and downstream boundaries are denoted by $x = x_u(t)$ (blue curve) and $x = x_d(t)$ (red curve). The mushy region first forms at $t = 0$, with $x_u(0) = x_d(0) = x_c$. The green lines show the characteristics $x + U_0t/2 =$ constant, with the limiting characteristic $x = x_c + U_0t/2$ marked with a dashed line. The characteristics propagate out of the upstream boundary for all time. The characteristics propagate out of the downstream boundary while $dx_d/dt > U_0/2$ (corresponding to $t < t_*$ in this schematic), and propagate into the downstream boundary while $dx_d/dt < U_0/2$ (corresponding to $t > t_*$). In the scenario depicted here, the downstream boundary is parallel to the characteristics at the critical point $(x, t) = (x_*, t_*)$.

We further find that

$$\left.\frac{dH}{dt}\right|_{t=0} = -\frac{\sqrt{2H_c^3}}{6\pi}, \tag{3.35}$$

$$x_c = \frac{-18\left.\frac{dH}{dt}\right|_{t=0} + \sqrt{12\left(\left.\frac{dH}{dt}\right|_{t=0}\right)^2 + 2U_0^2 H_c}}{9U_0}, \tag{3.36}$$

$$p(x_c, 0) = -8\left(\frac{U_0 x_c + 3\left.\frac{dH}{dt}\right|_{t=0}}{\left(x_c^2 + 2H_c\right)^2}\right) = -1. \tag{3.37}$$

We use $H = H_c$ and $x = x_c$ as initial conditions for this model.

To initialize the numerical solutions, we seek a short time expansion to the problem, using the ansatz:

$$H(t) = H_c + H_1 t + H_2 t^2 + O\left(t^3\right), \tag{3.38a}$$

$$x_u(t) = x_c - x_{u1} t + O\left(t^2\right), \tag{3.38b}$$

$$x_d(t) = x_c + x_{d1} t + O\left(t^2\right), \tag{3.38c}$$

$$\theta(x,t) = 1 - \theta_1(x)\, t + O(t), \tag{3.38d}$$

$$p_{u,d}(x,t) = p_{u0,d0}(x) + p_{u1,d1}(x)\, t + O\left(t^2\right), \tag{3.38e}$$

$$F_N = F_0 + F_1 t + O\left(t^2\right), \tag{3.38f}$$

where F_N is the expression for the force balance calculated from (3.22). Make the substitution,

$$\tau = \frac{x_c}{\sqrt{2H_c}} \qquad \text{and} \qquad \gamma = \frac{H_c}{U_0}, \tag{3.39}$$

the zeroth order terms for the pressure boundary conditions (3.20) and (3.21), evaluated at $x = x_c$, and the force balance, (3.22), are

$$p_{d0}(x_c) = -\frac{6\gamma\tau^2 + 4\gamma + 9\pi\tau^3 + 3\pi\tau}{2\pi\left(\tau^2+1\right)\sqrt{2U_0\gamma^3}} - \frac{3\left(2\gamma\tau + \pi\left(3\tau^2-1\right)\right)\left(2\tan^{-1}(\tau) + \pi\right)}{4\pi\sqrt{2U_0\gamma^3}} = -1, \tag{3.40}$$

$$p_{u0}(x_c) = -\frac{6\gamma\tau^2 + 4\gamma + 9\pi\tau^3 + 3\pi\tau}{2\pi\left(\tau^2+1\right)\sqrt{2U_0\gamma^3}} + \frac{3\left(2\gamma\tau + \pi\left(3\tau^2-1\right)\right)\left(\pi - 2\tan^{-1}(\tau)\right)}{4\pi\sqrt{2U_0\gamma^3}} = -1, \tag{3.41}$$

$$F_0 = \frac{6\pi H_1}{\sqrt{2(\gamma U_0)^3}} = 1. \tag{3.42}$$

From (3.42) we calculate H_1 to be

$$H_1 = \frac{\sqrt{2(\gamma U_0)^3}}{6\pi} \tag{3.43}$$

and notice dH/dt is continuous at the time the mushy region forms.

The first order terms are

$$
\begin{aligned}
p_{u1}\left(x_c\right) &= \left(\pi + 2\tan^{-1}\tau\right)\left(\frac{\gamma U_0^2\left(10\gamma\tau + 3\pi\left(5\tau^2 - 1\right)\right) + 12\pi U_0 x_{u1}(\gamma + 3\pi\tau) - 144\pi^2 H_2\tau}{16\pi^2\gamma^2 U_0^2}\right) \\
&+ \frac{\tau\left(3\tau^2 + 5\right)U_0 x_{u1}(\gamma + 3\pi\tau) - 12\pi H_2\left(3\tau^2 + 2\right)\left(\tau^2 + 1\right)}{2\pi\gamma^2\left(\tau^2 + 1\right)^2 U_0^2} + \chi, \qquad (3.44)\\
p_{d1}\left(x_c\right) &= -\frac{12H_2\left(3\tau^2 + 2\right) + \gamma U_0^2\sqrt{2}x_{d1}\nu}{2\gamma U_0^2\left(\tau^2 + 1\right)^2} + \frac{3\pi^2\tau\left(3\tau^2 + 5\right)\left(\tau^2 + 1\right)\theta_c}{2\pi^2\gamma\left(\tau^2 + 1\right)^2\sqrt{2\gamma U_0}} + \chi \\
&+ \left(\pi - 2\tan^{-1}\tau\right)\left(x_{d1}\nu + \frac{24H_2\tau\sqrt{2}}{\gamma^2 U_0^2} - \frac{36\pi^2\left(\tau^2 + 1\right)\theta_c + \left(10\gamma\tau - 3\pi\left(1 - 5\tau^2\right)\right)\sqrt{2\gamma U_0}}{6\pi^2\sqrt{\gamma^3 U_0}}\right), \\
& \qquad (3.45)\\
F_1 &= \frac{\left(x_{u1} + x_{d1}\right)\left(12\pi\tau + 4\gamma\right)}{2\pi\gamma^2\left(\tau^2 + 1\right)^2 U_0^2\sqrt{2U_0\gamma^3}} \\
&+ \frac{\left(-24\pi^2 H_2\left(\tau^2 + 1\right) - 6\sqrt{2\gamma U_0}\pi\theta_c(U_0 - 2x_{d1}) + \left(\tau^2 + 1\right)\gamma^2 U_0^2\right)}{2\sqrt{2}\pi\left(\tau^2 + 1\right)\sqrt{\left(\gamma U_0\right)^3}}, \qquad (3.46)
\end{aligned}
$$

which all have to be zero because the zeroth order terms satisfy the conditions (3.15) and (3.16). In (3.44)-(3.46),

$$
\begin{aligned}
\theta_c = \theta_1\left(x_c\right) &= \frac{2(\gamma + 3\pi\chi)(x_{u1} + x_{d1})}{3\pi\left(\chi^2 + 1\right)\left(U_0 + 2x_{u1}\right)}\sqrt{\frac{U_0}{2\gamma}}, \qquad (3.47)\\
\nu &= \frac{6\pi\theta_c\sqrt{\gamma}\left(\tau^2 + 1\right) + (3\pi\tau + \gamma)\sqrt{2U_0}}{\pi\gamma^2\sqrt{U_0^3}}, \qquad (3.48)\\
\chi &= \frac{2\gamma\left(15\tau^4 + 25\tau^2 + 8\right) + 3\pi\tau\left(15\tau^4 + 22\tau^2 + 3\right)}{24\pi^2\gamma\left(\tau^2 + 1\right)^2}. \qquad (3.49)
\end{aligned}
$$

Solving (3.44), (3.45), and (3.46) for x_{u1}, x_{d1}, and H_2, numerically with Newton's method, we find that $x_{d1} < U_0/2$ for sufficiently large $U_0 > U_0^* \approx 2.35 \times 10^{-2}$. Therefore, unless U_0 is extremely small, we have $dx_d/dt < U_0/2$ at $t = 0$ for all time, and we are therefore in case (ii) as summarised above. In this instance, we calculate θ on the downstream boundary $x = x_d(t)$ using (3.30), and the problem reduces to an algebraic equation for $x_u(t)$ and two differential equations for $x_d(t)$ and $H(t)$.

Numerical solutions to the algebraic-differential equations, (3.11)-(3.16) were solved using MATLAB's ode15s solver, with a time step of 10^{-4}.[3] Global variables were used to record the data for t, $x_u(t)$, and $H(t)$. In Figure 3.10 we show $x_u(t)$ as the blue curve and $x_d(t)$ as the red curve against time, while in Figure 3.9 we show the film thickness against time for $U_0 = 1$ with the initial conditions $x_c = 0.852$ and $H_0 = 0.81$, which were

---

[3] We refer the reader to Appendix A for details on MATLAB's Differential Algebraic Equation solver, ode15s, used to solve the mushy region model, further details are described in Shampine et al. (1999).

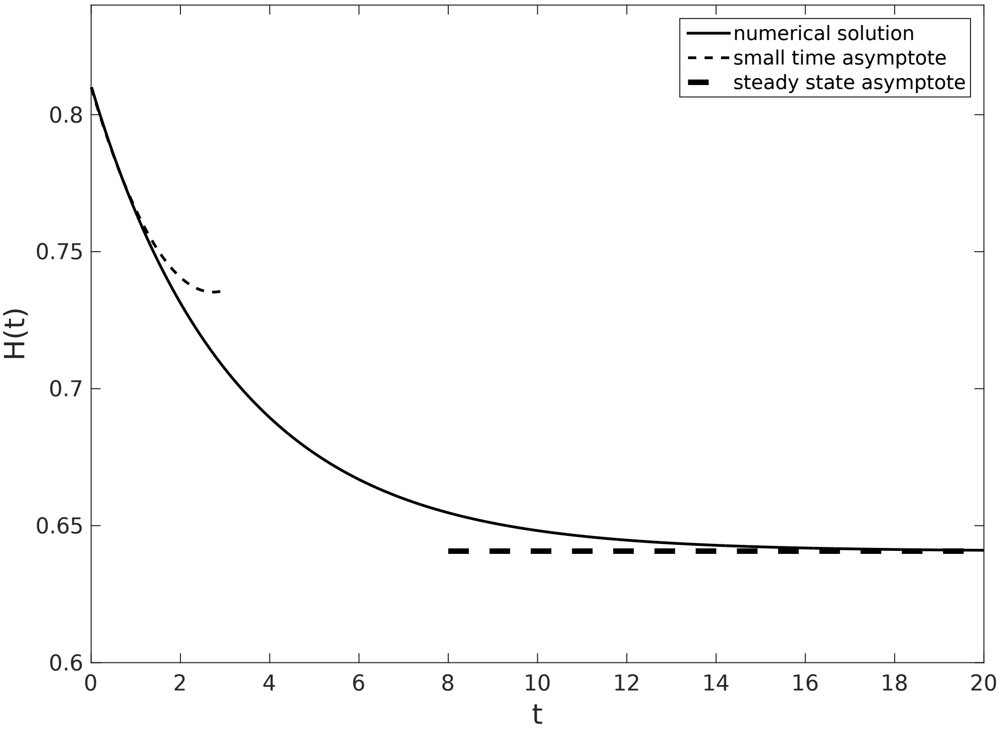

Figure 3.9: The minimum film thickness as a function of time, $H(t)$ when $U_0 = 1$. The steady state asymptote (3.50)-(3.52), is shown as the thick dashed line, and the thin dashed line is the initial behaviour, (3.43)-(3.46).

computed from equations (3.36) and (3.37). We see that, shortly after the film cavitates, the mushy region expands, drawing the displaced liquid through the upstream boundary and expelling it out the downstream boundary. The initial behaviour of the solutions, given by (3.38), is shown as the thin dashed lines in Figures 3.9 and 3.10. After sufficient time, the numerical solutions appear to approach an exponential decay to the steady state solution which is discussed in the next section, and shown as thick dashed curves in Figures 3.9 and 3.10.

3.3.3 Steady State Solution

We now consider the steady state solution of the mushy region model. In steady state, all the time-dependent terms from the system of equations (3.20)-(3.22) are zero, yielding equations

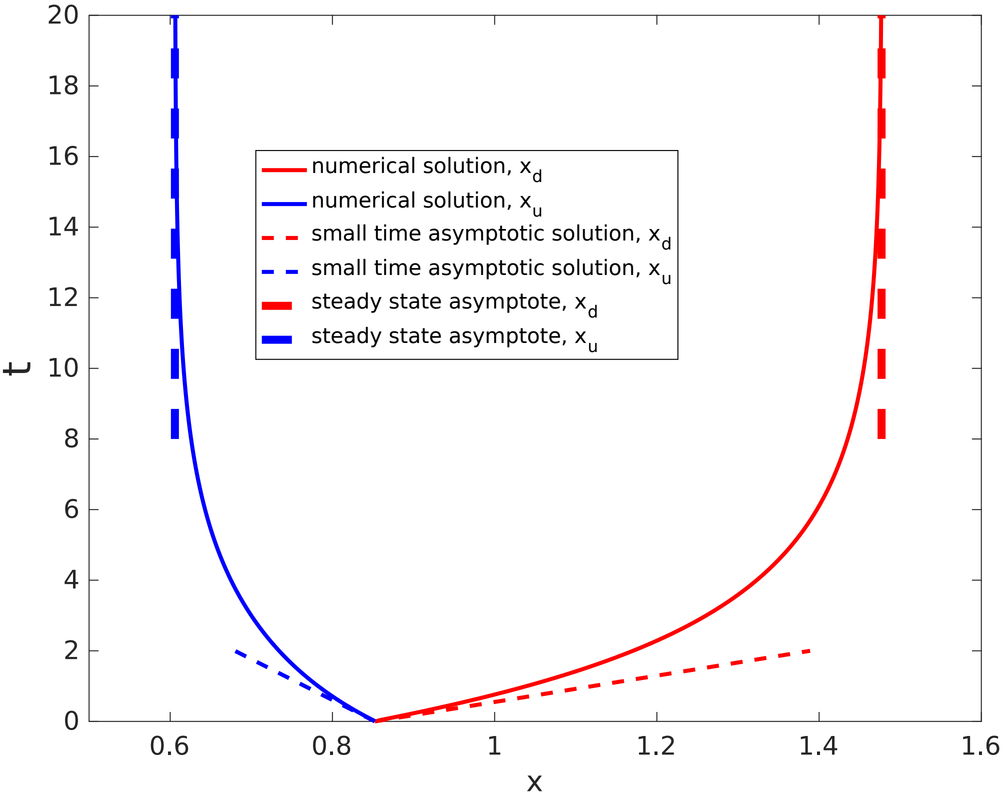

Figure 3.10: The boundaries of the mushy region as functions of time, the red curve shows $x_d(t)$ and the blue curve shows $x_u(t)$ when $U_0 = 1$. The steady state asymptote (3.50)-(3.52), is shown as the thick dashed line, and the thin dashed line is the initial behaviour, (3.43)-(3.46).

$$
\begin{aligned}
p_u\left(x_u\right) &= \frac{3U_0}{16}\left(\frac{4x_u\left(2H-3x_u^2\right)}{H^2\left(2H+x_u^2\right)} - \frac{16x_u}{2H^2+Hx_u^2} + \frac{2\left(2H-3x_u^2\right)\left(2\tan^{-1}\left(\frac{x_u}{\sqrt{2H}}\right)+\pi\right)}{\sqrt{2H^5}}\right) \\
&= -1, \qquad (3.50) \\
p_d\left(x_d\right) &= \frac{3U_0}{16}\left(\frac{4x_d\left(2H-3x_u^2\right)}{H^2\left(2H+x_d^2\right)}\right. \\
&\quad \left. - \frac{16x_d\left(2H+x_u^2\right)}{H\left(2H+x_d^2\right)^2} - \frac{2\left(2H-3x_u^2\right)\left(\pi-2\tan^{-1}\left(\frac{x_d}{\sqrt{2H}}\right)\right)}{\sqrt{2H^5}}\right) = -1, \qquad (3.51)
\end{aligned}
$$

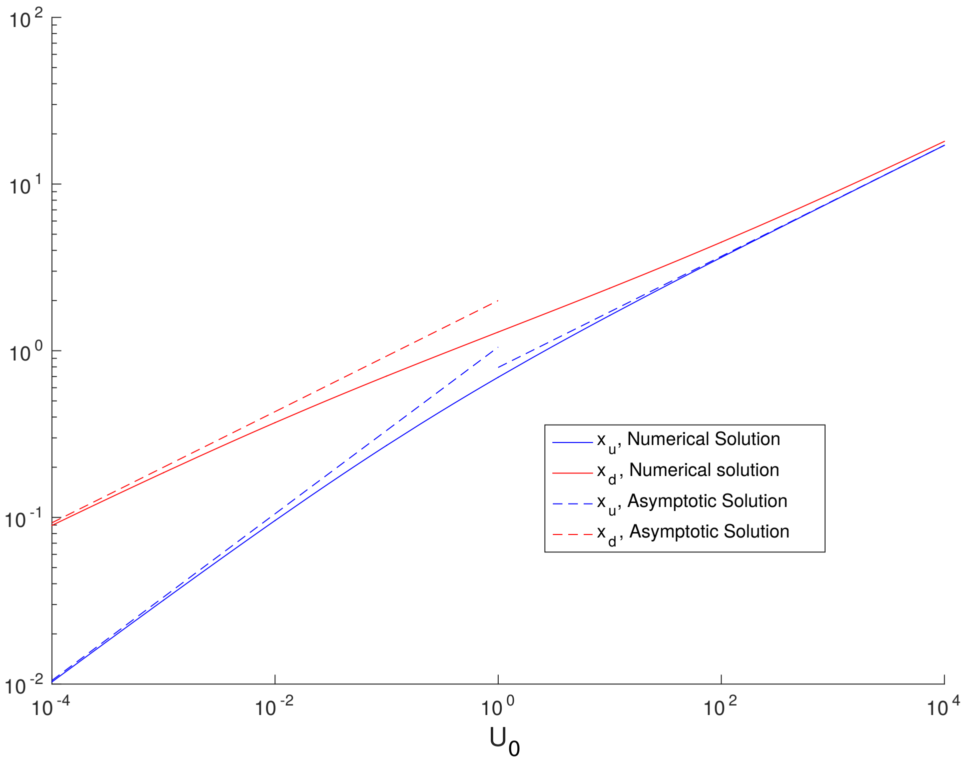

Figure 3.11: Steady state solutions x_d and x_u as functions of U_0. The asymptotic expressions in the limits $U_0 \to 0$ and $U_0 \to \infty$, (3.53a), (3.53b) and (3.60a), (3.60b) are shown as dashed lines.

$$\begin{aligned} F = U_0 \Bigg(& \frac{3\left(x_u^2+2H\right)}{H\left(2H+x_d^2\right)^2} + \frac{3}{4H^2}\left(\frac{5x_u^2-2H}{2H+x_d^2} + \frac{8H}{2H+x_u^2} - 5\right) \\ & + \frac{45x_u^2\left(x_u\left(2\tan^{-1}\left(\frac{x_u}{\sqrt{2H}}\right)+\pi\right)+2x_d\cot^{-1}\left(\frac{x_d}{\sqrt{2H}}\right)\right)}{16\sqrt{2H^7}} \\ & - \frac{9\left(x_u\left(2\tan^{-1}\left(\frac{x_u}{\sqrt{2H}}\right)+\pi\right)+2x_d\cot^{-1}\left(\frac{x_d}{\sqrt{2H}}\right)\right)}{8\sqrt{2H^5}}\Bigg) = 1. \end{aligned} \tag{3.52}$$

Numerical solutions to (3.50), (3.51), and (3.52), obtained using Newton's method are shown in Figures 3.11 and 3.12. The time-dependent solutions described in the previous section are shown to converge to the steady state solutions as $t \to \infty$. The thick dashed lines in Figures 3.9-3.10 are the steady state solutions.

To clarify the behavior observed in Figures 3.11 and 3.12, we now analyse how the steady

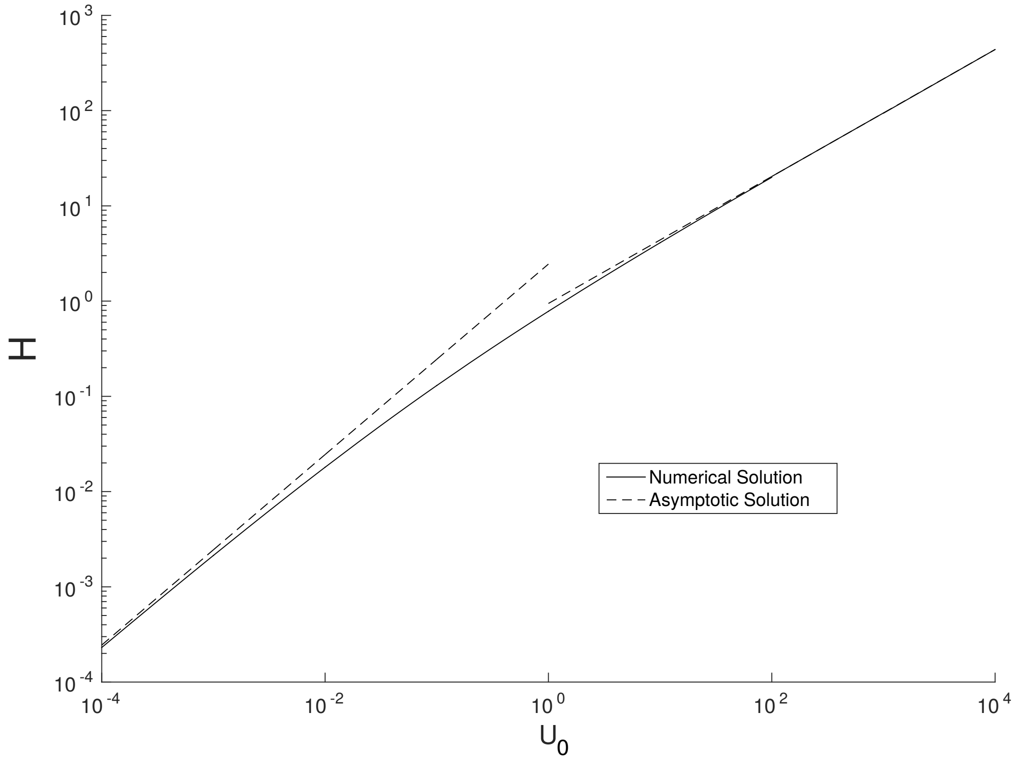

Figure 3.12: Steady state film thickness, H, as a function of U_0. The asymptotic expressions in the limits $U_0 \to 0$ and $U_0 \to \infty$, (3.53c) and (3.60c) are shown as dashed lines.

state solutions for x_u, x_d, and H vary as $U_0 \to 0$ and $U_0 \to \infty$. Using the ansatz

$$x_d = x_{ss,d} U_0^{1/3} + O\left(U_0^{\frac{2}{3}}\right) \text{ as } U_0 \to 0, \tag{3.53a}$$

$$x_u = x_{ss,u} U_0^{1/2} + O\left(U_0\right) \text{ as } U_0 \to 0, \tag{3.53b}$$

$$H = H_{ss,1} U_0 + O\left(U_0^2\right) \text{ as } U_0 \to 0, \tag{3.53c}$$

we calculate the limit for equations (3.50), (3.51), and (3.52) as $U_0 \to 0$ to leading order:

$$\frac{3\left(2H_{ss,1} - 3x_{ss,u}^2\right)}{8\sqrt{2H_{ss,1}^5}} \left[2\tan^{-1}\left(\frac{x_{ss,u}}{\sqrt{2H_{ss,1}}}\right) + \pi\right] - \frac{3\left(2H_{ss,1}x_{ss,u1} + 3x_{ss,u}^3\right)}{4H_{ss,1}^2\left(2H_{ss,1} + x_{ss,u}^2\right)} = 0, \tag{3.54}$$

$$-\frac{8}{x_{ss,d1}^3} = -1, \tag{3.55}$$

$$\frac{3\left(4H_{ss,1} - 3x_{ss,u}^2\right)}{4H_{ss,1}^2} + \frac{3x_{ss,u}\left(2H_{ss,1} - 3x_{ss,u}^2\right)}{8\sqrt{2H_{ss,1}^5}} \left[\pi + 2\tan^{-1}\left(\frac{x_{ss,u}}{\sqrt{2H_{ss,1}}}\right)\right] = 1. \tag{3.56}$$

From (3.55), $x_{ss,d1} = 2$, and by making the substitution,

$$x_{ss,u} = \eta\sqrt{H_{ss,1}}, \tag{3.57}$$

we may write the expression for $H_{ss,1}$ in terms of η as

$$H_{ss,1} = \frac{12 - 9\eta^2}{4} + \frac{3\eta\sqrt{2}\left(2 - 3\eta^2\right)}{16}\left(\pi + 2\tan^{-1}\left(\frac{\eta}{\sqrt{2}}\right)\right), \tag{3.58}$$

where η solves the equation

$$6\eta + \left(2 + 6\eta^2\right)\left(\pi + 2\tan^{-1}(\eta)\right) = 0, \tag{3.59}$$

and we find $\eta \approx 0.475$.

We use the following ansatz for x_u, x_d and H as $U_0 \to \infty$

$$x_u = x_{ss,1}U_0^{1/3} + O(1), \tag{3.60a}$$

$$x_d = x_{ss,1}U_0^{1/3} + O(1), \tag{3.60b}$$

$$H = H_{ss,2}U_0^{2/3} + O\left(U_0^{\frac{1}{3}}\right), \tag{3.60c}$$

reducing equations (3.50), (3.51) and (3.52) to

$$\frac{3\left(2H_{ss,2} - 3x_{ss,1}^2\right)\left(2\tan^{-1}\left(\frac{x_{ss,1}}{\sqrt{2H_{ss,2}}}\right) + \pi\right)}{8\sqrt{2H_{ss,2}^5}} - \frac{3\left(2H_{ss,2}x_{ss,1} + 3x_{ss,1}^3\right)}{4H_{ss,2}^2\left(2H_{ss,2} + x_{ss,2}^2\right)} = -1, \tag{3.61}$$

$$-\frac{3\left(2H_{ss,2} - 3x_{ss,1}^2\right)\left(\pi - 2\tan^{-1}\left(\frac{x_{ss,1}}{\sqrt{2H_{ss,2}}}\right)\right)}{8\sqrt{2H_{ss,2}^5}} + \frac{3x_{ss,1}}{H_3\left(2H_{ss,2} + x_{ss,1}^2\right)} - \frac{9x_{ss,1}}{4H_{ss,2}^2} = -1, \tag{3.62}$$

$$\frac{3\pi x_{ss,1}\left(2H_{ss,2} - 3x_{ss,1}^2\right)}{4\sqrt{2H_{ss,2}^5}} = 0, \tag{3.63}$$

and we find that

$$x_{ss,1} = 2^{1/3}, \quad H_{ss,2} = \frac{3}{2^{5/3}}. \tag{3.64}$$

We see from (3.53) that, as $U_0 \to 0$, the boundaries of the mushy region, x_u and x_d, and the film thickness, H, all approach zero. However, the ratio $x_d/x_u \to \infty$ as $U_0 \to 0$. In the opposite limit, as $U_0 \to \infty$, we find the boundaries, x_u and x_d, and the film thickness H all approach infinity, but x_d and x_u both approach the same limit. We conclude that the width of the mushy region decreases to zero, $x_d - x_u \to 0$, in the limit $U_0 \to \infty$, but x_d and x_u each become increasingly large.

3.3.4 Linear Stability of the Steady State

We now consider the stability of the steady state. We calculate the linear decay rate of perturbations to the steady state λ using the ansatz

$$x_d(t) = x_{d0} + x_{\lambda,d1}\epsilon e^{-\lambda t}, \tag{3.65a}$$

$$x_u(t) = x_{u0} + x_{\lambda,u1}\epsilon e^{-\lambda t}, \tag{3.65b}$$

$$H(t) = H_0 + H_{\lambda,1}\epsilon e^{-\lambda t}, \tag{3.65c}$$

$$\theta(x,t) = \theta_{\lambda,0}\left(x\right) + \theta_{\lambda,1}\left(x\right)\epsilon e^{-\lambda t}, \tag{3.65d}$$

where x_{d0}, x_{u0} and H_0 are the solutions to the steady state problem, (3.50), (3.51), and (3.52) and $0 < \epsilon \ll 1$. Substituting the expressions (3.65a)-(3.65d) into the thin film equation inside the mushy region (3.11), has the form

$$\begin{aligned}
&\frac{U_0}{2}\frac{d}{dx}\left(\theta_{\lambda,0}\left(x\right)\left(\frac{x^2}{2} + H_0\right)\right) + \epsilon\left(-\lambda\left[\theta_{\lambda,0}\left(x\right)H_{\lambda,1} + \left(\frac{x^2}{2} + H_0\right)\theta_{\lambda,1}\left(x\right)\right]\right.\\
&\left.+\frac{U_0}{2}\frac{d}{dx}\left[\theta_{\lambda,0}\left(x\right)H_{\lambda,1} + \left(\frac{x^2}{2} + H_0\right)\theta_{\lambda,1}\left(x\right)\right]\right)e^{-\lambda t} = O\left(\epsilon^2\right).
\end{aligned} \tag{3.66}$$

Using the initial condition $\theta = 1$ on $x = x_u(t)$, we solve the leading order terms of (3.66) for $\theta_{\lambda,0}$ and $\theta_{\lambda,1}$, giving

$$\theta_{\lambda,0}\left(x\right) = \frac{x_{u0}^2 + 2H_0}{x^2 + 2H_0}, \tag{3.67}$$

$$\theta_{\lambda,1}\left(x\right) = \frac{2(H_{\lambda,1} + x_{u0}x_{\lambda,u1})e^{\frac{2\lambda(x-x_{u0})}{U_0}}}{2H_0 + x^2} - \frac{2H_{\lambda,1}\left(2H_0 + x_{u0}^2\right)}{\left(2H_0 + x^2\right)^2}. \tag{3.68}$$

The zeroth order terms in ϵ for $x_u(t)$, $x_d(t)$, and $H(t)$ satisfy the steady state equations

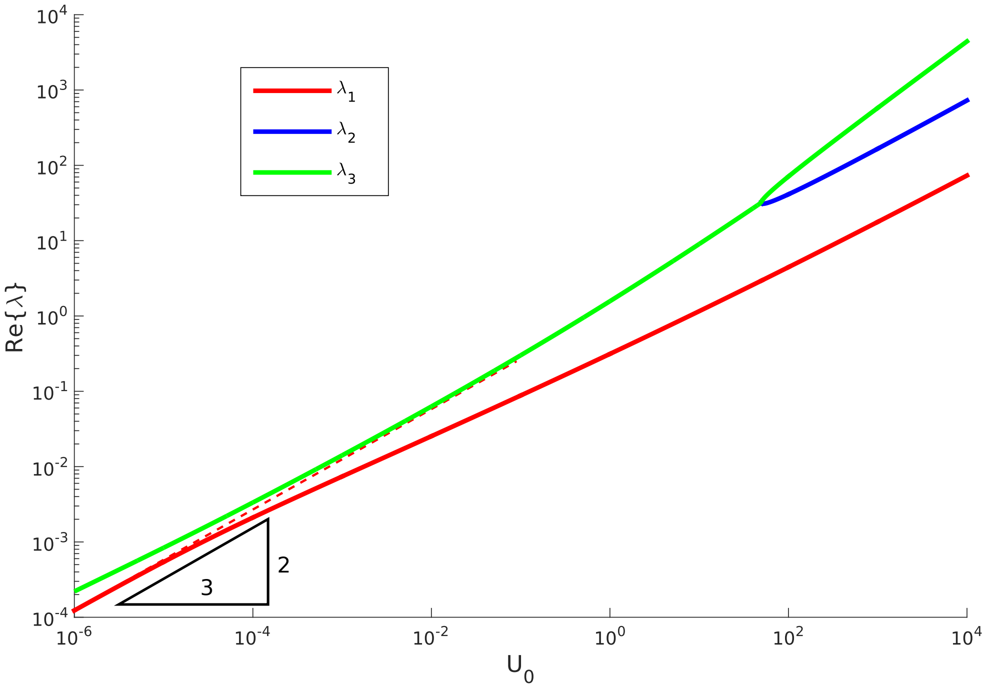

Figure 3.13: The linear decay rate λ as functions of U_0. For $U_0 > 49.5$, there are three real decay rates, and for $U_0 < 49.5$ two of those become complex. We observed that for all values of U_0, the real parts of all the linear decay rates are positive, showing that the solution is stable. The dashed line shows the asymptotic for the largest rate of decay, expressed in (3.71).

(3.50)-(3.52), while the first-order terms may be expressed in matrix form as

$$\begin{bmatrix} f_{11} & 0 & f_{13} \\ f_{21} & f_{22} & f_{23} \\ f_{31} & f_{32} & f_{33} \end{bmatrix} \begin{bmatrix} x_{\lambda,u1} \\ x_{\lambda,d1} \\ H_{\lambda,1} \end{bmatrix} = \begin{bmatrix} 0 \\ 0 \\ 0 \end{bmatrix}, \tag{3.69}$$

where $f_{m,n}$, $[m,n] \in [1,2,3]$ are listed in Appendix B. The determinant of (3.69) gives a transcendental equation for λ of the form

$$f_{11}\left(f_{22}f_{33} - f_{32}f_{23}\right) + f_{13}\left(f_{21}f_{32} - f_{22}f_{31}\right) = 0. \tag{3.70}$$

The numerically determined roots to equation (3.70) are plotted in Figure 3.13 as U_0 is varied. Over the range searched, all the roots λ were found to have positive real parts, suggesting the system is stable for all values of U_0. Indeed, we have observed in all simulations we have done that the steady state was stable. For $U_0 > 49.5$ there are three real roots and for $U_0 < 49.5$ there is only one. Only the real parts of the roots are shown, since the behaviour is dominated by the smallest rate of decay, (shown as the red curve), and the impact of the other roots is not observed when comparing with the numerical solutions.

In the limit $U_0 \to 0$, we observe from Figure 3.13 that λ has the form

$$\lambda \sim \lambda_0 U_0^{\frac{2}{3}} + O\left(U_0^{\frac{1}{3}}\right), \tag{3.71}$$

and, to leading order, (3.70) reduces to

$$\frac{(4\lambda_0 - 5)}{U_0^{\frac{7}{3}}} f(\eta) + O\left(U_0^{-2}\right) = 0, \tag{3.72}$$

where $f(\eta)$ is known, positive, and finite. Thus $\lambda = 5/4$, and we plot (3.72) as the dashed line in Figure (3.13). We note the time-scale of decay of perturbations to the steady state, which henceforth we refer to as the relaxation time-scale, approaches the asymptotic limit

$$T_S = \frac{1}{\lambda} \sim \frac{4}{5U_0^{\frac{2}{3}}} \text{ as } U_0 \to 0, \tag{3.73}$$

implying that the system of equations takes longer to reach an equilibrium in this limit. We note the dimensional relaxation time-scale may be calculated with the relation

$$\check{T}_S = \frac{4\mu R_c^2 \left(p_{atm} - p_{vap}\right)}{5F^2 U_0^{\frac{2}{3}}} \text{ as } U_0 \to 0. \tag{3.74}$$

3.4 Closing of the Mushy Region

3.4.1 Numerical Solutions

In previous sections in this chapter, we studied how the mushy region opens under constant velocity of the bottom surface and reaches a steady state. We now consider the closure of the mushy region caused by a slow decrease in the velocity of the bottom surface, using the steady state solutions from equations (3.50), (3.51), and (3.52), as initial conditions for the model. The governing equations that describe the motion of the liquid in the film are identical to (3.11)-(3.16), but we impose that the velocity of the bottom surface is now a decreasing function of time,

$$U_0(t) = \hat{U}_0 \left(1 - 2\alpha t\right), \tag{3.75}$$

where $\hat{U}_0$ is the maximum velocity, and $\alpha > 0$ is proportional to the rate at which the velocity decreases. As in section 3.3, we apply the boundary condition for θ

$$\theta(x,t) = 1 \text{ on } x = x_u(t) \qquad \text{while} \qquad \frac{dx_u}{dt} < \frac{\hat{U}_0\,(1 - 2\alpha t)}{2}. \tag{3.76}$$

No condition was placed on θ on the downstream boundary since we expected $dx_d/dt < 0 < U_0(t)$ for all time. Consequentially, θ was evaluated at $x = x_d$ using equations (3.30) and (3.31).

Due to the delay in the transport of information across the mushy region, the initial conditions for the model, x_d, x_u, and H were used during the interval $2\,(x_u - x_d)\,/\hat{U}_0 < t < 0$ to calculate $t_u(x,t)$ and $\theta(x,t)$ using (3.30) and (3.31).

Equations (3.11)-(3.16), (3.75) and (3.76) represent a closed system of equations that describe how the mushy region closes as the velocity is decreased to zero. Provided (3.76) is applied, we have to solve two differential equations for H and x_d, namely

$$\frac{dH}{dt} = G_{11}\left(x_u, x_d, H, \hat{U}_0, \alpha\right), \tag{3.77}$$

$$\frac{dx_d}{dt} = G_{12}\left(x_u, x_d, H, \hat{U}_0, \alpha\right), \tag{3.78}$$

(expressions for G_{11} and G_{12} can by found in Appendix C), along with the algebriac equation for x_u, (3.20).

The solution was computed using either $x_u = x_d$, and the mushy region had closed, or condition (3.76) was no longer applied. In the event of the latter, we remove condition (3.76), and solve for θ on the upstream boundary $x = x_u(t)$, using (3.30) and (3.31). In this case, we solve a set of three differential equations for x_u, x_d, and H, namely

$$\frac{dH}{dt} = G_{21}\left(x_u, x_d, H, \hat{U}_0, \alpha\right), \tag{3.79}$$

$$\frac{dx_d}{dt} = G_{22}\left(x_u, x_d, H, \hat{U}_0, \alpha\right), \tag{3.80}$$

$$\frac{dx_u}{dt} = G_{23}\left(x_u, x_d, H, \hat{U}_0, \alpha\right). \tag{3.81}$$

(expressions for G_{21}, G_{22} and G_{23} can by found in Appendix C). When condition (3.76) is not longer satisfied, the characteristics (3.31) are tangent to the upstream boundary, and we refer to this time as $t = t_I$. The numerator and denominator of dx_u/dt are both equal to zero at this time. However, in order to initialize the numerical solution, we use the small

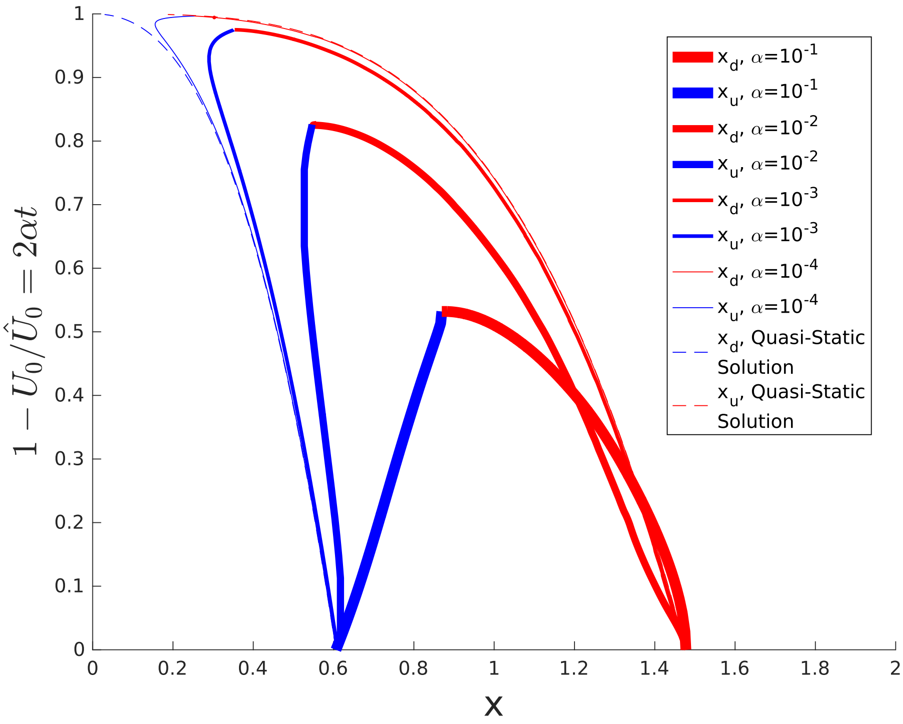

Figure 3.14: Graph showning the positions of x_u and x_d versus $1 - U_0(t)/\hat{U}_0 = 2\alpha t$, for four values of α. The parameters used in the computation are $\hat{U}_0 = 1$ and $\alpha = 10^{-4}$, 10^{-3}, 10^{-2} and 10^{-1}. The quasi-steady solution, shown as a dashed line, closely resembles the closing of the mushy region model in the limit $\alpha \to 0$ when $U_0(t)/\hat{U}_0 \approx 1$, but the similarity no longer holds as $U_0(t) \to 0$.

time analysis around $t = t_I + \epsilon$

$$x_d = x_{d0}^* + \epsilon \hat{t} x_{d1}^* + O(\hat{t}^2), \tag{3.82}$$

$$x_u = x_{u0}^* + \epsilon \hat{t} x_{u1}^* + O(\hat{t}^2), \tag{3.83}$$

$$H = H_i + \epsilon \hat{t} H_{i1} + O(\hat{t}^2), \tag{3.84}$$

where $x_{u0}^* = x_u(t_I)$, $x_{d0}^* = x_d(t_I)$ and $H_i = H(t_I)$. The terms H_{i1}, x_{d1}^* and x_{u1}^* are the first order terms in the expansion of x_u, x_d and H at $t = t_I$ respectively, and are derived in Appendix D. We verified the numerical solution is independent of ϵ provided it is sufficiently small.

Numerical solutions to (3.11)-(3.16), (3.75) and (3.76) were calculated using MATLAB's algebraic-differential equation solver, ode15s. The same MATLAB solver was used after the condition (3.76) was removed. The time step used in the computation is $10^{-4}/\alpha$. In Figure 3.14, we show how $x_u(t)$ and $x_d(t)$ (as the blue and red curves respectively) change as the normalized velocity, $U_0(t)/\hat{U}_0$ is reduced. We use the four values of $\alpha = 10^{-1}$, 10^{-2}, 10^{-3},

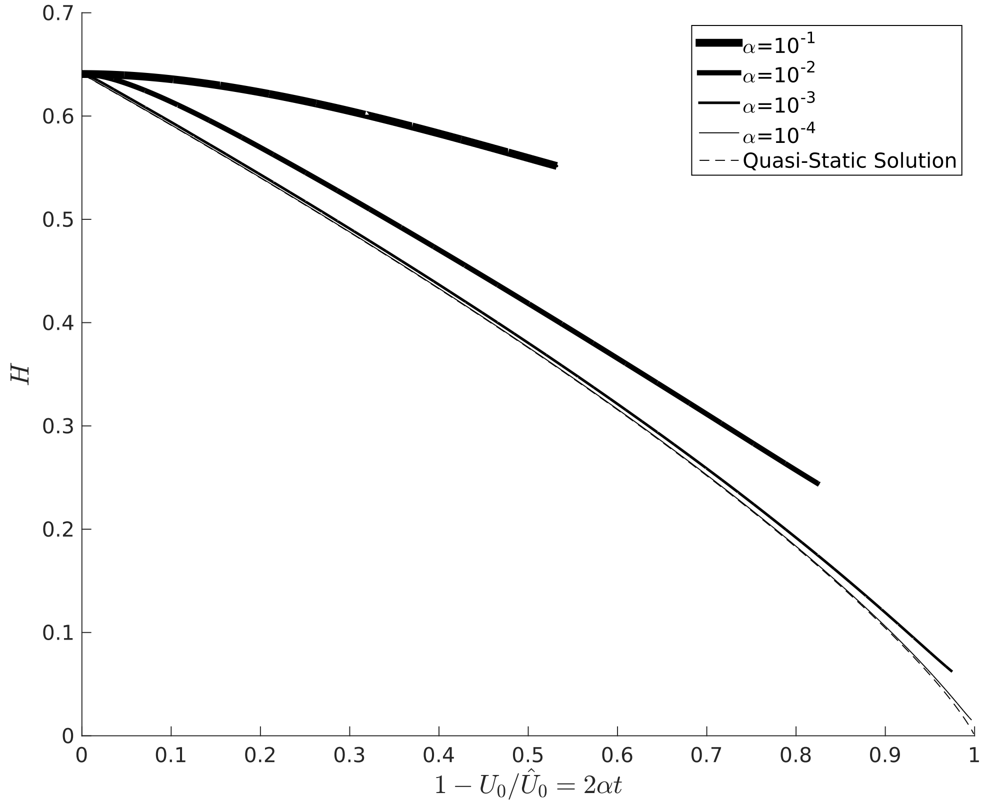

Figure 3.15: Graph showing the minimum film thickness H for the dynamic model and the quasi-steady model, plotted against $1 - U_0(t)/\hat{U}_0$ $(= 2\alpha t)$. The parameters used in the computation are $\hat{U}_0 = 1$ and $\alpha = 10^{-4}$, 10^{-3}, 10^{-2} and 10^{-1}. The quasi-steady solution closely resembles the dynamic model in the limit $\alpha \to 0$ when $U_0(t)/\hat{U}_0 \approx 1$.

and 10^{-4}, the thickest curve being $\alpha = 0.1$ and the thinnest being $\alpha = 10^{-4}$. We note that only the smallest value of α, (10^{-4}), met condition (3.76), at $U_0(t)/\hat{U}_0 = 0.98$, and shortly afterwards the mushy region was observed to close. We observe that, as α decreases, the mushy region remains in existence for longer, and that the solution approaches a quasi-steady state, which we discuss below. This observation is most obvious for the two smallest values of $\alpha = 10^{-3}$, 10^{-4}, when $U_0(t)/\hat{U}_0 \ll 1$. In Figure 3.15, we show the corresponding variation in the film thickness $H(t)$ against the normalized velocity $U_0(t)/\hat{U}_0$. We see that the film thickness decreases as α decreases.

3.4.2 Quasi-Steady Solution

In the case where the relaxation time-scale, T_S, is much faster than the deceleration time-scale, $1/\alpha$, the system is in a quasi-steady state. The equations that describe the quasi-steady equilibrium are identical to the steady state equations, (3.50), (3.51), and (3.52). We solve these equations, given U_0, to find x_d, x_u and H, and then vary $U_0 \in (0, \hat{U}_0)$ to find the quasi-steady solutions.

The quasi-steady solutions for $x_u(t)$ and $x_d(t)$ are shown as thin blue and red dashed curves in Figure 3.14 and $H(t)$ is shown as a thin black dashed curve in Figure 3.15. We see excellent agreement between the quasi-steady solution and the numerical solution as $\alpha \to 0$. This relation breaks down when $U_0(t) \approx 0$; the system is no longer quasi-steady but driven by the dynamics in the problem.

We explain this comparison in further detail using the relaxation time-scale, in relation to the deceleration time-scale. When $\hat{U}_0 = 1$, we calculate $\lambda = 0.313$ from (3.70), and so here the relaxation time-scale is $T_S = 1/\lambda = 3.2$. For $\alpha = 10^{-1}$, the velocity of the bottom surface varies so rapidly that the system is fully time-dependent. The numerical solution begins to depart from the quasi-steady solution when $T_S/(1/\alpha) = T_S\alpha =\approx 3.2 \times 10^{-2}$. We observe the numerical solution starts to separate from the quasi-steady solution when the relaxation time-scale, T_S, is approximately two orders of magnitude shorter than the deceleration time-scale, $1/\alpha$.

3.4.3 Summary

In Sections 3.3-3.4, we studied how a mushy region forms under constant velocity of the bottom surface, reaches a steady state, and then closes as the velocity slowly decreases with time. The linear rates of decay of perturbations to the steady state solution were calculated numerically, and we hypothesise that the solution is unconditionally stable for all values of U_0. We derived an expression for the relaxation time-scale, T_S, using the smallest decay rate, λ. We have shown that when the relaxation time-scale is significantly shorter than the deceleration time-scale of the bottom surface, $T_S\alpha \ll 1$ and when $U_0(t)$ is sufficiently large, the numerical solution closely approximates the quasi-steady solution. In the opposite limit, when $T_S \approx 1/\alpha$ or $U_0(t) \approx 0$, the numerical solution is dominated by the dynamics of the model.

In the following section, we study how the film behaves under the oscillatory motion of the bottom surface. We assume there are no cavities anywhere in the film initially. Once the pressure reduces below the cavitation pressure, cavities form in the film, dividing the liquid into three regions. The mushy region remains in the film until a second mushy region forms on the other side of the ring.

3.5 Mushy Region Model with an Oscillatory Velocity

In this Section, we consider the bottom surface to be oscillating rather than having constant velocity or linearly decreasing velocity as studied in Section 3.4. The oscillating behaviour gives us an inbuilt time scale for the problem, namely the inverse of the frequency of oscillation, $\check{T} = 1/\omega$. Hence, in this section we scale

$$\check{x} = \sqrt{R_c \check{H}} x, \quad \check{H} = \check{H} H, \quad \check{p} = p_{atm} + \frac{F}{\sqrt{R_c \check{H}}} p, \quad \check{t} = \frac{t}{\omega}, \quad \check{\mathbf{u}} = U \hat{\mathbf{u}}, \tag{3.85}$$

where ω and U are the frequency and magnitude of oscillation. We note that the dimensionless magnitude and frequency of the velocity of the bottom surface are both of unit magnitude. We choose to pick the thickness scale so that the dimensionless normal force also has unit magnitude and hence we set

$$\check{H} = \frac{\mu U R_c}{F}. \tag{3.86}$$

There are two free parameters in the model: δ is the ratio between horizontal length scale $\sqrt{R_c \check{H}}$ and the amplitude of oscillation of the bottom surface, U/ω; and Ω is the ratio of the length scales $F/\left(p_{atm} - p_{vap}\right)$, the length of the mushy region required to support the weight of the top surface, to U/ω:

$$\delta = \frac{\omega \sqrt{R_c \check{H}}}{U} = \omega R_c \sqrt{\frac{\mu}{FU}} \quad \text{and} \quad \Omega = \frac{\omega F}{\left(p_{atm} - p_{vap}\right) U}. \tag{3.87}$$

We note that the scaling in Section 3.4 may be recovered by setting

$$U_0 = \frac{\delta^2}{\Omega^2}. \tag{3.88}$$

In Figure 3.16, we show the non-dimensionalised experimental data for the film thickness $H(t)$, against time. All sixteen tests are shown, varying the frequency: $\omega = 300$ rpm, (black data point); 400 rpm, (red data points); 500 rpm, (blue data points); and 600 rpm, (green data points); and with the normal force: $F = 977$ N/m, (dots, $\cdot$); 1868 N/m, (crosses, +); 2354 N/m, (circles, o); and 2841 N/m, (asterisks, *). Of the sixteen tests, twelve are shown to collapse on to roughly the same curve, providing convincing evidence that the scaling captures the dominant physics. However, the tests with the smallest applied normal force,

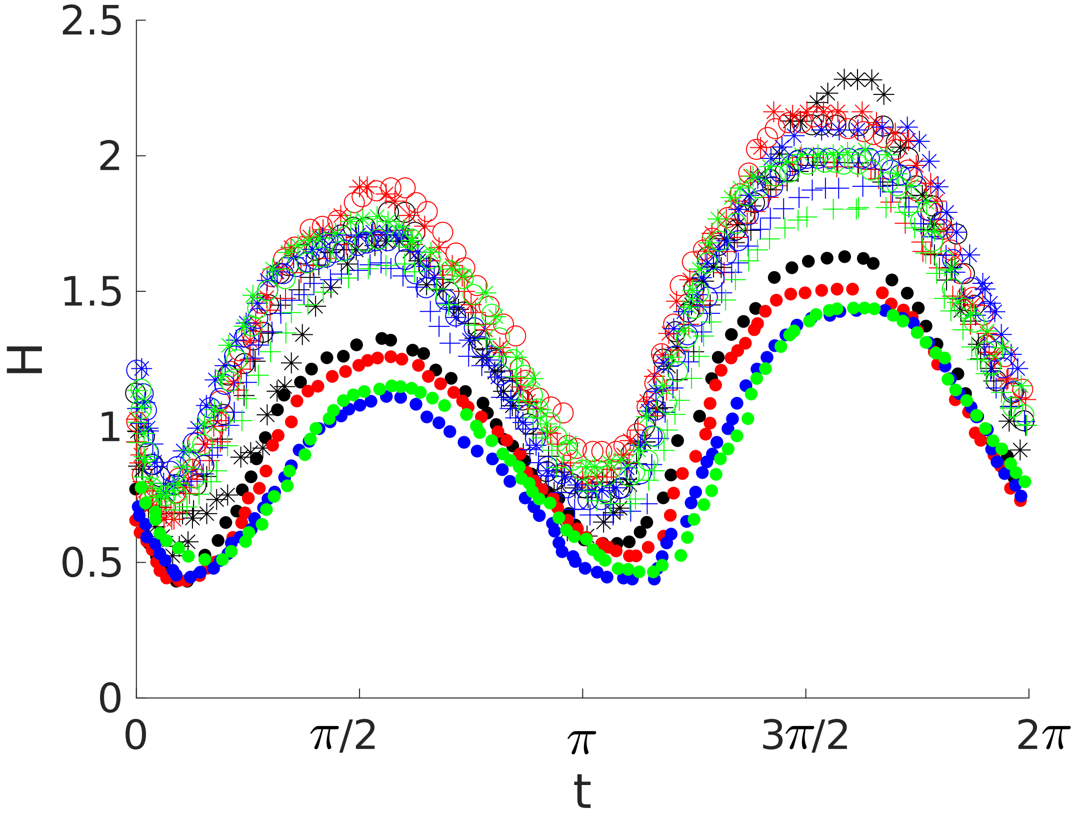

Figure 3.16: Experimental data showing the film thickness, $H(t)$, against time in dimensionless form. All sixteen tests are shown, varying with the frequency: $\omega = 300$ rpm, (black data point); 400 rpm, (red data points); 500 rpm, (blue data points); and 600 rpm, (green data points); and with the normal force: $F = 977$ N/m, (dots, $\cdot$); 1868 N/m, (crosses, $+$); 2354 N/m, (circles, o); and 2841 N/m, (asterisks, *).

$F = 977$ N/m, show the film thickness to be smaller than the other tests at certain points in the period. The other parameter values used to calculate the dimensional scalings are described later in Section 4.9.

The motion of the liquid in the film is described by the thin film equation

$$\delta \frac{\partial(\theta h)}{\partial t} + \frac{1}{2}\frac{\partial}{\partial x}\left(\left[u - \frac{h^2}{6}\frac{\partial p}{\partial x}\right]\theta h\right) = 0, \tag{3.89}$$

where $h(x,t) = x^2/2 + H(t)$, and the normalized velocity of the bottom surface is $u(t) = \sin(t)$. The far field boundary conditions, the force balance, and the initial film thickness are given by

$$p \to 0 \text{ as } x \to \pm\infty, \tag{3.90}$$

$$1 = \int_{-\infty}^{\infty} p \, dx, \tag{3.91}$$

$$H_0 = H(0). \tag{3.92}$$

We assume that at $t = 0$, the film has not cavitated and is entirely composed of liquid, implying the conditions $\theta = 1$ and $p > -\delta/\Omega$. Equations (3.89)-(3.92) describe a continuous liquid film with an oscillating bottom surface. In order to find when and where the film first cavitates, we integrate (3.89) once with respect to x and use the far field condition (3.90), we first derive Reynolds' equation with an oscillating velocity

$$\frac{\partial p}{\partial x} = 6\left(\frac{uh - q_0 + 2\delta x \frac{dH}{dt}}{h^3}\right), \tag{3.93}$$

where q_0 is an unknown integration function of time. Integrating (3.93) again and using the far field condition, (3.90), again yields

$$q_0 = \frac{4uH}{3}, \tag{3.94}$$

$$p = -8\left(\frac{ux + 3\delta \frac{dH}{dt}}{(x^2 + 2H)^2}\right). \tag{3.95}$$

The expression for the pressure, (3.95), may be thought of as the sum of two components, a squeezing pressure which is symmetric in x, and a sliding pressure which is axisymmetric. The squeeze pressure is an even function of x and comes from the motion of the top surface squeezing the liquid out from underneath it, and hence is positive everywhere in the film. The sliding pressure is caused by the horizontal motion of the bottom surface and is an odd function of x. Applying the force balance, (3.91), yields the equation

$$-\frac{6\pi\delta}{\sqrt{2H^3}} \frac{dH}{dt} = 1, \tag{3.96}$$

which with the initial condition (3.92) has the solution

$$H = \frac{H_0}{\left(1 + \frac{\sqrt{2H_0}t}{12\pi\delta}\right)^2}, \tag{3.97}$$

a similar result is shown in Leal (2007) for an axisymmetric liquid film.

We find the location of the minimum pressure by equating (3.93) to zero and solving for x_{min} which gives

$$x_{min} = \frac{-2\delta \frac{dH}{dt} + \sqrt{4\left(\delta \frac{dH}{dt}\right)^2 + 2u\left(h_0 - Hu\right)}}{u}. \tag{3.98}$$

Substituting expression (3.98) into the expression for the pressure (3.95) and setting this equal to the cavitation pressure allows us to calculate the time when the film cavitates, $t = t_c$, which satisfies the non-linear algebraic equation,

$$p\left(x_c(t_c), t_c\right) = -\frac{8u(t_c)^4\left(\frac{dH}{dt} + \sqrt{4\left(\delta\frac{dH}{dt}\right)^2 + \frac{2}{3}H(t_c)u(t_c)^2}\right)}{\left(2u(t_c)^2H(t_c) + \left(2\delta\frac{dH}{dt} - \sqrt{4\left(\delta\frac{dH}{dt}\right)^2 + \frac{2}{3}H(t_c)u(t_c)^2}\right)^2\right)^2} = -\frac{\delta}{\Omega}. \tag{3.99}$$

Cavitation happens when the negative pressure from the sliding motion exceeds the squeeze pressure by an amount equal to the cavitation pressure, $p = -\delta/\Omega$.

As before, once the film has cavitated, the fluid domain is divided into three regions, as shown in Figure 3.7, where in each region the pressure p and volume fraction θ take the form:

$$\begin{cases} x < x_u, & p = p_u \geq -\frac{\delta}{\Omega}, & \theta = 1, \\ x_u \leq x \leq x_d, & p = p_1 = -\frac{\delta}{\Omega}, & 0 < \theta \leq 1, \\ x_d < x, & p = p_d \geq -\frac{\delta}{\Omega}, & \theta = 1. \end{cases} \tag{3.100}$$

The flux boundary conditions on the mushy region boundaries are

$$\left(\frac{uh}{2} - \frac{h^3}{12}\frac{\partial p_u}{\partial x} - \delta h\frac{dx_u}{dt}\right)_{x_u^-} = \left(\theta\left[\frac{uh}{2} - \delta h\frac{dx_u}{dt}\right]\right)_{x_u^+}, \tag{3.101}$$

$$\left(\frac{uh}{2} - \frac{h^3}{12}\frac{\partial p_d}{\partial x} - \delta h\frac{dx_d}{dt}\right)_{x_d^+} = \left(\theta\left[\frac{uh}{2} - \delta h\frac{dx_d}{dt}\right]\right)_{x_d^-}, \tag{3.102}$$

and the pressure must be continuous on the mushy region interface,

$$p = -\frac{\delta}{\Omega} \text{ at } x = x_{u,d}. \tag{3.103}$$

Equations (3.89)-(3.91) and (3.100)-(3.103) are the governing equations for a single mushy region in a liquid film with an oscillating bottom surface.

As in Section 3.3, to prevent the pressure from reducing below the cavitation pressure, we apply the boundary conditions on θ

$$\theta = 1 \text{ on } x = x_u, \text{ while } \frac{dx_u}{dt} < \frac{u}{2\delta}, \tag{3.104}$$

$$\theta = 1 \text{ on } x = x_d, \text{ while } \frac{dx_d}{dt} > \frac{u}{2\delta}. \tag{3.105}$$

Inside the mushy region, the volume fraction θ is solved from (3.89), using method of characteristics to obtain the solution

$$\theta(x,t)h(x,t) = \frac{x_{u,d}\left(t_u(x,t)\right)^2}{2} + H\left(t_u(x,t)\right), \tag{3.106}$$

where $t_u(x,t)$ is the time when the characteristics that pass through the point (x,t) left either boundary and solves the equation

$$x - \frac{\cos(t)}{2\delta} = x_{u,d}(t_u(x,t)) - \frac{\cos(t_u(x,t))}{2\delta}. \tag{3.107}$$

The pressure boundary conditions on the up and downstream sides of the mushy region, (3.103), have the form

$$\begin{aligned} p_u\left(x_u,t\right) = {} & \frac{3(4Hu-3q_u)\left(\pi + 2\tan^{-1}\left(\frac{x_u}{\sqrt{2H}}\right)\right)}{4\sqrt{2H^5}} + \frac{x_u\left(4Hu-3q_u\right)\left(10H+3x_u^2\right)}{2H^2\left(2H+x_u^2\right)^2} \\ & - \frac{8\left(3\delta\frac{dH}{dt} + x_u u\right)}{\left(2H+x_u^2\right)^2} = -\frac{\delta}{\Omega} \end{aligned} \tag{3.108}$$

$$\begin{aligned} p_d\left(x_d,t\right) = {} & \frac{3(3q_d-4Hu)\left(\pi - 2\tan^{-1}\left(\frac{x_d}{\sqrt{2H}}\right)\right)}{4\sqrt{2H^5}} + \frac{x_d\left(4Hu-3q_d\right)\left(10H+3x_d^2\right)}{2H^2\left(2H+x_d^2\right)^2} \\ & - \frac{8\left(3\delta\frac{dH}{dt} + x_d u\right)}{\left(2H+x_d^2\right)^2} = -\frac{\delta}{\Omega} \end{aligned} \tag{3.109}$$

and the force balance gives the relationship

$$\begin{aligned} & 12u\left(\frac{1}{\left(2H+x_d^2\right)} - \frac{1}{\left(2H+x_u^2\right)}\right) - 12\left(\frac{q_d}{\left(2H+x_d^2\right)^2} + \frac{q_u}{\left(2H+x_u^2\right)^2}\right) \\ & + \frac{6\delta}{H}\frac{dH}{dt}\left(\frac{x_u\left(x_u^2-2H\right)}{\left(2H+x_u^2\right)^2} - \frac{x_d\left(x_d^2-2H\right)}{\left(2H+x_d^2\right)^2}\right) \\ & + \frac{6\delta}{\sqrt{2H^3}}\frac{dH}{dt}\left(\tan^{-1}\left(\frac{x_u}{\sqrt{2H}}\right) - \tan^{-1}\left(\frac{x_d}{\sqrt{2H}}\right) + \pi\right) = 1, \end{aligned} \tag{3.110}$$

where q_u and q_d are functions of integration that have the form

$$q_u(t) = \theta\left(x_u(t), t\right) u(t) h\left(x_u(t), t\right) + 2\delta x_u(t)\frac{dH}{dt} + 2\delta\left(1 - \theta\left(x_u(t), t\right)\right) h\left(x_u(t), t\right)\frac{dx_u}{dt}, \tag{3.111}$$

$$q_d(t) = \theta\left(x_u(t), t\right) u(t) h\left(x_u(t), t\right) + 2\delta x_d(t)\frac{dH}{dt} + 2\delta\left(1 - \theta\left(x_d(t), t\right)\right) h\left(x_d(t), t\right)\frac{dx_d}{dt}. \tag{3.112}$$

We note when conditions (3.104) or (3.105) apply, the derivatives for x_u and x_d vanish, reducing the number of derivatives in the system. Conditions (3.104) or (3.105) are not applied when the characteristics, given by (3.107), are tangent to the curvature of the respective boundary it is on. Physically, when $\theta = 1$ on a boundary, the boundary is moving so fast the displaced liquid is being drawn through the boundary and into the mushy region. The opposite happens when $\theta < 1$, for the liquid is exiting the mushy region.

3.5.1 Solutions

Assuming the conditions for θ on both boundaries $x = x_u(t)$ and $x_d(t)$, (3.104) and (3.105) apply, and the solution involves a single differential equation for H,

$$\frac{dH}{dt} = \frac{1}{\delta}\frac{6uH\sqrt{2}\left(\frac{1}{2H+x_u^2} - \frac{1}{2H+x_d^2}\right) + H}{\sqrt{2}\left(\frac{x_u}{2H+x_u^2} - \frac{x_d}{2H+x_d^2}\right) + \left(\tan^{-1}\left(\frac{x_u}{\sqrt{2H}}\right) - \tan^{-1}\left(\frac{x_d}{\sqrt{2H}}\right) + \pi\right)}, \tag{3.113}$$

which is solved using the normal force (3.110), and two algebraic equations for x_u and x_d, the pressure boundary conditions, (3.108) and (3.109). Using the initial conditions

$$H = H_c, \quad x_u = x_d = x_c, \text{ at } t = t_c, \tag{3.114}$$

we solve (3.113) numerically and truncated when condition (3.105) no longer applies at $t = t_1$. When (3.105) is not applied, we have to solve two differential equations for H and x_d, namely

$$\frac{dH}{dt} = F_{11}(x_u, x_d, H, \delta, \Omega), \tag{3.115}$$

$$\frac{dx_d}{dt} = F_{12}(x_u, x_d, H, \delta, \Omega), \tag{3.116}$$

(functions F_{11} and F_{12} can be found in Appendix E), and with the algebraic equation for x_u, (3.103).

The numerator and denominator of dx_d/dt are both equal to zero at $t = t_1$. A detailed asymptotic analysis of the local behaviour near $t = t_1$ is provided in Section 4.7. To circumvent this problem we evaluate $\theta(x, t)$ at $x_d(t_1 + \epsilon)$ using expressions (4.199) and (4.200), which are equivalent to

$$\theta\left(x_d\left(t_1+\epsilon\right), t_1+\epsilon\right) \rightarrow 1-\frac{\epsilon}{3}, \tag{3.117}$$

$$x_d\left(t_1+\epsilon\right) \rightarrow \left[\frac{2^9\Omega^2}{3^6 5^2 \delta}\right]^{\frac{1}{5}} \times \left[\frac{5}{2}\left(1+\left[\frac{2^{14}\Omega^2}{3^6 5^7}\right]^{\frac{1}{5}}\right)+\epsilon\left[\frac{2^{14}\Omega^2}{3^6 5^2}\right]^{\frac{1}{5}}\right], \tag{3.118}$$

and we verify that the numerical solution is independent of ϵ provided it is sufficiently small. In Section 4.7, we show x_u and H vary on an asymptotically slower timescale, and so we approximate them as being constant over this interval.

Again, the solution was computed until (3.104) no longer applies, at $t = t_2$. When neither (3.104) or (3.105) hold, we have to solve a set of three differential equations for H, x_u and x_d, namely

$$\frac{dH}{dt} = F_{21}(x_u, x_d, H, \delta, \Omega), \tag{3.119}$$

$$\frac{dx_d}{dt} = F_{22}(x_u, x_d, H, \delta, \Omega), \tag{3.120}$$

$$\frac{dx_u}{dt} = F_{23}(x_u, x_d, H, \delta, \Omega), \tag{3.121}$$

(functions F_{21}, F_{22} and F_{23} can be found in Appendix E), which were solved using equations, (3.108), (3.109), and (3.110).

Similar to (3.116), the numerator and denominator of dx_u/dt are both equal to zero at $t = t_2$. We will provide a detailed asymptotic analysis of the local behaviour near $t_2 = \delta^{2/3} T_c$ in Section 4.4.2. However, in order to initialize the numerical solution, we use this asymptotic analysis to find that

$$H\left(t_2+\epsilon\right) \sim \delta^{2/3} 11.3 - \epsilon 1.88, \tag{3.122}$$

$$x_u\left(t_2+\epsilon\right) \sim \delta^{1/3}\left(4.91+\epsilon 1.13\right). \tag{3.123}$$

The location of the downstream boundary, x_d was also assumed to remain constant over this interval. We verified that the numerically solution is independent of ϵ provided it is sufficiently small.

Some time after the velocity $u(t)$ changes sign, we find that the pressure reduces below

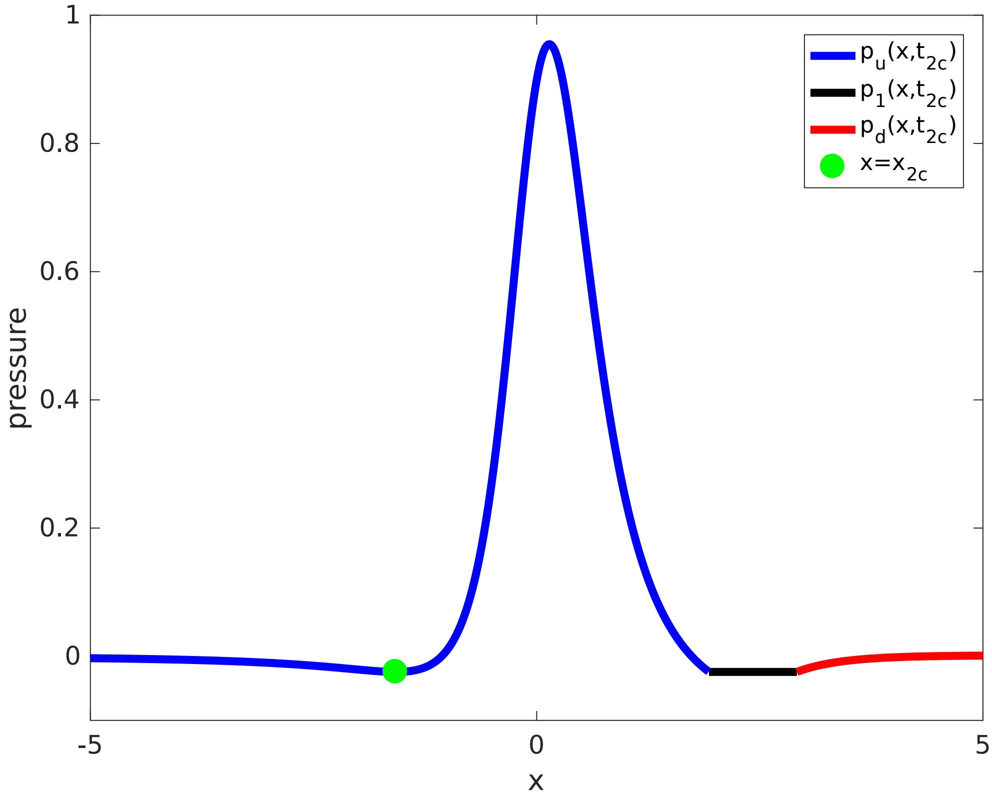

Figure 3.17: Pressure profile of the film when the second mushy region forms, $t = t_{2c}$. The green dot shows the location of the minimum pressure, $x = x_{2c}$. Parameters used in this computation are $\delta = 10^{-2}$ and $\Omega = 1$.

the cavitation pressure, $p = -\delta/\Omega$, on the other side of the film, at $t = t_{2c}$ and $x = x_{2c} < 0$, where

$$x_{2c}\left(t_{2c}\right) = \frac{-2\delta \frac{dH}{dt}\big|_{t=t_{2c}} + \sqrt{4\left(\delta \frac{dH}{dt}\big|_{t=t_{2c}}\right)^2 - 2H\left(t_{2c}\right)u\left(t_{2c}\right)^2 + 2q_u\left(t_{2c}\right)u\left(t_{2c}\right)}}{u\left(t_{2c}\right)}, \tag{3.124}$$

$$p\left(x_{2c}\left(t_{2c}\right), t_{2c}\right) = -\frac{\delta}{\Omega}, \tag{3.125}$$

implying the formation of a second mushy region on the opposite side of the film to the first mushy region. The pressure profile at $t = t_{2c}$ is shown in Figure 3.17, where the blue curve shows the pressure upstream of the mushy region, the red curve shows the pressure downstream, the black line shows the pressure in the mushy region, and the green dot the location, $x = x_{2c}$, of the minimum pressure. We use the notation $x_{uc} = x_u(t)$, $x_{dc} = x_d(t)$, and $H_{2c} = H(t)$ at $t = t_{2c}$ to represent the numerical values of the variables at the time when the second cavity forms.

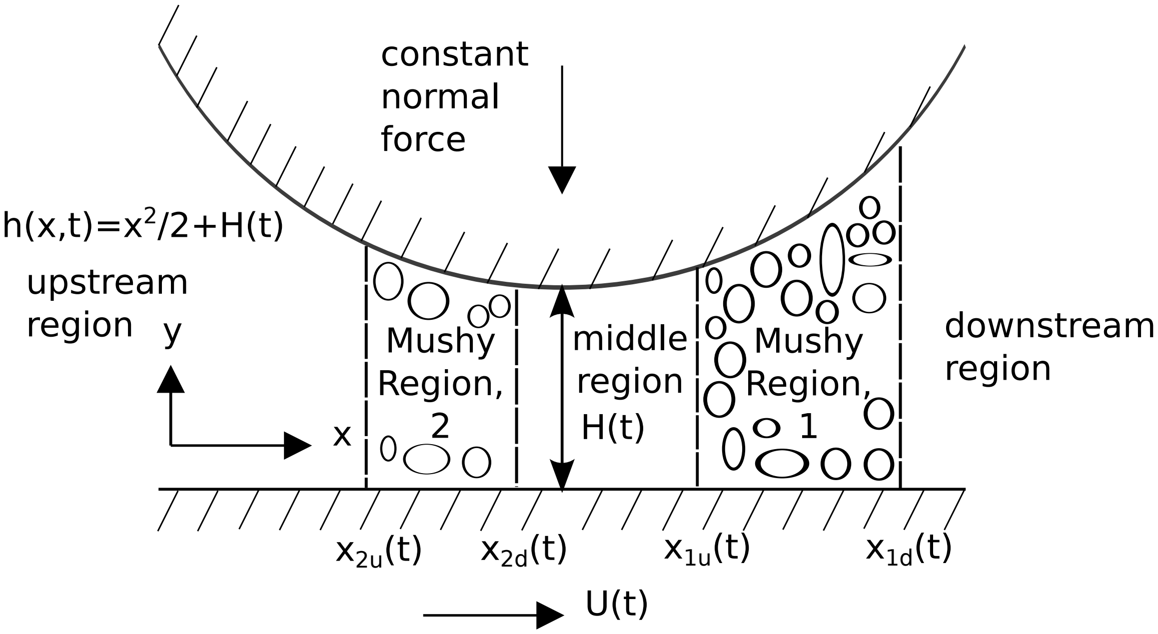

Figure 3.18: Schematic of the model showing the two mushy regions, 1 and 2, and the liquid regions u, M and d.

We now describe the model that involves two mushy regions in the film. We partition the domain into five sections: the upstream region occupies the space, $-\infty < x < x_{2u}(t)$, (denoted with subscript u); the opening second mushy region, $x_{2u}(t) < x < x_{2d}(t)$, (denoted with subscript 2); the middle region, $x_{2d}(t) < x < x_{1u}(t)$, (denoted with subscript M); the closing mushy region, $x_{1u}(t) < x < x_{1d}(t)$, (denoted with subscript 1); and the downstream region, $x_{1d}(t) < x < \infty$, (denoted with subscript d). A schematic of the model with the two mushy regions is shown in Figure 3.18. The pressure p and volume fraction θ take the form:

$$\begin{cases} x < x_{2u}, & p = p_u \geq -\frac{\delta}{\Omega}, & \theta = 1, \\ x_{2u} \leq x \leq x_{2d}, & p = p_2 = -\frac{\delta}{\Omega}, & 0 < \theta \leq 1, \\ x_{2d} < x < x_{1u}, & p = p_M \geq -\frac{\delta}{\Omega}, & \theta = 1, \\ x_{1u} \leq x \leq x_{1d}, & p = p_1 = -\frac{\delta}{\Omega}, & 0 < \theta \leq 1, \\ x_{1d} < x, & p = p_d \geq -\frac{\delta}{\Omega}, & \theta = 1. \end{cases} \tag{3.126}$$

In addition to the boundary conditions on the first mushy region, (3.101), (3.102), and

(3.103), the flux boundary conditions on the second mushy region are

$$\left(\frac{uh}{2}-\frac{h^3}{12}\frac{\partial p_u}{\partial x}-\delta h\frac{dx_{2u}}{dt}\right)_{x=x_{2u}^-}=\left(\theta\left[\frac{uh}{2}-\delta h\frac{dx_{2u}}{dt}\right]\right)_{x=x_{2u}^+}, \tag{3.127}$$

$$\left(\frac{uh}{2}-\frac{h^3}{12}\frac{\partial p_M}{\partial x}-\delta h\frac{dx_{2d}}{dt}\right)_{x=x_{2d}^+}=\left(\theta\left[\frac{uh}{2}-\delta h\frac{dx_{2d}}{dt}\right]\right)_{x=x_{2d}^-}, \tag{3.128}$$

and the pressure boundary conditions

$$p=-\frac{\delta}{\Omega}\text{ at }x=x_{2u,2d}. \tag{3.129}$$

Equations (3.89)-(3.91), (3.100)-(3.103), (3.126)-(3.129) are the governing equations for the mushy region cavitation problem, that includes two mushy regions, with an oscillating bottom surface. As previously, we apply the boundary conditions on θ_2

$$\theta_2=1\text{ on }x=x_{2u},\ \text{ while }\frac{dx_{2u}}{dt}>\frac{u(t)}{2\delta}, \tag{3.130}$$

$$\theta_2=1\text{ on }x=x_{2d},\ \text{ while }\frac{dx_{2d}}{dt}<\frac{u(t)}{2\delta}, \tag{3.131}$$

and θ_2 satisfies equations (3.106) and (3.107). The pressure boundary conditions for $p_u\left(x_{2u}(t),t\right)$ and $p_d\left(x_{1d}(t),t\right)$ are unchanged from (3.108) and (3.109), respectively. The pressure boundary condition at $x=x_{1u}$ and the force balance now have the forms

$$\begin{aligned}
p_M\left(x_{1u},t\right)={}&-24\frac{dH}{dt}\left(\frac{1}{\left(2H+x_{1u}^2\right)^2}+\frac{1}{\left(2H+x_{2d}^2\right)^2}\right)+\frac{12ux_{2d}}{\left(2H+x_{2d}^2\right)^2}\\
&+3q_Mx_{2d}\left(\frac{10H+3x_{2d}^2}{2H^2\left(2H+x_{2d}^2\right)^2}-\frac{10H+3x_{1u}^2}{2H^2\left(2H+x_{1u}^2\right)^2}\right)+\frac{6u}{H}\left(\frac{x_{1u}^3}{\left(2H+x_{1u}^2\right)^2}-\frac{x_{2d}^3}{\left(2H+x_{2d}^2\right)^2}\right)\\
&+\frac{9q_M-6uH}{2\sqrt{2H^5}}\left(\tan^{-1}\left(\frac{x_{2d}}{\sqrt{2H}}\right)-\tan^{-1}\left(\frac{x_{1u}}{\sqrt{2H}}\right)\right)=0,
\end{aligned} \tag{3.132}$$

$$\begin{aligned}
&\frac{6\delta}{H}\left(\frac{x_{2d}\left(2H-x_{2d}^2\right)}{\left(2H+x_{2d}^2\right)^2}+\frac{x_{1u}\left(2H-x_{1u}^2\right)}{\left(2H+x_{1u}^2\right)^2}+\frac{x_{2u}\left(x_{2u}^2-2H\right)}{\left(2H+x_{2u}^2\right)^2}+\frac{x_{1d}\left(2H-x_{1d}^2\right)}{\left(2H+x_{1d}^2\right)^2}\right)\frac{dH}{dt}\\
&+\frac{6\delta}{\sqrt{2H^3}}\left(\tan^{-1}\left(\frac{x_{1u}}{\sqrt{2H}}\right)-\tan^{-1}\left(\frac{x_{2d}}{\sqrt{2H}}\right)+\tan^{-1}\left(\frac{x_{2u}}{\sqrt{2H}}\right)-\tan^{-1}\left(\frac{x_{1d}}{\sqrt{2H}}\right)+\pi\right)\frac{dH}{dt}\\
&+12u\left(\frac{1}{\left(2H+x_{1u}^2\right)}-\frac{1}{\left(2H+x_{2d}^2\right)}+\frac{1}{\left(2H+x_{1d}^2\right)}-\frac{1}{\left(2H+x_{2u}^2\right)}\right)\\
&+12q_M\left(\frac{1}{\left(2H+x_{1u}^2\right)^2}-\frac{1}{\left(2H+x_{2d}^2\right)^2}+\frac{1}{\left(2H+x_{2u}^2\right)^2}-\frac{1}{\left(2H+x_{1d}^2\right)^2}\right)=1,
\end{aligned} \tag{3.133}$$

where q_M is a function of integration of the form

$$q_M = \theta_{1u} u \left(H + \frac{x_{1u}^2}{2} \right) + 2\delta x_{1u} \frac{dH}{dt} + 2\delta(1-\theta_{1u}) \left(H + \frac{x_{1u}^2}{2} \right) \frac{dx_{1u}}{dt}, \tag{3.134}$$

where $\theta_{1u} = \theta_1 (x_{1u}, t)$. Assuming condition (3.131) holds on the downstream boundary of the second mushy region, $x = x_{2d}$, until the first mushy region closes, $x_{1u} = x_{1d}$, the flux boundary condition (3.128), may be rewritten as

$$\begin{aligned} \left.\frac{dp_M}{dx}\right|_{x=x_{2d}} =& 24 \left\{ 4\delta \frac{dH}{dt}(x_{2d} - x_{1u}) - 2(\theta_{1u}-1)H \left(u - 2\delta \frac{dx_{1u}}{dt} \right) \right. \\ & \left. + 2\delta(\theta_{1u}-1)x_{1u}^2 \frac{dx_{1u}}{dt} + u\left(x_{2d}^2 - \theta_{1u}x_{1u}^2\right) \right\} \Big/ \left\{ \left(2H + x_{2d}^2\right)^3 \right\} = 0. \end{aligned} \tag{3.135}$$

Assuming condition (3.130) also holds on the upstream boundary of the second mushy region, $x = x_{2u}$, the three derivatives dH/dt, dx_{1d}/dt, dx_{1u}/dt, can be solved for using equations (3.108), (3.109), (3.135),

$$\frac{dH}{dt} = F_{31}(x_{2u}, x_{2d}, x_{1u}, x_{1d}, H, \delta, \Omega), \tag{3.136}$$

$$\frac{dx_{1d}}{dt} = F_{32}(x_{2u}, x_{2d}, x_{1u}, x_{1d}, H, \delta, \Omega), \tag{3.137}$$

$$\frac{dx_{1u}}{dt} = F_{33}(x_{2u}, x_{2d}, x_{1u}, x_{1d}, H, \delta, \Omega), \tag{3.138}$$

(functions F_{31}, F_{12} and F_{33} can be found in Appendix E). The position of the boundaries x_{2u} and x_{2d} are found using the two algebraic equations (3.132), and (3.133). The initial conditions for this system of equations are

$$x_{2u}(t) = x_{2d}(t) = x_{2c}, \quad x_{1u}(t) = x_{uc}, \quad x_{1d}(t) = x_{ud}, \quad H(t) = H_{2c}, \text{ at } t = t_{2c}. \tag{3.139}$$

The numerical solution was run for sufficient time until one of two events occurred: either condition (3.130) was no longer satisfied, or the first mushy region closed, $x_{1u} = x_{1d}$ at $t = t_f$. If condition (3.130) is no longer satisfied, but the first mushy region still exists in the film, we have to solve four coupled differential equations for H, x_{1u}, x_{1d} and x_{2u}, namely

$$
\begin{aligned}
\frac{dH}{dt} &= F_{41}(x_{2u}, x_{2d}, x_{1u}, x_{1d}, H, \delta, \Omega), && (3.140)\\
\frac{dx_{1u}}{dt} &= F_{42}(x_{2u}, x_{2d}, x_{1u}, x_{1d}, H, \delta, \Omega), && (3.141)\\
\frac{dx_{1d}}{dt} &= F_{43}(x_{2u}, x_{2d}, x_{1u}, x_{1d}, H, \delta, \Omega), && (3.142)\\
\frac{dx_{2u}}{dt} &= F_{44}(x_{2u}, x_{2d}, x_{1u}, x_{1d}, H, \delta, \Omega), && (3.143)
\end{aligned}
$$

(functions F_{41}, F_{42}, F_{43} and F_{44} can be found in Appendix E), which were solved using equations (3.108), (3.109), (3.132), and (3.135), and was solved using the single algebraic equation (3.133). In the event that condition (3.130) is no longer applied, and we refer to this time as $t = t_{12}$. Similar to the situation at $t = t_1$, we evaluate $\theta_2(x, t)$ at $x_{2u}(t_{12} + \epsilon)$ using expressions (4.199) and (4.200), which are equivalent to

$$\theta_2\left(x_{2u}\left(t_{12}+\epsilon\right), t_{12}+\epsilon\right) \to 1 - \frac{\epsilon}{3}, \tag{3.144}$$

$$x_{2u}\left(t_{12}+\epsilon\right) \to -\left[\frac{2^9\Omega^2}{3^6 5^2 \delta}\right]^{\frac{1}{5}} \times \left[\frac{5}{2}\left(1 + \left[\frac{2^{14}\Omega^2}{3^6 5^7}\right]^{\frac{1}{5}}\right) + \epsilon\left[\frac{2^{14}\Omega^2}{3^6 5^2}\right]^{\frac{1}{5}}\right], \tag{3.145}$$

and we verify that the numerical solution is independent of ϵ provided it is sufficiently small. Similar to (3.117)-(3.118), the values of x_{2d}, x_{1u}, x_{1d} and H were taken to remain constant across this interval.

After the first mushy region has closed, we must again solve (3.89)-(3.91), and (3.100)-(3.103) with the initial conditions

$$x_d(t) = x_{2u}(t), \quad x_u(t) = x_{2d}(t), \quad H(t) = H_f, \text{ at } t = t_f, \tag{3.146}$$

where H_f is the film thickness when the first mushy region closed. At each stage, MATLAB's algebraic-differential equation solver, (which is also capable of solving ordinary differential equations), ode15s, was used to solve the system of equations numerically with a time step of 10^{-4}.

3.5.2 Discussion

We now discuss the numerical solutions to the oscillatory problem. However, we delay a comparison with the experimental data until the end of Chapter 4, at which point we will have a greater understanding of the model. We now describe how the initial conditions

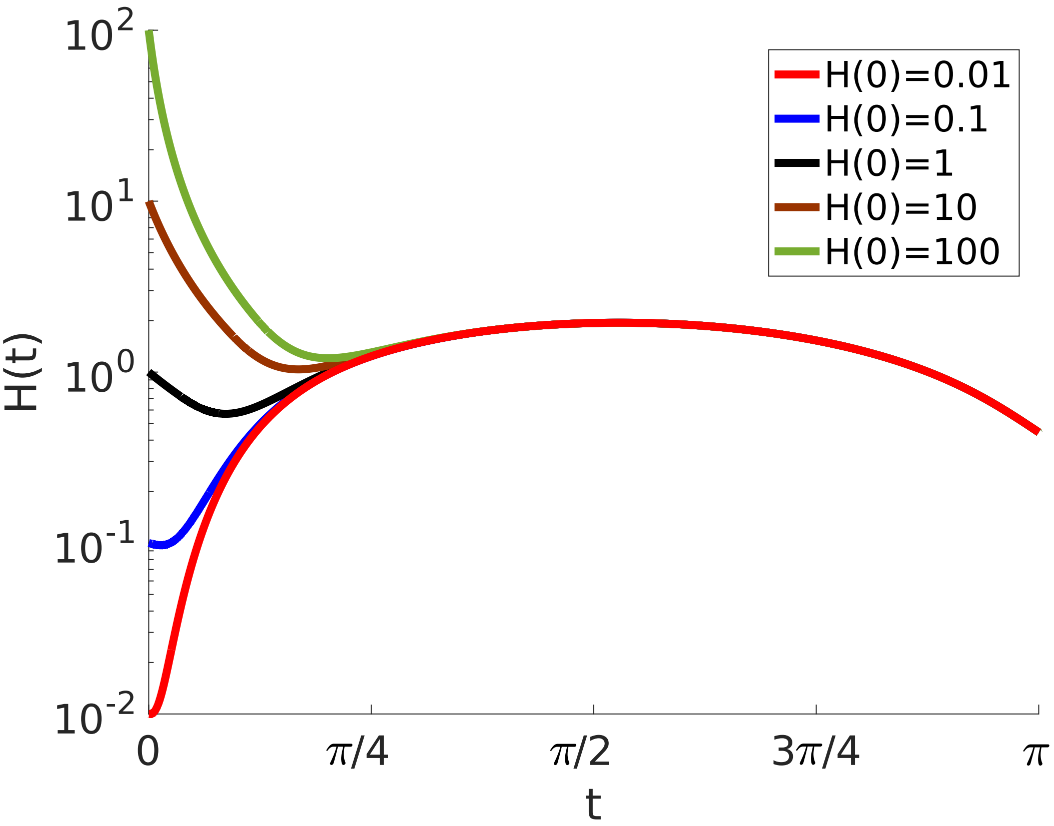

Figure 3.19: Film thickness during the first half of the period of oscillation, $0 < t < \pi$, solved using equations (3.89)-(3.91), (3.100)-(3.103), and (3.126)-(3.129), with different initial film thicknesses: red line, $H_0 = 0.01$; blue line, $H_0 = 0.1$; black line, $H_0 = 1$; brown line, $H_0 = 10$; and green line, $H_0 = 100$. Regardless of the initial film thickness, the film thickness at $t = \pi$ is the same for all. In this computation we used the parameters $\delta = 0.01$ and $\Omega = 1$.

influence the mushy region model.

In Figure 3.19, we show how the film thickness varies over the first half of the period of the first oscillation, $0 < t < \pi$ for five different values of H_0. Parameter values used in this computation are $\delta = 0.01$ and $\Omega = 1$, which are indicative of the parameter regime in the experiment. We observe that the film thickness at $t = \pi$ is independent of the initial film thickness, and all solutions collapse onto the same curve, implying part of the solution is quasi-steady. Similar to the solutions described in Section 3.4, when the velocity of the bottom surface is sufficiently small, we expect the quasi-steady solution to break down and the model to be driven by the dynamics in the system.

In Figures 3.20 and 3.21 we show how the shapes of the mushy region and the film thickness, found by solving (3.89)-(3.91), (3.100)-(3.103), and (3.126)-(3.129), vary with time, for different values of δ across 2 orders of magnitude: $\delta = 10^{-1}$, (thin line), $\delta = 10^{-2}$, (middle line), and $\delta = 10^{-3}$, (thick line); Ω was kept constant at $\Omega = 1$. The dashed

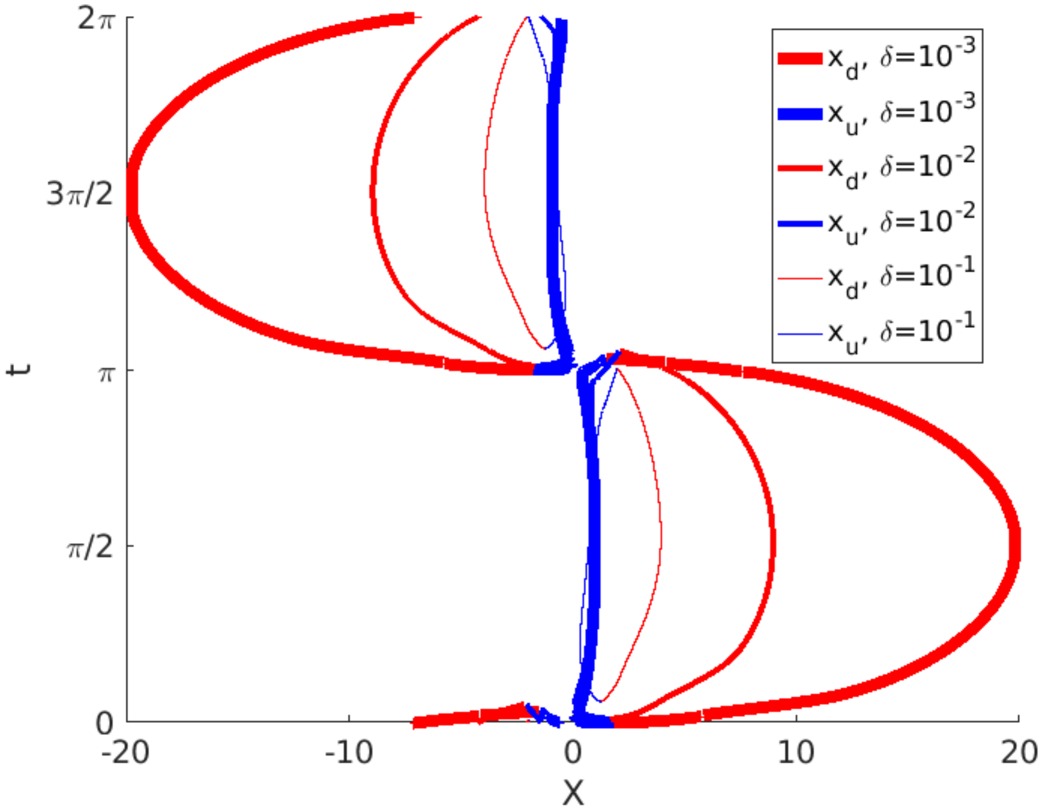

Figure 3.20: $x - t$ diagram showing the boundaries of the mushy region over the time, $0 < t < 2\pi$, solved using equations (3.89)-(3.91), (3.100)-(3.103), and (3.126)-(3.129). The blue curves show the 'inside' boundaries, $x_u\left(t\right)$, $x_{2d}\left(t\right)$ and $x_{1u}\left(t\right)$, and the red curves show the 'outer' boundaries, $x_d\left(t\right)$, $x_{1d}\left(t\right)$ and $x_{2u}\left(t\right)$. Three solutions are shown with varying values of δ: $\delta = 10^{-1}$, (thin line), $\delta = 10^{-2}$, (medium line), and $\delta = 10^{-3}$, (thick line); Ω was kept constant at $\Omega = 1$.

curve in Figure 3.21 is the quasi-steady solution, (4.19), found in Chapter 4.2.1, which solves the mushy region model with $\delta = 0$. The blue curves in Figure 3.20 show the 'inner' boundaries, $x_u\left(t\right)$, $x_{2d}\left(t\right)$ and $x_{1u}\left(t\right)$, and the red curves show the 'outer' boundaries, $x_d\left(t\right)$, $x_{1d}\left(t\right)$ and $x_{2u}\left(t\right)$. We see that the inner boundaries remain close to the origin, while the outer boundaries expand rapidly out into the film as δ is decreased. However, the form the boundaries take as a function of time appear to be converging to an asymptotic limit. The solution with the largest value of $\delta = 10^{-1}$ is the only solution of the three that did not have two mushy regions co-existing in the film at the same time.

The film thickness, H, varying as a function of time $0 < t < 2\pi$, is shown in Figure 3.21. We see that the film thickness varies periodically with time and that the amplitude of oscillation increases as δ decreases. In the limit $\delta \to 0$, the film thickness approaches the quasi-steady solution, provided the velocity of the bottom surface is $|u| = O(1)$. Over this time, the film thickness reaches its maximum near $t = \pi/2$ and $3\pi/2$. Conversely, the

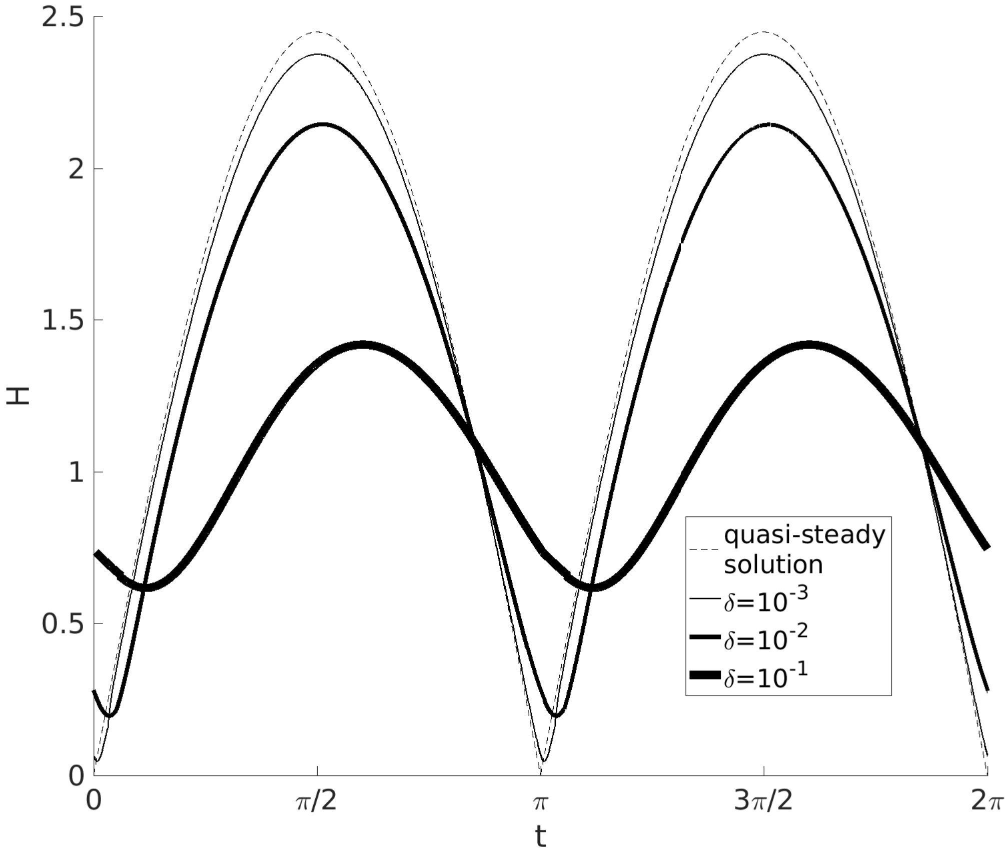

Figure 3.21: the film thickness $H(t)$ varying with time, $0 < t < 2\pi$, solved using equations (3.89)-(3.91), (3.100)-(3.103), and (3.126)-(3.129). Three solutions are shown with varying values of δ: $\delta = 10^{-1}$, (thin line), $\delta = 10^{-2}$, (medium line), and $\delta = 10^{-3}$, (thick line); Ω was kept constant at $\Omega = 1$. The dashed curve shows the quasi-steady solution, (4.19).

film thickness is minimum shortly after the velocity changes sign, near $t = 0$ and π. As δ is decreased, the film thickness near 0 and π sharpens. These qualities further indicate that as $\delta \to 0$, the solution is quasi-steady when $|u| = O(1)$, but breaks down as $u \to 0$, causing the solution to be driven by the dynamics in the system.

In Figures 3.22 and 3.23, we show how the shapes of the mushy region and the film thickness vary with time, as Ω is varied across two orders of magnitude: $\Omega = 10^{-1}$, (thick line); $\Omega = 1$, (medium line); $\Omega = 10$, thin line; δ was held constant at $\delta = 10^{-2}$. The boundaries of the mushy region, shown in Figure 3.22, display similarities to the solutions shown in Figure 3.20, in that x_d becomes considerably large and x_u remains of order $O(1)$. The most notable difference is that, in Figure 3.22, the inner boundaries show a lesser degree of variation with changes in Ω than changes in δ. The mushy region also persists longer in the film as Ω is increased. The maximum film thickness, shown in Figure 3.23, increases as Ω is increased. However, the minimum film thickness changes very little over this range.

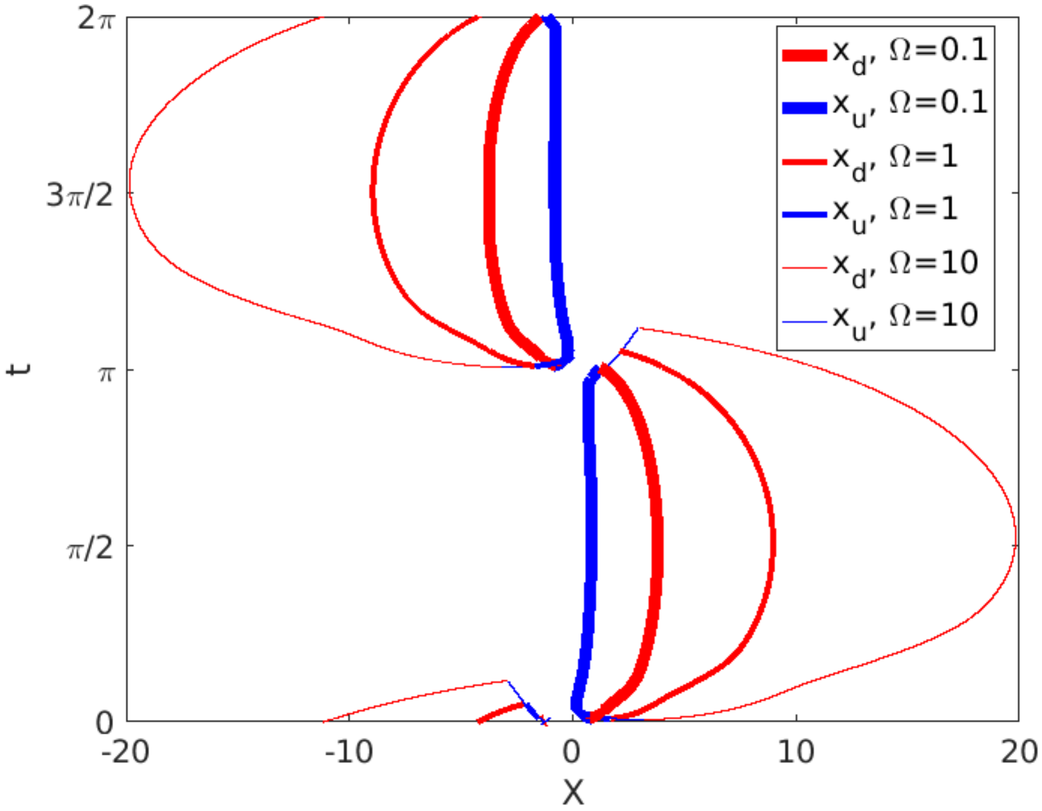

Figure 3.22: $x - t$ diagram showing the boundaries of the mushy region over the time, $0 < t < 2\pi$, solved using equations (3.89)-(3.91), (3.100)-(3.103), and (3.126)-(3.129). The blue curves show the 'inside' boundaries, $x_u\,(t)$, $x_{2d}\,(t)$ and $x_{1u}\,(t)$, and the red curves show the 'outer' boundaries, $x_d\,(t)$, $x_{1d}\,(t)$ and $x_{2u}\,(t)$. Three solutions are shown with varying values of Ω: $\Omega = 10$, (thin line), $\Omega = 1$, (medium line), and $\delta = 0.1$, (thick line); δ was kept constant at $\delta = 10^{-2}$.

This is in direct contrast to the solutions shown in Figure 3.21, where the minimum film thickness varied considerably with changes in δ.

The relaxation time-scale for each of the solutions shown in Figures 3.20-3.23 may be calculated using (3.73) along with the substitution $U_0 = \delta^2/\Omega^2$, to be

$$T_S = \frac{4}{5}\left(\frac{\Omega}{\delta}\right)^{\frac{4}{3}} \quad \text{as} \quad \delta \to 0, \tag{3.147}$$

and the period of oscillation using this parameter system takes the form $T_P = \Omega/\delta^2$. We see that as $\delta \to 0$, the ratio is of the order $T_S/T_P \sim O(\delta^{2/3})$, showing that the relaxation time-scale becomes significantly smaller than the period of oscillation. This again suggests, that in this limit, the solution has sufficient time for the dynamics to decay, approaching a quasi-steady solution that is driven by the velocity of the bottom surface, provided it is sufficiently large.

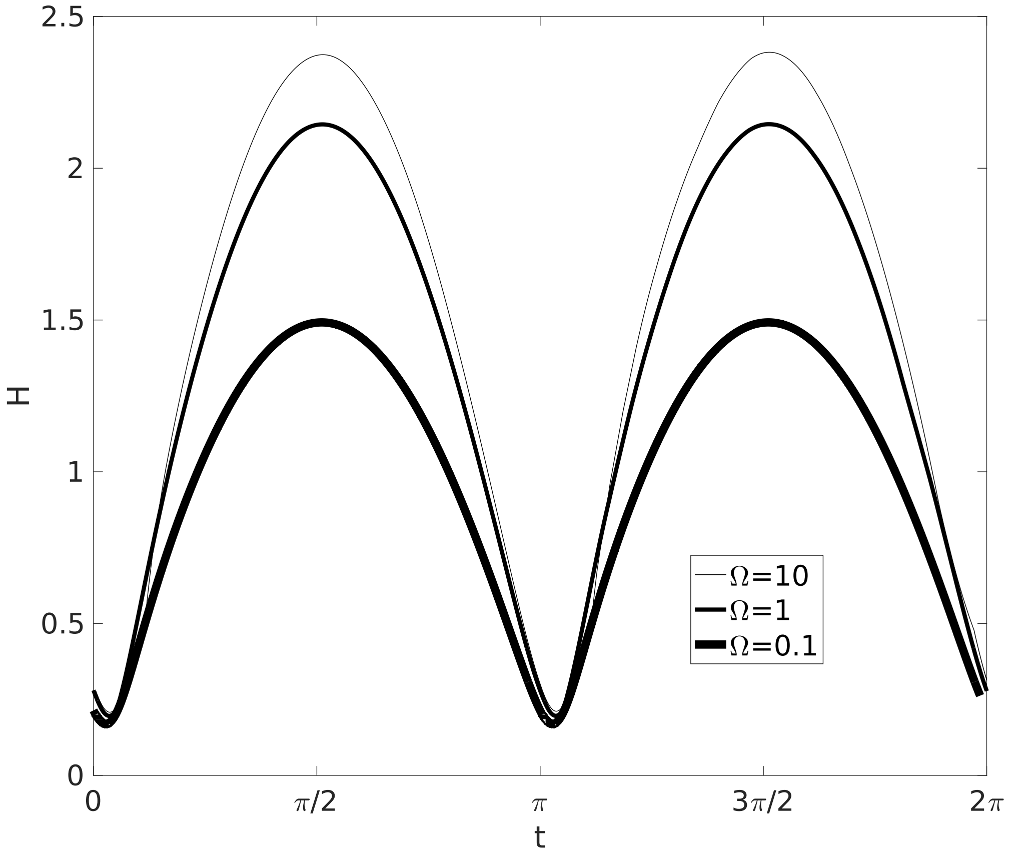

Figure 3.23: the film thickness $H(t)$ varying with time, $0 < t < 2\pi$, solved using equations (3.89)-(3.91), (3.100)-(3.103), and (3.126)-(3.129). Three solutions are shown with varying values of Ω: $\Omega = 10$, (thin line), $\Omega = 1$, (medium line), and $\delta = 0.1$, (thick line); δ was kept constant at $\delta = 10^{-2}$.

In Figure 3.24, we show the volume fraction of liquid at three different times throughout the lifetime of the first mushy region. In each image, the black line is the volume fraction of the liquid inside the mushy region, and the blue and red lines are the volume fraction up and downstream of the mushy region respectively, (which are always equal to one). In the top image (at $t = 0.14$) we see that the volume fraction is one on both x_u and x_d. Both boundaries are moving sufficiently fast that the displaced liquid is being drawn into the mushy region. Later, at time $t = 1.7$, the volume fraction at x_d is less than one, indicating liquid is now flowing out of the mushy region. Across this boundary, the volume fraction is discontinuous, being equal to one outside the mushy region. This is in agreement with the rapid change in the volume of liquid across the interface observed in the experiments and shown in Figure 3.6. The discontinuity propagates through the liquid film like a shock, and to satisfy (3.89), the pressure gradient is discontinuous across x_d. The final image was taken immediately prior to the closure of the first mushy region, but after the second

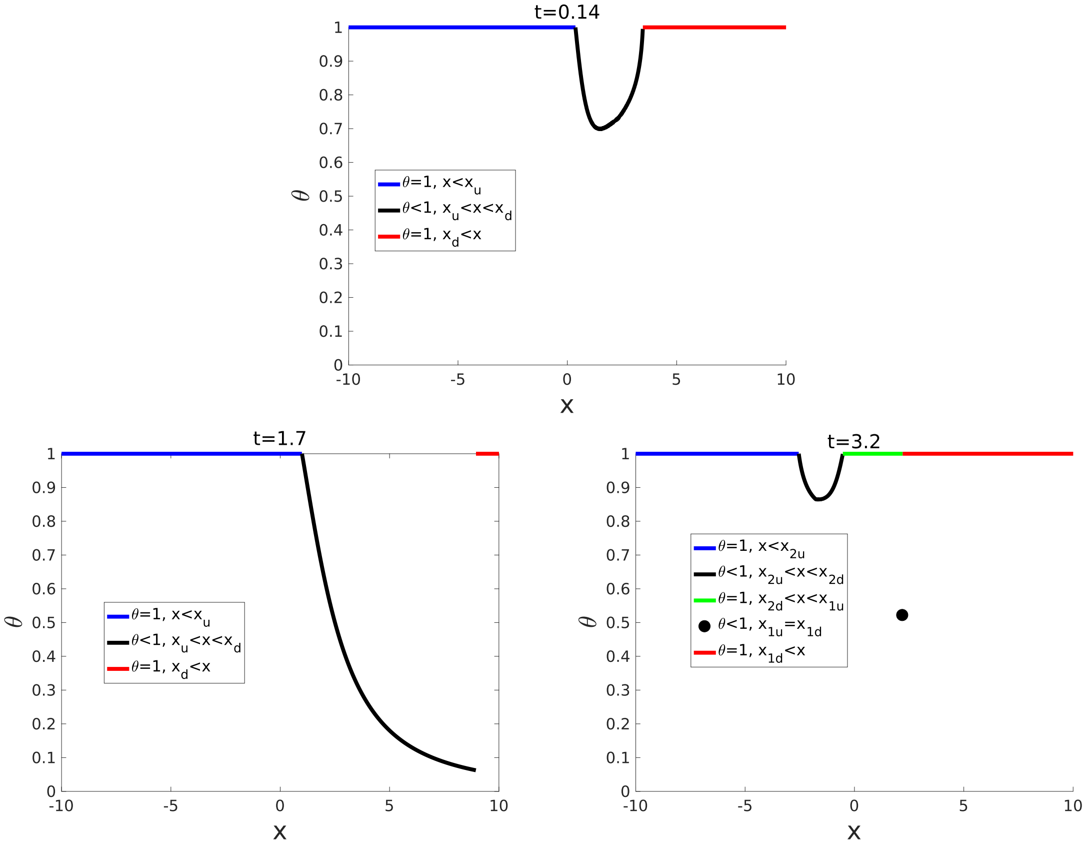

Figure 3.24: The volume fraction plotted against x at three times throughout the lifetime of the first mushy region, $t = 0.14$, $t = 1.7$, and $t = 3.2$. The final image was taken immediately prior to the closure of the first mushy region, and hence has reduced to a single point. Parameters in this figure are those from test number 1 with parameters: $\delta = 10^{-2}$ and $\Omega = 1$.

mushy region has opened. We see that the first mushy region has reduced to a single point at $x = 2.2$, with volume fraction $\theta = 0.52$.

In Figure 3.25, we show the pressure profile in the film immediately before the first mushy region closes as the red curve and the pressure profile immediately afterwards as the blue curve. The black line is the pressure inside the second mushy region. Immediately prior to the closure of the region, the pressure profile forms a corner. After the mushy region closes, the pressure must transition from the red curve to the blue curve instantaneously. In physical terms, the pressure in the mushy region is constant, but the volume fraction of liquid is determined by the thin film equation, (3.89), which is, in this instance, a hyperbolic partial differential equation. Immediately after the closure of the mushy region, the volume fraction becomes equal to one, and the pressure varies according to (3.89), which is now an elliptic equation. This transition is typical of the collapse of a mushy region in a liquid film, and often results in the deformation of the solid surfaces which bound the liquid. This process, commonly referred to as cavitation pitting, can leave a small hole in the surface

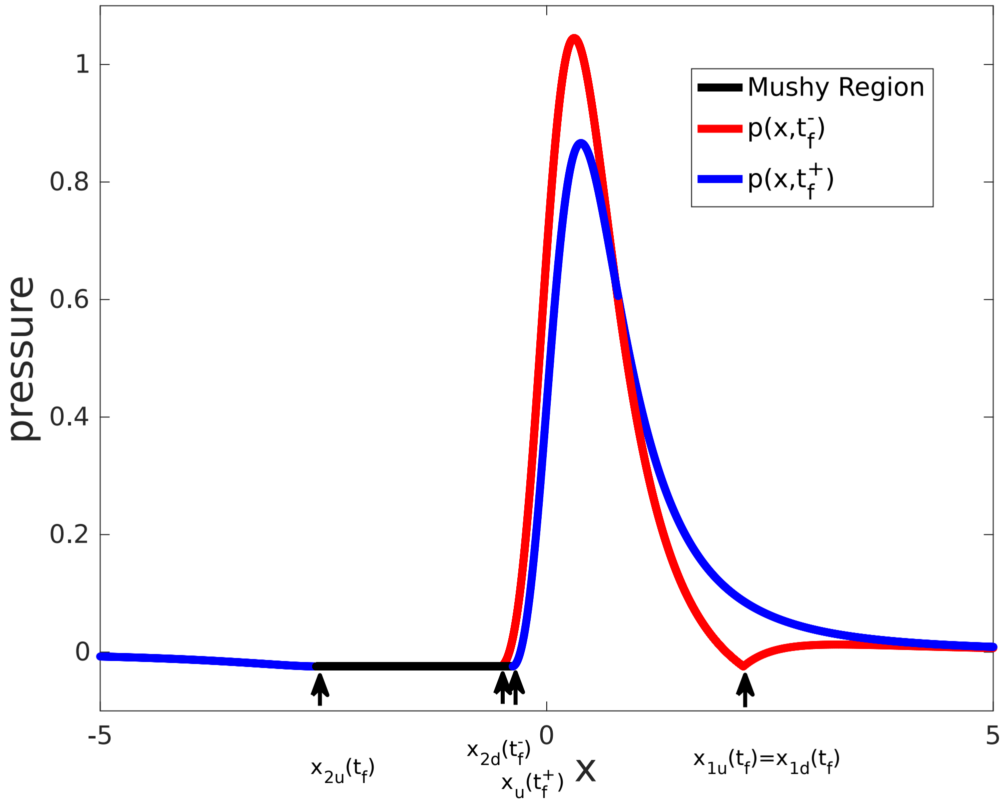

Figure 3.25: The pressure profile in the film, the red curve is shown immediately before the first mushy region closes, $t = t_f^-$, and the blue curve shows it immediately afterwards, $t = t_f^+$. The black line shows the pressure inside the mushy region, and the boundaries of the mushy region are also noted, $x_{2u}\,(t_f)$, $x_{2d}(t_f^-)$, $x_{1u}\,(t_f)$, $x_{1d}\,(t_f)$, and $x_u(t_f^+)$. Parameters used in this figure are: $\delta = 10^{-2}$ and $\Omega = 1$.

near where the collapse took place and contribute to the wear of the film (Stachowiak and Batchelor, 2013). Of course, the assumptions made in the derivation of this model may not hold in the final stages of the collapse of the mushy region. A more physically realistic model would show a smooth transition in both space and time between the pressure and volume fraction when such an event occurs. Such a model is not attempted in this thesis.

In Figure 3.25, we show an instantaneous and discontinuous jump in the right hand boundary of the second mushy region across the time when first mushy region closes, hence $x_{2d} \neq x_u$ at this moment. This suggests a volume of liquid instantaneously cavitates when the first mushy region closes, and that it is a consequence of the disruption caused by that closure. There are also discontinuities in x_d and dH/dt. However, all of the discontinuities are too small to be observed in Figures 3.20-3.23. We note that the film thickness remains continuous over this time though.

3.6 Conclusions

Our work in this chapter was motivated by the City Experiments in which gaseous cavities form and collapse inside a liquid film with variable thickness above an oscillatory moving surface. We described the City Experiments in Section 3.2. We modelled the physics of the cavitated region with a mushy region model, and divided the chapter into three main sections: Section 3.3, where the velocity of the bottom surface was constant, Section 3.4 where it decreases monotonically with time, and finally Section 3.5 where is assumed to oscillate sinusoidally.

In Section 3.3, we studied how a mushy region forms and reaches a steady state assuming the velocity of the bottom surface was constant. We calculated the linear decay rate of perturbations to the steady state solution, and estimated the relaxation time-scale. In Section 3.4, we used the steady state solutions as initial conditions to observe how the mushy region closes with a slowly decreasing velocity, which we compared to the quasi-steady solution. As expected, when the relaxation time-scale was significantly shorter than the deceleration time-scale of the bottom surface, the numerical and quasi-steady solutions showed excellent agreement. This agreement disappeared when the velocity of the bottom surface approaches zero, causing the solutions to become dynamic.

Finally, in Section 3.5, we studied the numerical solution to the mushy region model in the more realistic case when the bottom surface oscillates. Using different initial conditions, we have shown how the numerical solution varied over the first half of the first period of oscillation, $0 < t < \pi$. We found that the film thickness at $t = \pi$ was independent of the initial film thickness since all the solutions collapsed onto a single curve, for parameter values indicative of the experiment. We showed how the mushy region behaved with changes in δ and Ω. As Ω is increased, the maximum film thickness increases, but the minimum film thickness remains unchanged. We have shown that as δ is decreased to zero, the amplitude of oscillation of the film thickness increases and a second mushy regions forms on the opposite side of the parabolic surface before the first mushy region had closed. Also in this limit, we have shown the numerical solutions resemble the quasi-steady solution when the velocity of the bottom surface is sufficiently large. These observations are confirmed when we compare the relaxation time-scale, T_S, to the period of oscillation, T_P, finding that the ratio is of the order $T_S/T_P \sim O(\delta^{2/3})$ in the limit $\delta \to 0$.

We calculate the volume fraction, θ, and the pressure, p, throughout the period. Across the time the mushy region collapsed, the numerical model exhibited discontinuities in the volume fraction and pressure. The numerical solution also predicted discontinuities in the boundaries of the second mushy region on the other side of the film, x_u and x_d, and the vertical velocity of the top surface, dH/dt.

In the next chapter, we show how the solution transitions from being quasi-steady to dynamic as the velocity of the bottom surface changes magnitude. We do this by studying the asymptotic limit of the model as $\delta \to 0$, and compare it to the numerical solution. We also draw comparisons between the numerical solution and the experimental data.

Chapter 4

Asymptotic Analysis of the Mushy Region Problem

4.1 Introduction

In the previous chapter, we showed numerical solutions of the equations (3.89)-(3.91), (3.100)-(3.103), and (3.126)-(3.129) with δ varying in the range $10^{-1} < \delta < 10^{-3}$, where δ is the ratio between horizontal length scale $\sqrt{R_c \check{H}}$ and the amplitude of oscillation of the bottom surface, U/ω. From these solutions, we observed that the numerical solution exhibits two distinct behaviours in the limit $\delta \to 0$. The first is the quasi-steady solution, valid when the velocity of the bottom surface is large. The second behaviour emerges as the velocity approaches zero and the unsteady dynamics begin to dominate.

In this chapter, we study the asymptotic limits of the model in the limit $\delta \to 0$ and compare this to the numerical solutions presented in Chapter 3. In Figure 4.1, we show the asymptotic solutions discussed in this chapter; on the right we see an $x-t$ diagram, with each colour representing a different section of the analysis; the left hand image shows the velocity profile, $u = \sin(t)$. In Section 4.2, we derive the quasi-steady solution, which applies when the velocity of the bottom surface is sufficiently large compared to δ, (sketched in dark blue in the right hand image of Figure 4.1). In Section 4.3, we consider the unsteady dynamic motion of the downstream boundary (sketched in light green in the right hand image of Figure 4.1). In Section 4.4, we discuss the unsteady motion of the upstream boundary, (sketched in light blue in the right hand image of Figure 4.1).

The numerics suggest that the position of the upstream boundary is small compared to the position of the downstream boundary; we estimate the time the mushy region closes in

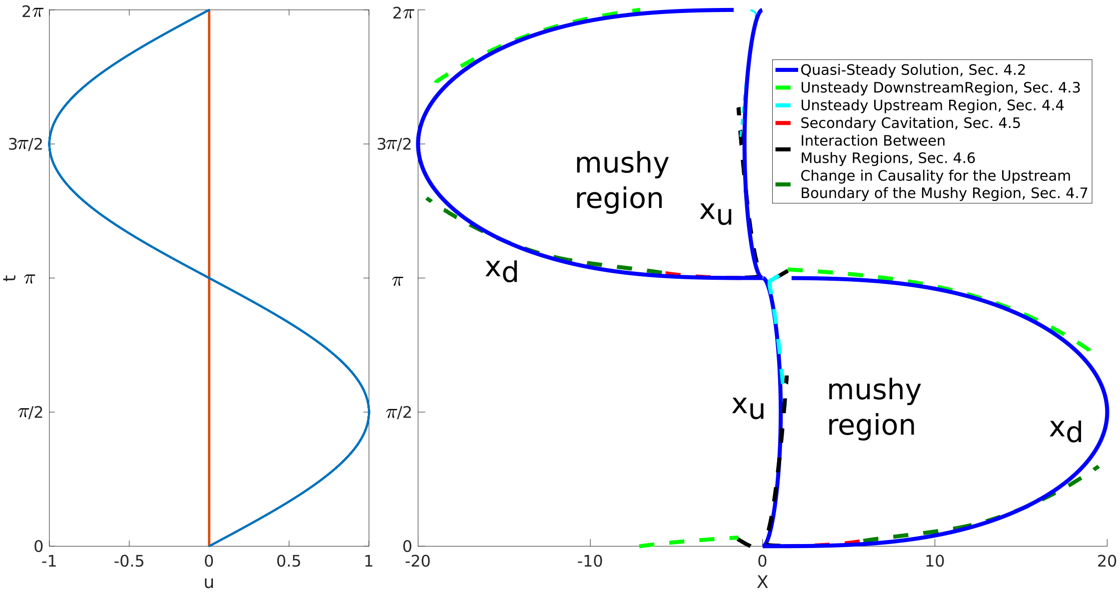

Figure 4.1: The right hand panel shows the $x-t$ diagram of the asymptotic solutions discussed in this chapter. Each section is represented by a different colour: the quasi-steady solution in Section 4.2 is shown as dark blue; the unsteady downstream boundary in Section 4.3 as light green; the unsteady upstream boundary in Section 4.4 as light blue; the secondary cavitation in Section 4.5 as red; the interaction between the mushy regions in Section 4.6 as black; and the change in causality for the upstream boundary of the mushy region in Section 4.7 as dark green. Asymptotic solutions shown here were calculated with parameter values $\Omega = 1$ and $\delta = 10^{-3}$. The left hand panel is the velocity profile, $u = \sin(t)$.

Section 4.3, finding the time at which the downstream boundary reaches the origin. The numerically determined timee at which the mushy region closes converges only slowly to the asymptotic limit; we therefore make a second order correction, discussed in Section 4.6, taking into account the movement of the upstream boundary.

After the velocity of the bottom surface changes sign, the pressure on the opposite side of the film from the mushy region is shown to reduce below the cavitation pressure, resulting in the formation of a second mushy region in the film, as described in Section 4.5, (shown as the red curve in the right hand image of Figure 4.1). After a short interval, the interaction between the mushy regions must be considered, since the dominant contribution to the force balance comes from the liquid separating these spaces; we discuss this in Section 4.6 finding the resulting evolution (the black curve in the right hand image of Figure 4.1). Finally, in Section 4.7, we show that a change in causality of the upstream boundary of the second mushy region is required so it matches to the quasi-steady solution, (shown as dark green in the right hand image of Figure 4.1). We summarize the asymptotic analysis of the mushy region model is make in Section 4.8. In Section 4.9, we discuss the comparison between the experimental results, and numerical and asymptotic solutions, showing the numerics does indeed converge to the asymptotic expression in the limit $\delta \to 0$. In Section 4.10, we draw our conclusions.

For convenience, we restate the equations below. In this chapter it will be easiest to describe the motion of the liquid inside and outside of the mushy region with separate equations in this chapter. As previously described, we first partition the fluid domain into three sections: a mushy region, and the liquid regions upstream and downstream of the mushy region, (denoted with subscripts u and d respectively). A schematic of the model was previously shown in Figure 3.7. In the liquid regions, the pressures are described by the Reynolds equation,

$$\frac{\partial p_u}{\partial x} = \frac{6}{h^3}\left(uh - q_u + 2\delta x \frac{dH}{dt}\right), \qquad \text{for } x < x_u(t), \tag{4.1a}$$

$$\frac{\partial p_d}{\partial x} = \frac{6}{h^3}\left(uh - q_d + 2\delta x \frac{dH}{dt}\right), \qquad \text{for } x > x_d(t), \tag{4.1b}$$

where h and u have the form

$$h = \frac{x^2}{2} + H, \quad u = \sin t, \tag{4.2}$$

we take $t \in [0, 2\pi]$, and q_u and q_d are determined from the flux boundary conditions (3.101) and (3.102); in particular, we have

$$q_{u,d} = \left[\theta u h + 2\delta(1-\theta) h \frac{dx_{u,d}}{dt} + 2\delta x_{u,d} \frac{dH}{dt}\right]\Bigg|_{x=x_{u,d}}. \tag{4.3}$$

The pressures approach atmospheric pressure in the far field and are equal to the cavitation pressure at the mushy region boundaries, i.e.,

$$p_u \to 0 \quad \text{as } x \to -\infty, \qquad p_u = -\frac{\delta}{\Omega} \quad \text{at } x = x_u, \tag{4.4a}$$

$$p_d \to 0 \quad \text{as } x \to \infty, \qquad p_d = -\frac{\delta}{\Omega} \quad \text{at } x = x_d, \tag{4.4b}$$

where Ω and δ are the two dimensionless parameters in the model defined as

$$\delta = \omega R_c \sqrt{\frac{\mu}{FU}} \quad \text{and} \quad \Omega = \frac{\omega F}{(p_{atm} - p_{vap})\, U}, \tag{4.5}$$

Ω is the ratio of the length scales $F/\left(p_{atm} - p_{vap}\right)$, the length of the mushy region required to support the weight of the top surface, to U/ω, the amplitude of oscillation of the bottom surface. In the mushy region, the pressure is constant, $p = -\delta/\Omega$, and the volume fraction, θ, of the liquid satisfies the conservation of liquid mass

$$\delta \frac{\partial}{\partial t}(h\theta) + \frac{u}{2}\frac{\partial}{\partial x}(h\theta) = 0, \tag{4.6}$$

for $x_u < x < x_d$. It is also necessary to specify θ at any boundary where characteristics propagate *into* the cavitated region, i.e.

$$\theta = 1 \quad \text{at } x = x_u \qquad\qquad \text{while} \quad \frac{u}{2\delta} > \frac{dx_u}{dt}, \tag{4.7a}$$

$$\theta = 1 \quad \text{at } x = x_d \qquad\qquad \text{while} \quad \frac{u}{2\delta} < \frac{dx_d}{dt}. \tag{4.7b}$$

We note when either condition (4.7a) or (4.7b) are applied, the pressure gradient, 4.1, evaluated on the respective boundary of which they are applied reduces to

$$\left.\frac{\partial p_{u,d}}{\partial x}\right|_{x=x_{u,d}} = 0 \quad \text{subject to condition 4.7(a or b).} \tag{4.8}$$

The shape of the characteristics is described further in Section 3.3 with Figure 3.8. Finally, we specify the net normal force:

$$\int_{-\infty}^{\infty} p\, dx = \int_{-\infty}^{x_u} p_u\, dx - (x_d - x_u)\frac{\delta}{\Omega} + \int_{x_d}^{\infty} p_d\, dx = 1. \tag{4.9}$$

By integrating by parts, this condition may be rewritten as

$$\int_{-\infty}^{x_u} x\frac{\partial p_u}{\partial x}\, dx + \int_{x_d}^{\infty} x\frac{\partial p_d}{\partial x}\, dx = -1. \tag{4.10}$$

We now solve for the boundaries of the mushy region, x_u and x_d, the film thickness, H, as well as the pressures, p_u and p_d, and the volume fraction θ.

4.2 Quasi-Steady Solution

We first consider the quasi-steady solution: we assume the velocity of the bottom surface is positive and large compared to δ and that the time scale over which the unsteady components decay is significantly shorter than the period of oscillation. To zeroth order in δ, we show the force balance is dominated by the liquid upstream of the mushy region, $x < x_u$, in

Section 4.2.1, yielding quasi-steady solutions for x_u and H. We determine the quasi-steady solution for the downstream boundary $x_d = O\left(\delta^{-1/3}\right)$ in Section 4.2.2.

4.2.1 Upstream Region

First we just let $\delta \to 0$ and assume $u = O(1)$ in the governing equations and boundary conditions (4.1)-(4.10). To leading order, the pressure in the mushy region equals the pressure in the far field, (4.4b). From this we conclude $x_d \to \infty$ in the limit $\delta \to 0$, and the pressure downstream of the mushy region, $x > x_u$, has a negligible effect on the force balance. With these assumptions, p_u satisfies the leading order problem;

$$\frac{\partial p_u}{\partial x} = \frac{6}{h^3}\left(uh - q_u\right), \qquad x < x_u(t), \tag{4.11}$$

$$p_u \to 0, \qquad x \to -\infty, \tag{4.12}$$

$$p_u = 0, \qquad x = x_u(t), \tag{4.13}$$

$$q_u = \theta u h, \qquad x = x_u(t), \tag{4.14}$$

$$\int_{-\infty}^{x_u} x\frac{\partial p_u}{\partial x}\, dx = -1, \tag{4.15}$$

In the limit $\delta \to 0$, we apply the boundary condition, (4.7a), $\theta = 1$ until $u = O(\delta^{2/3})$ when the derivatives dx_u/dt and dH/dt become of significant magnitude. The problem (4.11)-(4.15) is quasi-steady, and the solution depends only parametrically on t through the velocity u. Integrating equation (4.11) with (4.12), the pressure upstream of the mushy region is described by

$$p_u = \frac{3(4Hu - 3q_u)\left(2\tan^{-1}\left(\frac{x}{\sqrt{2H}}\right) + \pi\right)}{4\sqrt{2H^5}} + \frac{3x(4Hu - 3q_u)}{2H^2\left(2H + x^2\right)} - \frac{6q_u x}{H\left(2H + x^2\right)^2}. \tag{4.16}$$

The conservation of liquid mass equation in the mushy region (4.6) reduces to

$$\frac{\partial}{\partial x}(h\theta) = 0, \tag{4.17}$$

with $\theta = 1$ at $x = x_u$, since $u > 0$. Hence the liquid fraction in the mushy region is given by

$$\theta = \frac{H + x_u^2/2}{H + x^2/2} = \frac{6u}{6\left(1 - \beta^2\right)u + x^2}. \tag{4.18}$$

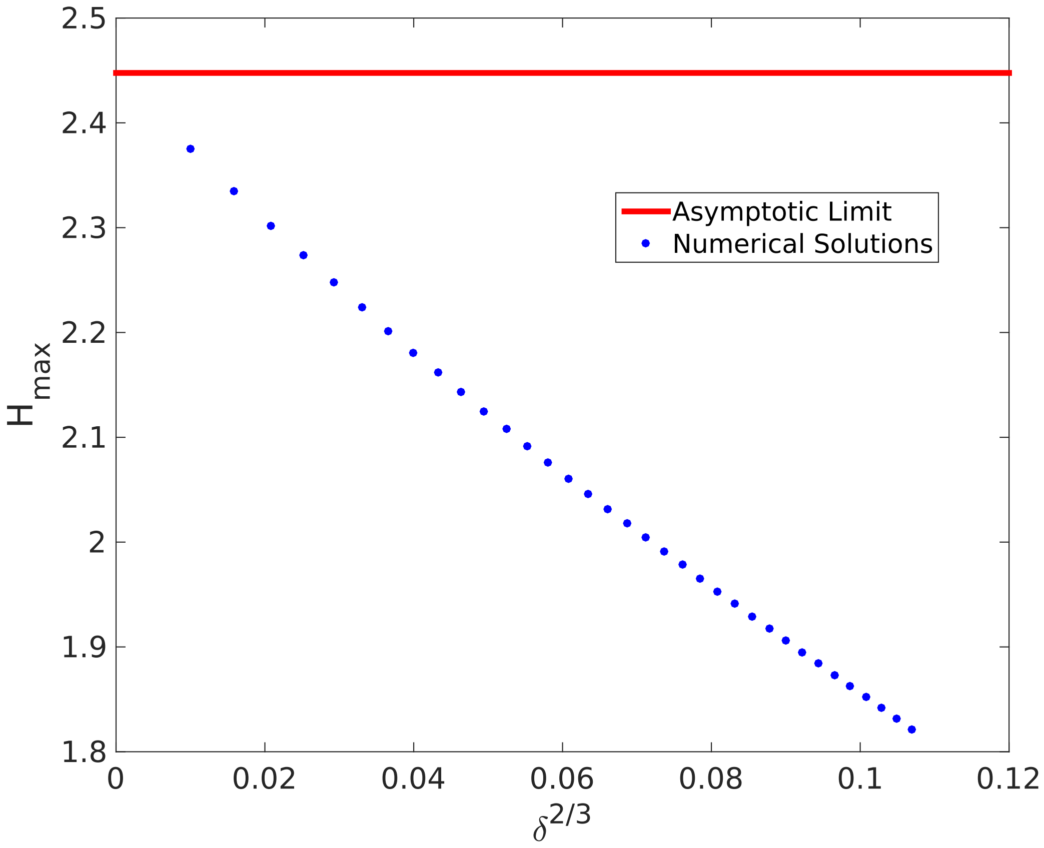

Figure 4.2: The maximum film thickness, determined numerically (blue dots), converges to the asymptotic prediction (4.21) (red line). In Section 4.2.2, we shall see that the first order correction to the maximum film thickness is at $O(\delta^{2/3})$; motivated by this we use $\delta^{2/3}$ as the abscissa.

Using the substitution

$$q_u = 3u^2, \qquad x_u = \beta\sqrt{6u}, \qquad H = 3\left(1-\beta^2\right)u, \tag{4.19}$$

the force balance, (4.15), is satisfied identically, and condition (4.13) reduces to a transcendental equation for β

$$\frac{\pi}{2} + \tan^{-1}\left(\frac{\beta}{\sqrt{1-\beta^2}}\right) - \frac{\beta\left(1+2\beta^2\right)\sqrt{1-\beta^2}}{1-4\beta^2} = 0. \tag{4.20}$$

We find numerically that $\beta \approx 0.429$. The film thickness is maximum when the velocity of the bottom surface is maximum, i.e. $u = 1$, and we have

$$H_{max} = 3\left(1-\beta^2\right) \approx 2.45, \quad \text{at} \quad t = \frac{\pi(2n-1)}{2} \tag{4.21}$$

where $n \in \mathbb{N}$. In Figure 4.2, we show the maximum film thickness H_{max} varying with $\delta^{2/3}$.

We show it varying with $\delta^{2/3}$ because the contribution the pressure in the downstream region has on the force balance is of this order, discussed in Section 4.2.2, and so we expect the first order correction to the maximum film thickness is of the same order. The numerical solutions (the blue dots) approach the asymptotic limit, given equation (4.21) (shown as the red line). However, even for the smallest value of δ, the numerical solution still differs noticeably from the quasi-steady solution. (All the numerical solutions were calculated with the value of $\Omega = 1$).

4.2.2 Downstream Region

We now study the downstream boundary of the mushy region in this quasi-steady state. We make the following assumptions: first, x_d is sufficiently large that for $x > x_d$, $H \ll x$, so that the film thickness $h = O\left(x^2\right)$; second, the pressure downstream of the mushy region has a negligible contribution to the force balance; and third, the causality condition on the downstream boundary, (4.7b), does not apply because $u \gg 2\delta(dx_d/dt)$. We must therefore solve for θ at the boundary $x = x_d$. Choosing to balance the terms uh with θuh in the pressure gradient, (4.1b), which may be integrated with respect to x, we find the pressure is of the order $p \sim x^{-3}$ as $x \to \infty$, which we equate to the boundary condition (4.4b) to derive the scaling $x_d = O\left(\delta^{-1/3}\right)$ as $\delta \to 0$. We therefore describe the downstream region using the scalings

$$x = \delta^{-1/3}\tilde{x}, \qquad h = \delta^{-2/3}\tilde{h}, \qquad \theta = \delta^{2/3}\tilde{\theta}, \qquad p_d = \delta\tilde{p}_d, \tag{4.22}$$

where the scaling for θ was found by taking the limit of (4.18) as $x \to \infty$. The governing equations and boundary conditions in this region therefore become

$$\frac{\partial \tilde{p}_d}{\partial \tilde{x}} = \frac{6}{\tilde{h}^3}\left[u\tilde{h} - \delta^{2/3}q_d + 2\delta^{4/3}\tilde{x}\frac{dH}{dt}\right], \qquad \tilde{x} > \tilde{x}_d \tag{4.23}$$

$$\tilde{p}_d \to 0, \qquad \tilde{x} \to \infty, \tag{4.24}$$

$$\tilde{p}_d = -\frac{1}{\Omega}, \qquad \tilde{x} = \tilde{x}_d, \tag{4.25}$$

$$q_d = \tilde{\theta}u\tilde{h} + 2\left(1 - \delta^{2/3}\tilde{\theta}\right)\tilde{h}\frac{d\tilde{x}_d}{dt} + 2\delta^{2/3}\tilde{x}_d\frac{dH}{dt}, \qquad \tilde{x} = \tilde{x}_d, \tag{4.26}$$

$$\delta^{2/3}\frac{\partial}{\partial t}\left(\tilde{h}\tilde{\theta}\right) + \frac{u}{2}\frac{\partial}{\partial \tilde{x}}\left(\tilde{h}\tilde{\theta}\right) = 0, \qquad \tilde{x} < \tilde{x}_d, \tag{4.27}$$

$$\tilde{h} = \delta^{2/3}H + \frac{\tilde{x}^2}{2}. \tag{4.28}$$

The solution strategy is to integrate (4.23) subject to the far field condition (4.24), to obtain an expression for p_d, and using the mushy region condition (4.25), we derive an expression for the downstream boundary, x_d. Hence, to lowest order we obtain

$$\tilde{p}_d = -\frac{8u}{\tilde{x}^3}, \qquad \tilde{x}_d = 2\Omega^{1/3}u^{1/3}, \qquad q_d = 3u^2 + \frac{8\Omega}{3}\frac{du}{dt} \tag{4.29}$$

and, integrating (4.27) and matching with (4.18), we find that

$$\tilde{\theta} = \frac{6}{\tilde{x}^2}. \tag{4.30}$$

We note that the contribution to the normal force from this region is

$$-\int_{x_d}^{\infty} p_d \, dx = -\delta^{2/3}\int_{\tilde{x}_d}^{\infty} \tilde{p}_d \, d\tilde{x} \sim \frac{3\delta^{2/3}u^{1/3}}{\Omega^{2/3}}, \tag{4.31}$$

which is indeed negligible to lowest order compared to the contribution from the liquid region upstream of the mushy region, which is of $O(1)$. We note that an error of $O(\delta^{2/3})$ in the force balance calculation is consistent with the observed error in the numerical solution for H_{max}, shown in Figure 4.2 .

As with the upstream region, the terms involving time derivatives of $\tilde{x}_d$ and H do not enter the leading-order problem, and the solution (4.29) depends only parametrically on t through the velocity profile $u(t)$. However, as $u \to 0$, this quasi-steady solution ceases to be valid, as described below.

4.3 Unsteady Downstream Region

We now describe the unsteady dynamics of the downstream boundary, x_d, as the mushy region closes. With $u(t)$ given by (4.2), we have $u(t) \sim \pi - t$ as $t \to \pi^-$. When u becomes sufficiently small, the quasi-steady solution found in Section 4.2 fails due to the dynamic terms in the model that were previously have assumed to be negligible, but now have a significant effect. The first failure corresponds to the dx_d/dt term (4.3) ceasing to be negligible. Again, as in Section 4.2.2, we assume the film thickness scales as $h = O\left(x^2\right)$ as $x \to \infty$, and that H and dH/dt both have a negligible effect on the behaviour at the downstream boundary. By assuming $dx_d/dt = O(1)$, we find the pressure is of order $p = O\left(x^{-5}\right)$ as $x \to \infty$, which by equating to the mushy region condition (4.4b), we derive the scaling $x_d = O(\delta^{-1/5})$ as $\delta \to 0$. By balancing q_d with the term uh in (4.1b), we also find the scaling $u = O\left(\delta^{2/5}\right)$, and from (4.18) θ is of the order $\theta \sim O(\delta^{4/5})$. These scalings results motivate the rescalings

$$t = \pi - \delta^{2/5}\hat{t}, \qquad u = \delta^{2/5}\hat{u}, \qquad x = \delta^{-1/5}\hat{x}, \tag{4.32a}$$

$$h = \delta^{-2/5}\hat{h}, \qquad H = \delta^{2/5}\hat{H}, \qquad \theta = \delta^{4/5}\hat{\theta}, \tag{4.32b}$$

where $-\infty < \hat{t}$, and we again employ

$$p_d = \delta\tilde{p}_d, \qquad q_d = O(1). \tag{4.32c}$$

The governing equations in the downstream region become

$$\frac{\partial \tilde{p}_d}{\partial \hat{x}} = \frac{6}{\hat{h}^3}\left[\hat{u}\hat{h} - q_d + 2\delta^{4/5}\hat{x}\frac{d\hat{H}}{d\hat{t}}\right], \qquad \hat{x} > \hat{x}_d, \tag{4.33}$$

$$\tilde{p}_d \to 0, \qquad \hat{x} \to \infty, \tag{4.34}$$

$$\tilde{p}_d = -\frac{1}{\Omega}, \qquad \hat{x} = \hat{x}_d, \tag{4.35}$$

$$q_d = \delta^{4/5}\hat{\theta}\hat{u}\hat{h} + 2\left(1 - \delta^{4/5}\hat{\theta}\right)\hat{h}\frac{d\hat{x}_d}{d\hat{t}} + 2\delta^{4/5}\hat{x}_d\frac{d\hat{H}}{d\hat{t}}, \qquad \hat{x} = \hat{x}_d, \tag{4.36}$$

$$\frac{\partial}{\partial \hat{t}}\left(\hat{h}\hat{\theta}\right) + \frac{\hat{u}}{2}\frac{\partial}{\partial \hat{x}}\left(\hat{h}\hat{\theta}\right) = 0, \qquad \hat{x} < \hat{x}_d, \tag{4.37}$$

$$\hat{h} = \delta^{4/5}H + \frac{\hat{x}^2}{2}, \tag{4.38}$$

where

$$\hat{u} = -\hat{t} + O\left(\delta^{4/5}\right). \tag{4.39}$$

Now letting $\delta \to 0$, we integrate (4.33), subject to (4.34), to find

$$\tilde{p}_d = \frac{48q_d}{5\hat{x}^5} + \frac{8\hat{t}}{\hat{x}^3}. \tag{4.40}$$

The boundary condition (4.35) implies that

$$\frac{48q_d}{5\hat{x}_d^5} + \frac{8\hat{t}}{\hat{x}_d^3} = -\frac{1}{\Omega} \tag{4.41}$$

while (4.36) reduces to

$$q_d = \hat{x}_d^2\frac{d\hat{x}_d}{d\hat{t}}. \tag{4.42}$$

Therefore $\hat{x}_d$ satisfies the ODE

$$\frac{d\hat{x}_d}{d\hat{t}} + \frac{5}{48\Omega}\,\hat{x}_d^3 = -\frac{5\hat{t}}{6}, \tag{4.43}$$

while matching with the quasi-steady solution (4.29) requires that

$$\hat{x}_d \sim 2\Omega^{1/3}\left(-\hat{t}\right)^{1/3} \quad \text{as } \hat{t} \to -\infty. \tag{4.44}$$

We normalize the problem (4.43) via the scalings

$$\hat{t} = \left(\frac{12}{5}\right)^{3/5}\Omega^{1/5}T, \qquad\qquad \hat{x}_d\left(\hat{t}\right) = 2\left(\frac{12}{5}\right)^{1/5}\Omega^{2/5}X(T), \tag{4.45}$$

so that $X(T)$ satisfies

$$\frac{dX}{dT} + X^3 + T = 0. \tag{4.46}$$

We show the numerical solution to (4.46) in Figure 4.3. Balancing the second and third terms of (4.46) in the limit $T \to -\infty$, X matches to the quasi-steady solution

$$X(T) \sim (-T)^{1/3} \quad \text{as } T \to -\infty \tag{4.47}$$

which we also plot as a dashed line in Figure 4.3.

From the numerical solution, it is clear that X remains positive as T passes through zero, giving us a key result that the mushy region remains open after $u(t)$ has changed sign. However, $X(T) \to 0$ at a finite positive value of $T = T_f \approx 1.10$, which corresponds to

$$\hat{t}_* = \left(\frac{12}{5}\right)^{3/5} T_f\,\Omega^{1/5} \approx 1.85\,\Omega^{1/5}. \tag{4.48}$$

This provides a leading-order estimate of the closure time of the mushy region, namely

$$t_f \sim 1.8513\,\delta^{2/5}\,\Omega^{1/5}. \tag{4.49}$$

As $T \to T_f$, X becomes very small, and by balancing the first and last terms in (4.46)

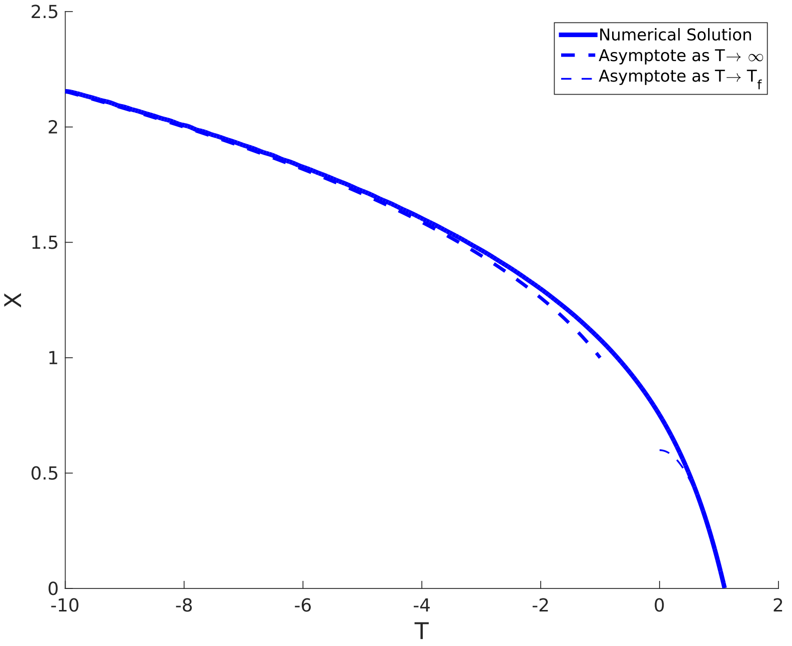

Figure 4.3: Solution $X(T)$ of the problem (4.46). The thick dashed curve shows the leading-order behaviour (4.47) as $T \to -\infty$; and the thin dashed curve shows (4.50), which is valid as $T \to T_f$.

together, we show X approaches the limit

$$X(T) \sim \frac{T_f^2 - T^2}{2} + O\left(T_f - T\right)^4 \quad \text{as} \quad T \to T_f, \tag{4.50}$$

shown as the thin dashed curve in Figure 4.3. In Figure 4.4 we compare the numerical solution for the time at which the mushy region closes, to the asymptote (4.49) with $\Omega = 1$. The smallest value of δ at which we ran the numerical solution is $\delta = 5 \times 10^{-4}$, as the problem becomes too stiff to compute below this value. We see in the inset in Figure 4.4 that the error between the numerical solution and the asymptotic limit decreases to zero as $\delta \to 0$; however, a significant discrepancy remains. We will derive a second-order correction to (4.49) in Section 4.6, where the motion of the upstream boundary will be taken into account also.

Next we solve (4.37) for the scaled liquid fraction $\hat{\theta}$, subject to

$$\hat{\theta} \sim \frac{-6\hat{t}}{\hat{x}^2} \quad \text{as } \hat{t} \to -\infty, \tag{4.51}$$

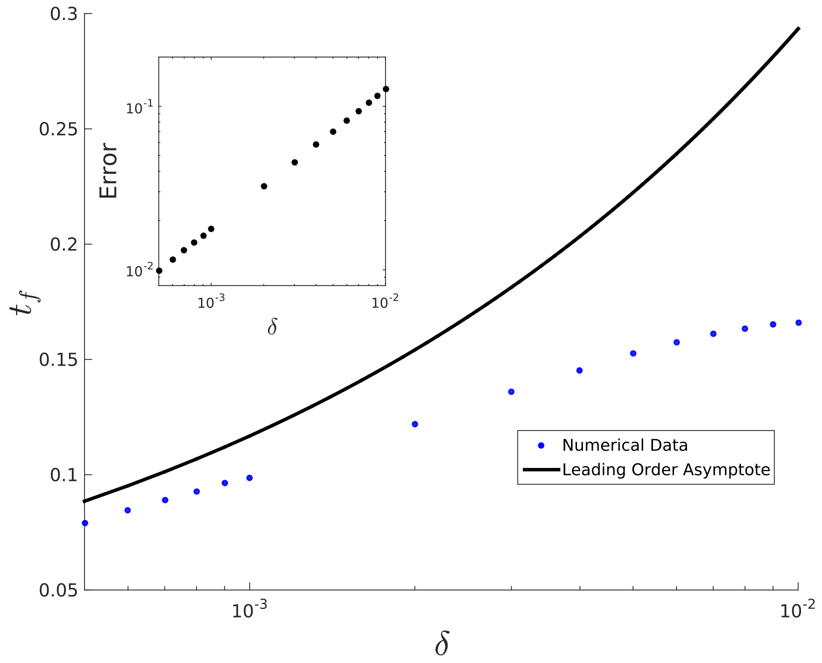

Figure 4.4: The time the mushy region closes, t_f plotted against δ, with $\Omega = 1$. The black curve shows the asymptote (4.49), and the blue dots show the time at which the the mushy region closes, as calculated from the numerical solution. The inset shows the error between the numerical solution and the asymptote reduces as $\delta \to 0$; we shall also provide a second order correction to (4.49) in Section 4.6.

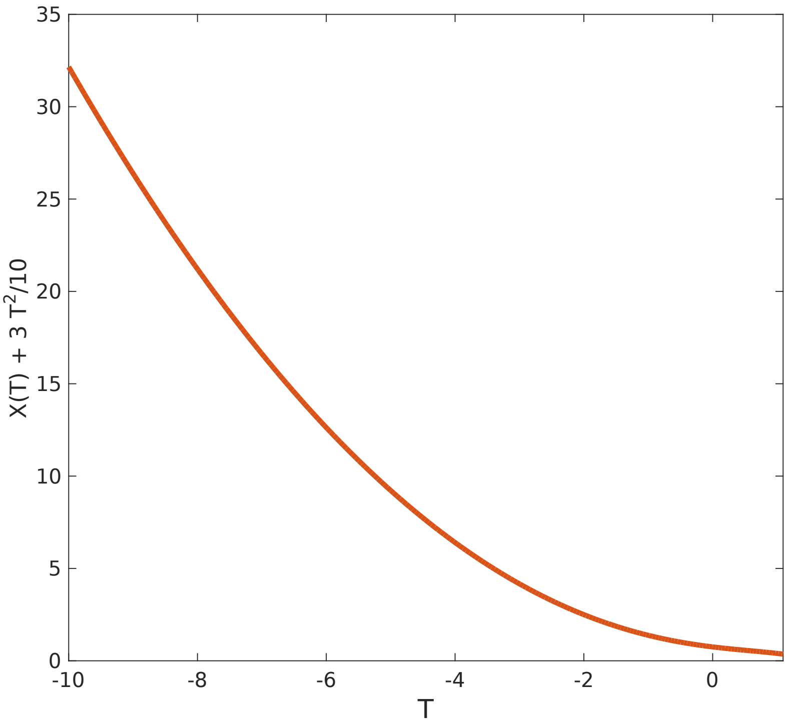

Figure 4.5: Plot of $X(T) + 3T^2/10$ against T, where $X(T)$ is the solution of the problem (4.46). The quantity remains positive for all $T < T_f = 1.10$.

which follows from matching with the quasi-steady solution (4.30). Using the transformation

$$\frac{d\hat{t}}{ds} = 1, \quad \frac{d\hat{x}}{ds} = -\frac{\hat{t}}{2}, \tag{4.52}$$

(4.37) becomes

$$\frac{d\left(\hat{\theta}\hat{h}\right)}{ds} = 0. \tag{4.53}$$

Integrating (4.52) and (4.53) we find

$$\hat{t} = s + c_1, \quad \hat{x} = -\frac{(s+c_1)^2}{4} + c_2, \quad \hat{\theta}\hat{h} = c_3, \tag{4.54}$$

where c_1, c_2, and c_3 are functions of integration. Solving for $c_2 = \hat{x} + \hat{t}^2/4$, $\hat{\theta}\hat{h}$ may be rewritten as

$$\hat{\theta}\hat{h} = f(\hat{x} + \hat{t}^2/4) = g(4\hat{x} + \hat{t}^2), \tag{4.55}$$

Matching (4.55) to (4.51), we find $g(z) = 3\sqrt{z}$, and therefore $\hat{\theta}\hat{h}$ has the form

$$\hat{\theta}\hat{h} = 6\sqrt{\hat{t}^2 + 4\hat{x}}, \quad \hat{\theta} = \frac{6\sqrt{\hat{t}^2 + 4\hat{x}}}{\hat{x}^2}, \tag{4.56}$$

which is valid provided

$$\hat{x}_d + \frac{\hat{t}^2}{4} > 0, \tag{4.57}$$

which corresponds to the characteristics of the PDE (4.37) all emanating from the upstream boundary. Condition (4.57) is equivalent to the inequality

$$X(T) + \frac{3}{10}T^2 > 0. \tag{4.58}$$

In Figure 4.5 we demonstrate that (4.58) is indeed satisfied by the numerical solution $X(T)$, and thus justify *a posteriori* the assumptions that led to the problem (4.43).

4.4 Unsteady Upstream Region

We now consider the movement of the upstream boundary, x_u, as the speed of the bottom surface approaches zero. From the quasi-steady solution of Section 4.2.1, we expect the characteristics will still travel out from the upstream boundary. However, when condition (4.7a) is removed, the characteristics travel into the upstream boundary. At this time, the upstream boundary is unsteady and the derivative $x_u'(t)$ must be solved for using (4.3); we discuss this in Section 4.4.2.

4.4.1 Outward-Travelling Characteristics

In this section we make three assumptions: first, the force balance in the film is dominated by the small, localised, region near the origin, and thus we assume, $|x| \lesssim H^{1/2}$; second, we assume the solution becomes unsteady as $t \approx \pi^-$, and so look locally near $\pi - t$; and finally, the time-derivatives dH/dt and dx_u/dt are now of leading order, and hence $H \sim x_u \sim \pi - t$. Balancing the terms in (4.1a): uh, q_u and xdH/dt with each other, suggest the rescaling

$$t = \pi - \delta^{2/3}\bar{t}, \qquad u = \delta^{2/3}\bar{u}, \qquad x = \delta^{1/3}\bar{x}, \tag{4.59a}$$

$$h = \delta^{2/3}\bar{h}, \qquad H = \delta^{2/3}\bar{H}, \qquad p_u = \delta^{-1/3}\bar{p}_u, \qquad q_u = \delta^{4/3}\bar{q}_u. \tag{4.59b}$$

The governing equations in the upstream region then become

$$\frac{\partial \bar{p}_u}{\partial \bar{x}} = \frac{6}{\bar{h}^3}\left[\bar{u}\bar{h} - \bar{q}_u + 2\bar{x}\frac{d\bar{H}}{d\bar{t}}\right], \qquad \bar{x} < \bar{x}_u \tag{4.60}$$

$$\bar{p}_u \to 0, \qquad \bar{x} \to -\infty, \tag{4.61}$$

$$\bar{p}_u = -\frac{\delta^{4/3}}{\Omega}, \qquad \bar{x} = \bar{x}_u, \tag{4.62}$$

$$\bar{q}_u = \theta\bar{u}\bar{h} + 2(1-\theta)\bar{h}\frac{d\bar{x}_u}{d\bar{t}} + 2\bar{x}_u\frac{d\bar{H}}{d\bar{t}}, \qquad \bar{x} = \bar{x}_u, \tag{4.63}$$

$$\frac{\partial}{\partial \bar{t}}\left(\bar{h}\theta\right) + \frac{\bar{u}}{2}\frac{\partial}{\partial \bar{x}}\left(\bar{h}\theta\right) = 0, \qquad \bar{x} > \bar{x}_u, \tag{4.64}$$

where

$$\bar{h} = \frac{\bar{x}^2}{2} + \bar{H}, \text{ and } \bar{u} = -\bar{t} + O\left(\delta^{4/3}\right) \tag{4.65}$$

and $-\infty < \bar{t}$.

We recall that in the quasi-steady regime characteristics always enter the mushy region from the upstream boundary, so that condition (4.7a) holds: $\theta = 1$, at $x = x_u$. We suppose that this continues to be the case, initially at least, and thus (4.63) reduces to

$$\bar{q}_u = \bar{u}\left(\bar{H} + \frac{1}{2}\bar{x}_u^2\right) + 2\bar{x}_u\frac{d\bar{H}}{d\bar{t}}, \qquad \text{so long as } -\frac{\bar{t}}{2} > \frac{d\bar{x}_u}{d\bar{t}}. \tag{4.66}$$

We will determine when this inequality no longer holds, and hence when (4.7a) no longer holds. Substituting (4.66) into (4.60), we find

$$\left.\frac{\partial \bar{p}_u}{\partial \bar{x}}\right|_{\bar{x}=\bar{x}_u} = 0, \qquad\qquad \text{so long as } -\frac{\bar{t}}{2} > \frac{d\bar{x}_u}{d\bar{t}}. \tag{4.67}$$

Several simplifications occur in the limit $\delta \to 0$. The cavitation pressure term in the boundary condition (4.62) becomes negligible, and we can use (4.65) to simplify $\bar{u}$. Finally, we note from the scalings (4.32) that the contribution to the net normal force from the downstream region is of $O(\delta^{4/5})$ and thus the upstream region continues to dominate the net force balance. We again have that:

$$\int_{-\infty}^{x_u(t)} x\frac{\partial p_u}{\partial x}\,dx = -1. \tag{4.68}$$

We need to solve (4.60) with boundary conditions (4.61), (4.62) and (4.67) and (4.68). To do this we first integrate (4.60) subject to the far-field condition (4.61) to find

$$p_u = -\frac{24\frac{d\bar{H}}{dt}\bar{H} + 6\bar{q}_u\bar{x})}{\bar{H}\left(2\bar{H}+\bar{x}^2\right)^2} - \frac{3\bar{x}(4\bar{H}\bar{t}+3\bar{q}_u)}{4\bar{H}^2\left(2\bar{H}+\bar{x}^2\right)} - \frac{3(4\bar{H}\bar{t}+3\bar{q}_u)}{4\sqrt{2\bar{H}^5}}\left(2\tan^{-1}\left(\frac{\bar{x}}{\sqrt{2\bar{H}}}\right)+\pi\right). \tag{4.69}$$

The force balance (4.68) yeilds

$$\frac{3}{\sqrt{2\bar{H}^3}}\frac{d\bar{H}}{dt}\left(2\tan^{-1}\left(\frac{\bar{x}_u}{\sqrt{2\bar{H}}}\right)+\pi\right) + \frac{12(\bar{q}_u - 2\frac{d\bar{H}}{dt}\bar{x}_u)}{\left(2\bar{H}+\bar{x}_u^2\right)^2} + \frac{6(\frac{d\bar{H}}{dt}\bar{x}_u + 2\bar{H}\bar{t})}{\bar{H}\left(2\bar{H}+\bar{x}_u^2\right)} = -1, \tag{4.70}$$

which is an equation relating $\bar{x}_u$ and $\bar{H}$. To find a second such equation we apply the condition (4.62), $p_u = 0$. Using the substitutions

$$X = \frac{\bar{x}_u}{\sqrt{2\bar{H}}}, \qquad\qquad Y = \frac{\bar{H}}{3\bar{u}}, \qquad\qquad Z = \frac{1}{(3\bar{u})^{3/2}}\frac{d\bar{H}}{d\bar{t}}, \tag{4.71}$$

the two equations may be written

$$\frac{3Z\left(2\tan^{-1}(X)+\pi\right)}{\sqrt{2Y^3}} - \frac{6XZ+\sqrt{2Y}}{\left(X^2+1\right)\sqrt{2Y^3}} = -1, \tag{4.72}$$

and

$$-\frac{\left(\pi+2\tan^{-1}(X)\right)\left(\left(3X^2-1\right)\sqrt{2Y}+36XZ\right)}{8\sqrt{-3t}Y^2}-\frac{\left(3X^3+X\right)\sqrt{2Y}+12\left(3X^2+2\right)Z}{4\sqrt{-3t}\left(X^2+1\right)Y^2}=0. \tag{4.73}$$

We may solve these equations giving Y and Z as functions of X:

$$Y(X)=\frac{1}{18X^2\left(1+X^2\right)}\left[-\frac{4}{E_1(X)}+4\left(1+3X^2\right)+\left(3X^2-1\right)E_1(X)\right], \tag{4.74}$$

$$Z(X)=\frac{12}{E_1(X)^{3/2}}\sqrt{\frac{E_2(X)^2+4}{3X^2-1}}\left[\left(1+X^2\right)E_2(X)+2X\left(2+3X^2\right)\right], \tag{4.75}$$

where

$$E_1(X)=2+3X^2+3X\left(1+X^2\right)\left[\frac{\pi}{2}+\tan^{-1}X\right], \tag{4.76}$$

$$E_2(X)=-3X+\left(3X^2-1\right)\left[\frac{\pi}{2}+\tan^{-1}X\right]. \tag{4.77}$$

Using the chain rule, we take the derivative of (4.74), and equating that to the derivative of Y, given by (4.71), we find

$$\frac{dY}{d\bar{t}}=\frac{dX}{d\bar{t}}\frac{dY}{dX}=-\frac{Y}{\bar{t}}+\sqrt{-3\bar{t}}Z, \tag{4.78}$$

which may be viewed as an equation for $dX/d\bar{t}$. We therefore obtain an ODE for X as a function of $T=-\bar{t}$, namely

$$\frac{dX}{dT}+\frac{Y(X)}{TY'(X)}+\frac{\sqrt{3T}\,Z(X)}{Y'(X)}=0. \tag{4.79}$$

In the limit $T\to\infty$ ($\bar{t}\to-\infty$), we expect $X=x_u/\sqrt{2\bar{H}}$ to approach the quasi-steady solution given by (4.19). Using (4.71), the initial condition we use for the differential equation (4.79) is

$$X\to X_*=\frac{\beta}{\sqrt{1-\beta^2}} \qquad \text{as } T\to\infty, \tag{4.80}$$

with β as in equation (4.20).

The numerical solution of the problem (4.79) is plotted in Figure 4.6, along with the asymptotic behaviour (4.80). In the inset, we show $X(T)T$ as $T\to 0$ and conclude in this

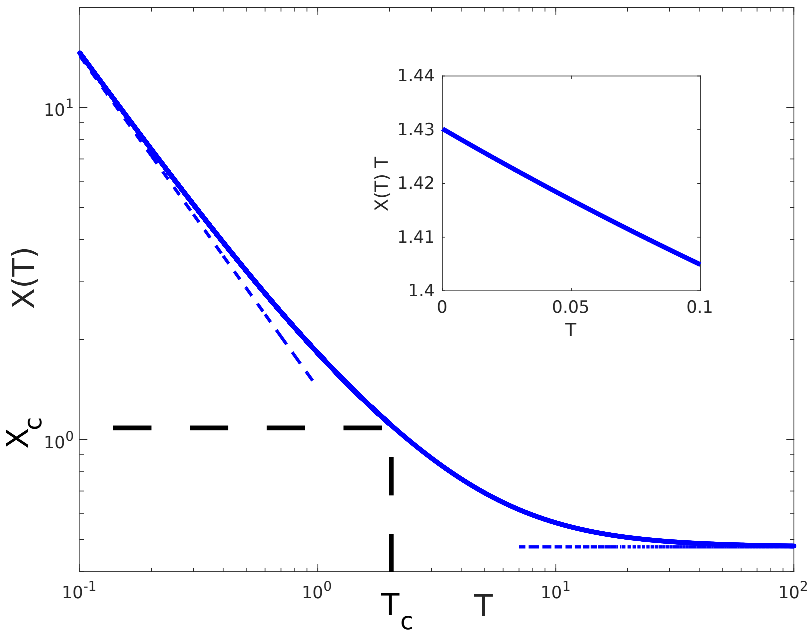

Figure 4.6: Numerical solution of the problem (4.79) for $X(T)$. The thin, blue, dashed curves show (4.80) as $T \to \infty$ and (4.81) as $T \to 0$. The thick, black, dashed lines indicate $X = X_c \approx 1.0928$ at $T = T_c \approx 2.0695$, which is the time when the characteristics are tangent to the upstream boundary. The inset shows $X(T)T$ against T as $T \to 0$, and extrapolating this to the y-axis we find $X(T)T \to 1.43$.

limit X approaches the asymptote

$$X(T) \sim \frac{C}{T} \quad \text{as } T \to 0. \tag{4.81}$$

Extrapolating $X(T)T$ to $T = 0$, we calculate $X(T)T \to C \approx 1.43$.

We recall that the problem (4.79) for $X(T)$ was derived by applying the boundary condition (4.67), and we must check whether the corresponding condition $d\bar{x}_u/dT > -T/2$ is satisfied. In terms of $X(T)$, this condition reads

$$R(T) = \frac{1}{\sqrt{3}\,T^{3/2}} + \left(\frac{1}{Y(X)} - \frac{XY'(X)}{2Y(X)^2}\right) Z(X) - \frac{Y'(X)}{6\sqrt{2}Y(X)^{3/2}} < 0. \tag{4.82}$$

We plot $R(T)$ versus T in Figure 4.7, where we see that the condition (4.82) is satisfied only for $T > T_c$, i.e. for $\bar{t} < -T_c$, where $T_c \approx 2.07$ is determined numerically. We label the time when the upstream boundary changes causality as $t = t_2 = -T_c\delta^{2/3}$: at this point condition (4.7a) is no longer satisfied and the upstream boundary is tangent to the characteristics. We display this physically in Figure 4.8, which shows numerical solutions to the mushy region model, (3.89)-(3.91), (3.100)-(3.103), and (3.126)-(3.129) with $\delta = 10^{-2}$ and $\Omega = 1$ (blue

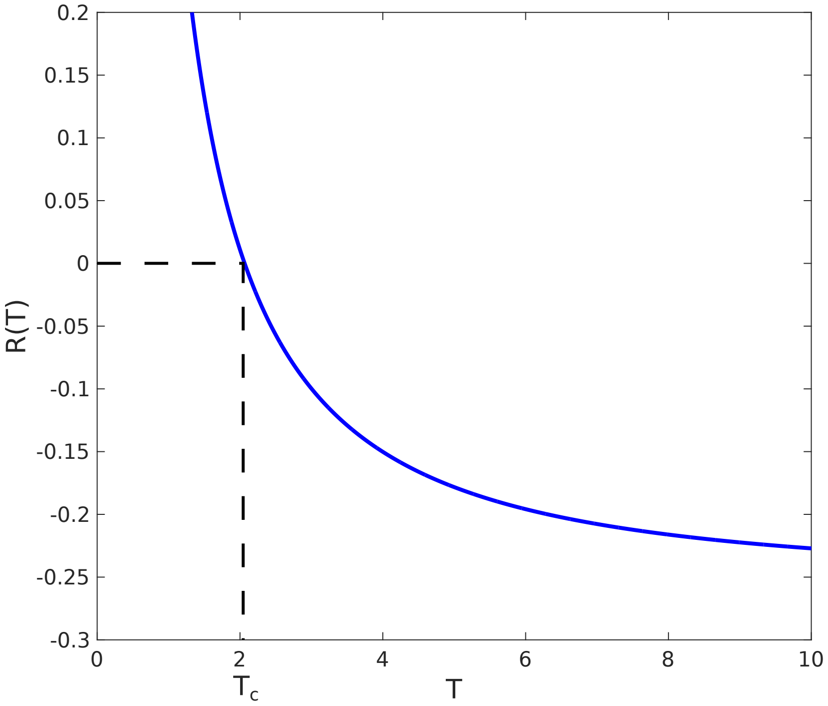

Figure 4.7: The function $R(T)$ defined by equation (4.82). The dashed lines show $R(T_c) = 0$, at which point the characteristics no longer travel outwards from the upstream boundary.

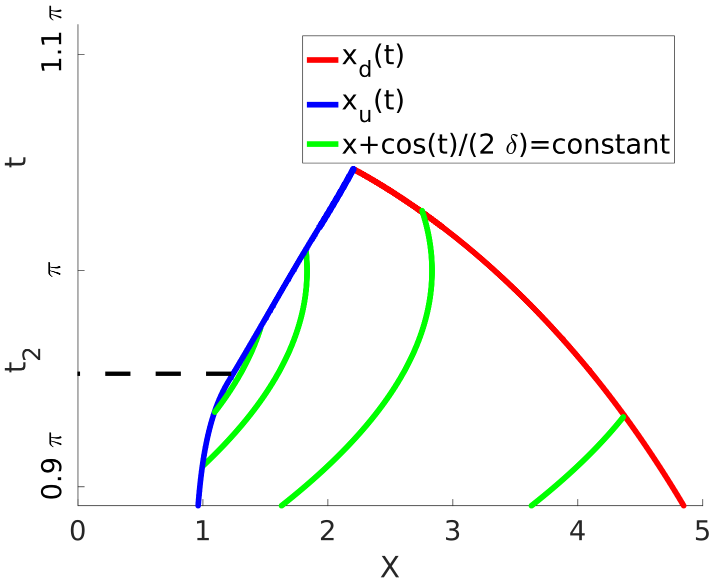

Figure 4.8: At time $t = t_2$, the upstream boundary is tangent to the characteristics. We show this physically with the numerical solutions to (3.89)-(3.91), (3.100)-(3.103), and (3.126)-(3.129) with parameters $\delta = 10^{-2}$ and $\Omega = 1$, as the red and blue curves. The green curves are the characteristics from equation (3.31).

and red curves), and the green lines are the characteristics from equation (3.31). We show the numerical solution, (evaluated with $\Omega = 1$), converges to the asymptotic expression $t_2 = -T_c\delta^{2/3}$ in Figure 4.9. The corresponding value $X(T_c) = X_c \approx 1.09$ is indicated by

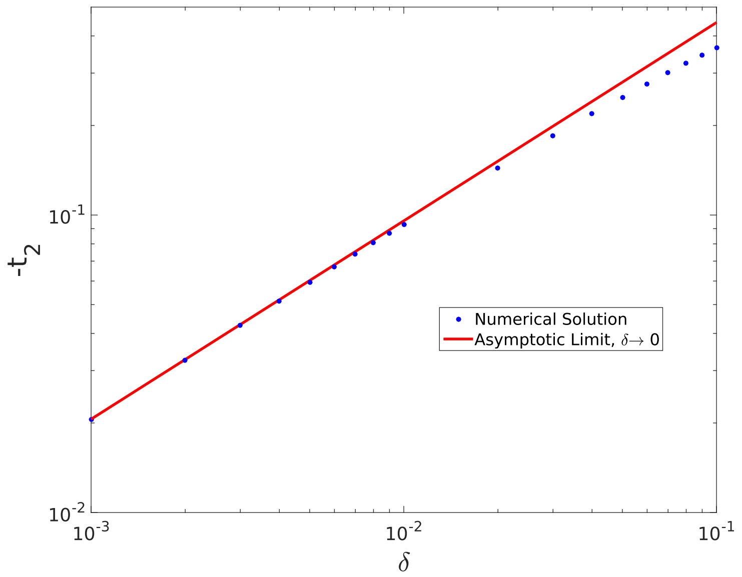

Figure 4.9: The time when the characteristics start to intersect the upstream boundary. The numerics are shown as the blue dots, (calculated with $\Omega = 1$), and the red curve is the asymptote, $-t_2 = T_c\delta^{2/3}$.

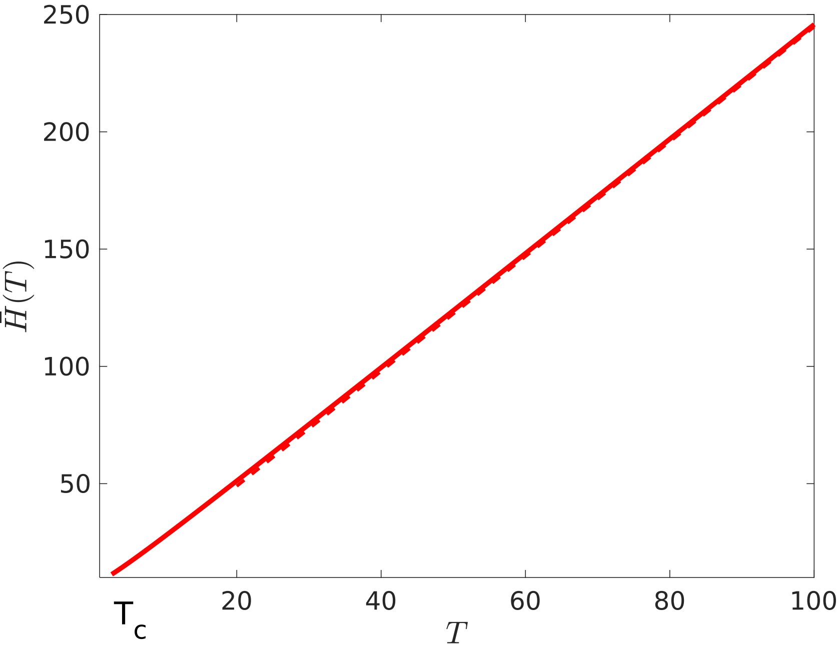

Figure 4.10: The scaled minimum thickness $\bar{H}(T)$ plotted versus $T = -\bar{t}$. The solid curve shows the numerical solution (4.79), and the dashed line shows the far-field behaviour (4.83).

the dotted lines in Figure 4.6. For $\bar{t} > -T_c$, the characteristics of the PDE (4.64) travel *into* the boundary $\bar{x} = \bar{x}_u$, and the solution procedure must be modified accordingly, as described below in Section 4.4.2.

For the moment, then, we consider only $T > T_c$. Given the solution for $X(T)$ plotted in Figure 4.6, we can obtain the corresponding behaviours of $\bar{H}$ and $\bar{x}_u$ from the definitions

(4.71), as plotted in Figures 4.10 and 4.11 respectively. These results are also compared to the far field behaviour

$$H(T) \sim 3\left(1-\beta^2\right)T, \quad \bar{x}_u(T) \sim \beta\sqrt{6T} \qquad \text{as } T \to \infty, \tag{4.83}$$

which confirms that these solutions match with the quasi-steady solution (4.19). For the moment, the solutions terminate at $T = T_c$, with $\bar{H} = \bar{H}_c \approx 11.3$ and $\bar{x}_u = \bar{x}_{uc} \approx 4.91$, found from the numerical solutions (see Figures 4.10 and 4.11). From Figure 4.11, we note in particular, that $\bar{x}_u(T)$ is a non-monotonic function, which achieves its minimum value $\bar{x}_{um} \approx 3.93$ at $T = T_m \approx 5.77$. Thus we expect the upstream boundary to move upstream until $t \sim \pi - T_m\delta^{2/3}$, with $x_u \sim \bar{x}_{um}\delta^{1/3}$, before turning around and briefly propagating downstream.

Still limiting our attention, for the moment, to values of $T > T_c$, we find the liquid fraction in the cavitated region by solving the PDE (4.64). Using the transformation

$$\frac{dT}{ds} = 1, \quad \frac{d\bar{x}}{ds} = \frac{T}{2}, \tag{4.84}$$

(4.64) becomes

$$\frac{d\left(\bar{\theta}\bar{h}\right)}{ds} = 0. \tag{4.85}$$

Integrating (4.52) and (4.53) we find

$$T = s + c_1, \quad \bar{x} = -\frac{\left(s+c_1\right)^2}{4} + c_2, \quad \bar{\theta}\bar{h} = c_3, \tag{4.86}$$

where c_1, c_2, and c_3 are functions of integration. Solving for $c_2 = \bar{x} + T^2/4$, $\bar{\theta}\bar{h}$ may be rewritten as

$$\bar{\theta}\bar{h} = F(\bar{x} + T^2/4), \tag{4.87}$$

where F is an arbitrary integration function. So long as characteristics propagate into the cavitated region from the upstream boundary, we may apply the condition (4.7a), (i.e. $\theta = 1$ at $\bar{x} = \bar{x}_u$) to get

$$F\left(\bar{x}_u + T^2/4\right) = \bar{H} + \bar{x}_u^2/2, \tag{4.88}$$

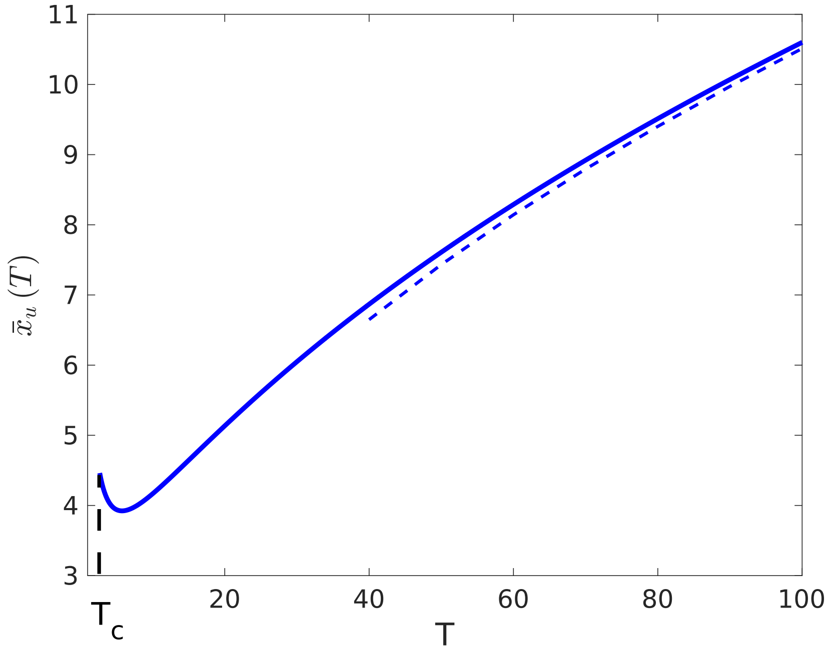

Figure 4.11: The scaled upstream free boundary $\bar{x}_u(T)$ plotted versus $T = -\bar{t}$. The dashed curve shows the far-field behaviour (4.83). The minimum $\bar{x}_u(T)$ is $\bar{x}_{um} \approx 3.93$, which is attained at $T = T_{xm} \approx 5.77$.

or, using the definitions (4.71),

$$F\left(\sqrt{6TY}\,X + T^2/4\right) = 3T\left(1 + X^2\right)Y. \tag{4.89}$$

Given the numerically determined function $X(T)$, plotted in Figure 4.6, and the definition (4.74) of $Y(X)$, equation (4.89) defines the function F parametrically. The resulting function is plotted in Figure 4.12 as a function of $\xi = \sqrt{6TY\left(X(T)\right)}\,X(T) + T^2/4$. From condition (4.66), we find (4.89) is valid only for $T > T_c$, it defines F only for values of its argument greater than

$$\xi_c = \sqrt{6T_cY(X_c)}\,X_c + \frac{T_c^2}{4} \approx 6.00, \quad F_c = F(\zeta_c) = 3T_c\left(1 + X_c^2\right)Y(X_c) \approx 22.3. \tag{4.90}$$

On the other hand, we know that $X \to X_*$ as $T \to \infty$, where X_* is given by (4.80), and from (4.71), the corresponding value of Y is $Y_* = Y(X_*) = 1 - \beta^2$. Hence (4.89) reduces to

$$F\left(T^2/4\right) \sim 3T \quad \text{as } T \to \infty, \tag{4.91}$$

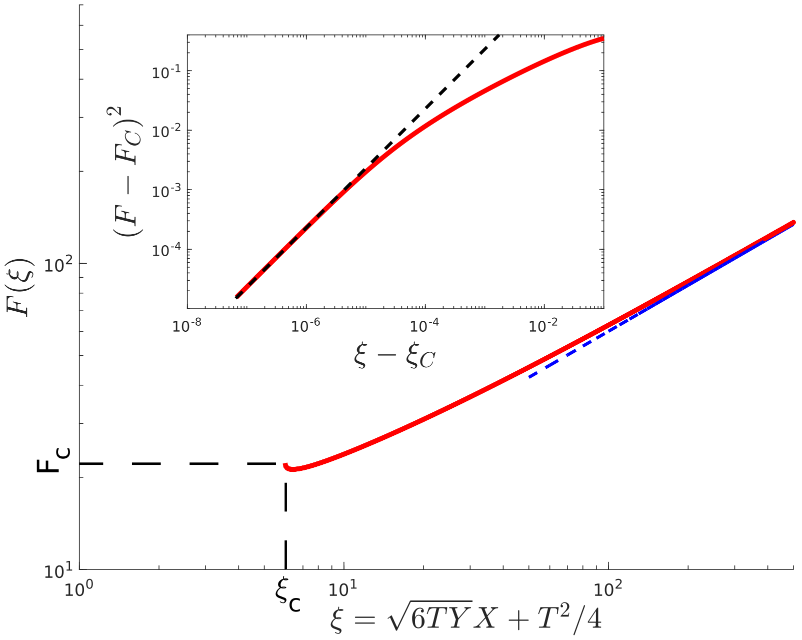

Figure 4.12: The function F defined by (4.89) against $\xi = \sqrt{6TY\big(X(T)\big)}\,X(T) + T^2/4$. The dashed line shows the far-field behaviour (4.92); the dashed line in the inset shows the behaviour (4.95) of $F(\xi)$ close to the critical value $\xi_c \approx 6.00$.

and the far-field behaviour of the function F is therefore given by

$$F(\xi) \sim 6\sqrt{\xi} \quad \text{as } \xi \to \infty, \tag{4.92}$$

as indicated by the dashed curve in Figure 4.12.

We also observe in Figure 4.12 the appearance of square-root behaviour in $F(\xi)$ at $\xi = \xi_c$, corresponding to the characteristics of the PDE (4.64) being tangential to the free boundary $\bar{x} = \bar{x}_u$ at $T = T_c$. To verify this local behaviour, we expand both sides of (4.89) about the critical time $T = T_c$:

$$\begin{aligned} \xi = \sqrt{6TY}\,X + \frac{T^2}{4} \sim \xi_c + \Bigg[& \sqrt{\frac{3T}{32Y}}X\left(2\frac{d^2Y}{dT^2} - \frac{1}{Y}\left(\frac{Y}{T} - \frac{dY}{dT}\right)^2\right) \\ & + \sqrt{\frac{3TY^3}{2}}\left(T\frac{d^2X}{dT} + \frac{dX}{dT}\left(\frac{T}{Y}\frac{dY}{dT} + 1\right)\right) + \frac{1}{4}\Bigg]_{T=T_c}(T-T_c)^2 + O(T-T_c)^3, \end{aligned} \tag{4.93}$$

$$\begin{aligned} F(\xi) \sim {} & 3T_c\left(1 + X_c^2\right)Y(X_c) \\ & + \left[3\left(2TX\frac{dX}{dT} + X^2 + 1\right)Y + 3T\left(X^2+1\right)\frac{dY}{dT}\right]_{T=T_c}(T-T_c) + O(T-T_c)^2. \end{aligned} \tag{4.94}$$

Hence

$$F(\xi) \sim F_c - \kappa\sqrt{\xi - \xi_c} \quad \text{as } \xi \to \xi_c, \tag{4.95}$$

where

$$\begin{aligned}\kappa = -2 \Bigg[& \left(3\left(2TX\frac{dX}{dT} + X^2 + 1\right)Y + 3T\left(X^2+1\right)\frac{dY}{dT}\right) \Bigg/ \\ & \left\{\sqrt{\frac{3T}{32Y}}X\left(2\frac{d^2Y}{dT^2} - \frac{1}{Y}\left(\frac{Y}{T} - \frac{dY}{dT}\right)^2\right)\right. \\ & \left. + \sqrt{\frac{3TY^3}{2}}\left(T\frac{d^2X}{dT} + \frac{dX}{dT}\left(\frac{T}{Y}\frac{dY}{dT} + 1\right)\right) + \frac{1}{4}\right\}^{1/2} \Bigg]_{T=T_c} \approx 15.2,\end{aligned} \tag{4.96}$$

and this local behaviour is indicated by the dashed line in the inset of Figure 4.12.

4.4.2 Inward-Travelling Characteristics

For values of $\bar{t} > -T_c$ (i.e. $T < T_c$), we still have to solve the problem (4.60)-(4.64), but we can no longer set $\theta = 1$ at the free boundary $\bar{x} = \bar{x}_u$. This is because the characteristics along which $\theta\left(\bar{H} + \bar{x}^2/2\right)$ are constant no longer travel out of the upstream boundary, but rather towards the boundary, as shown by the green lines in the schematic, Figure 4.8 at $t = t_2$. The volume fraction, θ, must therefore be determined by the solution (4.87) obtained from the characteristics that originated from x_u when $T > T_c$, the boundary condition (4.63) becomes

$$\bar{q}_u = \left(T + 2\frac{d\bar{x}_u}{dT}\right)F\left(\bar{x}_u + T^2/4\right) - 2\left(\bar{H} + \frac{1}{2}\bar{x}_u^2\right)\frac{d\bar{x}_u}{dT} - 2\bar{x}_u\frac{d\bar{H}}{dT} \quad \text{at } \bar{x} = \bar{x}_u, \tag{4.97}$$

where F is the function determined by (4.89) and plotted in Figure 4.12.

Again, the strategy is to integrate (4.60) subject to the far-field condition (4.61) and then apply the boundary conditions (4.62), (4.68) and (4.97). Using the substitution $X =$

$\bar{x}_u/(2\bar{H})^{1/2}$, (4.62), (4.68) and (4.97) now have the form

$$\begin{aligned}
\bar{q}_u &= F\left(X\sqrt{2\bar{H}}+\frac{T^2}{4}\right)\left(\frac{2}{\sqrt{2\bar{H}}}\left(\frac{d\bar{H}}{dT}X+2\bar{H}\frac{dX}{dT}\right)+T\right) \\
&\quad -\sqrt{2\bar{H}}\left(X^2+1\right)\left(\frac{d\bar{H}}{dT}X+2\bar{H}\frac{dX}{dT}\right)-2X\sqrt{2\bar{H}}\frac{d\bar{H}}{dT}, \qquad (4.98)\\
0 &= \frac{3\left(2\frac{d\bar{H}}{dT}\sqrt{2\bar{H}}-\bar{q}_u X\right)}{\sqrt{2\bar{H}^5}\left(X^2+1\right)^2}+\frac{3X(4\bar{H}T-3\bar{q}_u)}{2\sqrt{2\bar{H}^5}\left(X^2+1\right)}+\frac{3(4\bar{H}T-3\bar{q}_u)}{4\sqrt{2\bar{H}^5}}\left(2\tan^{-1}(X)+\pi\right),\\
&\qquad (4.99)\\
-1 &= -\frac{3\sqrt{2\bar{H}}\frac{d\bar{H}}{dT}\left(2X\left(X^2-1\right)\right)-6\bar{q}_u}{2\bar{H}^2\left(X^2+1\right)^2}-\frac{4T}{2\bar{H}\left(X^2+1\right)}-\frac{d\bar{H}}{dT}\frac{\left(\pi+2\tan^{-1}(X)\right)}{\sqrt{2\bar{H}^3}}. \qquad (4.100)
\end{aligned}$$

Using (4.99) and (4.100) to solve for the derivatives $d\bar{H}/dT$ and dX/dT, the problem may then be reduced to a coupled system of two ODEs, namely

$$\begin{aligned}
\frac{dX}{dT} = &\frac{\left(1+X^2\right)^2}{2\sqrt{2\bar{H}}\left[E_3(X)^2-4\left(3+4X^2\right)\right]\left[(1+X^2)\bar{H}-F\left(X\sqrt{2\bar{H}}+T^2/4\right)\right]}\times\\
&\left\{F\left(X\sqrt{2\bar{H}}+T^2/4\right)\left[\bar{H}X\left(E_3(X)+4X\right)\right.\right.\\
&\left.+9T\left(1+X^2\right)^2\left(\tan^{-1}X+\pi/2\right)^2-3T\left(4+3X^2\right)\right]\\
&+6T\left(1+X^2\right)\bar{H}\left[4+3X^2+\left(1+X^2\right)\left(\tan^{-1}X+\pi/2\right)\left(3X-2\tan^{-1}X-\pi\right)\right]\\
&\left.+\left(1+X^2\right)\bar{H}^2\left[5+X^2-3\left(1+X^2\right)\left(3+X^2\right)\left(1+X\tan^{-1}X+\pi X/2\right)\right]\right\}, \qquad (4.101)
\end{aligned}$$

$$\begin{aligned}
\frac{d\bar{H}}{dT} &= \\
&\sqrt{\frac{\bar{H}}{2}}\,\frac{\left(1+X^2\right)^2\left(E_3(X)+4X\right)-6T\left(1+X^2\right)^2\left[\left(1+3X^2\right)\left(\tan^{-1}X+\pi/2\right)+3X\right]}{E_3(X)^2-4\left(3+4X^2\right)},\\
&\qquad (4.102)
\end{aligned}$$

where

$$E_3(X)=X\left(1+3X^2\right)+3\left(1+X^2\right)^2\left(\frac{\pi}{2}+\tan^{-1}X\right). \qquad (4.103)$$

The numerator and denominator of the right-hand side of (4.101) are both equal to zero at $T=T_c$. Using (4.95) and L'Hôpital's rule, we expand (4.101) and (4.102) around $T=T_c$,

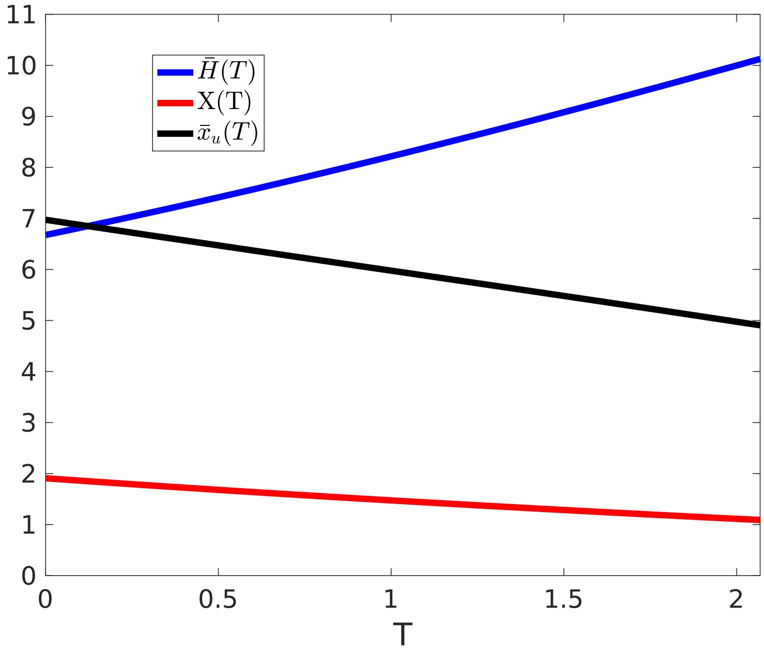

Figure 4.13: The solutions $X(T)$ and $\bar{H}(T)$ to the problem (4.101)-(4.102) with the initial value (4.107), and the position of the free boundary $\bar{x}_u = (2\bar{H})^{1/2}\, X$, with $\epsilon = 10^{-4}$.

leading to

$$\frac{dX}{dT} \to -\frac{1}{6}\sqrt{\frac{T_c}{6Y(X_c)}}\left(\frac{5+3X_c^2}{2} + \frac{1}{E_1(X_c)}\right) \approx -0.331, \tag{4.104}$$

$$\frac{d\bar{H}}{dT} \to \frac{1}{X_c}\sqrt{\frac{T_cY(X_c)}{6}}\left(\frac{3X_c^2-1}{2} + \frac{1}{E_1(X_c)}\right) \approx 1.88, \tag{4.105}$$

as $T \to T_c$, where $E_1(X)$ is still defined by (4.76). Using the definition of X (4.71), we calculate the derivative of $\bar{x}_u(T)$ as $T \to T_c$ to be

$$\frac{d\bar{x}_u}{dT} = \frac{X}{\sqrt{6T_cY(X_c)}}\frac{d\bar{H}}{dT} + \sqrt{6T_cY(X_c)}\frac{dX}{dT} \approx -1.13. \tag{4.106}$$

We can therefore solve the system (4.101)-(4.102) as an initial-value problem starting from $T = T_c - \epsilon$, using (4.71), where $0 < \epsilon \ll 1$, with

$$X\left(T_c - \epsilon\right) \sim X_c - \epsilon\frac{dX}{dT}(T_c), \qquad \bar{H}\left(T_c - \epsilon\right) \sim 3T_cY(X_c) - \epsilon\frac{d\bar{H}}{dT}(T_c). \tag{4.107}$$

In Figure 4.14 we show how $\bar{H}$ evaulated at $T = 0$ varies as ϵ is increased. Provided ϵ is sufficiently small ($\epsilon \lessapprox 10^{-4}$), the solution is insensitive to the value of ϵ chosen.

Numerical solutions to (4.101) and (4.102) for $X(T)$ and $\bar{H}(T)$ are plotted in Figure 4.13, along with the free boundary position $\bar{x}_u(T) = (2\bar{H}(T))^{1/2}\, X(T)$. The solutions are defined

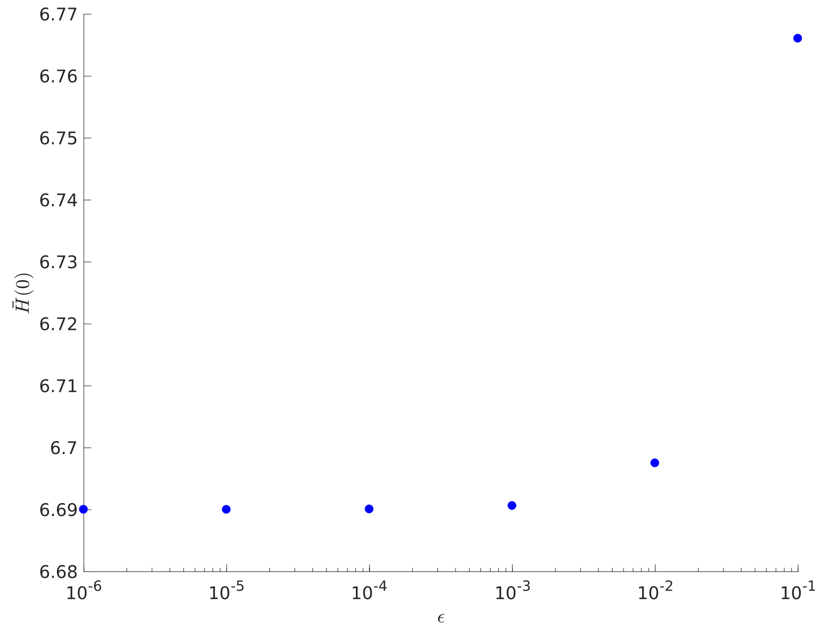

Figure 4.14: The film thickness, $\bar{H}$, evaluated at $T = 0$ varying with changes in ϵ. For $\epsilon \approx 10^{-4}$, no change in $\bar{H}(0)$ was observed, indicating the solution is insensitive for values of ϵ approximately less than this.

for $0 \leq T < T_c \approx 2.07$, and we read off from the numerical solution the values $X_0 = X(0) \approx 1.91$ and $\bar{H}_0 = \bar{H}(0) \approx 6.69$. When $T < 0$, corresponding to $t > 0$, the sign of the velocity u changes, and we expect a second mushy region to form in $x < 0$, as described in Section 4.5. The values X_0 and $\bar{H}_0$ will provide initial conditions for the subsequent problem where both mushy regions exist simultaneously.

4.5 Secondary Cavitation

We note from the full Reynolds equation (4.1a) and the parabolic approximation of $h(x,t)$, (4.2), that the far-field pressure takes the form

$$p_{u,d} \sim -\frac{8u}{x^3} \quad \text{as } |x| \to \infty \tag{4.108}$$

when $t > \pi$, (when $u < 0$). The pressure p_u in the upstream region must therefore be negative for sufficiently large negative values of x. From the numerical solutions discussed in Section 3.5, we know that for sufficiently small δ, the pressure in the film reduces below the dimensionless cavitation pressure $p = -\delta/\Omega$, forming a second cavitation mushy region somewhere in $x < 0$. To determine the time and location of formation of this second cavitation region, we make four additional assumptions: first, the location of formation is sufficiently far from the origin such that we make the approximation $h = O(x^2)$; second, by matching with the previous solution, the vertical velocity of the moving surface is constant and of order $dH/dt = O(1)$; thirdly, the movement of the upstream boundary is negligible; and lastly, the velocity of the bottom surface is sufficiently small such that $u \sim \pi - t$. With these assumptions, we balance the terms uh and xdH/dt in (4.1a) prompting the scalings:

$$t = \pi + \delta\acute{t}, \qquad u = \delta\acute{u}, \qquad p_u = \delta\acute{p}_u, \qquad x = O(1), \tag{4.109a}$$

where we retain the scalings from Section 4.4.1

$$H = \delta^{2/3}\bar{H}_0 + \delta\bar{H}_1, \qquad q_u = \delta^{4/3}\bar{q}_u, \tag{4.109b}$$

while

$$h = \delta^{2/3}\bar{H}_0 + \frac{x^2}{2} = O(1), \quad \acute{u} = -\acute{t} + O\left(\delta^2\right), \quad \text{and } \acute{t} > 0. \tag{4.110}$$

where $\bar{H}_0 = \bar{H}(0)$ and is given in 4.4.2. Referring back to the assumptions made above, we note that $\bar{H}$ varies over the longer time-scale $\bar{t} = \delta^{1/3}\acute{t}$.

Following these scalings, the Reynolds equation (4.1a) in the upstream region becomes

$$\frac{\partial \acute{p}_u}{\partial x} = \frac{6}{h^3}\left(-\acute{t}h - \delta^{1/3}q_u(t) + 2x\bar{H}_1\right). \tag{4.111}$$

To leading order as $\delta \to 0$, equation (4.111) therefore reduces to

$$\frac{\partial \acute{p}_u}{\partial x} = -\frac{24\acute{t}}{x^4} - \frac{96\bar{H}_{T0}}{x^5}, \tag{4.112}$$

which due to the substitution $T = -\bar{t}$ used in Section 4.4.1, $\bar{H}_{T0}$ was calculated from

$$\bar{H}_{T0} = -\bar{H}_1 = \left.\frac{d\bar{H}}{dT}\right|_{T=0} = \frac{\bar{H}_0^{3/2}}{\sqrt{2}}\,\frac{\left(1 + X_0^2\right)^2\left[E_3(X_0) + 4X_0\right]}{E_3(X_0)^2 - 4\left(3 + 4X_0^2\right)} \approx 1.41. \tag{4.113}$$

The solution of (4.112) subject to $\acute{p}_u \to 0$ as $x \to -\infty$ is

$$\acute{p}_u = \frac{8\acute{t}}{x^3} + \frac{24\bar{H}_{T0}}{x^4}. \tag{4.114}$$

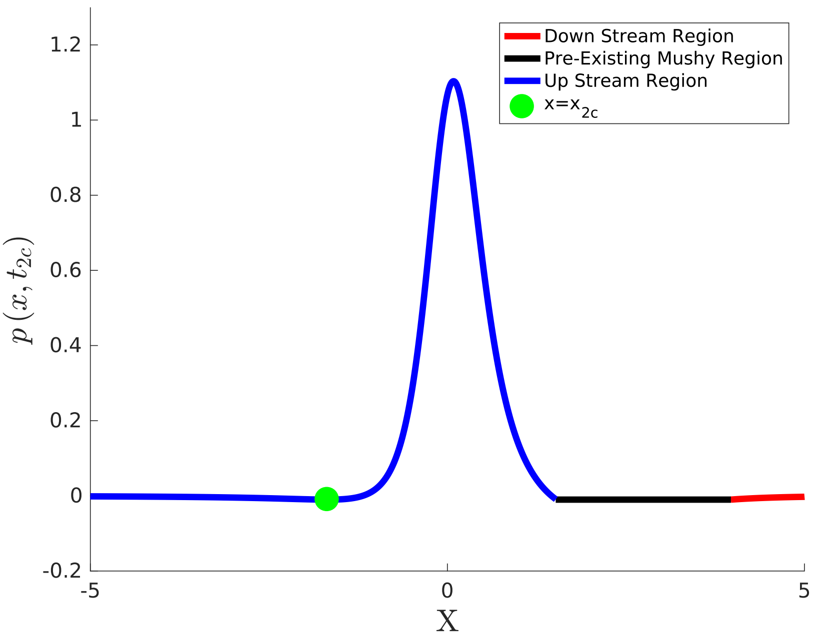

Figure 4.15: The pressure profile of liquid in the film when $t = \delta \acute{t}_{2c}$, the time when the pressure equals the cavitation pressure on the other side of the film and a second mushy region forms. The parameters used in the computation are $\delta = 10^{-2}$ and $\Omega = 1$. The position of the newly cavitated region is shown as the green dot.

The conditions for cavitation are

$$\acute{p}_u = -1/\Omega \quad \text{and} \quad \frac{\partial \acute{p}_u}{\partial x} = 0, \tag{4.115}$$

and using expressions (4.112) and (4.114) we find

$$x = x_{2c} = -\left(8\Omega \bar{H}_{T0}\right)^{1/4}. \tag{4.116}$$

Hence we expect the second mushy region to form at time

$$\acute{t} = \acute{t}_{2c} = \frac{2^{5/4} \bar{H}_{T0}^{3/4}}{\Omega^{1/4}}. \tag{4.117}$$

In Figure 4.15, we show the pressure profile of the liquid in the film at time $t = t_{2c}$, i.e., the time the second mushy region forms, using parameters $\delta = 10^{-2}$ and $\Omega = 1$. The blue and red curves show the pressure profiles in the liquid upstream and downstream of the pre-existing mushy region. The black line shows the pressure in this mushy region, and the green dot is the location at which the second mushy region forms, $x = x_{2c}$. In

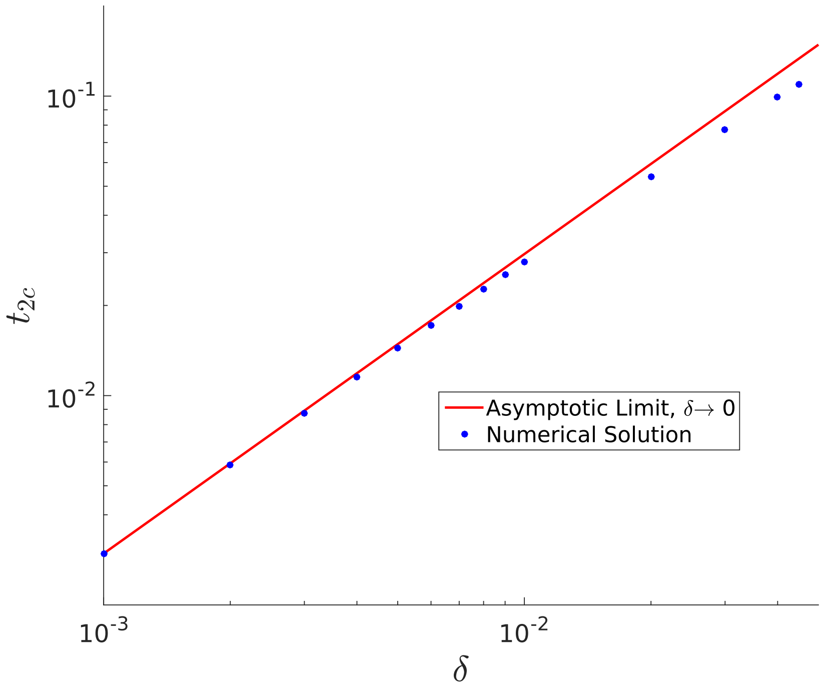

Figure 4.16: The time the second mushy region opens, t_{2c} plotted against δ, with $\Omega = 1$. The red line shows the asymptote $t_{2c} = \delta \acute{t}_{2c}$, with $\acute{t}_{2c}$ given by (4.117); the blue dots show the numerically determined time at which the mushy region forms.

Figure 4.16, we show the time at which the second mushy region forms, as determined from our numerical solutions as the dots. We see that as δ decreases, the results converge to the asymptotic solution, given by (4.117).

For $\acute{t} > \acute{t}_{2c}$ (corresponding to $t \gtrsim \acute{t}_{2c}\delta$), we have to consider two cavitated regions existing simultaneously, and modify our notation accordingly. We now suppose that we have a second mushy region occupying the interval $-\infty < x_{2u} < x < x_{2d} < 0$, with another mushy region occupying the interval $0 < x_{1u} < x < x_{1d} < \infty$. A new subscript "M" is introduced for the "middle" fluid region that separates them. Thus the pressure is denoted by p_u in the upstream region $x < x_{2u}$, by p_M in the middle region $x_{2d} < x < x_{1u}$, and by p_d in the downstream region $x > x_{1d}$. A schematic of this model was shown in Figure 3.18.

The numerical solutions suggest that when the second mushy region forms, the free boundaries $x = x_{2u}$ and $x = x_{2d}$ both expand rapidly away from $x = x_{2c}$,

$$\frac{dx_{2u}}{d\acute{t}} < -\frac{\acute{t}}{2} < \frac{dx_{2d}}{d\acute{t}} \tag{4.118}$$

provided δ is sufficiently small. Hence, initially at least, we impose the boundary condition $\theta = 1$ at both free boundaries. Physically, the speed at which the boundaries move away from each other immediately after the formation of the second mushy region is so fast that the liquid on the boundary cannot move away but is instead drawn through the boundary and into the mushy region. Since that $\theta = 1$ on both boundaries, we conclude

$$\left.\frac{\partial \acute{p}_u}{\partial x}\right|_{x=x_{2u}} = \left.\frac{\partial \acute{p}_M}{\partial x}\right|_{x=x_{2d}} = 0 \quad \text{as long as} \quad \frac{dx_{2u}}{d\acute{t}} < -\frac{\delta\acute{t}}{2} < \frac{dx_{2d}}{d\acute{t}}. \tag{4.119}$$

The leading-order problem for the pressure in the middle region reads

$$\frac{\partial \acute{p}_M}{\partial x} = -\frac{24\acute{t}}{x^4} - \frac{96\bar{H}_{T0}}{x^5}, \qquad x > x_{2d}, \tag{4.120}$$

$$\acute{p}_M = -\frac{1}{\Omega}, \quad \frac{\partial \acute{p}_M}{\partial x} = 0, \qquad x = x_{2d}, \tag{4.121}$$

Following the assumption that the location where the second mushy region forms is sufficiently far from the origin, $x_{2c} = O(1)$, we assume the movement of x_{1u} has a negligible effect on the evolution of x_{2d}, at least initially. The leading-order position of the downstream boundary of the second mushy region is given by

$$x_{2d} = -\frac{4\bar{H}_{T0}}{\acute{t}} \qquad \text{for} \quad \acute{t} > \acute{t}_{2c}. \tag{4.122}$$

Reassuringly this result is consistent with $x_{2d} = x_2$ when $\acute{t} = \acute{t}_{2c}$.

Since the upstream fluid region is now completely separate from the middle region there is no need for the scaling of the flux term q_u to agree with (4.59). A balance in equation (4.111) suggests the scaling

$$\bar{q}_u = \delta^{-1/3}\acute{q}_u, \quad \text{i.e.} \quad q_u = \delta\acute{q}_u, \tag{4.123}$$

and the leading-order problem for the pressure in the upstream region is then

$$\frac{\partial \acute{p}_u}{\partial x} = -\frac{24\acute{t}}{x^4} - \frac{96\bar{H}_{T0}}{x^5} - \frac{48\acute{q}_u}{x^6}, \qquad x < x_{2u}, \tag{4.124}$$

$$\acute{p}_u \to 0, \qquad x \to -\infty, \tag{4.125}$$

$$\acute{p}_u = -\frac{1}{\Omega}, \quad \frac{\partial \acute{p}_u}{\partial x} = 0, \qquad x = x_{2u}. \tag{4.126}$$

The solution of (4.124)-(4.126) yields an algebraic equation for the position x_{2u} of the upstream boundary of the second mushy region, namely

$$x_{2u} + \frac{5\,x_{2u}^4}{16\Omega\acute{t}} = \frac{3\bar{H}_{T0}}{2\acute{t}} \qquad \text{for} \quad \acute{t} > \acute{t}_{2c}. \tag{4.127}$$

We normalize equation (4.127) via the rescaling

$$x_{2u} = -\left(\frac{16\Omega\acute{t}}{5}\right)^{1/3} \xi, \tag{4.128}$$

so that ξ satisfies

$$\xi - \xi^4 = \left(\frac{5}{2\Omega}\right)^{1/3} \frac{3\bar{H}_{T0}}{4\acute{t}^{4/3}}. \tag{4.129}$$

The right-hand side of equation (4.129) takes the value $3 \cdot 5^{1/3}/16$ when secondary cavitation first occurs at $\acute{t} = \acute{t}_{2c}$, using the definition in (4.117). This gives a value of $\xi = 5^{1/3}/2$, corresponding to $x = x_{2c}$. Subsequently, the right-hand side of equation (4.129) decreases as a function of $\acute{t}$, and therefore ξ increases, with $\xi \to 1$ and

$$x_{2u} \sim -\left(\frac{16\Omega\acute{t}}{5}\right)^{1/3} \qquad \text{as } \acute{t} \to \infty. \tag{4.130}$$

Conservation of liquid mass in the mushy region reads

$$\frac{\partial}{\partial\acute{t}}(h\theta) + \delta\,\frac{\acute{u}}{2}\frac{\partial}{\partial x}(h\theta) = 0. \tag{4.131}$$

Given that $\theta = 1$ at the two boundaries $x = x_{2u}$, $x = x_{2d}$, we confirm our assumption made ealier that $\theta \equiv 1$ to leading order in this region.

According to equation (4.122), the downstream boundary x_{2d} approaches $x = 0$ as $\acute{t}$ increases. Eventually, x_{2d} becomes of the same order as x_{1u}, so that the downstream boundary of the second mushy region starts to interact with the upstream boundary of the first mushy region. We analyse this interaction next.

4.6 Interaction Between The Mushy Regions

Using the scalings from Section 4.4, we see the two mushy regions start to interact when $t = O\left(\delta^{2/3}\right)$, so we return to the scalings from:

$$t = \pi + \delta^{2/3}\bar{t}, \qquad u = \delta^{2/3}\bar{u}, \qquad x = \delta^{1/3}\bar{x}, \qquad h = \delta^{2/3}\bar{h}, \tag{4.132a}$$

$$H = \delta^{2/3}\bar{H}, \qquad p_M = \delta^{-1/3}\bar{p}_M, \qquad q_M = \delta^{4/3}\bar{q}_M. \tag{4.132b}$$

The leading-order governing equations in the middle region then read

$$\frac{\partial \bar{p}_M}{\partial \bar{x}} = \frac{6}{\bar{h}^3}\left[\bar{u}\bar{h} - \bar{q}_M + 2\bar{x}\frac{d\bar{H}}{d\bar{t}}\right], \qquad \bar{x}_{2d} < \bar{x} < \bar{x}_{1u} \tag{4.133}$$

$$\bar{p}_M = \frac{\partial \bar{p}_M}{\partial \bar{x}} = 0, \qquad \bar{x} = \bar{x}_{2d}, \tag{4.134}$$

$$\bar{p}_M = 0, \qquad \bar{x} = \bar{x}_{1u}, \tag{4.135}$$

$$\bar{q}_M = \theta\bar{u}\bar{h} + 2\left(1-\theta\right)\bar{h}\frac{d\bar{x}_{1u}}{d\bar{t}} + 2\bar{x}_{1u}\frac{d\bar{H}}{d\bar{t}}, \qquad \bar{x} = \bar{x}_{1u}, \tag{4.136}$$

$$\frac{\partial}{\partial \bar{t}}\left(\bar{h}\theta\right) + \frac{\bar{u}}{2}\frac{\partial}{\partial \bar{x}}\left(\bar{h}\theta\right) = 0, \qquad \bar{x} > \bar{x}_{1u}, \tag{4.137}$$

$$\bar{h} = \bar{H} + \frac{\bar{x}^2}{2} \quad \text{and} \quad \bar{u} = -\bar{t} + O\left(\delta^{4/3}\right), \tag{4.138}$$

where $0 < \bar{t} < \infty$.

We note from the scalings in Section 4.3 that the middle region still dominates the normal force balance, which implies that

$$-\int_{x_{2d}}^{x_{1u}} x\frac{\partial p_M}{\partial x}dx = 1, \tag{4.139}$$

to leading order. We have assumed that, initially at least, characteristics continue to travel into the first mushy region through $\bar{x} = \bar{x}_{1u}$ and out of the second mushy region through $\bar{x} = \bar{x}_{2d}$. Since the characteristics of the PDE (4.137) emanate from $\bar{x} > \bar{x}_{1u}$, the relevant solution is still given by equation (4.87). Therefore, the boundary condition (4.136) may be rewritten as

$$\bar{q}_M = -\left(\bar{t} + 2\frac{d\bar{x}_{1u}}{d\bar{t}}\right)F\left(\bar{x}_{1u} + \frac{\bar{t}^2}{4}\right) + 2\bar{h}\frac{d\bar{x}_{1u}}{d\bar{t}} + 2\bar{x}_{1u}\frac{d\bar{H}}{d\bar{t}} \quad \text{at } \bar{x} = \bar{x}_{1u}, \tag{4.140}$$

where F is the function defined in equation (4.89) and plotted in Figure 4.12. By integrating the Reynolds equation (4.133) and applying the pressure condition (4.135), $p_M = 0$ at

$x = x_{2d}$, the pressure in the region $\bar{x}_{2d} < \bar{x} < \bar{x}_{1u}$ is given by the expression

$$p_M = -\frac{48\frac{d\bar{H}}{d\bar{t}}\bar{H}^2 + 3\bar{x}\left(8\bar{H}^2\bar{t} + 10\bar{H}\bar{q}_M\right) + 3\bar{x}^3(4\bar{H}\bar{t} + 3\bar{q}_M)}{2\bar{H}^2\left(2\bar{H} + \bar{x}^2\right)^2} + \frac{12H(4\frac{d\bar{H}}{d\bar{t}}\bar{H} + \bar{q}_M\bar{x}_{2d})}{2\bar{H}^2\left(2\bar{H} + \bar{x}_{2d}^2\right)^2}$$
$$+ \frac{3\bar{x}_{2d}(3\bar{q}_M + 4\bar{H}\bar{t})}{2\bar{H}^2\left(2\bar{H} + \bar{x}_{2d}^2\right)} - \frac{(4\bar{H}\bar{t} + 3\bar{q}_M)\left(\tan^{-1}\left(\frac{\bar{x}}{\sqrt{2\bar{H}}}\right) - \tan^{-1}\left(\frac{\bar{x}_{2d}}{\sqrt{2\bar{H}}}\right)\right)}{2\sqrt{2\bar{H}^5}}. \quad (4.141)$$

Using the second boundary condition at x_{2d}, (4.134), the boundary condition at x_{1u} (4.135), and the force balance equation (4.139), we obtain three equations relating the unknowns $\bar{x}_{2d}$, $\bar{x}_{1u}$ and $\bar{H}$. Using the substitutions

$$X_1 = \frac{\bar{x}_{1u}}{\sqrt{2\bar{H}}}, \qquad X_2 = \frac{\bar{x}_{2d}}{\sqrt{2\bar{H}}}, \qquad Y = \frac{\bar{H}}{3\bar{t}}, \quad (4.142)$$

we may then write Y as a function of X_1 and X_2, namely

$$Y = \frac{1}{18\left(1 + X_1^2\right)^2 X_2^2\left(1 + X_2^2\right)}\left\{\frac{4\left(X_1 - X_2\right)^2\left(2 + X_1^2 + 2X_1X_2 + 3X_2^2\right)}{E_4(X_1, X_2)}\right.$$
$$\left. + 4\left(X_1 - X_2\right)^2\left(2 + X_1(X_1 + 2X_2)(1 + 3X_2^2)\right) - \left(3X_2^2 - 1\right)E_4(X_1, X_2)\right\}, \quad (4.143)$$

where

$$E_4(X_1, X_2) = 3\left(1 + X_1^2\right)^2 X_2\left(1 + X_2^2\right)\left(\tan^{-1} X_1 - \tan^{-1} X_2\right)$$
$$- (X_1 - X_2)\left[2X_1(2 + X_1^2) - X_2(1 + X_1^2) + X_1X_2^2(5 + 3X_1^2)\right], \quad (4.144)$$

while the time derivatives of $\bar{H}$ and $\bar{x}_{1u}$ are given by

$$\frac{d\bar{H}}{d\bar{t}} = \sqrt{\frac{3\bar{t}^3Y}{2}}\left[(X_1^2 - X_2^2)^2 - (1 + X_1^2)(1 + X_2^2)\right] \times$$
$$\left[\left(1 + X_1^2\right)^2\left(1 + X_2^2\right)\left(\tan^{-1} X_1 - \tan^{-1} X_2\right)\right.$$
$$\left. - (X_1 - X_2)\left(1 - X_1^2 + X_1X_2 + X_1^3X_2 + 2X_2^2\right)\right]^{-1}, \quad (4.145)$$

$$\frac{d\bar{x}_{1u}}{d\bar{t}} = \frac{(X_1 - X_2)\sqrt{6\bar{t}Y}\,\frac{d\bar{H}}{d\bar{t}} - \frac{\bar{t}}{2}\left[F\left(\sqrt{6\bar{t}Y}\,X_1 + \bar{t}^2/4\right) - 3\left(1 + X_2^2\right)\bar{t}Y\right]}{F\left(\sqrt{6\bar{t}Y}\,X_1 + \bar{t}^2/4\right) - 3\left(1 + X_1^2\right)\bar{t}Y}. \quad (4.146)$$

We can then form a system of nonlinear ODEs for $X_1\left(\bar{t}\right)$ and $X_2\left(\bar{t}\right)$ written below

$$\frac{dX_1}{d\bar{t}} = \frac{1}{\sqrt{6\bar{t}Y}}\frac{d\bar{x}_{1u}}{d\bar{t}} - \frac{X_1}{6\bar{t}Y}\frac{d\bar{H}}{d\bar{t}}, \tag{4.147}$$

$$\frac{dX_2}{d\bar{t}} = \frac{1}{\partial Y/\partial X_2}\left[\frac{1}{3\bar{t}}\frac{d\bar{H}}{d\bar{t}} - \frac{Y}{\bar{t}} - \frac{\partial Y}{\partial X_1}\frac{dX_1}{d\bar{t}}\right]. \tag{4.148}$$

To find the initial behaviour of the system of equations (4.147) and (4.148), we assume that X_1 matches to X as $\bar{t} \to 0$, letting

$$X_1 \to X_0 \approx 1.91 \quad \text{as } \bar{t} \to 0. \tag{4.149}$$

(The value of X_0 was found numerically in Section 4.4.2.) We also expect $X_2\sqrt{2\bar{H}}$ to match to the solution (4.122), and so use the anastz

$$X_2 \sim -\frac{A}{\bar{t}} - O(1) \quad \text{as } \bar{t} \to 0. \tag{4.150}$$

Making these substitutions and expanding (4.143) in the limit $\bar{t} \to 0$, we find

$$Y \sim -\frac{3A}{2\bar{t}}\left(\frac{E_3(X_0)^2 - 4\left(3 + 4X_0^2\right)}{\left(1 + X_0^2\right)^2\left(E_3(X_0) + 4X_0\right)}\right) + O(1) \text{ as } \bar{t} \to 0, \tag{4.151}$$

where $E_3(X_0)$ is defined in (4.103). Matching (4.151) to (4.142) we find that

$$A = \frac{2\bar{H}_0\left(E_3(X_0) + 4X_0\right)\left(1 + X_0^2\right)^2}{E_3(X_0)^2 - 4\left(3 + 4X_0^2\right)}, \tag{4.152}$$

where $\bar{H}_0 = \bar{H}(T_0) \approx 6.69$ was also found numerically in Section 4.4.2. Taking the limit of (4.145) and (4.147) as $\bar{t} \to 0$, and using conditions (4.149) and (4.150), we find the derivatives $d\bar{H}/d\bar{t}$ and $d\bar{x}_{1u}/d\bar{t}$ are continuous with (4.101) and (4.102) across $\bar{t} = 0$ and also match with the inner solution (4.122), i.e.

$$\bar{x}_{2d} \sim -\frac{4\bar{H}_{T0}}{\bar{t}} \quad \text{as } \bar{t} \to 0. \tag{4.153}$$

The numerical solutions of the system (4.147)-(4.148), subject to the initial behaviour (4.149) and (4.150), are plotted in Figure 4.17. The small-$\bar{t}$ asymptotic behaviour (4.149) and (4.150) are shown using dashed lines, as is the large-$\bar{t}$ behaviour, which will be analysed now.

As $\bar{t} \to \infty$, we observe from Figure 4.17 that X_2 approaches a constant value and

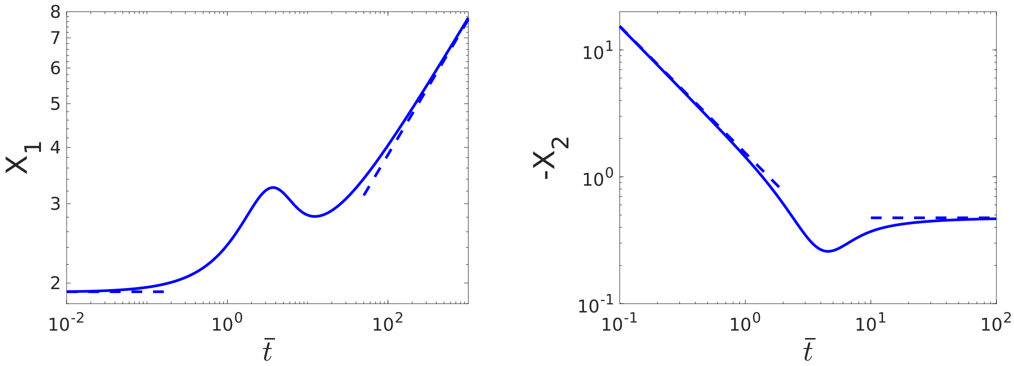

Figure 4.17: The numerically determined evolution of $X_1(\bar{t})$ and $-X_2(\bar{t})$ (obtained by solving the system (4.147)-(4.148) subject to the initial condition (4.149) and (4.150). The dashed lines show the small-$\bar{t}$ behaviour (4.149) and (4.150) and the large-$\bar{t}$ asymptotic behaviour (4.160) and (4.155).

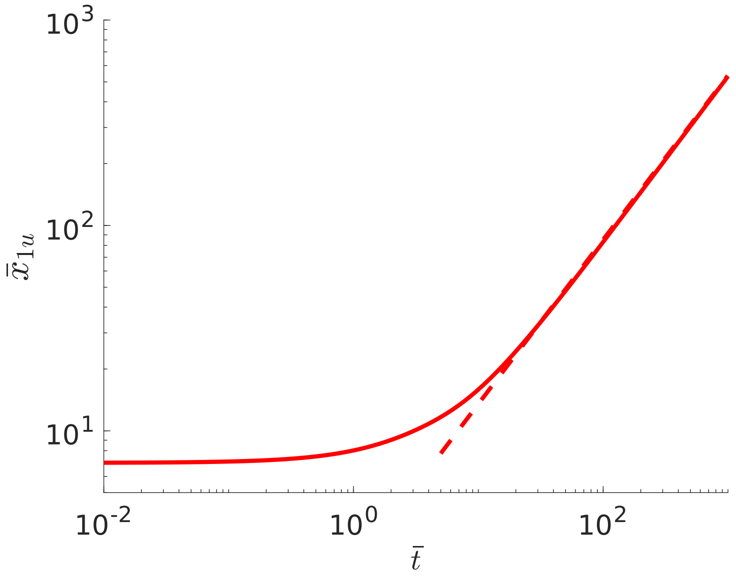

Figure 4.18: The normalized position $\bar{x}_{1u}$ of the upstream boundary of the first mushy region, plotted versus normalized time $\bar{t}$. The dashed line shows the large-$\bar{t}$ behaviour, (4.161).

$X_1 \to \infty$. Taking the limit of (4.148) as $\bar{t}$ and $X_1 \to \infty$, we find

$$\frac{dX_2}{d\bar{t}} = -\frac{4X_2 + 6X_2\left(X_2^2+1\right)}{\left(X_2^2+1\right)} - \left(3X_2^2-1\right)\left(\pi - 2\tan^{-1}(X_2)\right) + O\left(\bar{t}^{-1}, X_1^{-2}\right) \text{ as } \bar{t}, X_1 \to \infty. \tag{4.154}$$

We note that $X_2(\bar{t}) = -\beta/\sqrt{1-\beta^2} < 0$, satisfies (4.154) at leading order, since β satifies

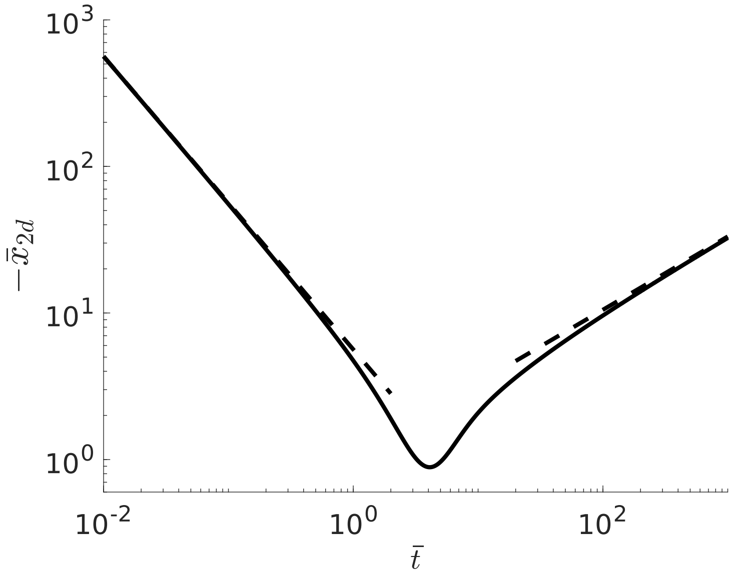

Figure 4.19: The normalized position $-\bar{x}_{2d}$ of the downstream boundary of the second mushy region, plotted versus normalized time $\bar{t}$. The dashed lines show the small-t behaviour (4.153) and the large-$\bar{t}$ behaviour (4.161).

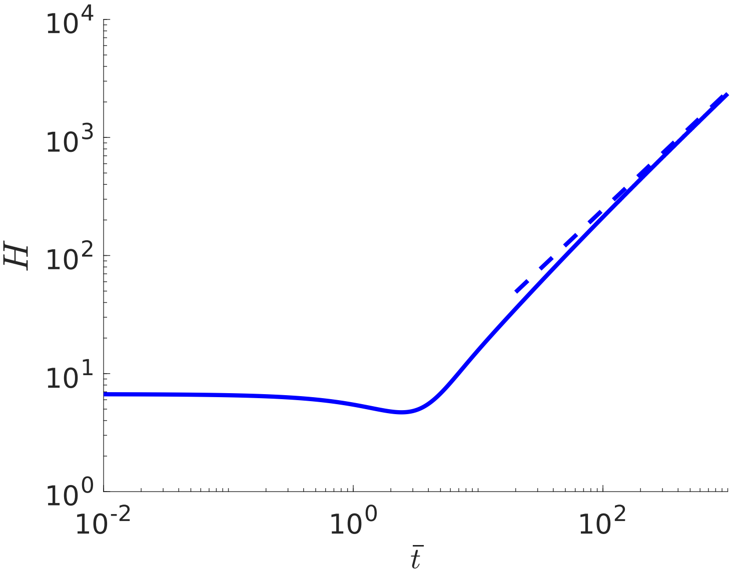

Figure 4.20: The normalized film thickness $\bar{H}$ versus normalized time $\bar{t}$ as determined numerically. The dashed line shows the large-$\bar{t}$ behaviour (4.161). The minimum film thickness is $\bar{H}_m \approx 4.698$ and is attained at $\bar{t} = \bar{t}_{Hm} \approx 2.435$.

(4.20). We conclude that X_2 approaches the quasi-steady limit

$$X_2(\bar{t}) \to -X_* = -\frac{\beta}{\sqrt{1-\beta^2}} \approx -0.475 \text{ as } \bar{t} \to \infty, \tag{4.155}$$

where X_* and β are the previously encountered quantities, defined in (4.80) and (4.20), respectively. To study this behaviour further, we consider the expression for Y (4.143),

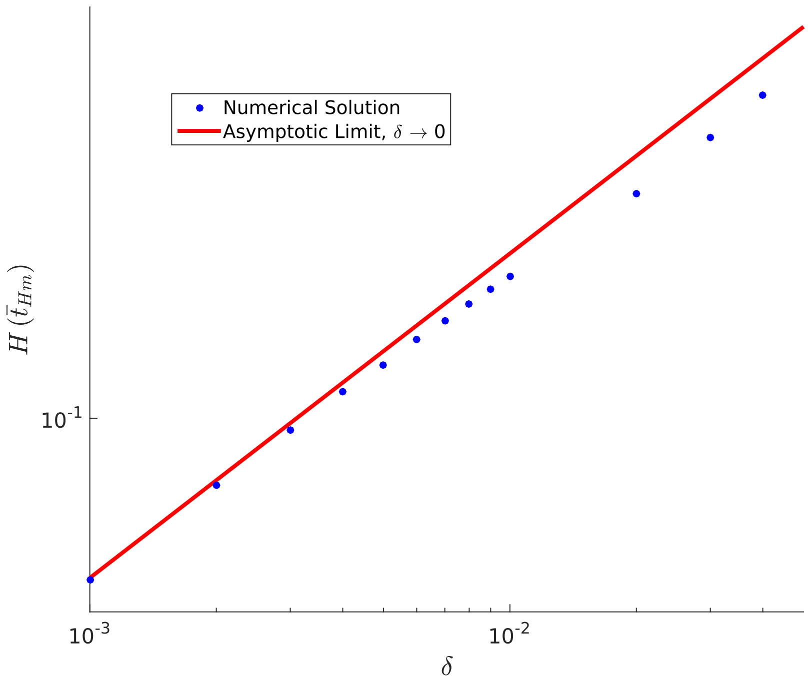

Figure 4.21: The minimum film thickness computed in the numerical solution, (blue dots), recovers the asymptotic result $H \sim \bar{H}_m \delta^{2/3}$ (red line), as $\delta \to 0$. Here, $\Omega = 1$.

which as $t \to \infty$ we expect Y to approach the quasi-steady limit $Y \to 1 - \beta^2$, using (4.19). We substitute the expansion for X_2,

$$X_2 \sim -X_* + \frac{C_1}{X_1} + \frac{C_2}{X_1^2} + \frac{C_3}{X_1^3} + \frac{C_4}{X_1^4} + \frac{C_5}{X_1^5} \cdots \quad \text{as } X_1 \to \infty \tag{4.156}$$

into (4.143) and equate the leading order terms to derive the expressions for the coefficients

$$C_1 = C_2 = C_4 = 0, \tag{4.157}$$

$$C_3 = \frac{\left(1 + X_*^2\right)\left(1 - 3X_*^2\right)}{6X_*^2}, \tag{4.158}$$

$$C_5 = \frac{8\left(1 + X_*^2\right)^2\left(1 + 3X_*^2\right)\left(1 - 3X_*^2\right)}{5\left(5 - X_*^2 + 15X_*^4 + 5X_*^6\right)}. \tag{4.159}$$

By substituting the expansion (4.156) into (4.147)-(4.148), we find that

$$X_1\left(\bar{t}\right) \sim \left(\frac{25}{96}\right)^{1/10} \frac{\bar{t}^{\,3/10}}{\sqrt{1 - \beta^2}} \quad \text{as } \bar{t} \to \infty. \tag{4.160}$$

The dashed lines in Figure 4.17 show how the asymptotic behaviours (4.155) and (4.160) are approached at large values of $\bar{t}$.

Having solved for X_1 and X_2, we recover the physically relevant quantities $\bar{x}_{1u}$, $\bar{x}_{2d}$ and

$\bar{H}$ by using equations (4.142) and (4.143) and plot the results in Figures 4.18–4.20, along with the asymptotic behaviours corresponding to (4.155) and (4.160), namely

$$\bar{x}_{1u}(\bar{t}) \sim 45^{1/5}\,\bar{t}^{4/5}, \quad \bar{x}_{2d}(\bar{t}) \sim -\beta\sqrt{6\bar{t}}, \quad H(\bar{t}) \sim 3\left(1-\beta^2\right)\bar{t} \qquad \text{as } \bar{t} \to \infty. \tag{4.161}$$

In Figure 4.18, we show that $\bar{x}_{1u}$ increases monotonically as a function of $\bar{t}$. However, we see in Figure 4.19 that the maximum value of $\bar{x}_{2d}$, (the minimum of $-\bar{x}_{2d}$), occurs at $\bar{t} = \bar{t}_{xm} \approx 4.09$, before decreasing again. Thus the downstream boundary of the second mushy region turns around and starts to retract at $t \sim \pi + \bar{t}_{xm}\delta^{2/3}$, and its closest distance of approach to the origin is $|x| \sim \bar{x}_{2dm}\delta^{1/3}$. Similarly, in Figure 4.20 we see that the normalized film thickness $\bar{H}$ reaches a minimum value $\bar{H}_m \approx 4.698$ at $\bar{t}_{Hm} \approx 2.435$. In Figure 4.21 we show using blue dots the minimum film thickness obtained from the numerical solution of the full problem (3.89)-(3.91), (3.100)-(3.103), and (3.126)-(3.129). Also shown is the asymptotic expression $H \sim \bar{H}_m\delta^{2/3}$ which agrees well with the numerics as $\delta \to 0$.

4.6.1 Time When First Mushy Region Closes

In Section 4.3 we derived (4.49) for the time at which the first mushy region closes. This analysis was based on the assumption that the upstream boundary x_u is small compared to x_d. However, a significant discrepancy remains between the asymptotic limit (4.49) and the numerical solution over the range of δ (see Figure 4.4). We now provide a second order correction to (4.49) by equating the asymptotic limit for x_d as $T \to T_f$, (4.50), (the right hand side of equation (4.162)), to the asymptotic limit for x_u as $\bar{t} \to \infty$, (4.161), (the left hand side of equation (4.162)),

$$\frac{45^{1/5}t^{4/5}}{\delta^{1/5}} = \frac{5}{12\delta}\left(\Omega^{2/5}\delta^{4/5}\left(\frac{12}{5}\right)^{6/5} T_f^2 - t^2\right) \tag{4.162}$$

where $T_f \approx 1.10$ from Section 4.3. We find as $\delta \to 0$, t_f has the form

$$t_f \sim \left(\frac{12}{5}\right)^{3/5} T_f\Omega^{1/5}\delta^{2/5} - B\delta^{18/25} + O(\delta), \tag{4.163}$$

$$B = \frac{2^{19/25}3^{32/25}}{5^{17/25}\Omega^{1/25}T_f^{1/5}} \approx \frac{2.2715}{\Omega^{1/25}}. \tag{4.164}$$

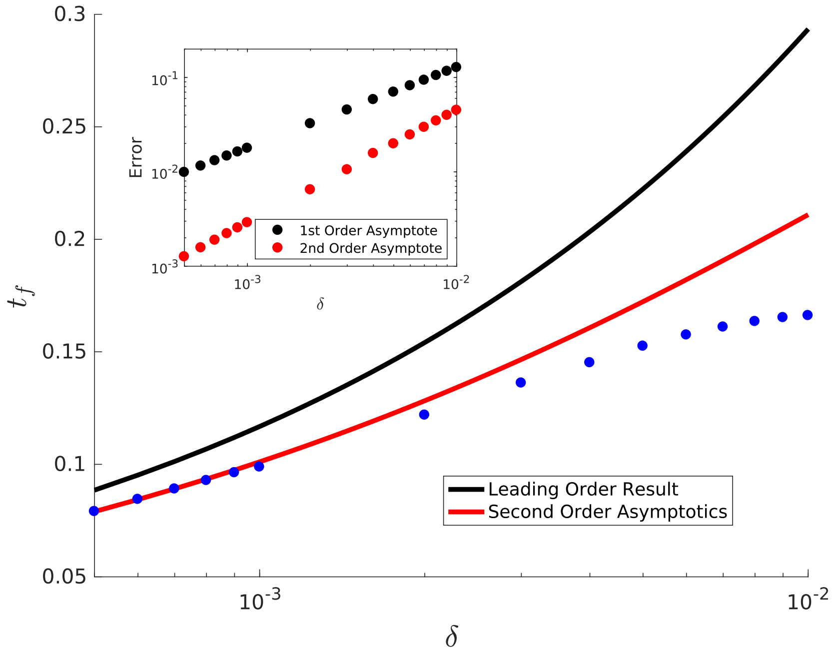

Figure 4.22: The time at which the mushy region closes, t_f, plotted against δ, with $\Omega = 1$. Main Figure: the numerically determined value for t_f are shown (dots) together with the leading order asymptotic result (4.49) (black curve). The second order asymptotic result (4.163), (red curve), agrees much better with the numerical results. The inset shows the error between the numerical solution and the two asymptotic results (4.49) (black dots), and (4.163) (red dots).

We compare the asymptotic result (4.163) with the numerically determined values of t_f in Figure 4.22. Here, Ω is kept constant at $\Omega = 1$. The smallest value of δ for which the numerical results for t_f are computed is $\delta = 5 \times 10^{-4}$, since the problem becomes too stiff below this value. We see much better agreement when we include the next term in the asymptotic solution. The inset in Figure 4.22 shows the error between the numerical solution and the two asymptotic results (4.49) and (4.163); as expected the error in (4.163) is smaller and occurs an order lower in δ.

4.7 Change in Causality for the Upstream Boundary of the Mushy Region

The large-$\bar{t}$ behaviours of $\bar{x}_{2d}$ and $\bar{H}$ given in equation (4.161) match directly with the quasi-steady solution (4.19), indicating that the downstream boundary of the second mushy region becomes quasi-steady for values of $t - \pi \gtrsim \delta^{2/3}$. However, the far-field solution (4.130) for x_{2u} is not consistent with the outer quasi-steady solution (4.29). The explanation for this is that the solution obtained in Section 4.5 used the boundary condition $\theta = 1$ at $x = x_{2u}$.

However, the boundary condition should change when characteristics start propagating out of the boundary at $x = x_{2u}$ (as they must eventually, for consistency with the quasi-steady solution). To analyse this change in behaviour we perform rescalings analogous to (4.32), that is we let

$$t = \pi + \delta^{2/5}\hat{t}, \qquad u = \delta^{2/5}\hat{u}, \qquad x = \delta^{-1/5}\hat{x}, \tag{4.165a}$$

$$h = \delta^{-2/5}\hat{h}, \qquad H = \delta^{2/5}\hat{H}, \qquad p_u = \delta\tilde{p}_u, \qquad q_u = O(1). \tag{4.165b}$$

We assume for the moment that $\theta = O(1)$ so that the resulting problem for the upstream region is

$$\frac{\partial \tilde{p}_u}{\partial \hat{x}} = \frac{6}{\hat{h}^3}\left[\hat{u}\hat{h} - q_u + 2\delta^{4/5}\hat{x}\frac{d\hat{H}}{d\hat{t}}\right], \qquad \hat{x} < \hat{x}_{2u}, \tag{4.166}$$

$$\tilde{p}_u \to 0, \qquad \hat{x} \to -\infty, \tag{4.167}$$

$$\tilde{p}_u = -\frac{1}{\Omega}, \qquad \hat{x} = \hat{x}_{2u}, \tag{4.168}$$

$$q_u = \theta\hat{u}\hat{h} + 2(1-\theta)\hat{h}\frac{d\hat{x}_{2u}}{d\hat{t}} + 2\delta^{4/5}\hat{x}_{2u}\frac{d\hat{H}}{d\hat{t}}, \qquad \hat{x} = \hat{x}_{2u}, \tag{4.169}$$

$$\frac{\partial}{\partial \hat{t}}\left(\hat{h}\theta\right) + \frac{\hat{u}}{2}\frac{\partial}{\partial \hat{x}}\left(\hat{h}\theta\right) = 0, \qquad \hat{x} > \hat{x}_{2u}, \tag{4.170}$$

$$\hat{h} = \delta^{4/5}H + \frac{\hat{x}^2}{2}, \tag{4.171}$$

where

$$\hat{u} = -\hat{t} + O\left(\delta^{4/5}\right). \tag{4.172}$$

We impose the additional condition

$$\theta = 1 \text{ at } \hat{x} = \hat{x}_{2u} \quad \text{so long as} \quad -\frac{\hat{t}}{2} > \frac{d\hat{x}_{2u}}{d\hat{t}}. \tag{4.173}$$

Integrating (4.166) subject to (4.167), and apply (4.173), the pressure may be written as

$$\tilde{p}_u = -\frac{8\hat{t}\left(3\hat{x}_{2u}^2 - 5\hat{x}^2\right)}{5\hat{x}^5}. \tag{4.174}$$

Using condition (4.168), we see that

$$\hat{x}_{2u}\left(\hat{t}\right) = -\left(\frac{16\Omega\hat{t}}{5}\right)^{1/3}, \tag{4.175}$$

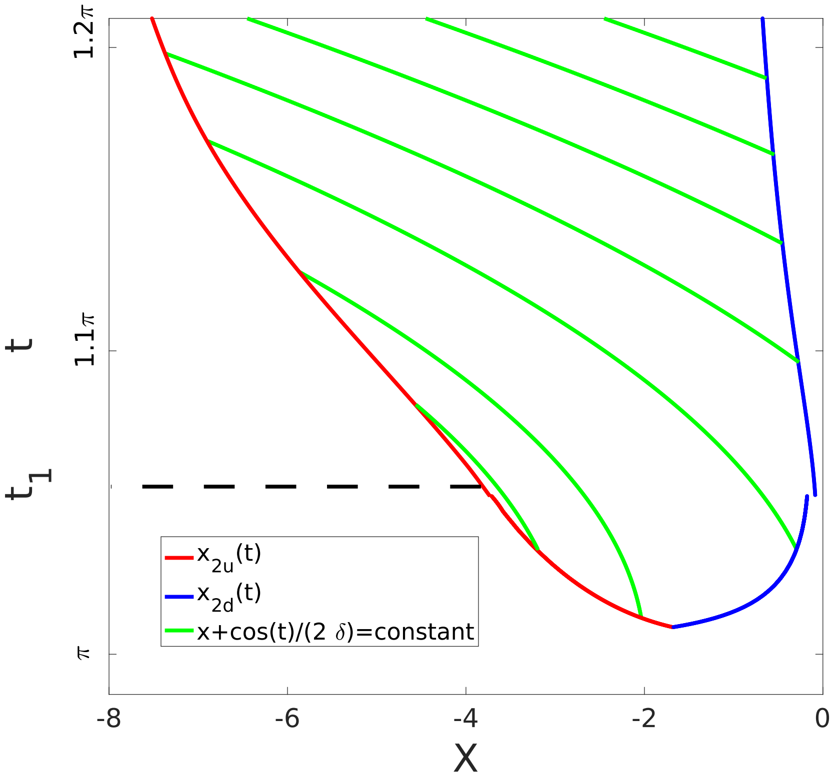

Figure 4.23: At time $t = t_1$, the upstream boundary is tangent to the characteristics. We show this physically with the numerical solutions to (3.89)-(3.91), (3.100)-(3.103), and (3.126)-(3.129) with parameters $\delta = 10^{-2}$ and $\Omega = 1$, as the red and blue curves. The green curves are the characteristics from equation (3.31).

which is consistent with the inner solution (4.130). Using the solution (4.175), we find that the causality condition in (4.173) fails at a critical time

$$\hat{t} = \hat{t}_1 = \left(\frac{128\Omega}{135}\right)^{1/5}. \tag{4.176}$$

We note the time when the upstream boundary changes causality is $t = t_1 = \delta^{2/5}\hat{t}_1$, which occurs when condition (4.7b) is no longer satisfied. At this time, the upstream boundary is tangent to the characteristics. We display this physically in Figure 4.23, which shows numerical solutions to the mushy region model, (3.89)-(3.91), (3.100)-(3.103), and (3.126)-(3.129) with $\delta = 10^{-2}$ and $\Omega = 1$ (blue and red curves), and the green lines are the characteristics from equation (3.31). In Figure 4.24, we show the asymptotic expression $t_1 = \delta^{2/5}\hat{t}_1$, with $\hat{t}_1$ from (4.176) compared to the numerical solutions with $\Omega = 1$; we see that the numerics reproduce the asymptotic result when $\delta \to 0$. The corresponding position

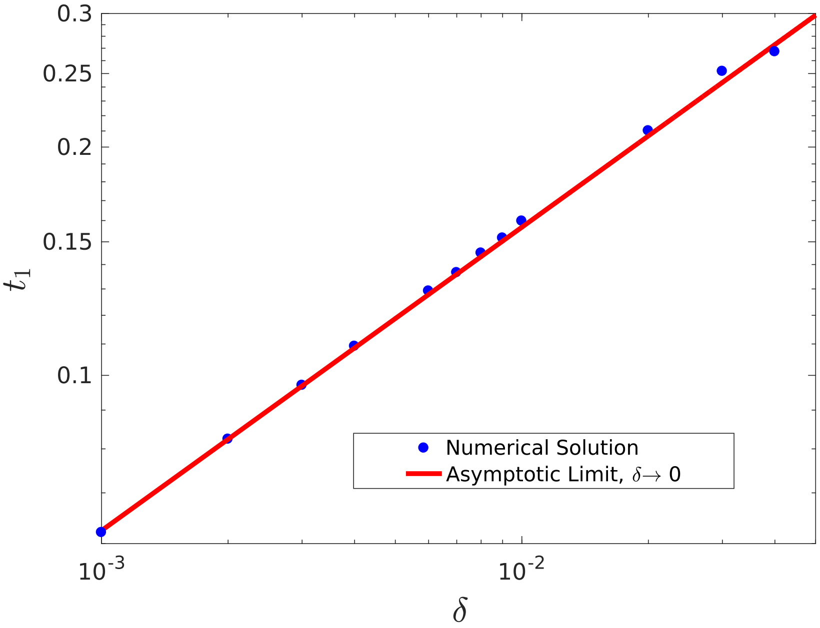

Figure 4.24: The time at which the characteristics start to intersect the upstream boundary of the second mushy region, t_1, when $\Omega = 1$. Numerical results are shown as the blue dots while the red line shows the asymptote $t_1 = \delta^{2/5}\hat{t}_1$, and $\hat{t}_1$ comes from (4.176).

of the upstream boundary is

$$\hat{x}_{2u1} = -\left(\frac{16\Omega\hat{t}_1}{5}\right)^{1/3} = -\frac{2^{9/5}\Omega^{2/5}}{3^{1/5}5^{2/5}}. \tag{4.177}$$

To describe the solution in $\hat{t} > \hat{t}_1$, we use the transformation

$$\frac{d\hat{t}}{ds} = 1, \quad \frac{d\hat{x}}{ds} = -\frac{\hat{t}}{2}, \tag{4.178}$$

(4.170) becomes

$$\frac{d\left(\theta\hat{h}\right)}{ds} = 0. \tag{4.179}$$

Integrating (4.178) and (4.179) we find

$$\hat{t} = s + c_1, \quad \hat{x} = -\frac{(s+c_1)^2}{4} + c_2, \quad \theta\hat{h} = c_3, \tag{4.180}$$

where c_1, c_2, and c_3 are functions of integration. Solving for $c_2 = \hat{x} + \hat{t}^2/4$, $\theta\hat{h}$ may be rewritten as

$$\theta\hat{h} = \hat{F}(\hat{x} + \hat{t}^2/4). \tag{4.181}$$

Using condition (4.173) and (4.175), and the approximation for $\hat{h} = \hat{x}^2/2$, we evaluate $\theta\hat{h}$ on the boundary $\hat{x} = \hat{x}_{2u}$

$$\left(\frac{32}{25}\right)^{1/3}\Omega^{2/3}\hat{t}^{2/3} = \hat{F}\left(-\left(\frac{16\Omega}{5}\right)^{1/3}\hat{t}^{1/3} + \frac{\hat{t}^2}{4}\right). \tag{4.182}$$

Letting the arguement of $\hat{F}$ be

$$-\left(\frac{16\Omega}{5}\right)^{1/3}\hat{t}^{1/3} + \frac{\hat{t}^2}{4} := \eta, \tag{4.183}$$

we eliminate $\hat{t}^2$ in favour of $\hat{F}$ (using 4.182) and η may then be expressed as an implicit function of $\hat{F}(\eta)$

$$\eta = \frac{25}{128\Omega^2}\,\hat{F}(\eta)^3 - \sqrt{2\hat{F}(\eta)} \qquad \text{where} \qquad 0 \leq \hat{F}(\eta) < \frac{2^{13/5}\Omega^{4/5}}{3^{2/5}5^{4/5}}. \tag{4.184}$$

The argument of $\hat{F}$ in (4.182) takes its maximum value at $\hat{t} = \hat{t}_1$. As $\hat{t}$ decreases, the argument of $\hat{F}$ also decreases, reaching zero at $\hat{t} = 0$, with $\hat{F}(0) = 0$. This corresponds to the characteristic emerging from $\hat{x} = 0$ at $\hat{t} = 0$. For $\hat{t} < 0$, instead of the boundary condition (4.173), we instead impose

$$\theta = 1 \quad \text{at } \hat{x} = \hat{x}_{2d} \sim -\delta^{2/5}\beta\sqrt{6\hat{t}} \sim 0, \tag{4.185}$$

by matching with (4.161). It follows that $\theta \sim 0$ to leading order on characteristics that originate on the downstream boundary, and hence (4.184) is replaced by $\hat{F}(\eta) = 0$ when $\eta < 0$.

Let us re-scale the relation (4.184) by defining

$$\hat{F}(\eta) = \frac{2^{13/5}\Omega^{4/5}}{3^{2/5}5^{4/5}}\,\Phi(\zeta), \qquad \text{where} \qquad \zeta = \frac{3^{1/5}5^{2/5}}{2^{9/5}\Omega^{2/5}}\,\eta, \tag{4.186}$$

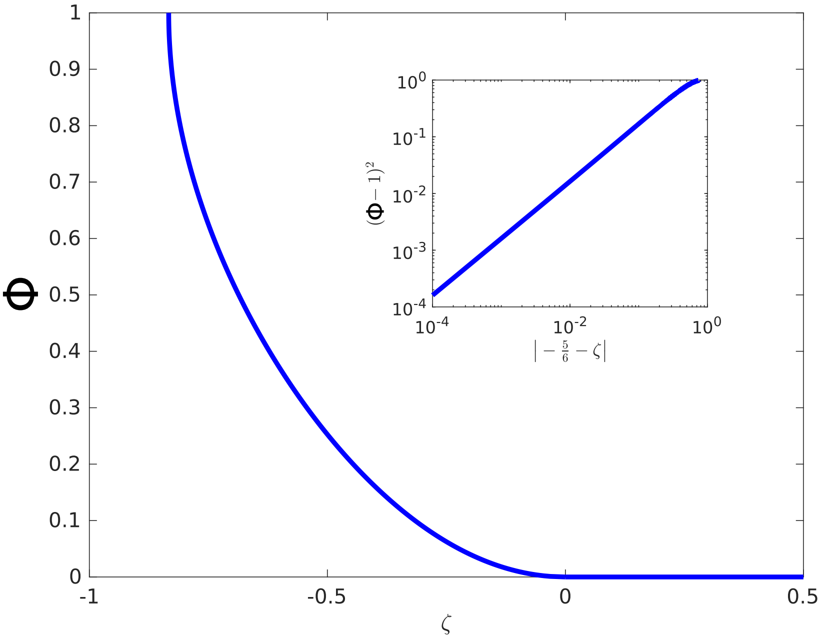

Figure 4.25: The function $\Phi(\zeta)$ defined by equation (4.187). The solution exhibits a square root behaviour at $\zeta = -5/6$ which corresponds to the tangency of the characteristics to the free boundary at $\hat{t} = \hat{t}_c$.

so that the function Φ is defined implicitly by

$$\zeta = \frac{\Phi(\zeta)^3}{6} - \sqrt{\Phi(\zeta)} \qquad \text{for} \quad 0 \leq \Phi(\zeta) \leq 1, \qquad \text{i.e.} \quad -5/6 \leq \zeta \leq 0, \tag{4.187a}$$

$$\Phi(\zeta) = 0 \qquad \text{for} \quad \zeta > 0. \tag{4.187b}$$

A plot of $\Phi(\zeta)$ for $\zeta \geq -5/6$ is shown in Figure 4.25. The solution for (4.187a) exhibits a square-root behaviour at $\zeta = -5/6$, shown in the inset in Figure 4.25. This behaviour is caused by the tangency of the characteristics to the free boundary at $\hat{t} = \hat{t}_1$.

Now we are ready to examine the solution for $\hat{t} > \hat{t}_1$. Instead of the boundary condition (4.173), we use the solution (4.182) to evaluate the fluid volume fraction θ at $\hat{x} = \hat{x}_{2u}$. To leading order in δ, the boundary condition (4.169) therefore becomes

$$q_u = -\left(2\frac{d\hat{x}_{2u}}{d\hat{t}} + \hat{t}\right)\hat{F}\left(\hat{x}_{2u} + \frac{\hat{t}^2}{4}\right) + 2\hat{h}\frac{d\hat{x}_{2u}}{d\hat{t}} \quad \text{at } \hat{x} = \hat{x}_{2u}, \tag{4.188}$$

and the pressure upstream of the mushy region is described by

$$\tilde{p}_u = \frac{48\left[-(2\frac{d\hat{x}_{2u}}{dt} + \hat{t})\hat{F}\left(\hat{x}_{2u} + \frac{\hat{t}^2}{4}\right) + \frac{d\hat{x}_{2u}}{dt}\hat{x}_{2u}^2\right]}{5\hat{x}^5} + \frac{8\hat{t}}{\hat{x}^3}, \tag{4.189}$$

where the function $\hat{F}$ is still defined by equations (4.186)–(4.187). Using condition (4.168), we find that $\hat{x}_{2u}$ satisfies the ODE

$$\left[\hat{x}_{2u}^2 - 2\hat{F}\left(\hat{x}_{2u} + \frac{\hat{t}^2}{4}\right)\right]\frac{d\hat{x}_{2u}}{d\hat{t}} = \hat{t}\hat{F}\left(\hat{x}_{2u} + \frac{\hat{t}^2}{4}\right) - \frac{5\hat{t}}{6}\,\hat{x}_{2u}^2 - \frac{5}{48\Omega}\,\hat{x}_{2u}^5, \tag{4.190}$$

subject to

$$\hat{x}_{2u} \to \hat{x}_{2u1} \quad \text{as } \hat{t} \to \hat{t}_1. \tag{4.191}$$

We can simplify the problem (4.190) by exploiting the normalisation (4.186). Let

$$\hat{x}_{2u}\left(\hat{t}\right) = \hat{x}_{2u1}\,X(T), \qquad\qquad \text{where} \quad \hat{t} = \hat{t}_1\,T, \tag{4.192}$$

so that (4.190) is transformed to

$$\left(X^2 - \Phi\right)\frac{dX}{dT} + \frac{2X^5}{9} + \frac{T}{3}\left(\Phi - \frac{5X^2}{3}\right) = 0. \tag{4.193}$$

where $\hat{t}_1$ and $\hat{x}_{2u1}$ are given by (4.177) and (4.176), respectively. Using (4.183), (4.186), (4.187a), and (4.192), ζ may be alternatively expressed as a function of X and T, namely

$$\zeta = -X + \frac{T^2}{6} = \frac{\Phi^3}{6} - \sqrt{\Phi} \tag{4.194}$$

which may be solved for X, yielding

$$X = \frac{T^2}{6} + \sqrt{\Phi} - \frac{\Phi^3}{6} \qquad \text{while} \quad 0 \le \Phi \le 1, \tag{4.195}$$

and the initial conditions are

$$X = \Phi = 1 \quad \text{at } T = 1. \tag{4.196}$$

We can eliminate X from (4.193)-(4.196) to obtain a single nonlinear ODE for Φ as a function of T, namely

$$\frac{d\Phi}{dT} = -\frac{\sqrt{\Phi}\left(T^2 + 6\sqrt{\Phi} - \Phi^3\right)^2}{486\left(1 - \Phi^{5/2}\right)\left(T + \Phi^{3/2}\right)\left(T^2 + 12\sqrt{\Phi} - \Phi^3\right)}\Big\{\Phi^{15/2} + T\Phi^6 - 18\Phi^5 - 2T^2\Phi^{9/2}$$
$$-18T\Phi^{7/2} - 2T^3\Phi^3 + 108\Phi^{5/2} + 18T^2\Phi^2 + T^4\Phi^{3/2} + 108T\Phi + 18T^3\Phi^{1/2} + T^5 - 216\Big\}. \tag{4.197}$$

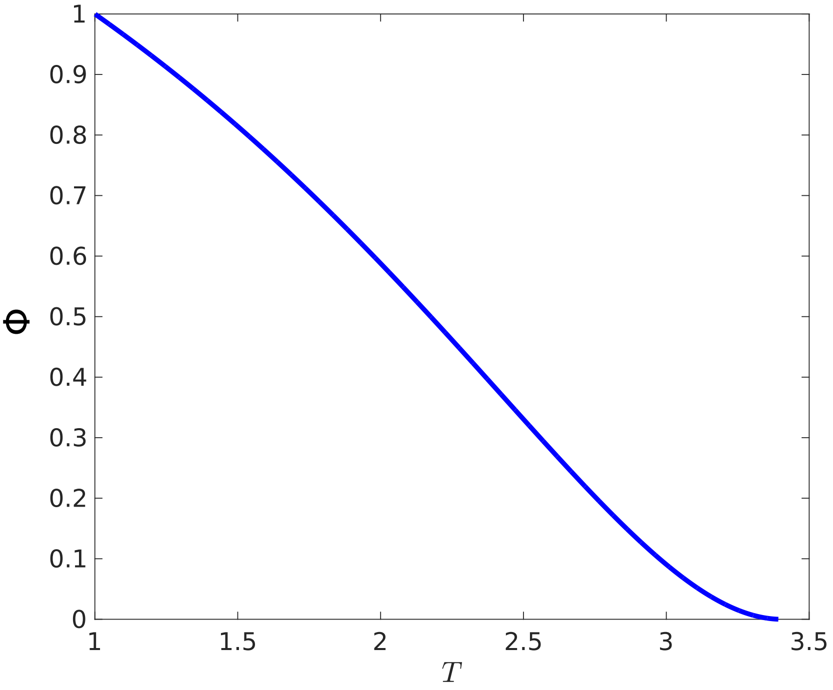

Figure 4.26: Numerical solution $\Phi(T)$ of the ODE (4.197) subject to the initial condition (4.199) with $\epsilon = 10^{-4}$.

The numerator and the denominator of the right-hand side of equation (4.197) are both equal to zero when $\Phi = T = 1$. By L'Hôpital's rule, we find that

$$\frac{d\Phi}{dT} \to -\frac{1}{3} \quad \text{as } T,\, \Phi \to 1, \tag{4.198}$$

and we can therefore use the initial condition

$$\Phi = 1 - \frac{\epsilon}{3} \quad \text{at } T = 1 + \epsilon, \tag{4.199}$$

to solve (4.197) numerically, with $0 < \epsilon \ll 1$; we verify that the solution is insensitive to the precise value of ϵ chosen provided it is sufficiently small. Using (4.192) and (4.195), we state the equivalent expansion to (4.199) for $\hat{x}_{2u}$ is

$$\hat{x}_{2u}\left(t_1 + \epsilon\right) \to -\left[\frac{2^9\Omega^2}{3^6 5^2 \delta}\right]^{\frac{1}{5}} \times \left[\frac{5}{2}\left(1 + \left[\frac{2^{14}\Omega^2}{3^6 5^7}\right]^{\frac{1}{5}}\right) + \epsilon\left[\frac{2^{14}\Omega^2}{3^6 5^2}\right]^{\frac{1}{5}}\right]. \tag{4.200}$$

The resulting numerical solution for $\Phi(T)$ is plotted in Figure 4.26. We find that the solution halts ($\Phi = 0$) at a finite time $T_s \approx 3.4043$. For $T > T_s$, we instead set $\Phi = 0$ in

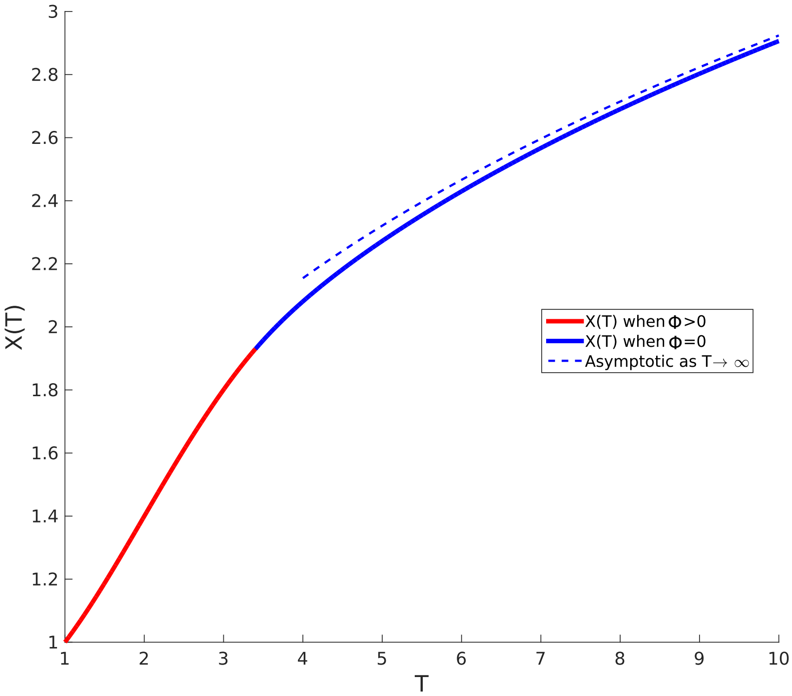

Figure 4.27: normalized free-boundary position $X(T) = \hat{x}_{2u}/\hat{x}_{2u1}$. The dashed curve shows the large-T behaviour (4.203). For $1 < T \leq T_s$, $X(T)$ is given by equation (4.195), where $\Phi(T)$ is the function plotted in Figure 4.26 (and determined numerically); for $T > T_s$, $X(T)$ is found by solving equations (4.201)-(4.202) numerically.

equation (4.193) to get the ODE

$$\frac{dX}{dT} + \frac{2X^3}{9} = \frac{5T}{9} \tag{4.201}$$

(which is just a scaled version of equation (4.46)) and continuity of X at $T = T_s$ implies the initial condition

$$X = \frac{T_s^2}{6} \approx 1.9315 \quad \text{at } T = T_s. \tag{4.202}$$

We plot the combined solution for $X(T)$ in Figure 4.27. For $1 < T \leq T_s$ we evaluate X using equation (4.195), the solution for which is shown as the red curve, and for $T > T_s$ we solve the problem (4.201), shown as the blue curve.

We also show in Figure 4.27 the asymptotic behaviour

$$X(T) \sim \left(\frac{5T}{2}\right)^{1/3} \quad \text{as } T \to \infty. \tag{4.203}$$

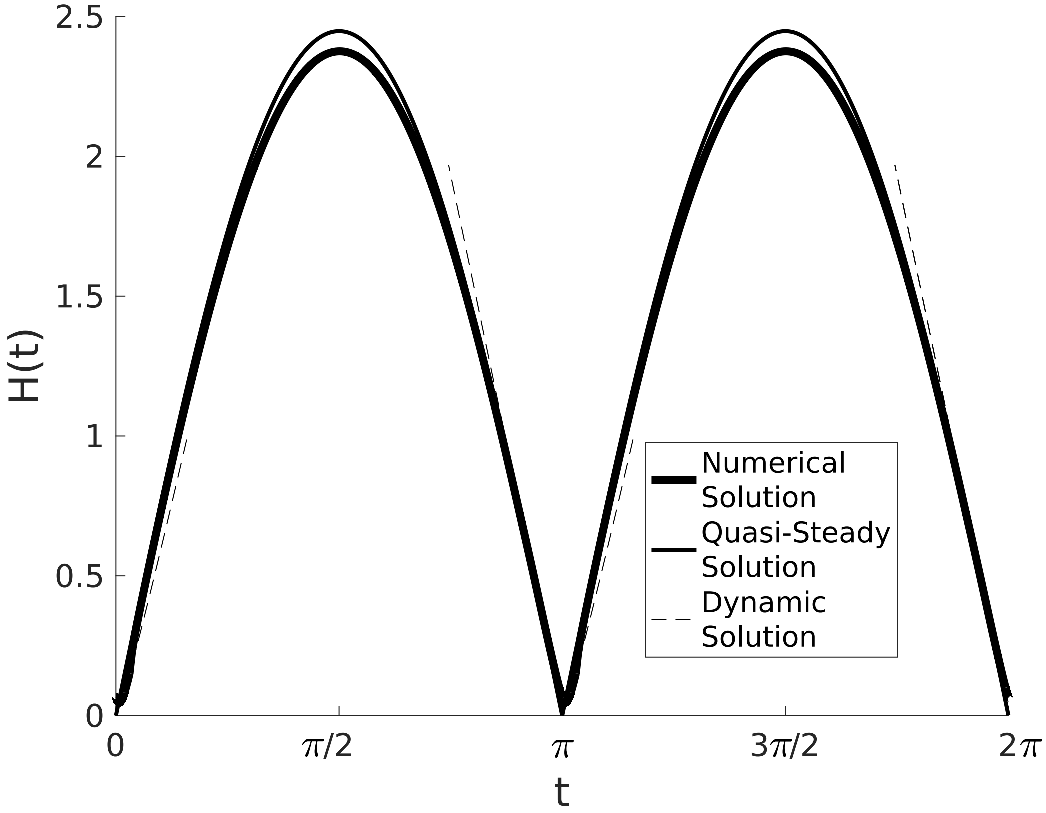

Figure 4.28: The film thickness $H(t)$ of a periodic solution calculated with $\delta = 10^{-3}$ and $\Omega = 1$. The numerical solution approximates the asymptotic solution so closely it is difficult to differentiate between them. The thick solid curve shows the numerical solution, (3.89)-(3.91), (3.100)-(3.103), and (3.126)-(3.129) the thin solid curve shows the quasi-steady solution, (4.19), and the thin dashed curve shows the dynamic solution, (4.79), (4.101) and (4.102), (4.147) and (4.148), with their respective scaling.

By reversing the scalings (4.192), we infer that

$$\hat{x}_{2u}\left(\hat{t}\right) \sim -2\left(\Omega\hat{t}\right)^{1/3} \quad \text{as } \hat{t} \to \infty, \tag{4.204}$$

which matches with the quasi-steady solution (4.29).

4.8 Summary

In this chapter, we have studied the limit of low oscillation frequency (or high load), i.e.: $\delta \to 0$. We show that in this limit, the numerical solution can be approximated with a quasi-steady solution parameterized by the velocity of the bottom surface, $u(t)$. In this situation, we expect the relaxation time-scale is significantly shorter than the period of oscillation. However, the quasi-steady solution breaks down when $u(t) \approx 0$, at which point the numerical solution is driven by the dynamics in the model.

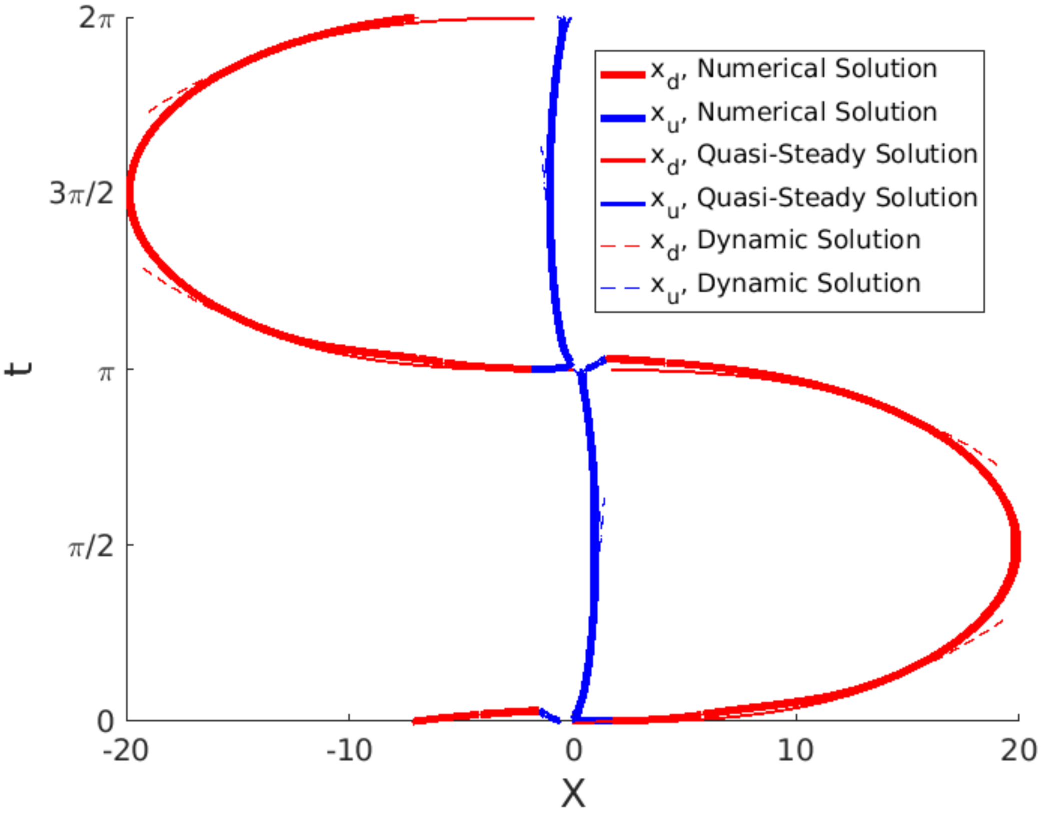

Figure 4.29: The $x-t$ diagram of a periodic solution calculated with $\delta=10^{-3}$ and $\Omega=1$. The numerical solution approximates the asymptotic solution so closely it is difficult to differentiate between them. The blue curves show the upstream boundaries, $x_u\left(t\right)$, $x_{2d}\left(t\right)$ and $x_{1u}\left(t\right)$, and the red curves show the downstream boundaries, $x_d\left(t\right)$, $x_{1d}\left(t\right)$ and $x_{2u}\left(t\right)$. The thick solid curves show the numerical solution,(3.89)-(3.91), (3.100)-(3.103), and (3.126)-(3.129), the thin solid curves show the quasi-steady solution, (4.19) and (4.29), and the thin dashed curves are the dynamic solution, (4.46), (4.79), (4.101) and (4.102), (4.122), (4.129), (4.147) and (4.148), (4.197) and (4.201), with their respective scaling.

We have shown that as $\delta\to 0$ the minimum film thickness approaches the limit $H_{min}=O\left(\delta^{2/3}\right)$ and the maximum film thickness remains of the order $H_{max}=O\left(1\right)$. In considering the minimum film thickness, we note one of the primary causes of wear in liquid films is two solid surfaces coming into contact with each other (Fusaro, 1981). We conclude, because the minimum film thickness decreases as $\delta\to 0$, the solid surfaces are more likely to come into contact in this limit, and hence increase the volume of wear in the film. We found that the time at which the mushy region opens is of the order $t=O\left(\delta\right)$, and, assuming $x_u(t)\ll x_d(t)$, that the time the mushy region closes may be approximated simply as when the asymptote for the downstream boundary is zero. The first order approximation is then of the order $t=O\left(\delta^{2/5}\right)$. However, the rate at which the numerical solution converges to this asymptote is very slow and so we obtained a second order correction by equating the asymptotes of the upstream and downstream boundaries in the limit $x_u(t)\to x_d(t)$. The numerical solutions are shown to converge to various asymptotic limits as $\delta \to 0$, including the maximum and minimum film thickness, the times when $x_u(t)$ and $x_d(t)$ change causality, and the times the mushy region opens and closes, validating our numerical results.

In Figures 4.28 and 4.29 we show the $x - t$ diagram and the film thickness $H(t)$ respectively with the parameters $\delta = 10^{-3}$ and $\Omega = 1$. As noted previously, the thick solid curves show the numerical solution, the thin solid curves show the quasi-steady solution, and the thin dashed curves show the dynamic solutions. We observe the numerical solution resembles the quasi-steady solution for most of the period of oscillation, over which time the solution variables change slowly. As the velocity of the bottom surface changes sign, the numerical solution is dominated by the unsteady dynamics in the model, showing significant and rapid change over a continuously shorter length of time. These characteristics are indications that the model is 'stiff' in the limit $\delta \to 0$. For values $\delta < 5 \times 10^{-4}$, the problem becomes too stiff for the numerical solution to compute. Discontinuities in the boundary of the mushy region remain, but are so small they are not noticeable in Figure 4.29.

4.9 Comparison with Experiments

We now compare the available experimental data without numerical solutions. The parameters of the experiment are as follows: the amplitude of oscillation of the moving surface is $A = 11$ mm, the radius of curvature of the top surface $R_c = 88$ mm, atmospheric pressure taken to be $p_{atm} = 101$ kPa, and the vapour pressure (read from the cavitated region of the pressure profile in Figure 3.6) is $p_{vap} = 50$ kPa. Sixteen tests were conducted with four different normal forces: $F = 977$ N/m, 1868 N/m, 2354 N/m and 2841 N/m and four different frequencies of oscillation: $\omega = 300$ rpm, 400 rpm, 500 rpm and 600 rpm.

However, the viscosity of the liquid used was not provided. Fortunately, we can use the information we have learnt from the quasi-steady solution to circumvent this issue. Due to the roughness of both solid surfaces, we expect our lubrication model to be most appropriate when the film thickness is large. In particular, our results have shown that the dimensionless quantity:

$$\frac{H_{max} F}{3\left(1-\beta^2\right) U R_c} \tag{4.205}$$

is constant to leading order in δ. Of course, we also see that the effect of $\delta > 0$ is non-negligible, the correction to the dimensionless film thickness enters at order $(\delta/\Omega)^{2/3} \propto$

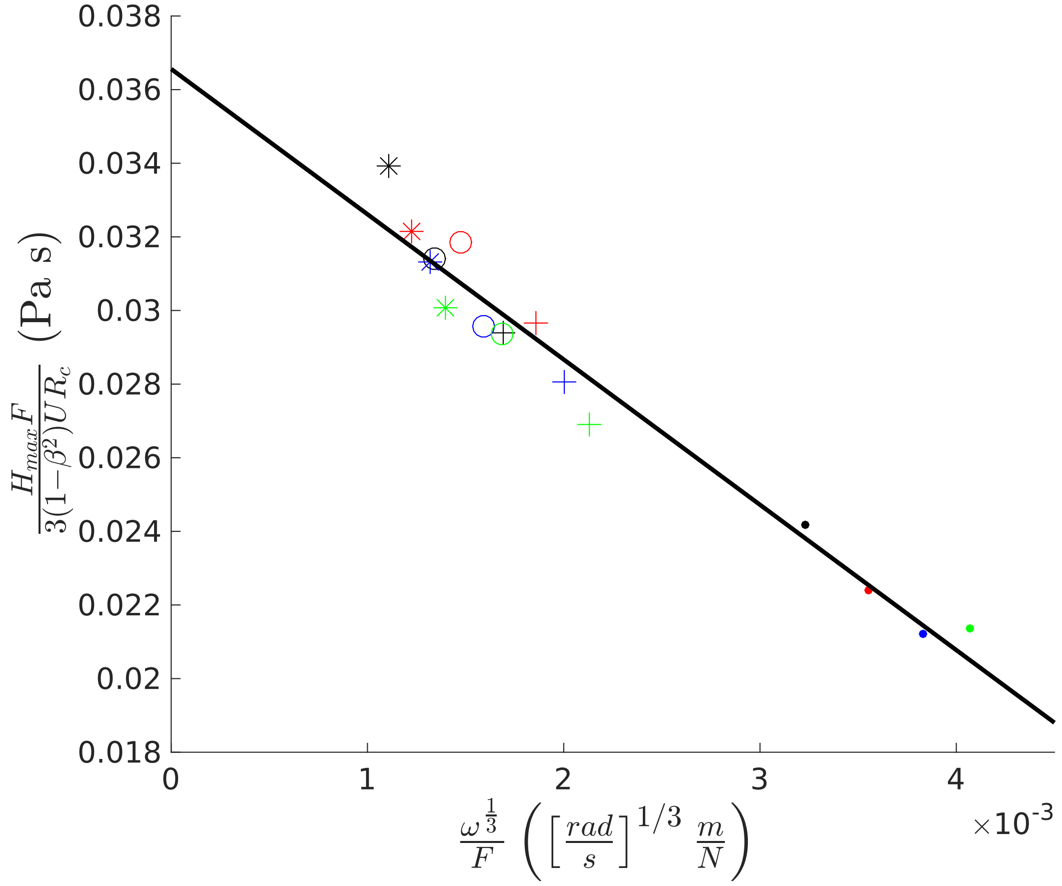

Figure 4.30: The quantity $H_{max}F/\left[3(1-\beta^2)UR_c\right]$ calculated for each of the 16 experimental runs performed by Nouri (2016), plotted as a function of $\omega^{1/3}/F$. Runs varied the oscillation frequency: $\omega = 300$ rpm, (black data points); 400 rpm, (red data points); 500 rpm, (blue data points); and 600 rpm, (green data points); and the normal force: $F = 977$ N/m, (dots, $\cdot$); 1868 N/m, (crosses, +); 2354 N/m, (circles, o); and 2841 N/m, (asterisks, *). The black solid line is the line of best fit to the data, $y = -13.963x + 0.0366$.

$\omega^{1/3}/F$. Motivated by this, we expect that the quantity $H_{max}F/\left[3\left(1-\beta^2\right)UR_c\right]$ only depends on $\omega^{1/3}/F$. Figure 4.30 therefore shows the quantity in (4.205) plotted as a function of $\omega^{1/3}/F$. The data collapses remarkably well, with the black line to the data being the line of best fit, $y = -13.963x + 0.0366$. We note how the data with the smallest normal force, shown as dots, have the largest value of $(\delta/\Omega)^{2/3}$, and therefore would be expected to resemble the quasi-steady solution the least of all the data. According to our calculations the $y-$intercept of this plot should be precisely the viscosity of the liquid. Here we find that the corresponding viscosity is $\mu_m = 0.0366$ Pa s. Our estimate for the viscosity is consistent with the standard to which the lubricant is designed, 5W-40[1], and is within the range of viscosities set by the standard, 0.0119 Pa s $< \mu < 0.0703$ Pa s. Assuming the estimate of

---

[1] http://msdspds.castrol.com/bpglis/FusionPDS.nsf/Files/B1704B6B8F69DFB380257F390029A168/File-/BPXE-9MXMAS.pdf

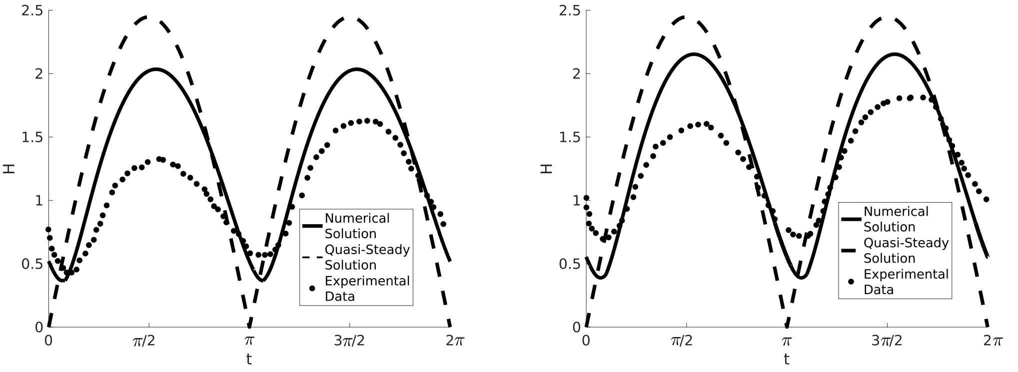

(a) Test 1: $\delta = 0.028$, $\Omega = 1.74$; ($\omega = 300$ rpm, $F = 977$ N/m).

(b) Test 2: $\delta = 0.029$, $\Omega = 3.33$; ($\omega = 600$ rpm, $F = 1868$ N/m).

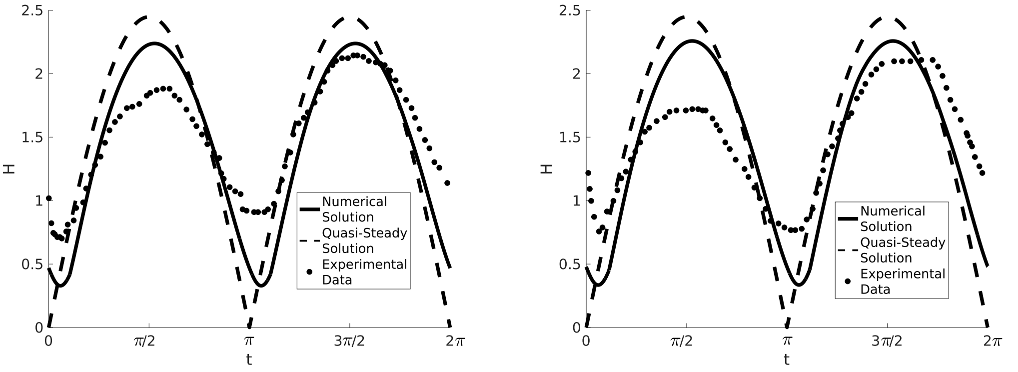

(c) Test 3: $\delta = 0.021$, $\Omega = 4.19$; ($\omega = 400$ rpm, $F = 2354$ N/m).

(d) Test 4: $\delta = 0.022$, $\Omega = 5.06$; ($\omega = 500$ rpm, $F = 2841$ N/m).

Figure 4.31: Comparison between four experimental sets of data and the numerical and quasi-steady solutions of our model. The thick solid curves are the numerical solution, (3.89)-(3.91), (3.100)-(3.103), and (3.126)-(3.129), the thin solid curves are the quasi-steady solution, (4.19) and (4.29), and black dots are the experimental data.

Parameter Values for each Test

test number	Figure Number	Frequency of Oscillation, ω, (rpm)	Applied Normal Force, F, (N/m)	δ	Ω
test 1	4.31(a)	300	977	0.028	1.74
test 2	4.31(c)	400	1868	0.029	4.19
test 3	4.31(d)	500	2354	0.021	5.06
test 4	4.31(b)	600	2841	0.022	3.33

Table 4.1: Parameter values for each of the 4 tests.

the mean viscosity is accurate, the parameters δ and Ω lie in the ranges $\delta \in (0.017 - 0.041)$ and $\Omega \in (1.74 - 5.06)$.

In Figure 4.31 we show the evolution of the film thickness for the numerical and quasi-steady solutions together with the experimental data. We show four tests that are representative of the variation in the film thickness across all the tests. We show the parameter values for each test in Table 4.1. In each figure, the thick solid curves show the numerical

Relaxation Time-Scale and Period of Oscillation Comparison

test number	Relaxation Time-Scale, $\check{T}_S$, (s), given by equation (3.74)	Period of Oscillation, $\check{T}_P$, (s)
test 1	0.00411	0.2
test 2	0.00268	0.15
test 3	0.00226	0.12
test 4	0.00225	0.1

Table 4.2: The relaxation time-scale, $\check{T}_S$, calculated using equation (3.74), and the period of oscillation for each of the four tests.

solution, (3.89)-(3.91), (3.100)-(3.103), and (3.126)-(3.129), the thin solid curves show the quasi-steady solution, (4.19), and black dots are the experimental data. These plots are based on our calculation of $\mu = 0.0366$ Pa s.

The four experimental data sets shown in Figure 4.31 display considerable variation between each other. The experimental data for test number 1 is consistently smaller over the entire period of oscillation compared to the other tests. The numerical solution, however, does not reflect this behaviour, showing similar qualitative solutions to the other figures. The experimental data and numerical and quasi-steady solutions for test number 2 show similar qualitative behaviour to those in Figure 4.31(a), but to a lesser extent. We note δ is larger for these tests than the other tests, shown in Figures 4.31(c) and 4.31(d). The experimental data in Figures 4.31(c) and 4.31(d) tests compares remarkably well to the numerical solutions, particularly so for the second half of oscillation where the film thickness is generally larger than the first half this is by construction because of our fit of μ and H_{max}). We shall consider possible causes of the experimentally observed asymmetry between the first and second halves of the period of oscillation in Chapter 5.

The relaxation time-scale, $\check{T}_S$, calculated from equation (3.74), are displayed in the second column in Table 4.2, together with the period of oscillation, $\check{T}_P$. We see that the relaxation time-scale is approximately two orders of magnitude smaller than the period of oscillation for each of the tests. These results are comparable to the lines in Figures 3.14 and 3.15 where $\alpha = 10^{-2}$. As such, we expect the motion to be quasi-steady provided $u(t)$ is not small. This is consistent with what is seen in Figure 4.31, particularly for the smaller values of δ, see Figures 4.31(c) and 4.31(d).

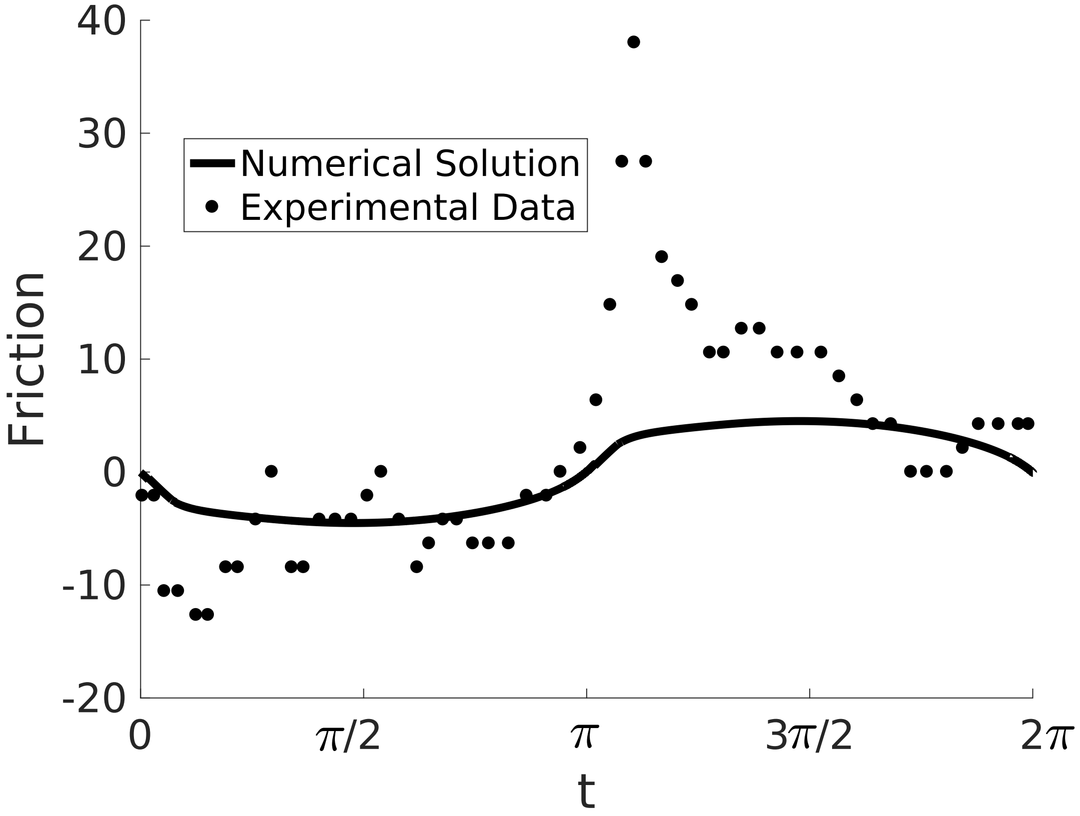

Figure 4.32: The friction force, F_{fric}, in the oscillatory solution against time, $0 < t < 2\pi$, solved using equations (4.207). The black curve shows the numerical solution, while the black dots show the experimental data. Parameters in this figure are those from test number 1 with parameters: $\delta = 0.028$ and $\Omega = 1.74$.

As a final comparison with the experiment, we consider the dimensionless friction force

$$\bar{F}_{fric} = F\sqrt{\frac{\check{H}}{R_c}}F_{fric} = \sqrt{\mu U F}F_{fric} \tag{4.206}$$

where F_{fric} is calculated using the expression

$$F_{fric} = -\int_{\infty}^{\infty}\left(\frac{\partial h}{\partial x}p + \frac{\partial u}{\partial y}\right)\bigg|_{y=h} dx = -\int_{\infty}^{\infty}\left(xp + \frac{h}{2}\frac{\partial p}{\partial x} - \frac{u}{h}\right)dx. \tag{4.207}$$

In Figure 4.32 we show the prediction of our numerical simulations (solid curve) together with the experimental data (dots). The numerical solution is the solid line and the experimental data are the black dots. When the velocity of the bottom surface is large enough, the numerical solution closely represents the experimental data, particularly in the first half of the period. The experimenters note that when the velocity of the bottom surface is sufficiently large, the film thickness is large enough that the surface roughness on both surfaces may be neglected, and hence the largest contribution to the friction in the system will come from the liquid. However, as the velocity approaches zero, the experimental data deviates from the model, showing a sharp and sudden increase in the friction. Through personal communication, it is believed that this increase in friction is primarily due to the solid surfaces coming into contact and sliding against each other (Nouri, 2016). The deviation of our model from the experimental data in this region supports this hypothesis. We discuss the impact of surface roughness in the experiment further in Chapter 5.

4.10 Conclusions

In this chapter, we have studied how the mushy region model film behaves in the limit $\delta \to 0$. In Section 4.2, we let $\delta = 0$ and derived the quasi-steady solution that describes the pressure upstream of the mushy region. Rescaling the problem, we derived the quasi-steady solution for the downstream of the mushy region. We showed that during the time when the solution is quasi-steady, the film thickness reaches its maximum height, and both boundaries of the mushy region reach their maximum distance from the origin. However, as the velocity of the bottom surface approaches zero, $u(t) \to 0$, the model transitions through a series of stages. The downstream boundary, $x_d(t)$, departs from the quasi-static solution when $u(t) = O\left(\delta^{2/5}\right)$ shown in Section 4.3. The same happens with the upstream boundary, $x_u(t)$, and film thickness, $H(t)$, when $u = O\left(\delta^{2/3}\right)$, discussed in Section 4.4. In Section 4.5 we showed that a second mushy region forms on the other side of the film after the velocity of the bottom surface changes sign, implying that in the limit $\delta \to 0$, we expect two mushy regions to exist in the film simultaneously (although only briefly). The two mushy regions start to interact with each other when $t = O\left(\delta^{2/3}\right)$, and in Section 4.6 we described the dynamics of the inner boundaries of the two mushy regions and the film thickness over this time. During this interval, we showed that the film thickness reaches its minimum value, and decreases proportional to $\delta^{2/3}$ as $\delta \to 0$. In Section 4.7 we describe the movement of the upstream boundary on the second mushy region. We summarize the findings of the asymptotic analysis in Section 4.8.

We have shown that the numerical solution and the asymptotic analysis converge in the limit $\delta \to 0$ by comparing various points of interest throughout the cycle of the film. These points include the times at which the flux boundary conditions on both mushy region interfaces change causality, the times when the mushy region opens and closes and the maximum and minimum film thickness. We provided further evidence that the numerical and asymptotic solutions agree with each other over the entire period of oscillation in the limit $\delta \to 0$ by comparing the solutions with parameters $\delta = 10^{-3}$ and $\Omega = 1$. Here the two solutions agreed so closely it is difficult to distinguish them from each other.

The asymptotic analysis showed that as $\delta \to 0$, the model becomes increasingly stiff. As $\delta \to 0$, the amount of time that the solution resembles the quasi-steady solution increases, over which the solution varies slowly in time. However, when the velocity of the bottom surface is small, a series of significant changes occurs over a decreasing length of time. These are characteristic qualities of a stiff system which the numerical solution has difficulty computing.

Section 4.9 provided a discussion of the discrepancies between the numerical solutions, the quasi-steady solution, and experimental data. By matching the maximum film thickness from the experiment to the quasi-steady solution and plotting this against $\omega^{1/3}/F$, showed that experimental data from a range of experiments collapse remarkably well onto a single straight line. Extrapolating that line to the y-axis, we estimated the viscosity of the liquid. We compared four tests considered to be representative of all the results in the experiment to the numerical and quasi-steady solutions. For the smallest values of δ the numerical solutions showed a close level of agreement to the experimental data when the velocity of the bottom surface was large. However, for the larger values of δ, the numerical solutions resemble the experimental data to a lesser degree. For each of the four tests considered, we have shown the relaxation time-scale is approximately two orders of magnitude below the period of oscillation. Relating this information back to the constant velocity case in Figures 3.14 and 3.15, we concluded that the numerical solution is approximately quasi-steady when the velocity is large, particularly for the smaller values of δ. We calculated the friction exerted on the bottom surface and compared it to the experimental data. Again, the results showed remarkable agreement when the velocity is large, but deviated when it is small; we attribute this discrepancy to surface roughness effects.

Chapter 5

Real-World Applications of the Mushy Region Model

In Chapter 4 we developed a mushy region model of a set of experiments conducted at City University of London, referred to as the City Experiments, on cavitation in a thin liquid film between a curved steel surface and a flat glass plate. We compared four sets of data from the City Experiments to our numerical solutions, with varying degrees of success. For the smallest values of δ (the ratio between the horizontal length scale $\sqrt{R_c \check{H}}$ and the amplitude of oscillation of the bottom surface, U/ω) we found that the data and the numerical solutions agreed quite well when the velocity of the bottom surface is large, $u(t) \gg O(\delta^{2/3})$. However, for larger values of δ, the discrepancy between the data and the numerical solution was more pronounced. Similarly, when the velocity of the bottom surface is small, the numerical solutions consistently under-predict the minimum film thickness obtained in all the experimental tests. Experimentally, the film thickness also exhibited some time asymmetry, with one of the two maxima being larger than the other, something that was not observed in our model. This chapter is devoted to attempting to explain these discrepancies between the mushy region model and the data from the City Experiments.

We assess in turn the significance of various physical effects that may be important in the City Experiments but are neglected in our model; we partition this analysis into six sections. In Sections 5.1.1-5.1.5 we estimate the influence of a variety of physical phenomena including elasticity of the solid surfaces, the inertia of the top surface, the piezo-viscous effect, viscous heating, and the liquid compressibility. However, we find that each of these plays a negligible role in the experiment. In Section 5.1.6 we discuss the effect of surface roughness on the mushy region model and conclude it has a significant effect on the dynamics in the liquid when the film thickness is near its minimum.

In Section 5.2, we consider how the mushy region model is affected by the finite width of the bearing. This section is divided into two subsections: first, we investigate how the mushy region model behaves when the far-field boundaries are in fact located at arbitrary finite (but symmetric) distances from the origin. Second, we compare this model to the data from the City Experiments, implementing the boundary conditions at points corresponding to the edges of the ring profile. By including the finite boundaries in our model, we show noticeable improvement between the numerical solutions and the experimental data. However, this model cannot explain the asymmetry observed in the experimental results. We attempt to answer this question in Section 5.3, which is divided into two subsections. We first consider a model that includes a small degree of asymmetry by translating the centre of the parabolic surface from the middle of the film by a small distance ϵ. We also consider how small variations in the velocity of the bottom surface affect the mushy region model.

We also note that the City Experiments are in themselves a model system, neglecting various complications typically experienced in an engine. In Section 5.4, we study how the normal force, now a non-uniform function of time, affects the mushy region model. The motivation for this model is provided by variations in the piston ring tension due to rapid changes in the gas chamber pressure as the gases are ignited. We draw conclusions in Section 5.5.

5.1 Additional Physical Effects

5.1.1 Elastic Deformation of the Surfaces

In previous chapters, we assume the solid surfaces bounding the liquid film are rigid. Here we study the validity of this assumption by estimating the deformation of the surfaces bounding the film.

The force exerted by the liquid on the solid surface, (per unit length) may be estimated as the pressure, $\breve{p}$, multiplied by the horizontal length scale, $\sqrt{R_c\breve{H}}$:

$$\breve{p}\sqrt{R_c\breve{H}} \sim F, \tag{5.1}$$

where in the City Experiments $F \gtrsim 10^3$ N/m. We expect the greatest deformation to occur in the flat glass plate, which has an elastic modulus of $E \sim 100$ GPa, (and hence is softer than steel, $E = 200$ GPa[1]). We calculate the typical solid deformation, L_d, to be of the order

$$L_d = \frac{\breve{p}\sqrt{R_c \breve{H}}}{E} = \frac{F}{E} \approx 0.01\ \mu\text{m}. \tag{5.2}$$

Given that the minimum film thickness is approximately 0.2 μm for all tests, we consider the elastic deformation of the glass surface to have a negligible effect on the profile of the lubricating film.

5.1.2 Inertia of the Top Surface

Previously, we have neglected the inertial effects of the top while relating the applied normal force to the integral of the pressure in the film. However, during the small interval in time for which the motion is not quasi-static, it could be that the acceleration $d^2\breve{H}/d\bar{t}^2$ plays a role due to the rapid variation in the film thickness. To assess the influence of inertia of the top surface, we rewrite the force balance, (3.91), as

$$F - \int_{-\infty}^{\infty} \bar{p}\, d\bar{x} = M\frac{d^2\breve{H}}{d\bar{t}^2}, \tag{5.3}$$

where $M = F/g$ is the mass per unit width of the top surface, and $g = 9.81$ m/s^2 is the acceleration due to gravity. Using the non-dimensionalisation described in Section 3.5, the dimensionless version of equation (5.3) is

$$1 - \int_{-\infty}^{\infty} p\, dx = m\frac{d^2 H}{dt^2}, \tag{5.4}$$

where

$$m = \frac{\mu U R_c \omega^2}{gF} \tag{5.5}$$

is the dimensionless mass of the top surface. We note that because of the non-dimensionalization, m decreases as F is increased. We calculate m to vary between $2 \times 10^{-4} < m < 6 \times 10^{-4}$ for parameters typical of the City Experiments. From Chapter 4, we calculate the maximum dimensionless acceleration of the top surface is of the order $d^2H/dt^2 \sim \delta^{-2/3}$, which for the range of δ relevant to the experiments correlates to $d^2H/dt^2 \approx 10$. We conclude that the vertical acceleration of the glass plate is not significant enough for the

---

[1] http://www.engineeringtoolbox.com/young.modulus.d.417.html

inertial effects of the top surface to have a noticeable influence on the liquid film.

5.1.3 Piezo-Viscous Effect

Previously, we have assumed the viscosity of the liquid to be constant. However, this may not be true: lubricants typically used in car engines have a viscosity that may vary significantly with pressure. We expect that when the film thickness is at a minimum the pressure will be largest, which may potentially have a significant impact on the viscosity of the liquid. We investigate the magnitude of this piezo-viscous effect using the relation

$$\breve{\mu} = \mu_0 e^{G\breve{p}}, \tag{5.6}$$

where G is the pressure-viscosity coefficient (which lies in the interval $10 - 15$ GPa^{-1}, Berthe and Vergne (1990)), and μ_0 is the base viscosity of the liquid. Using the non-dimensionalisation described in Section 3.5, equation (5.6) takes the form

$$\breve{\mu} = \mu_0 e^{\alpha p}, \tag{5.7}$$

where

$$\alpha = \frac{GF}{R_c}\sqrt{\frac{F}{\mu_0 U}} \tag{5.8}$$

is the dimensionless pressure-viscosity coefficient. We calculate the maximum value of α obtained experimentally to be 1.3×10^{-3}. Using the scaling from Section 4.6 the pressure scales as $p = \delta^{-1/3}\bar{p}$ and using equation (4.141), we found the maximum pressure in the film over this time to be of the order $\bar{p}_{max} \approx 0.248$. Using the range of δ relevant to the experiment, we calculate the modified viscosity is $\breve{\mu} \approx 1.0015\mu_0$: i.e. the viscosity changes by 0.15 % because of changes in pressure. We therefore consider this effect to be negligible.

5.1.4 Viscous Heating

Previously we have assumed any variation in the temperature of the liquid in the film to have a negligible effect on the liquid properties. However, it is possible viscous dissipation in the film to cause heating of the liquid, potentially causing variation in other physical properties, most notably the viscosity. We estimate the dominant process through which energy is transported in the film and the magnitude of the temperature variation due to viscous heating.

The energy equation in the liquid is

$$\rho C_p \left(\frac{\partial \bar{T}}{\partial \bar{t}} + \bar{u} \cdot \nabla \bar{T} \right) = k \nabla^2 \bar{T} + \mu \left(\frac{\partial \bar{u}}{\partial \bar{y}} \right)^2 , \tag{5.9}$$

where $\bar{T}$ is the dimensional temperature, $k = 0.15$ W/mK [2] is the thermal conductivity, and $C_p = 1.7$ kJ/kgK [3] is the specific heat capacity. Using the non-dimensionalisation for the mushy region model, defined in Chapter 3.5, we find that the reduced Péclet number is of the order

$$P\acute{e} = \frac{\rho C_p \check{H}^2 \omega}{k} = O(10^{-4}). \tag{5.10}$$

We conclude that the convection terms in (5.9) are negligible, and the transfer of heat in the film is between the conduction and viscous heating terms. Balancing these two, we calculate the rise in temperature of the lubricant generated through viscous heating to be of the order

$$\Delta \bar{T} = \frac{\mu U^2}{k} = O(0.1) \text{ K}. \tag{5.11}$$

We consider $\Delta \bar{T}$ to be so small that it is unlikely to cause any significant variation in the lubricant viscosity or vapour pressure, we conclude that viscous heating has a negligible effect on the liquid film.

5.1.5 Liquid Compressibility

In deriving the mushy region model, we have assumed the liquid to be incompressible. To examine this assumption, we calculate the compressibility ratio

$$\gamma = \frac{\bar{p}}{B} = \frac{F}{B R_c} \sqrt{\frac{F}{\mu U}} \tag{5.12}$$

where $\bar{p}$ is the dimensional pressure and $B = 1.4 \times 10^9$ Pa [4] is the compressibility of the lubricant, (i.e. the relative change in density as a response to a change in pressure). We calculate $\gamma = O(10^{-2})$ and so we conclude the lubricant may be approximated as

---

[2] http://www.engineeringtoolbox.com/thermalconductivityliquidsd1260.html

[3] http://www.engineeringtoolbox.com/specificheatcapacityliquidsd1260.html

[4] http://www.halocarbon.com/halocarbonmedia/OilBrochure59.pdf

incompressible, validating our assumption.

5.1.6 Surface Roughness

In the mushy region model derived in Chapter 3 we assume that the roughness of the solid surfaces in the City Experiments is significantly smaller than the film thickness, and hence that they may be represented as smooth. This assumption is reasonable when the velocity of the bottom surface is large since the maximum film thickness is of the order 2 μm thick and the combined RMS surface roughness of both surfaces is 0.5 μm. We relate this description of the film to the Stribeck Curve, shown in Figure 1.1, taken from Heshmat (2010), which describes the Coefficient of Friction (the ratio of the absolute value of the friction force and the applied normal force), varying against the Stribeck Number, $U\mu/F$. We infer the film resides between the Mixed and Full Film Regimes when the velocity of the bottom surface is large. However, when the film thickness is close to its minimum value we cannot neglect the roughness of both surfaces, for the minimum film thickness is approximately 0.2 μm. This is less than the combined surface roughness. We infer that the film transitions to the Boundary Regime when the velocity of the bottom surface, and hence the Stribeck Number, is small. In this regime, the liquid is unable to prevent the solid surfaces from coming into contact and scraping against each other.

Further evidence that shows the surfaces come into contact with each other in shown is Figure 4.32, which compares the friction measured in the City Experiments and that calculated from the model using equation (4.207). Near the times $t = \pi/2$ and $3\pi/2$, when the film thickness is large, the numerical solution approximates the friction force to a reasonable level of accuracy. However, as the velocity of the bottom surface changes sign as $t \to 0$ and π, the friction measured in experiments rapidly increases due to contact between the surfaces.

5.1.7 Summary

In this Section, we have considered various physical effects that could contribute to the deviation we observe between the City Experiments and our numerical models. Of those considered, the phenomena we have shown to have a negligible effect on the film include: elasticity of the solid surfaces, inertia of the top surface, piezo-viscous effect, viscous heating, and the liquid compressibility. In the final section, we have shown the film thickness actually reduces below the RMS surface roughness of the two surfaces. We consider this to be outside

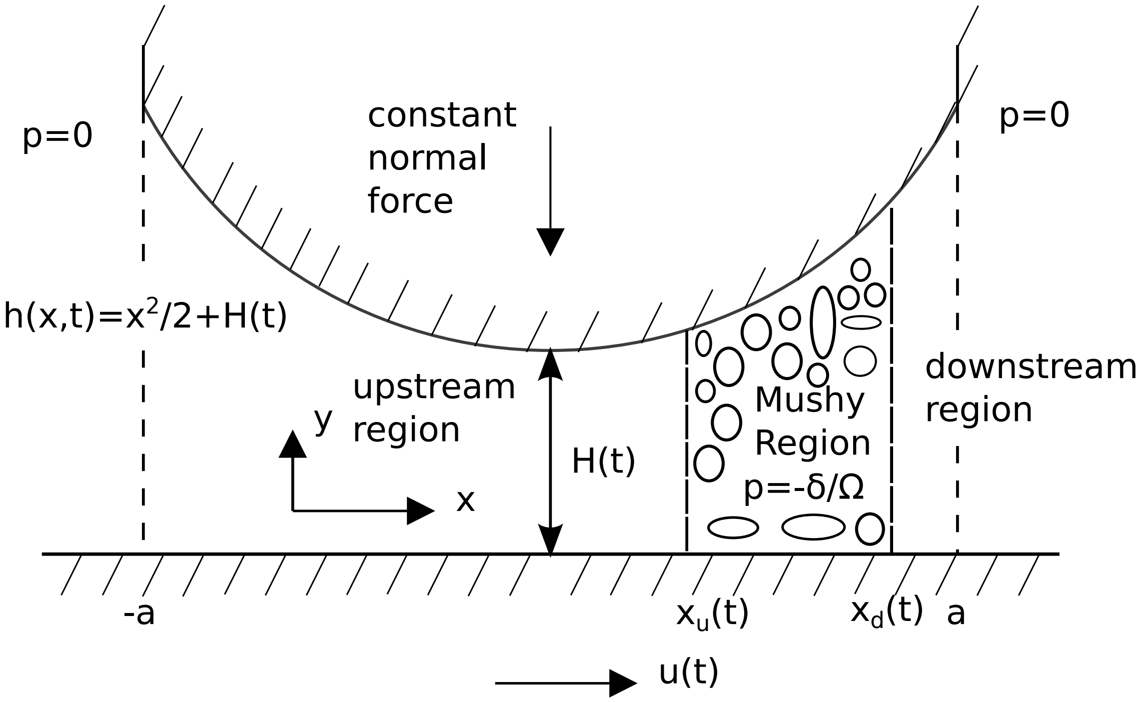

Figure 5.1: Schematic of the mushy region model with boundary conditions located at $x = \pm a$.

the scope of this thesis, and leave further study of this effect to future work.

5.2 Finite Width Slider

In the derivation of the mushy region model in Section 3.5, we assume that the boundaries of the ring profile are sufficiently far from the centre of the film that they have a negligible effect, so that the pressure returns to atmospheric at infinity. However, in each of the tests shown, we calculate that the maximum extent of the mushy region may be comparable to the distance between the edges of the ring profile and its centre. This motivates us to investigate the influence the position at which the pressure boundary condition is applied has on the mushy region. To observe this effect, we consider the model described by equations (3.89), (3.91), (3.92), (3.100)-(3.105), (3.126)-(3.131) and re-locate the boundary conditions (3.90), to a finite distance from the origin, i.e.

$$p = 0 \text{ at } x = \pm a. \tag{5.13}$$

A schematic of the model is shown in Figure 5.1. In this section, we only consider a symmetric model because the ring profile, illustrated in Figure 5.2, is shown to be roughly symmetric about the origin.

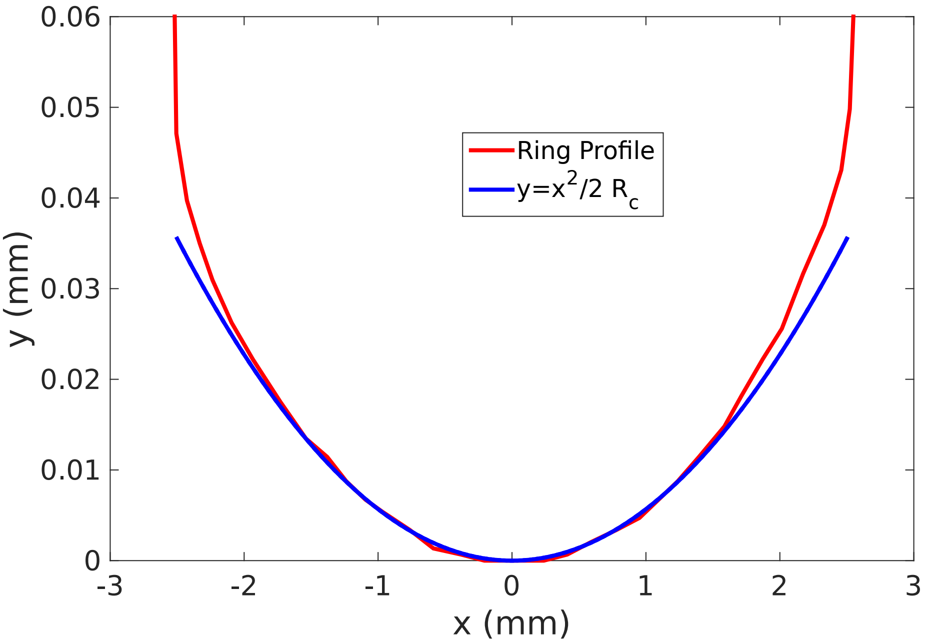

Figure 5.2: Ring profile used in the City Experiments, shown in red, and the parabola $y = x^2/(2R_c)$, shown in blue.

We divide the analysis below into two parts. First, we consider how the location of the pressure boundary condition influences the mushy region model, by locating them a finite and symmetric distance from the origin. Second, we compare the data from the City Experiments with the current model by using values of a corresponding to the edges of the experimental ring profile.

5.2.1 Influence of Finite Width of the Ring

We now consider how the mushy region model behaves as the pressure boundary conditions are shifted from infinity to a finite distance from the origin. To describe this behaviour, we use the parameter values $\delta = 0.01$ and $\Omega = 1$, and $a = 10$, 5, 2, and 1. In each case we compare the solutions to those in which $a \to \infty$, shown as dashed curves, and we denote as $x_{u,\infty}$, $x_{d,\infty}$ and H_∞.

In Figure 5.3, we show how the boundaries of the mushy region vary as a function of time. In the case when $a = 10$, the boundaries of the mushy region remain close to $x_{u,\infty}$ and $x_{d,\infty}$. The only exception to this is the outer boundary x_d, near its maximum. This observation suggests the pressure boundary conditions located at $x = \pm a$, have little influence on the model provided they are sufficiently far from the origin, as expected. When $a = 5$, the inner boundary x_u still appears to remain unaffected. However, the same is not true for x_d. Shortly after the mushy region forms, x_d no longer resembles the boundary $x_{d,\infty}$,

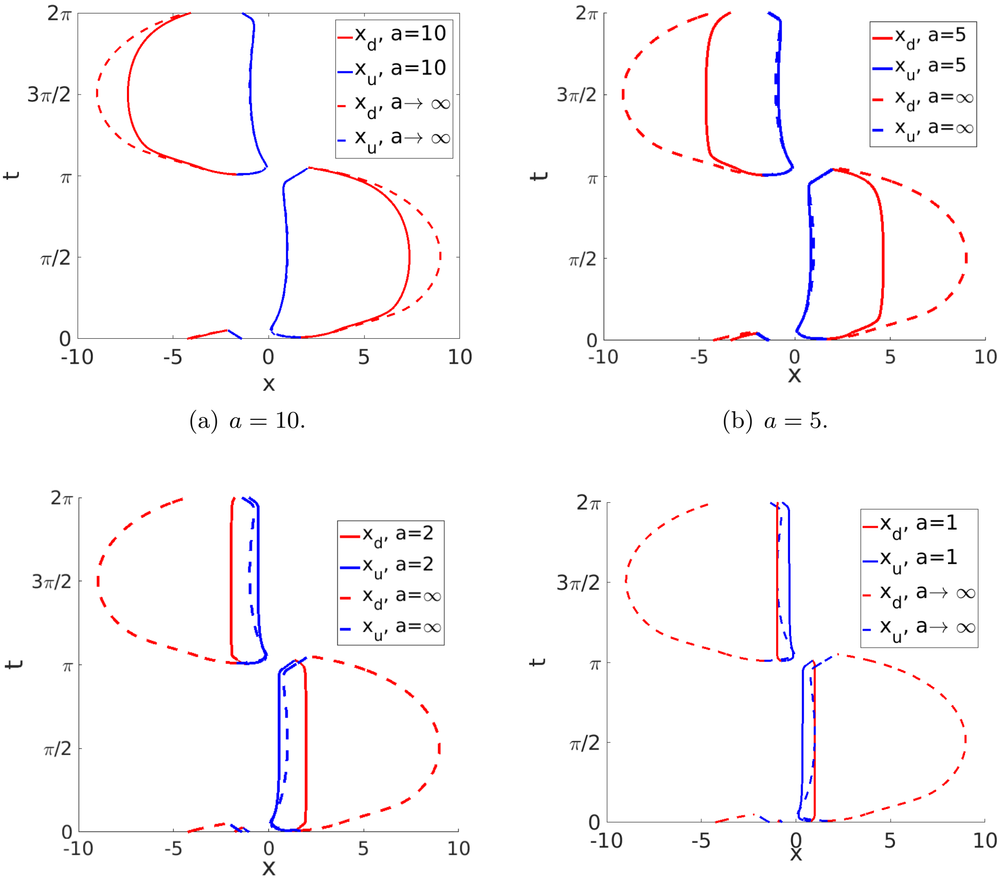

(a) $a = 10$.

(b) $a = 5$.

(c) $a = 2$.

(d) $a = 1$.

Figure 5.3: Comparison of the boundaries of the mushy region, x_d (red curves), and x_u (blue curves), when the ring boundaries are at $x = \pm a$. Four computations are shown with $a = 1$, 2, 5, and 10. The solid curves show the numerical solutions to the mushy region model with the edges of the top surface located symmetrically about the origin, $x = \pm a$, solved using equations (3.89), (3.91), (3.92), (3.100)-(3.105), (3.126)-(3.131), and (5.13), and dashed curves show the infinite boundary case, $a \to \pm\infty$, solved with equations: (3.89)-(3.92), (3.100)-(3.105), (3.126)-(3.131). In each of the solutions, the parameters used are $\delta = 0.01$ and $\Omega = 1$.

its growth having rapidly decreased, and remains roughly constant at $x \approx \pm 4.8$ until the mushy region begins to close. In the case $a = 2$, the right hand boundary x_d is significantly affected by the pressure boundary condition for the entire duration of the oscillation. After the film cavitates, x_d quickly approaches the value of $x_d \approx \pm 1.977$ where it remains until the mushy region is about to close. Shortly after x_u reaches its minimum, it no longer resembles $x_{u,\infty}$, but remains closer to the origin showing significantly less variation with time over the duration of the cycle. These trends continue when $a = 1$; the right hand boundary now approaching the value $x_d \approx \pm 0.996$, not changing except when the mushy region is very close to either opening or closing. The upstream boundary is similar, quickly approaching the value of $x_u \approx \pm 0.358$ where it remains until the time when the mushy

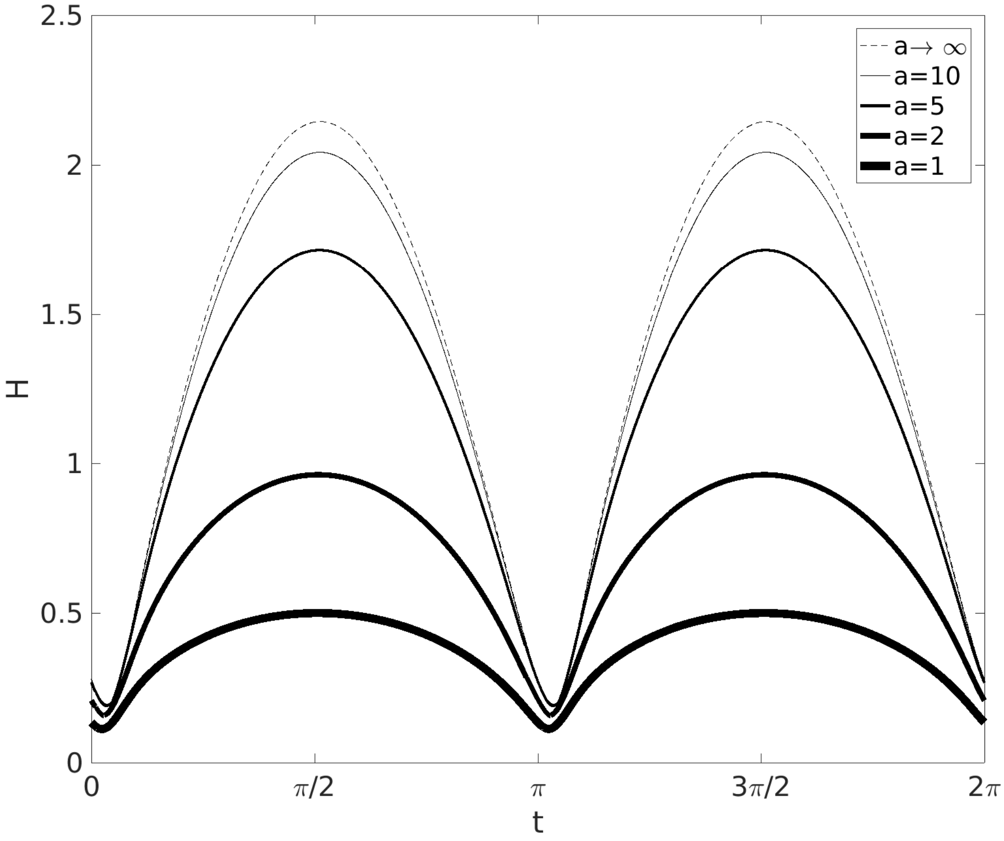

Figure 5.4: The effect of a finite ring width on the evolution of the film thickness, H. The solid curves show the numerical solutions to the model with the pressure boundary conditions located symmetrically about the origin, $x = \pm a$, solved using equations (3.89), (3.91), (3.92), (3.100)-(3.105), (3.126)-(3.131), and (5.13), and dashed curves show the infinite boundary case, $a \rightarrow \pm\infty$, solved with equations: (3.89)-(3.92), (3.100)-(3.105), (3.126)-(3.131). In each of the solutions, the parameters used are $\delta = 0.01$ and $\Omega = 1$.

region closes. These four solutions show that as the pressure boundary conditions approach the origin symmetrically, they limit the growth of the boundaries of the mushy region, especially when x_d becomes of a similar order to a.

In Figure 5.4, we show how the film thickness, H, varies as a function of time for different values of a. In the case $a = 10$, the film thickness closely resembles H_∞, only deviating slightly when H_∞ is close to its maximum. This discrepancy becomes larger when $a = 5$, however, the solutions still resemble each other when the film thickness is close to its minimum. In the cases of $a = 1$ and 2, the film thickness no longer resembles H_∞ at any time throughout the duration of the cycle, for H is significantly smaller than H_∞.

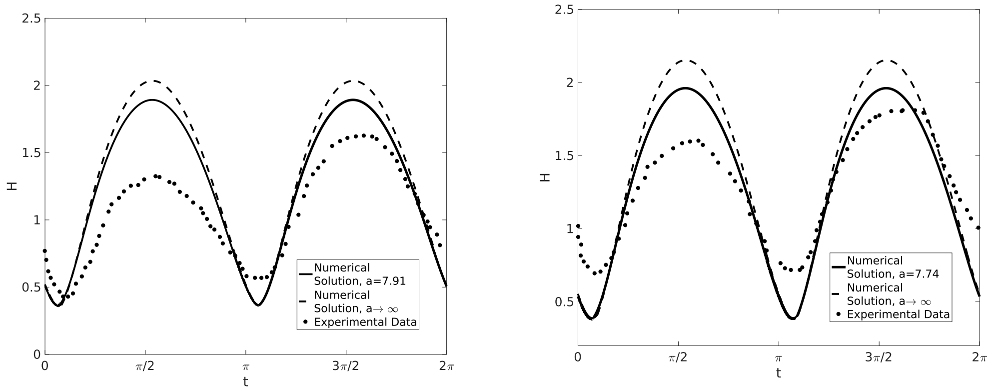

(a) Test 1: $a = 7.91$, $\delta = 0.028$, $\Omega = 1.74$; ($\omega =$ 300 rpm, $F = 977$ N/m).

(b) Test 2: $a = 7.74$, $\delta = 0.029$, $\Omega = 3.33$; ($\omega =$ 600 rpm, $F = 1868$ N/m).

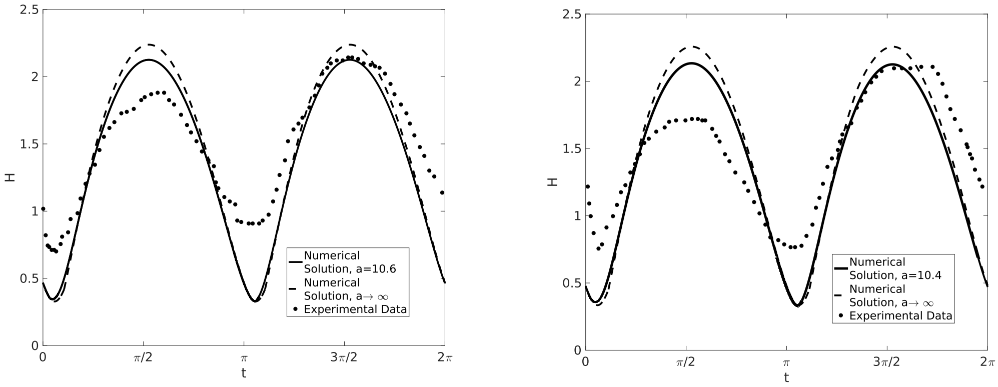

(c) Test 3: $a = 10.6$, $\delta = 0.021$, $\Omega = 4.19$; ($\omega =$ 400 rpm, $F = 2354$ N/m).

(d) Test 4: $a = 10.4$, $\delta = 0.022$, $\Omega = 5.06$; ($\omega =$ 500 rpm, $F = 2841$ N/m).

Figure 5.5: Comparing the film thickness for four sets of data from the City Experiments (black dots) and the numerical solutions for the mushy region with the pressure boundary conditions implemented at infinity, (dashed curves), (solved using equations (3.89)-(3.92), (3.100)-(3.105), (3.126)-(3.131)), and $x = \pm a$, (solid curves), (solved using equations (3.89), (3.91), (3.92), (3.100)-(3.105), (3.126)-(3.131), and (5.13)). The position at which the pressure boundary condition is implemented corresponds to the edges of the ring profile.

5.2.2 Comparison with Experiment

In Figure 5.5, we compare the data from the City Experiments (black dots), to the numerical solutions of the mushy region model with the ring boundaries located at $a = \pm a$, (solid curves), and $x \to \pm\infty$, (dashed curves). We compare the same four tests that we compared in Figure 4.31, and all the other parameters are as before. We choose the location of the boundary conditions to correspond to the edges of the ring profile, which is located approximately at $x = \pm L/\sqrt{R_c \check{H}}$, where $L = 2.5$ mm is the distance between the edges of the ring profile and the origin and $\sqrt{R_c \check{H}}$ is the dimensional length scale defined in (3.85) and (3.86).

For each test shown, we observe the ring width to have a small effect on the numerical

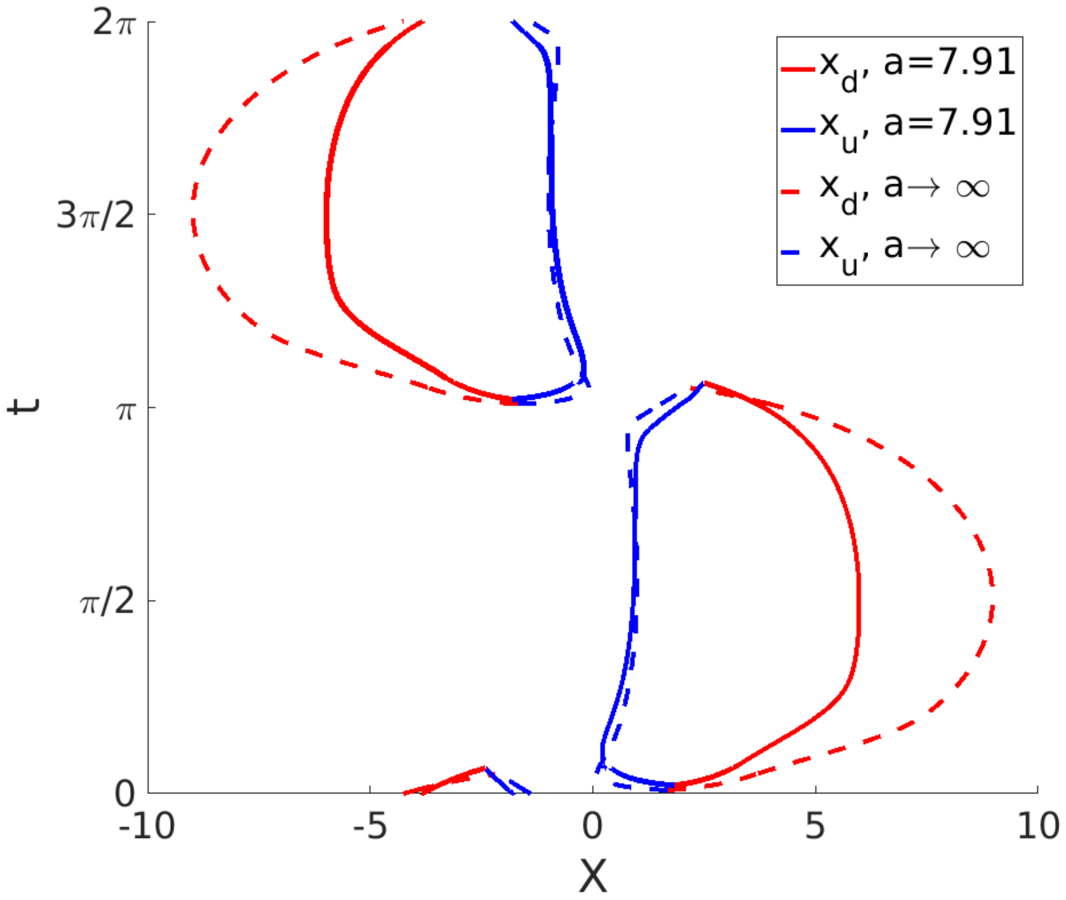

Figure 5.6: The boundaries of the mushy region as a function of time over the period of oscillation with x_d (red curve), and x_u (blue curve). Solid curves show the numerical solution with the pressure boundaries implemented at $x = \pm a$, (solved using equations (3.89), (3.91), (3.92), (3.100)-(3.105), (3.126)-(3.131), and (5.13)); dashed curves show the numerical solutions when $a \to \pm\infty$, (solved using equations (3.89)-(3.92), (3.100)-(3.105), (3.126)-(3.131)). We only show how x_u and x_d for a single solution, (test 1, $a = 7.91$, $\delta = 0.028$, $\Omega = 1.74$), because each solution shows qualitatively similar.

solution improving the agreement with the experimental data, but only when the film thickness is near its maximum. The closest approximation to the maximum film thickness occurs for Figures 5.5(b), ($a = 7.74$); 5.5(c), ($a = 10.6$); and 5.5(d), ($a = 10.4$). However, the discrepancy between the finite width model and the experimental data shown in Figure 5.5(a) is still considerable. We also note that the current model continues to underpredict the minimum film thickness observed in the City Experiments.

In Figure 5.6, we show how the boundaries of the mushy region evolve for only a single case (test 1, $a = 7.91$, $\delta = 0.028$, $\Omega = 1.74$); the other tests show similar qualitative behaviour. The upstream boundaries, (shown as blue), appear not affected at all by the finite ring width. However, as expected, the downstream boundaries, (shown as red), are restricted by the boundary conditions at $x = \pm a$.

5.2.3 Summary

In this section, we have studied how the position of the pressure boundary conditions affect the results of the mushy region model. First, we have shown how the expansion of the mushy region is limited by the finite width of the ring. We have shown that the maximum film thickness reduces as the pressure boundary conditions, located at $x = \pm a$, approach the origin symmetrically. The agreement between the City Experiments and this refined model shows varying degrees of improvement, particularly when the film thickness is near its maximum, although significant discrepancies remain.

5.3 Sources of Asymmetry

We now consider the asymmetry observed in the results of the City Experiments. The experimental results show the film thickness reaches two maxima throughout the period of oscillation, with the first maximum being consistently lower than the second. The ratio of the two maxima being roughly 0.84. We consider two models: the first model considers how a small degree of asymmetry in the geometry of the film may affect the mushy region. The second model studies the effects of small variations in the driving velocity of the bottom surface on the mushy region model.

5.3.1 Asymmetry of Ring Profile

In Section 5.2, we have considered how the finite width of the ring affects the mushy region model by implementing the atmospheric pressure boundary conditions at a finite (and symmetric) distance from the origin. We have shown that this improves the agreement with the experimental data; however, several discrepancies remain. The ring profile, shown in Figure 5.2, is roughly symmetric about its minimum and only departs from the parabolic profile $y = x^2/(2R_c)$ towards its edges. Despite this, it is clear that in each experiment the results show a consistent temporal asymmetry in the film thickness. We hypothesize that small asymmetries in the ring profile might cause the asymmetry observed in the experimental results, and test this theory by introducing some asymmetry into the model. In particular, we change the locations of the pressure boundary conditions to be

$$p = 0 \quad \text{at} \quad x = -a - \epsilon, \text{ and } a - \epsilon, \tag{5.14}$$

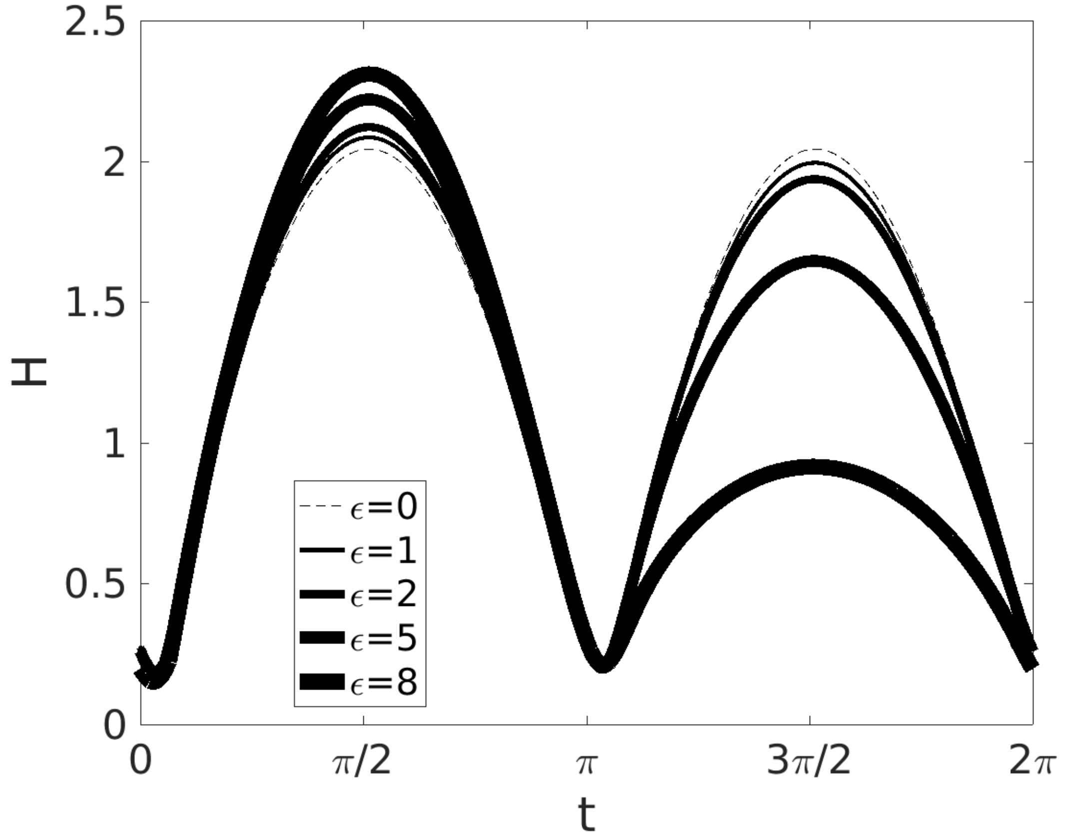

Figure 5.7: The effect of ring asymmetry on the film thickness. To obtain these solutions, we solved equations (3.89), (3.91), (3.92), (3.100)-(3.105), (3.126)-(3.131), (5.13), and (5.14) with parameters: $a = 10$, $\delta = 10^{-2}$, $\Omega = 1$ and four values of $\epsilon = 1$, 2, 5, and 8. The thinnest curve shows $\epsilon = 1$, the thickest curve shows $\epsilon = 8$, and the dashed curve shows the symmetric case $\epsilon = 0$.

where ϵ is the dimensionless horizontal distance between the minimum of the parabolic surface, and the mid-point of the ring, as indicated in Figure 5.11. We note, as $a \to \infty$, the shift in ϵ has a decreasingly significant effect. To study the effect ϵ has on the film we solve equations (3.89), (3.91), (3.92), (3.100)-(3.105), (3.126)-(3.131), and (5.14).

In Figure 5.7, we show how the film thickness behaves for increasing degrees of asymmetry. The solid curves show the film thickness with $\delta = 10^{-2}$, $\Omega = 1$, $a = 10$, and four values of $\epsilon = 1$, 2, 5 and 8. The thinnest curve shows $\epsilon = 1$, the thickest curve shows $\epsilon = 8$, and the dashed curve shows the symmetric case, $\epsilon = 0$. Over the first half of the cycle, $0 < t < \pi$, the film thickness increases slightly with increasing ring asymmetry. However, the opposite is true for the second half of the cycle, $\pi < t < 2\pi$. In this interval the film thickness consistently reduces from the symmetric case. Furthermore, the decrease in film height for $\pi < t < 2\pi$ is a more sensitive function of ϵ than the increase seen for $0 < t < \pi$.

In Figure 5.8, we show how the boundaries of the mushy region are affected by the asymmetry in the film. In contrast to the film thickness, the downstream boundary of the

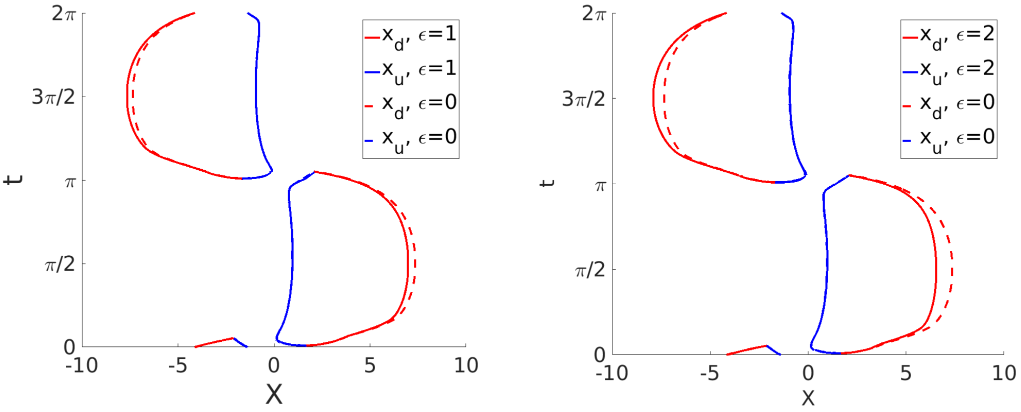

(a) $\epsilon = 1$. (b) $\epsilon = 2$.

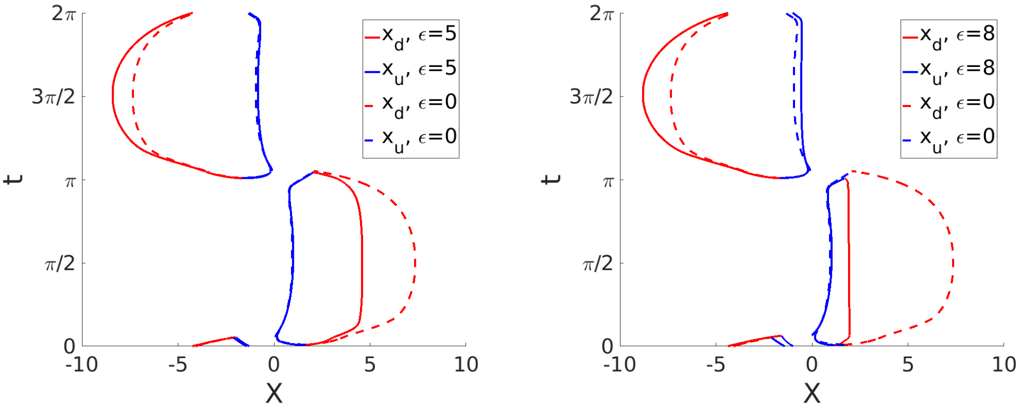

(c) $\epsilon = 5$. (d) $\epsilon = 8$.

Figure 5.8: We study the effect of asymmetry on the boundaries of the mushy region, shown as a function of time with x_d (red curve), and x_u (blue curve). The asymmetric model, shown as the solid curves, solved equations (3.89), (3.91), (3.92), (3.100)-(3.105), (3.126)-(3.131), (5.13), and (5.14) with parameters: $a = 10$, $\delta = 10^{-2}$, $\Omega = 1$, and four values of ϵ.

mushy region (on the right-hand side of the first mushy region) is significantly affected over the first half of the cycle, between $0 < t < \pi$, as it is confined to a smaller space as ϵ increases. For the largest asymmetry, $\epsilon = 8$, the first mushy region is shown to approach the edge of the ring profile very quickly where it remains for almost the entire half of the cycle, deviating only as the mushy region closes. Over the second half of the cycle, between $\pi < t < 2\pi$, the mushy region extends further into the liquid. Over this time, the downstream boundary (now on the left-hand side of the second mushy region) increases further into the film as ϵ increases. These results may be attributed to the decreasing influence of the pressure boundary condition in this limit. The upstream boundaries (on the left of the first mushy region and on the right of the second) remain largely unaffected throughout the cycle of oscillation.

We explain these observations in further detail with Figure 5.9, which shows the pressure

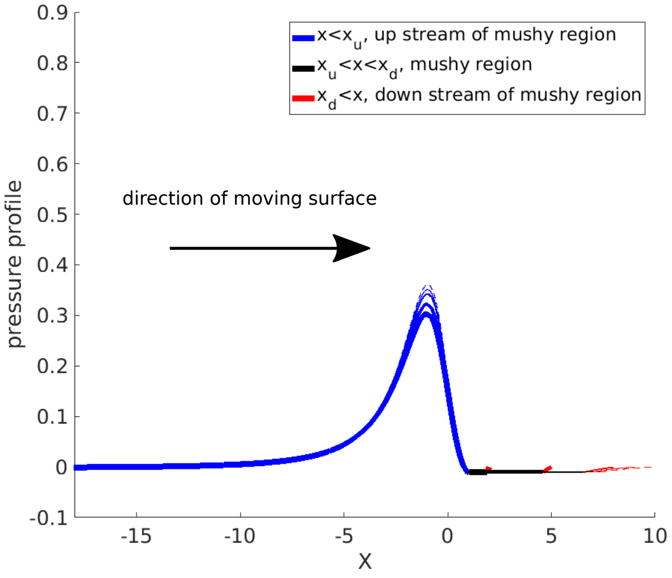

(a) $t = \pi/2$.

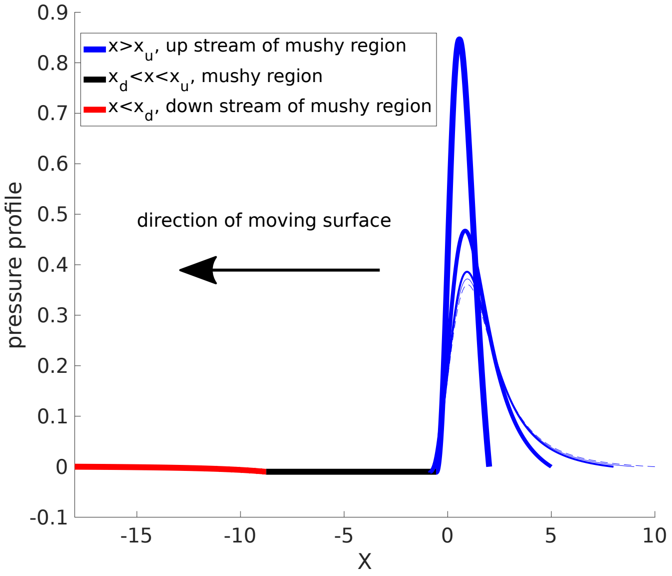

(b) $t = 3\pi/2$.

Figure 5.9: Pressure in the film with an increasing degree of asymmetry at two different times in the period of oscillation. Numerical solutions solve equations (3.89), (3.91), (3.92), (3.100)-(3.105), (3.126)-(3.131), (5.13), and (5.14) with parameters: $a = 10$, $\delta = 10^{-2}$, $\Omega = 1$, and four values of ϵ (1, 2, 5, and 8). The thinnest curve shows $\epsilon = 1$, the thickest curve shows $\epsilon = 8$, and the dashed curve shows the symmetric case $\epsilon = 0$. The blue curves show the pressure upstream of the mushy region, the red curves show the pressure downstream of the mushy region, and the black curve shows the pressure in the mushy region.

profile in the film between $-a < x < a$ at times $t = \pi/2$ and $t = 3\pi/2$, with parameters: $a = 10$, $\delta = 10^{-2}$, $\Omega = 1$, and varying with ϵ. Again, the dashed curve shows the symmetric case, and the solid curves show the asymmetric cases with $\epsilon = 1$ shown as the thinnest curve and $\epsilon = 8$ the thickest. The blue curves in the figure show the pressure upstream

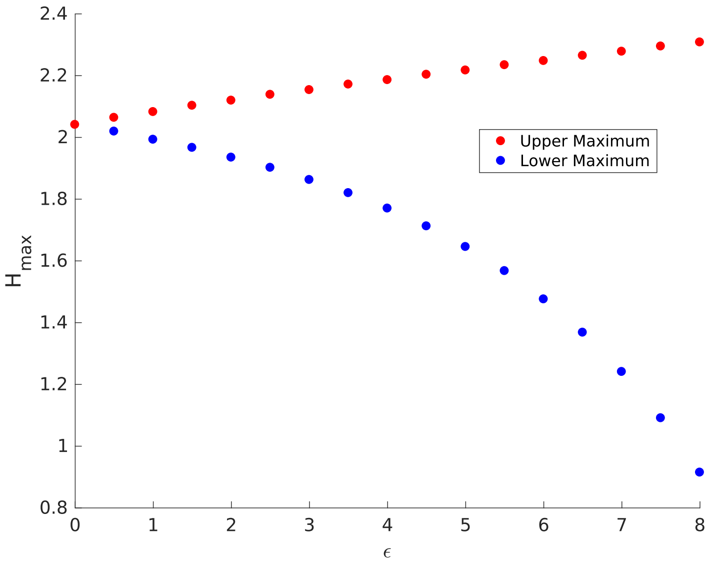

Figure 5.10: The upper and lower maximum film thickness, shown as red and blue dots respectively, over the range $0 < \epsilon < 8$. We note for small values of ϵ, the asymmetry between these two beaks increases in proportion to the asymmetry in the ring profile. Equations used to produce these solutions are (3.89), (3.91), (3.92), (3.100)-(3.105), (3.126)-(3.131), (5.13), and (5.14), with parameters: $a = 10$, $\delta = 10^{-2}$, and $\Omega = 1$.

of the mushy region, the red curves show the pressure downstream of the mushy region, and the black curves show the pressure inside the mushy region. In Figure 5.9(a), the bottom surface is moving to the right and the mushy region reduces in width as ϵ increases, contributing a smaller negative force to the force balance. To satisfy the force balance, the pressure upstream of the mushy region (which makes the largest contribution to the force balance) reduces accordingly; ultimately leading to an increase in the film thickness. In Figure 5.9(b), we show the pressure in the film at $t = 3\pi/2$ when the bottom surface is moving to the left. The mushy region, which is now to the left of the maximum pressure, occupies a larger area as the asymmetry in the film is increased. The mushy region, at this time, contributes very little to the force balance, which is mostly dominated by the pressure downstream of the mushy region, p_d. However, as the asymmetry is increased, the area over which p_d varies decreases, and therefore (to satisfy the force balance) the maximum pressure must increase. Eventually, as the asymmetry in the film becomes extreme, the weight of the top surface is supported by a small region of high pressure. As a consequence of the rapid increase in pressure, the film thickness decreases accordingly.

In Figure 5.10, we show the upper and lower maximum film thicknesses for increasing values of ϵ in the range $0 < \epsilon < 8$ with $a = 10$, $\delta = 10^{-2}$ and $\Omega = 1$. For small values of ϵ, increasing the ring asymmetry increases the asymmetry between the two maxima in the film

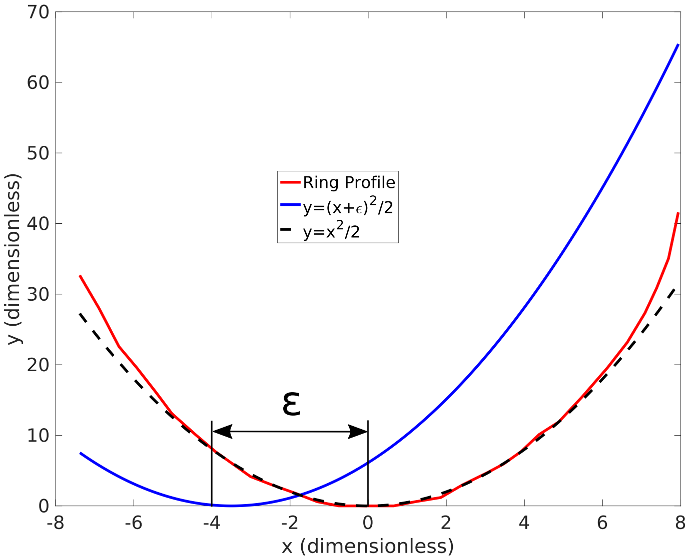

Figure 5.11: Ring profile used in the City Experiments, shown in red, the parabola with the offset, $y = (x + \epsilon)^2/2$, shown in blue, and the parabola $y = x^2/2$ without the offset, shown as a black dashed curve. In order to explain the asymmetry of the experimental results, ϵ would have to be of the order $\epsilon \approx 3.5$. We conclude the ring profile does not exhibit this degree of asymmetry, and so the asymmetry included in this model cannot fully explain the asymmetry in the experimental results. The ring profile was non-dimensionalized using parameters from test 1, $F = 977$ N/m and $\omega = 300$ rpm.

thickness. As ϵ is increased, the upper maximum changes comparatively very little, while for the lower maximum, the rate of decrease increases considerably. The ratio of the two maxima in the experimental data is roughly 0.84. Using Figure 5.10, we find a comparable ratio between the maximum film thicknesses in the numerical solution only occurs when ϵ is of the order $\epsilon \approx 3.5$. In Figure 5.11 we show the ring profile used in the experiment (red line) and the parabola $y = (x + \epsilon)^2/2$ (blue line). We dimensionalized the ring profile using parameters from test 1, $F = 977$ N/m and $\omega = 300$ rpm. Due to the significant difference in the location of the edges of the ring profile and the parabola, we conclude this effect cannot fully explain the asymmetry observed in the experimental results.

5.3.2 Asymmetry in the Velocity of the Bottom Surface

We now investigate whether the asymmetry observed in the City Experiment's results could be a result of temporal asymmetry in the velocity of the bottom surface. The City Experiment uses a Scotch Yoke mechanism, a diagram of which is shown in Figure 5.12, originally shown in Sawyer et al. (2003). To study the effect this would have on the system, we add

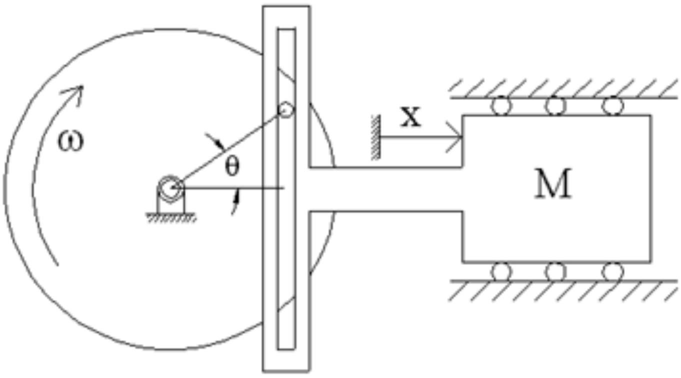

Figure 5.12: A diagram of a Scotch Yoke mechanism, as used in the City Experiments. A circular disk rotates in the clockwise direction which causes the horizontal movement of the mass M.

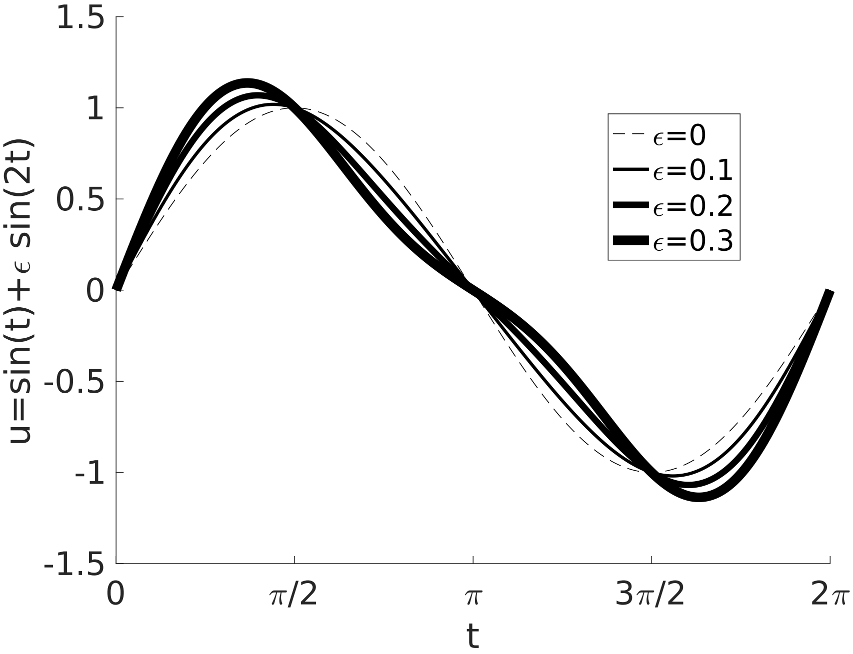

Figure 5.13: The velocity of the bottom surface against t for different values of ϵ: $\epsilon = 0$ case is the dashed curve, and the solid curves show $\epsilon = 0.1$ (thin curve), 0.2 (middle curve), and 0.3 (thick curve).

a small correction to the velocity on the bottom surface. In particular, we take

$$u = \sin(t) + \epsilon \sin(2t), \tag{5.15}$$

where $\epsilon \ll 1$. This form of the velocity was motivated to observe changes in the solution when in the solution is quasi-steady, and hence $u = O(1)$. We show u varying as a function of time in Figure 5.13 with the dashed curve showing $\epsilon = 0$ and the solid curves showing $\epsilon = 0.1$ (thin curve), 0.2 (middle curve), and 0.3 (thick curve).

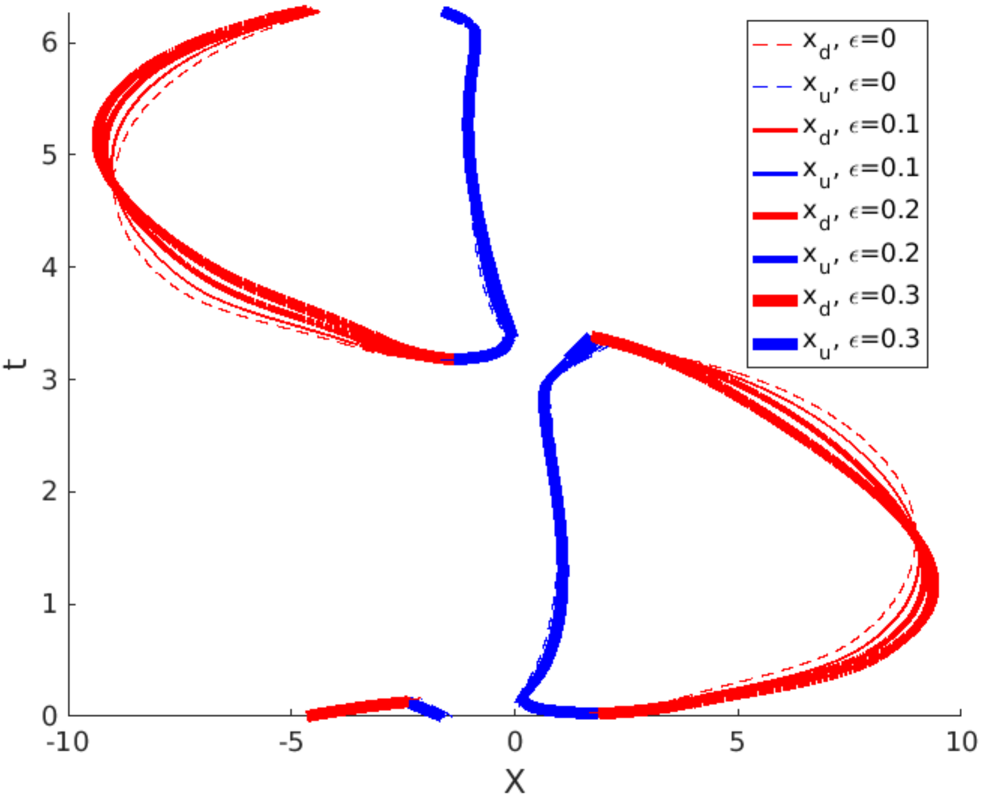

Figure 5.14: The boundaries of the mushy region as functions of time over the period of oscillation with x_d (red curve), and x_u (blue curve). Solutions were computed for four values of ϵ: 0, (dashed curve), and the solid curves show $\epsilon = 0.1$ (thin curve), 0.2 (middle curve), and 0.3 (thick curve). These solutions were obtained by solving equations (3.89)-(3.91), (3.100)-(3.103), (3.126)-(3.129), and (5.15) numerically with parameters $\delta = 10^{-2}$ and $\Omega = 1$.

We show the boundaries of the mushy region and the film thickness obtained from numerical solutions to equations (3.89)-(3.91), (3.100)-(3.103), (3.126)-(3.129), and (5.15) in Figures 5.14 and 5.15, respectively. The numerical solutions were computed with parameters $\delta = 10^{-2}$, $\Omega = 1$, and three values of $\epsilon = 0.1$ (thin curve), 0.2 (middle curve), and 0.3 (thick curve). The dashed curves show the case, $\epsilon = 0$.

Near the time $t = 0$ and $t = 2\pi$, we observe as ϵ is increased, the bottom surface accelerates at a faster rate, the downstream boundary extends a greater distance into the film, and the film thickness increases. We also note the film thickness, the downstream boundary, and the velocity of the bottom surface all reach a greater maxima as ϵ increases over the time $0 < t < \pi/2$ and $3\pi/2 < t < 2\pi$. However, at $t = \pi/2$ and $3\pi/2$, the velocity is $|u| = 1$ regardless of the value of ϵ, while the film thickness and downstream boundary approach the $\epsilon = 0$ solution. Contrary to this, near the time $t = \pi$, the opposite happens. When compared to the $\epsilon = 0$ case, the velocity of the bottom surface is slower,

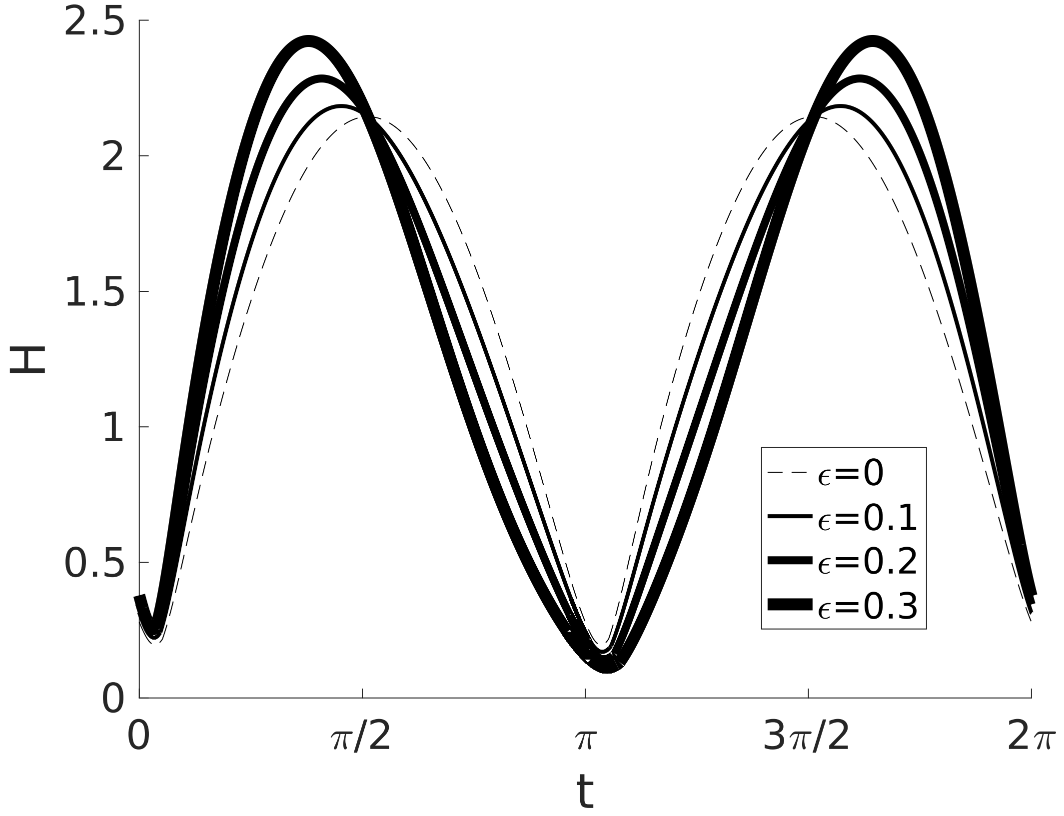

Figure 5.15: The film thickness against t for different values of ϵ: $\epsilon = 0$ case is the dashed curve, and the solid curves show $\epsilon = 0.1$ (thin curve), 0.2 (middle curve), and 0.3 (thick curve). These solutions were obtained by solving equations (3.89)-(3.91), (3.100)-(3.103), (3.126)-(3.129), and (5.15) numerically, with parameters $\delta = 10^{-2}$ and $\Omega = 1$.

the downstream boundary does not extend as far into the film, and the film thickness is smaller. We note that the upstream boundary shows similar behaviour to the downstream boundary in the different stages of the oscillation, but is difficult to observe on this scale. We explain these observations by referring back to Section 4.2. We know that as $\delta \to 0$, the numerical solution approaches the quasi-steady solution which is determined by the velocity of the bottom surface, u. We conclude that by changing the form of u, the numerical solution changes accordingly. However, the type of asymmetry shown in Figure 5.15 is not represented in the experimental results. We therefore conclude that any asymmetry of $u(t)$ is insignificant since this is the most natural type of asymmetry, which we describe more below. We conclude that this effect may be neglected.

Motion of the Piston-Crank Assembly in an Engine

We also consider how a more accurate representation of the motion of the piston-crank assembly in an engine affects the mushy region. Inside a car engine, the linear motion of

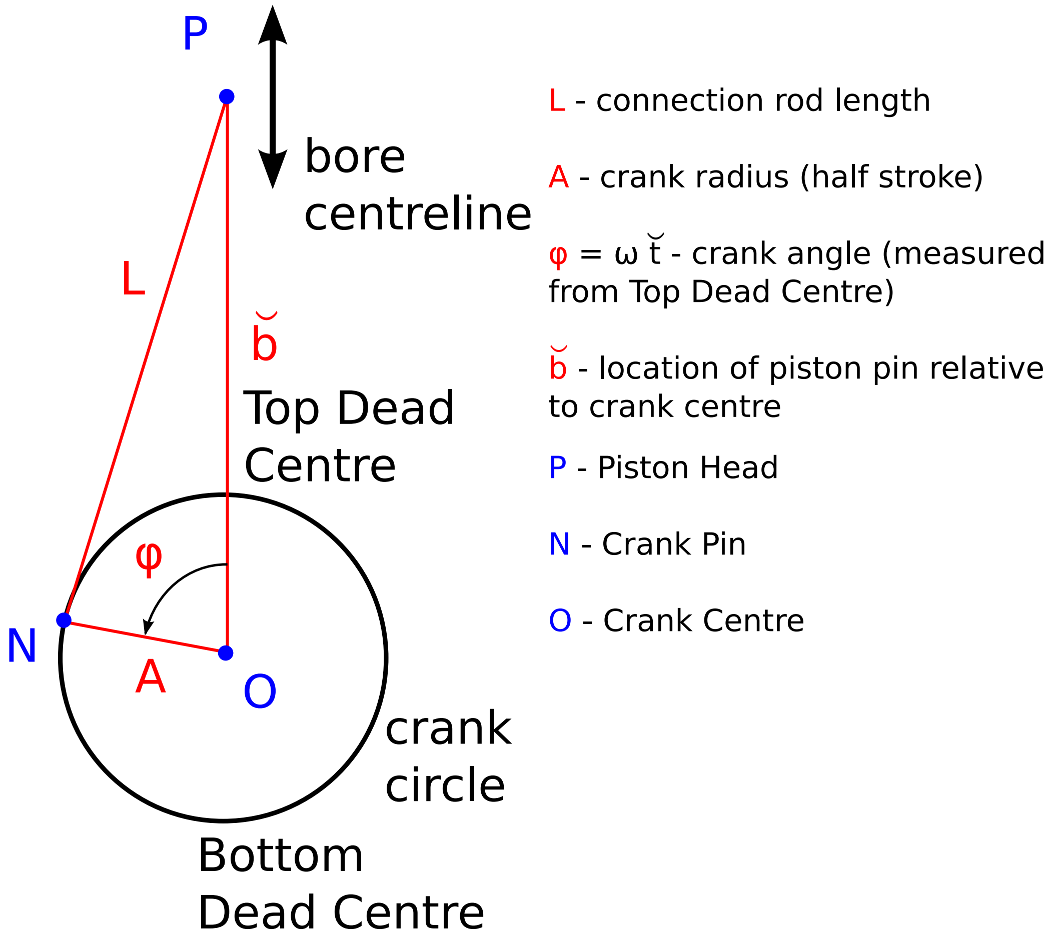

Figure 5.16: Schematic diagram showing the rotation of the crankshaft in relation to the motion of and piston head along the bore centre-line of an engine.

the piston is only approximately sinusoidal with time. A more accurate description of this motion includes an additional term that accounts for the connection between the piston head and crankshaft. Here, we seek an expression for the motion of a piston head as a function of time and investigate how, if at all, it changes the prediction of the mushy region model with a perfectly sinusoidal velocity.

The geometry of the piston-crank assembly in a car engine is shown in Figure 5.16. The crank radius rotates around the crank centre, point O, in an anti-clockwise direction at constant angular velocity, ω. The crank radius, which has length A, joins the connection rod at the point N (the crank pin). The piston head, point P, is at the opposite end of the connection rod; the connection rod has length L. We are interested in the motion of the point P, as a function of the crank angle, $\phi = \omega\breve{t}$, an overbar to denote dimensional variables, $\breve{t}$. Using the *cosine* rule, we write

$$L^2 = A^2 + \breve{b}(\breve{t})^2 - 2A\breve{b}(\breve{t})\cos(\omega\breve{t}), \tag{5.16}$$

and solving for $\breve{b}(\breve{t})$,

$$\breve{b}(\breve{t}) = A\cos(\omega\breve{t}) + \sqrt{L^2 - A^2\sin(\omega\breve{t})^2}. \tag{5.17}$$

The derivative of $\breve{b}(\breve{t})$ is the velocity of the bottom surface, $\breve{u}$, of the piston ring, i.e.:

$$\frac{d\breve{b}}{d\breve{t}} = \breve{u} = -A\omega\left(\sin(\omega\breve{t}) + \frac{A\sin(\omega\breve{t})\cos(\omega\breve{t})}{\sqrt{L^2 - A^2\sin(\omega\breve{t})}}\right). \tag{5.18}$$

Using the same non-dimensionalization as in section 3.5, this may be written

$$\breve{t} = \frac{t}{\omega}, \quad \breve{u} = \omega A u, \tag{5.19}$$

we introduce a third dimensionless parameter, the dimensionless crank radius κ, which is the ratio between the crank radius and the length of the connection rod:

$$\kappa = \frac{A}{L} < 1. \tag{5.20}$$

Typically, for a car engine, $\kappa \sim 0.3$ (Leach, 2016). The dimensionless velocity of the bottom surface, u, now has the form

$$u = \sin(t) + \frac{\kappa\sin(t)\cos(t)}{\sqrt{1 - \kappa^2\sin(t)}}. \tag{5.21}$$

Note that as $\kappa \to 0$, (5.21) reduces to simple sinusoidal motion. Qualitatively, for small values of $\kappa \approx 0.3$, the numerical solutions we computed show no discernible difference to the solutions shown in Figures 5.14 and 5.15 with a velocity given by (5.15).

5.3.3 Asymmetry of Oil Supply

The apparatus used in the City Experiments sits in a chamber flooded by the lubricant. The lubricant is recycled and filtered through a closed circuit and supplied to the chamber through a nozzle. It is possible that the orientation of the nozzle in the chamber may generate an unintended pressure gradient at one of the ring boundaries, making it easier for the lubricant to flow in a particular direction and contributing to the asymmetry observed in the experimental results. However, we do not have a way to estimate the effect this has on the experiment as the flow rate of the oil was not provided to us.

5.3.4 Summary

In this section, we have considered two potential causes that could explain the temporal asymmetry observed in the experimental results. We have shown that the effect of asymmetry in the ring profile is qualitatively right but is smaller than required to explain the experiments. The asymmetry of the driving velocity produces a different kind of asymmetry from that observed and so may be safely ignored.

5.4 Applications to Operating Engine Environments

So far in this thesis, we have mostly used the mushy region model to understand the City Experiments. We now consider how our model may be applied to more realistic operating engine environments. In particular, we consider the effect of periodic variations in the ring tension during the engine cycle, which ultimately cause a periodic variation in the normal force applied to the liquid film.

The tension in a piston ring, which exerts a normal force on the liquid film between the ring and the cylinder wall, may vary significantly throughout an engine cycle. One of the key factors that cause the variation in the ring tension is the gas chamber pressure, p_{ch}, which experiences a rapid increase as the combustion gases are ignited. We show how the gas pressure varies as the fuel is ignited on the right-hand axis in Figure 5.17 using data provided by BP. The high pressure from the combusted gases may flow between the piston ring and the piston head, pushing the piston ring against the cylinder wall and creating an additional force on the liquid film; a schematic of the piston head geometry is shown in Figure 1.3. We calculate the magnitude of the additional normal force ΔF, relative to the diametral tension of the ring $T_d = O(100 \text{ N/m})$, to be of the order

$$\Delta F = \frac{p_{ch} W_r}{T_d} = O(10) \tag{5.22}$$

where $W_r = O(1 \text{ mm})$ is the ring width Sang-Myung (2009).

Ignition in automobile engines occurs a short time, T, after the piston passes through Top Dead Centre (TDC), and hence near when the velocity of the bottom surface changes sign. In the experimental data shown in Figure 5.17, ignition occurs at $t = \pi + T$ where $T = 0.436$. Such a pressure peak only occurs once every two cycles: the first cycle being for combustion, and the second being used to clean out the products of combustion in the

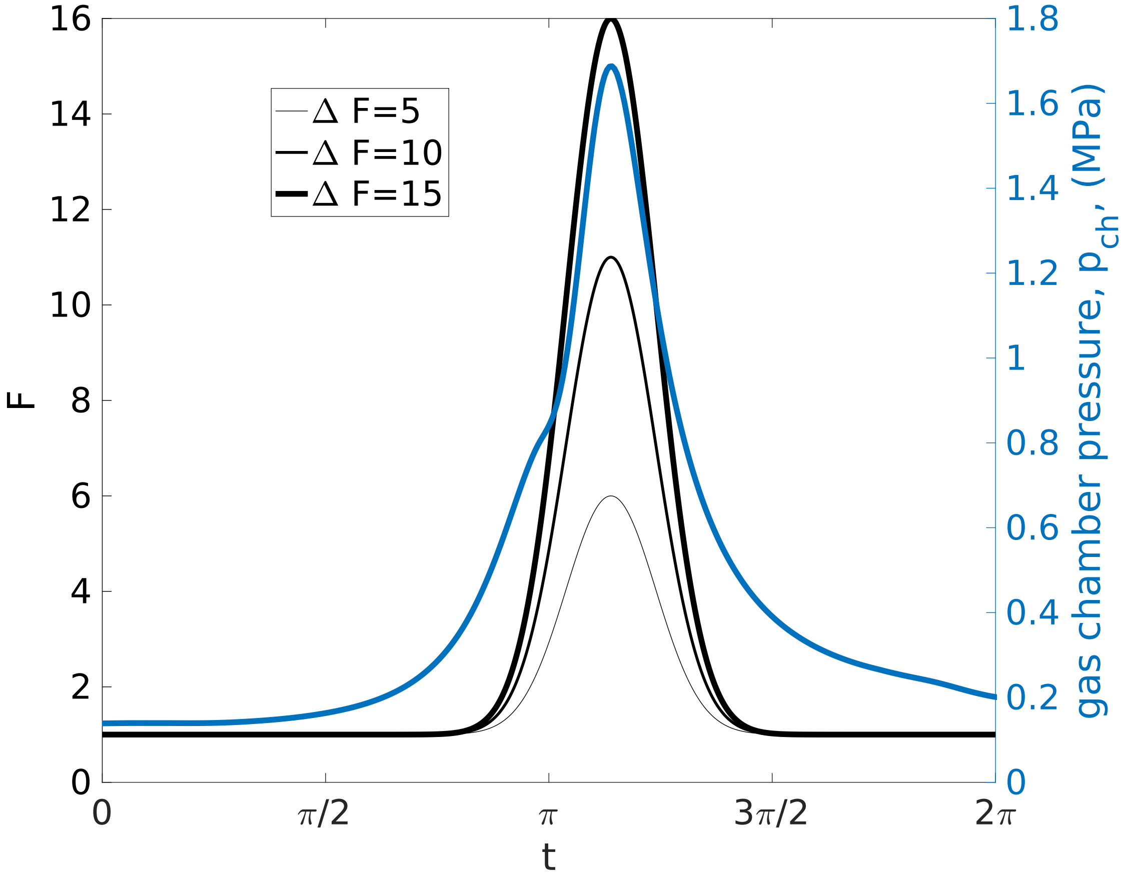

Figure 5.17: On the right-hand axis we show how the gas pressure, p_{ch}, in the combustion chamber varies as the fuel is ignited. The gas may flow between the piston head and piston ring, causing an additional normal force on the liquid film separating the piston ring and cylinder wall (a schematic of the piston head geometry is shown in Figure 1.3). The magnitude of this additional force could be as large as 10 times that of the diametral tension of the ring, motivating us to investigate the effect it has on the liquid film. On the left-hand axis, we show the normal force exerted on the liquid film used to develop the numerical solutions for this model, as described in (5.23). Three values of ΔF are shown: 5, (thin curve); 10, (middle curve); and 15, (thick curve). We chose the offset $T = 0.436$, so the peak in the normal force occurs at the same time as the peak in the gas pressure.

gas chamber. This motivates us to rewrite the force balance equation to include a normal force that varies with time,

$$\int_{-\infty}^{\infty} p dx = 1 + \Delta F e^{-(t-\pi-T)^2/4.9}. \tag{5.23}$$

Equation (5.23) is shown as a function of time for three values of ΔF: 5, (thin curve); 10, (middle curve); and 15, (thick curve) on the left-hand axis in Figure 5.17. We choose the width of the peak in the normal force to correspond as closely as possible to the width of the peak in the gas chamber pressure.

Figures 5.18 and 5.19 show the film thickness and the boundaries of the mushy region

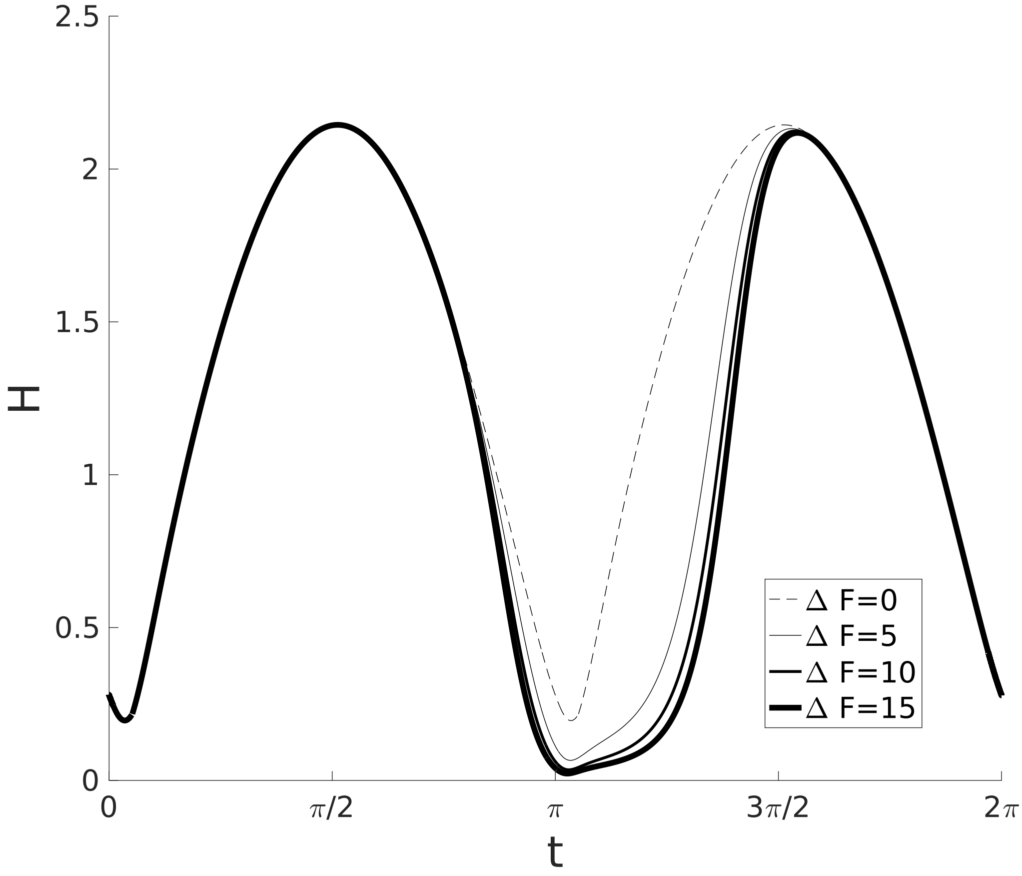

Figure 5.18: The film thickness as a function of time with variable applied force. We show four solutions, varying with the size of the non-uniformity in F, ΔF : 0, (dashed curve); 5, (thin solid curve); 10, (middle solid curve); and 15, (thick solid curve). Solutions are plotted from the numerical solutions to equations (3.89)-(3.91), (3.100)-(3.103), (3.126)-(3.129), and (5.23) with parameters $\delta = 10^{-2}$, $\Omega = 1$, and $T = 0.436$.

as functions of time with parameters $\delta = 10^{-2}$, $\Omega = 1$, and $T = 0.436$ and four values of ΔF: 0, (dashed curve); 5, (thin solid curve); 10, (middle solid curve); and 15, (thick solid curve). Numerical solutions have been computed by solving equations (3.89)-(3.91), (3.100)-(3.103), (3.126)-(3.129), and (5.23).

We note that when the normal force is close to one, the numerical solutions remain unchanged, even after the normal force has passed through its maximum. When the normal force increases, the film thickness decreases due to the increase in pressure required to satisfy the force balance. The most significant change observed in the boundaries of the mushy region occurs in the upstream boundary of the second mushy region, which persists further upstream towards the centre of the film. These results suggest that regardless of how the solution varies with the normal force, when the normal force is close to unity, the solution remains close to the $\Delta F = 0$ case. We also conclude that if the normal force increases with

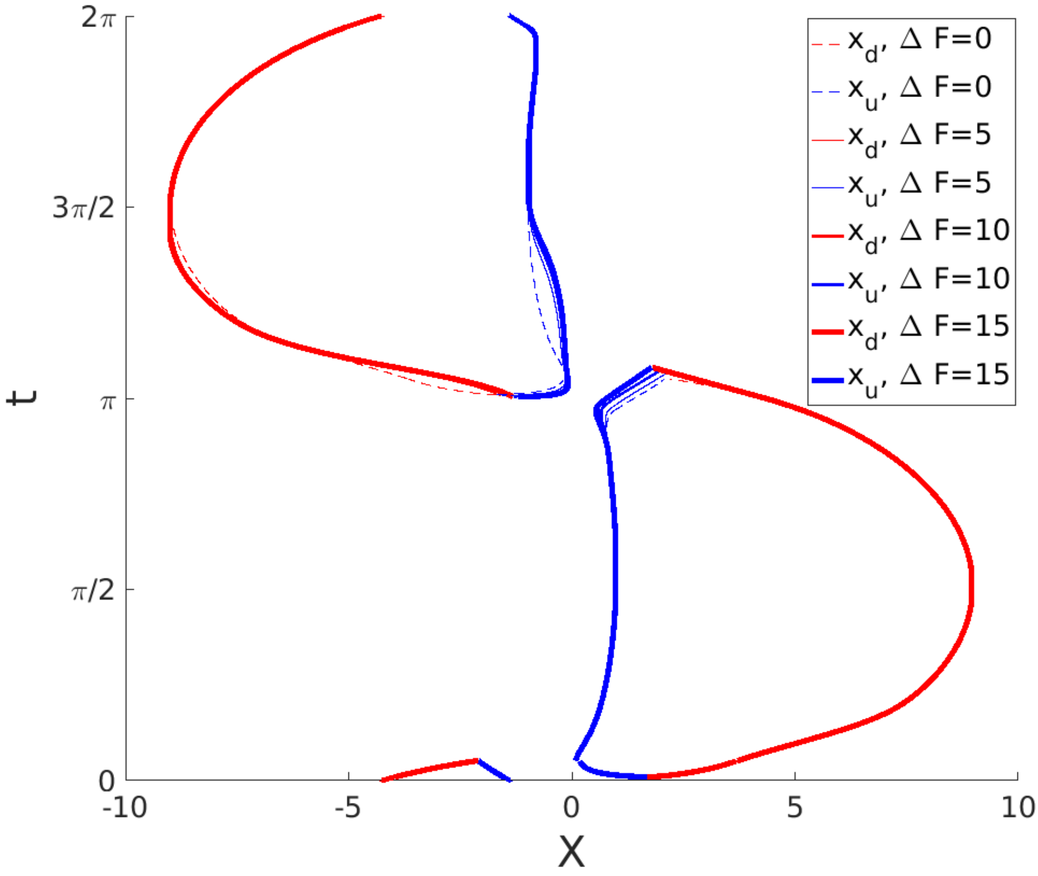

Figure 5.19: Boundaries of the mushy region, as functions of time with x_d (red curves) and x_u (blue curves). We show four solutions, varying with the size of the non-uniformity in the normal force, ΔF : $\Delta F = 0$, (dashed curve); $\Delta F = 5$, (thin solid curve); $\Delta F = 10$, (middle solid curve); and $\Delta F = 15$, (thick solid curve). Solutions are plotted from the numerical solutions to equations (3.89)-(3.91), (3.100)-(3.103), (3.126)-(3.129), and (5.23) with parameters $\delta = 10^{-2}$, $\Omega = 1$, and $T = 0.436$

time, the film thickness should decrease significantly, while the upstream boundary of the mushy region would extend towards the centre of the film.

5.5 Conclusions

In this chapter, we have investigated a number of modifications to the mushy region model described in Chapter 3. These modifications were intended to mimic important features of real-world experiments. In Section 5.1 we estimated the magnitude of various physical effects and showed these to be insignificant. The effects considered include: elasticity of the solid surfaces, the inertia of the top surface, the piezo-viscous effect, the compressibility of the liquid, and viscous heating. However, we showed that the roughness of both surfaces is greater than the minimum film thickness. From this, we conclude that the film transitions from the Full Film and Mixed Regime to the Boundary Regime (in the Stribeck Curve) during this time. This conclusion is consistent with the experimental observation that the friction increases dramatically during this part of the cycle. A common way to include the effects of surface roughness is to introduce an effective slip length between the solid and liquid surfaces. However, this is a significant undertaking and we make no such attempt here.

In Section 5.2, we considered how the finite width of the slider affects the mushy region model. We divided this section into two subsections. First, we showed how the mushy region model behaves when these edges are located symmetrically about the origin. Second, we compared the experimental data to the numerical solutions, choosing the location of the boundaries to correspond to the edges of the ring profile. This modification improved the agreement between, the mushy region model and the experimentally observed film thickness when it was near its maximum; however, other discrepancies still exist.

In Section 5.3 we considered three potential explanations of the asymmetry observed in the experimental results. We first considered how a small degree of asymmetry in the ring profile affects the film. Numerical solutions showed similar asymmetric qualities to the City Experiment's results, causing the maximum film thickness to increase in one half of the cycle, and decreases in the other. However, to achieve a degree of asymmetry similar to that observed in the experimental results, we found ϵ had to be significantly larger than the asymmetry exhibited in the ring profile. The second model considered how small variations in the velocity of the bottom surface affects the film thickness. The quasi-steady nature of the problem indicates that the solutions are driven by the velocity of the bottom surface, and hence any variations in the velocity will be reflected in the film thickness. We concluded that to achieve a similar degree of asymmetry to that observed in the City Experiments, the maxima of the velocity of the bottom surface in the respective halves of the period of oscillation would have to be a similar ratio to that of the maximum film thickness. We consider this to be unlikely to happen given the geometry used in the experiment. Lastly, we speculated whether an asymmetric supply of oil to the lubricant film could cause a pressure gradient across the film. However, we were not able to estimate the effect this has on the experiment as the rate at which the oil was supplied to the chamber was not provided. Further experimental investigations must be made to determine the cause of the asymmetry observed in the City Experiments.

In Section 5.4, we modified the mushy region model to consider more realistic operating conditions in an engine. In particular, we changed the normal force to vary as a function of time, which was motivated by an increase in the ring tension as the combustion gases are ignited. We approximated the increase in the normal force as a Gaussian curve, fitting the location and width of the peak in the curve to experimentally measured gas pressure data from a cylinder over the time of combustion, which was provided by BP. We concluded that an increase in the normal force correlates to a decrease in the film thickness, and the upstream boundary to persist further upstream, towards the centre of the film.

Chapter 6

Conclusions

Our principal aim has been to study cavitation in lubricating liquid films with a particular focus on the role of cavitation in wear and friction. For BP, who are the CASE collaborators of this study, the primary objective is to understand how to minimize both wear and friction experienced in engine parts. Summaries and discussions at the end of Chapters 2, 3, 4, and 5 provide detailed reviews of the key results obtained in those chapters. Here, we aim to give an overarching summary of the conclusions of our work and to suggest directions for future work. An executive summary is provided at the end of this chapter.

6.1 Review of Thesis

In Chapter 2 we consider the experiments of Zhu and Granick (2002c), in which the maximum normal force on a vertically oscillating solid sphere (immersed in oil) was measured. They observe that, above a critical shear rate, the maximum normal force deviates from the classical lubrication model, and attribute this to fluid slipping at the solid-liquid interface. We estimate the change in pressure in the film due to the vertical oscillation of the surface, and show that it is comparable to atmospheric pressure. This leads us to hypothesize that their results may, in fact, be caused by cavitation of the liquid. We show that the formation of cavities in the film is dependent on a single parameter, the dimensionless cavitation pressure, given by

$$p_c = (p_{atm} - p_{vap})\,\frac{H^2}{\mu A \omega R_c}, \tag{6.1}$$

where p_{atm} is the atmospheric pressure, p_{vap} is the vapour pressure of the liquid, H is the time-averaged minimum film thickness, μ is the viscosity of the liquid, R_c is the radius of curvature of the two surfaces, and A and ω are the amplitude and frequency of oscillation, respectively. We show that the pressure in the liquid only reduces below the cavitation pressure when p_c takes a value such that $0 < p_c < 3$. When $p_c = 3$, a cavitated region exists in the film, but only for a single point in time and location. For values of $p_c > 3$, the pressure in the liquid is never large enough to exceed the cavitation pressure, and so the film does not experience cavitation.

We consider two models of cavitation. In the first model, the bubble model, we assume a single cavitation bubble exists in the film, composed entirely of vapour. On the liquid-bubble interface, we apply the kinematic boundary condition, preventing liquid from crossing the interface. As the bubble expands radially, we find that the liquid pressure immediately outside the bubble reduces below the cavitation pressure. We, therefore, expect that further cavitation bubbles would form. This observation motivates us to consider a second model for cavitation, originally considered by Ockendon et al. (2003), which we refer to as the mushy region model. In this model, the cavitated region is a mixture of vapour and liquid (a mushy region), the physics of which we describe using macroscopic properties, such as pressure and volume fraction.

In the final section of Chapter 2 we compare the bubble model and mushy region model to two sets of experimental data from Zhu and Granick (2002c): (i) a control test that contains a small amount of surfactant, and (ii) an experiment that contains twice as much surfactant as the control test. The results from the control test are accurately predicted by the mushy region model for published physical properties of the liquid. In the second test, the mushy region model is able to reproduce the experimental results, but only when we use parameter values that are not consistent with those reported by Zhu and Granick (2002c). We also note that several important parameters in the model are not reported by Zhu and Granick (2002c).

In Chapter 3, we present a mathematical description of a set of experiments conducted at City University of London, referred to as the City Experiments, on cavitation in a liquid film undergoing oscillatory sliding motion, as might be found in the liquid film that lubricates a piston. In this chapter, we consider three variants of the model. In the first variation, we describe the cavitated region as a mushy region and assume the bottom surface moves at a constant speed. The non-dimensionalized model depends on a single parameter, the non-dimensionalized speed of the bottom surface. We study the steady state problem and determine the stability of this steady state. The second variant describes how the mushy region model closes as the velocity of the bottom surface decreases to zero dynamically. We show that, provided the intrinsic relaxation time-scale is sufficiently small, and the velocity itself is sufficiently large, the numerical solution closely approximates the quasi-steady solution. However, as the speed of the bottom surface reduces to zero, the dynamics really enter the problem.

We then consider how the mushy region evolves when the bottom surface oscillates in time. This model depends on two dimensionless parameters,

$$\delta = \omega R_c \sqrt{\frac{\mu}{FU}} \quad \text{and} \quad \Omega = \frac{\omega F}{(p_{atm} - p_{vap})\, U}, \tag{6.2}$$

where F is the applied normal force per unit width, U is the magnitude of the velocity of the bottom surface, ω is the frequency of oscillation, R_c is the radius of curvature, μ is viscosity of the liquid, and p_{atm} and p_{vap} are the atmospheric and vapour pressure respectively. Physically δ and Ω may be interpreted as follows: δ is the ratio between the horizontal length scale $\sqrt{R_c \check{H}}$ (where $\check{H} = R_c \mu U/F$ is the vertical length scale) and the amplitude of oscillation of the bottom surface U/ω; and Ω is the ratio $F/(p_{atm} - p_{vap})$, the length of the mushy region required to support the weight of the top surface, to U/ω. We show that, for the range of parameter values relevant to the City Experiments, the numerical solutions become independent of the initial conditions after the first half of the first period of oscillation. We also show how the mushy region behaves as δ and Ω change. Increasing Ω increases the maximum film thickness, while the minimum film thickness remains unchanged. As δ decreases to zero, the amplitude of oscillation in the film thickness increases and a second mushy regions forms on the opposite side of the parabolic surface before the first mushy region has closed. We also show that in the limit $\delta \to 0$, the numerical solutions recover the quasi-steady solution when the velocity of the bottom surface is sufficiently large, $u(t) \gg O(\delta)$.

In Chapter 4 we present analytical results for the asymptotic limit $\delta \to 0$, i.e. low oscillation frequency (or high load). Provided u is sufficiently large, and δ is sufficiently small, the problem becomes quasi-steady. As the velocity changes sign (small u), the model departs from the quasi-steady solution and is driven by the dynamics of the system. Over this time, the causality conditions on both of the mushy region boundaries change. Our key result is that the minimum film thickness decreases proportional to $\delta^{2/3}$ as $\delta \to 0$.

In the final section of Chapter 4, we discuss the discrepancies between the numerical and quasi-steady solutions and the experimental data. We compare four tests considered to be representative of all the results of the experiment to the numerical and quasi-steady solutions, showing varying degrees of success. For smaller values of δ, the numerical solutions agree with the data well when the velocity of the bottom surface is large. However, for larger values of δ, this comparison is not as good. We also calculate the friction generated from the shear of the liquid on the bottom surface and compare this with measured experimental data. We find good agreement when the velocity of the bottom surface is sufficiently large, but a significant deviation at small thicknesses where boundary friction is likely to take over.

In Chapter 5 we discuss extensions to the mushy region model to include additional effects. We first estimate the influence of various physical effects (elasticity, the inertia of the top surface, the Piezo-Viscous effect, the compressibility of the liquid, and viscous heating) and find them to be insignificant. However, we conclude that the roughness of the solid surfaces has a significant effect on the results of the experiment, particularly when the film thickness is small, so that the surfaces may come into contact.

In the second section of Chapter 5, we consider the influence of boundaries of the ring profile on the mushy region model. When the boundaries are located closer to the origin, we observe that the maximum film thickness decreases and the expansion of the mushy region into the liquid is restricted. We also compare the experimental data to the numerical solutions, choosing the location of the boundaries of the film to correspond to the edges ring profile. Including the finite width of the ring in the mushy region model improves the agreement between the numerical solutions and the experimental data when the film thickness is near its maximum; however other discrepancies, such as the minimum film thickness and the temporal asymmetry in the experimental data, remain unaccounted for. In the third section of the chapter, we consider three potential causes for the asymmetry observed in experimental results. First, we consider how a small degree of asymmetry in the geometry of the solid surfaces affects the mushy region model. However, we note that (for realistic parameter values) this is not able to generate as much asymmetry as seen experimentally. Second, we consider the effect of small variations in the velocity of the bottom surface on the mushy region model. The quasi-steady nature of the problem suggests that the solutions are driven by the velocity of the bottom surface, and hence any variation in the velocity will be reflected in the solution. However, we find that the variations in velocity typically present, are too small to explain the experimental observations. The final effect we discuss is whether an asymmetric supply of oil to the test chamber could cause a pressure gradient across the film. However, we are unable to estimate the effect this has on the experiment as the oil supply rate was not provided.

In the final section of Chapter 5, we apply the mushy region model to more realistic operating conditions as might occur in an engine. We modify the normal force to vary as a function of time (motivated by changes in the piston ring tension due to the rapid increase in pressure in the combustion chamber as the combustion gases are ignited). We conclude that an increase in the normal force causes a decrease in the film thickness and the upstream boundary of the mushy region briefly moves upstream towards the centre of the film.

6.2 Future Work

In this chapter, we have presented a summary of the major findings of this thesis. We now make suggestions for future research that could build on these findings and enhance the discussions provided in the relevant chapters.

Effects of Surfactant and Amplitude of Oscillation in Zhu and Granick (2002c)

In Chapter 2 we show that the experimental results of Zhu and Granick (2002c) can be accurately reproduced with our mushy region model. However, we were required to use parameter values that are inconsistent with those reported, specifically: the amplitude of oscillation A and vapour pressure of the liquid p_{vap}. Due to compliance from the glue holding the mica sheets onto the glass cylinder, it is possible that the amplitude of oscillation reported by Zhu and Granick (2002c) is not the true amplitude experienced by the liquid film. Also, in each of their experiments, Zhu and Granick (2002c) include various concentrations of the surfactant 1-hexadecylamine in the liquid. Krotov and Rusanov (1982) show that surfactants absorbed onto the liquid-vapour interface will cause the vapour pressure to increase (because of a decrease in surface energy). However, Krotov and Rusanov (1982) only study a single bubble in an infinite medium and not a region of vaporous bubbles formed by cavitation. We also note that, due to potentially rapid variations in the surface area of a cavitation bubble, the vapour-liquid interface may not be in equilibrium with the bulk of the liquid as the change in surface area would have to be considered. We recommend studying the influence that these effects may have on the mushy region model in further detail, to see whether the experimental results of Zhu and Granick (2002c) can be reproduced with more realistic parameter values.

Surface Roughness in City Experiments

In Chapter 4, we compare the mushy region model to the results of the City Experiment. The numerical solutions consistently under-predict the minimum film thickness for all tests. We also calculate the friction generated by the liquid on the stationary surface and compare with the experiments. When the velocity of the bottom surface is large, the two are in good agreement, indicating that the liquid is the main source of friction in the film for this part of the cycle. When the velocity of the bottom surface changes sign, the model predicts that the friction would pass through zero smoothly. However, the experimental data shows that the friction rapidly increases over this time, and the maximum measured friction is an order of magnitude larger than the maximum predicted by the numerical model. The experimenters hypothesize that the rapid increase in friction as the velocity changes sign is due to the rough solid surfaces making physical contact and sliding against each other. It would be interesting to explore how the models developed here could be extended to include a region of elastic contact between the surfaces.

Asymmetry in City Experiments

In Chapter 5 we attempt to understand why the experimental data is asymmetric: the maximum of the film thickness in the second half of the cycle is greater than that observed in the first. We develop two models to explain this behaviour: the first includes an asymmetric ring profile and the second studies the effect of a small correction to the time dependence in the velocity of the bottom surface. However, neither model could account for the asymmetry exhibited in the experimental results. We speculate that the asymmetry may be caused by a non-uniformity in the supply of oil to the lubricating film. Such an asymmetry could cause the pressure at one edge of the ring profile to be non-zero, hence assisting or preventing the liquid from flowing in a particular direction. However, details of the oil supply were not provided to us, and therefore, we do not have reliable ways to estimate the magnitude of this effect. We believe that if this information could be obtained, it might provide an explanation for the asymmetry in the experiment and therefore suggest this as an area of study for future research. Further experimental investigations, conducted in tandem with the mathematical models used to study them, would provide a wealth of knowledge that could answer to these questions.

Experimental Validation of Mushy Region Model as Applied to Engine Environments

We develop two models in Chapter 5 that extend the mushy region model to be more applicable to a 'real-world' engine environment. Firstly, we modified the velocity of the bottom surface to be more representative of a piston-crank assembly. Secondly, we modified the normal force exerted on the liquid film so that it varies as a function of time (this was motivated by the change in the tension of the piston ring as the combustion gases are ignited). We recommend the results of these models be validated against experiments.

6.3 Executive Summary

In this thesis, we have developed models that describe the process of cavitation in thin lubricant films. We systematically derived a range of models that show how a mushy region (a region in the liquid that is a combination of liquid and vapour) forms as a result of low pressure in the film, expands and eventually collapses. We have compared our mushy region model to experimental data, and have made suggestions on what could be done to improve the comparison. This model has provided a basic framework to quantify and understand the dynamic processes of cavitation in lubricant films.

The key findings relevant to cavitation in liquid squeeze films that undergo purely vertical forced oscillatory motion are:

- A single bubble in a liquid film will form smoothly, but exhibit a violent collapse as it closes.
- Due to the Saffman–Taylor instability, a single bubble expanding into liquid is likely to break up into a multitude of smaller bubbles; we model this as a mushy region.
- The evolution of the mushy region is symmetric in time; it expands and collapses rapidly as it opens and closes.
- Cavitation is a plausible physical mechanism that explains the experiments of Zhu and Granick (2002c) without resorting to slip.

The key findings relevant to a liquid film that experiences cavitation in a slider bearing-like geometry are:

- A liquid film that cavitates due to low pressures generated from a sliding surface may be successfully modelled as a mushy region.
- Care should be taken when the direction of information flows from the boundaries of the mushy region changes.
- If the horizontal length scale of the lubricant film ($\sqrt{\check{H}R_c}$) is much smaller than the amplitude of oscillation of the bottom surface, A, then the solution is quasi-steady for some region between Top Dead Center (TDC) and Bottom Dead Center (BDC). Otherwise, the evolution is truly dynamic.
- When the system is quasi-steady, any variations in the velocity of the bottom surface are reflected in the solution.
- Soon after the velocity of the bottom surface changes sign, two mushy regions may briefly exist simultaneously on opposite sides of the film.
- The film thickness is maximal when the velocity of the bottom surface is near its maximum but the film thickness is minimal shortly *after* the velocity of the bottom surface changes sign.
- Neither the upstream nor the downstream boundaries of the mushy region pass through the centre of the film; this restricts the location of the mushy region to whichever half of the film it originated in.
- The asymmetry in the experimental data is not caused by the asymmetry in the ring profile or the scotch-yoke mechanism used to drive the bottom surface.

Appendix A

ode15s Algebraic Differential Equation Solver

Here we describe the numerical method used to solve the mushy region model, ode15s, and refer the reader to Shampine et al. (1999) for more details on the solver. ode15s is based on a variant of backward differentiation formulas called numerical differentiation formulas. It was developed to integrate stiff differential equations of the form

$$\mathbf{M}(t)\mathbf{y}'(t) = \mathbf{F}(\mathbf{y}(t), t) \tag{A.1}$$

where $\mathbf{M}(t)$ is the mass matrix and $\mathbf{y}(t)$ is the solution vector. ode15s is a quasi-constant step size code of numerical differentiation formulas using backward differences. Let $\mathbf{U}\boldsymbol{\Sigma}\mathbf{V}^T$ be the singular decomposition to $\mathbf{M}(t_0)$, where $\mathbf{U}$ and $\mathbf{V}$ are orthogonal matrices, $\boldsymbol{\Sigma} = \operatorname{diag}(\mathbf{D}\ 0)$, and $\mathbf{D}$ is a diagonal matrix of non-singular values of $\mathbf{M}(t_0)$, at $t = t_0$. Using the time independent transformation $\mathbf{Y} = \mathbf{V}^T\mathbf{y}$, (A.1) becomes

$$\boldsymbol{\Sigma}\left(\frac{\tilde{\mathbf{Y}} - \mathbf{Y}_0}{h}\right) = \mathbf{U}^T hbfF\left(t_0, \mathbf{V}\tilde{\mathbf{Y}}\right) = \tilde{\mathbf{F}}\left(t_0, \tilde{\mathbf{Y}}\right), \tag{A.2}$$

and h is the time step. The structure of $\boldsymbol{\Sigma}$ yields a partition of $\mathbf{Y}$ into $\left(\mathbf{u}^T\mathbf{v}^T\right)^T$ and $\tilde{\mathbf{F}}$ into $\left(\hat{\mathbf{f}}_1^T\mathbf{f}_2^T\right)^T$ where $\mathbf{f}_1\left(t_0, \tilde{\mathbf{u}}, \tilde{\mathbf{v}}\right) = D^{-1}\hat{\mathbf{f}}_1\left(t_0, \tilde{\mathbf{u}}, \tilde{\mathbf{v}}\right)$. Equation (A.2) reads

$$\tilde{\mathbf{u}} - \mathbf{u}_0 - h\mathbf{f}_1\left(t_0, \tilde{\mathbf{u}}, \tilde{\mathbf{v}}\right) = 0, \quad \mathbf{f}_2\left(t_0, \tilde{\mathbf{u}}, \tilde{\mathbf{v}}\right) = 0. \tag{A.3}$$

We write system (A.3) as $\mathbf{G}\left(\mathbf{u}_0, h; \tilde{\mathbf{u}}, \tilde{\mathbf{v}}\right) = 0$. When evaluated at $\left(\mathbf{u}\left(t_0\right), 0; \mathbf{u}\left(t_0\right), \mathbf{v}\left(t_0\right)\right)$, the Jacobian of (A.3), $\mathbf{J}$, with respect to $\tilde{\mathbf{u}}$ and $\tilde{\mathbf{v}}$ has the form

$$\mathbf{J} = \begin{pmatrix} \mathbf{I} & 0 \\ \frac{\partial \mathbf{f}_2}{\partial \mathbf{u}} & \frac{\partial \mathbf{f}_2}{\partial \mathbf{v}} \end{pmatrix}. \tag{A.4}$$

Assuming the index of $\mathbf{M}(t)$ is of order 1, the block $\partial \mathbf{f}_2 / \partial \mathbf{v}$ is non-singular at $\left(\mathbf{u}\left(t_0\right)^T \mathbf{v}\left(t_0\right)^T\right)^T$, and hence $\mathbf{J}$ is non-singular as well. Provided $\mathbf{f}_1$ and $\mathbf{f}_2$ are smooth, both the function $\mathbf{G}$ and its Jacobian are continuous in a neighbourhood of $\left(\mathbf{u}\left(t_0\right), 0; \mathbf{u}\left(t_0\right), \mathbf{v}\left(t_0\right)\right)$. The implicit function theorem implies that for all $\mathbf{u}_0$ sufficiently close to $\mathbf{u}\left(t_0\right)$ and all sufficiently small h, (A.2) has solution $\left(\tilde{\mathbf{u}}^T \tilde{\mathbf{v}}^T\right)^T$, and as $h \to 0$, it converges to $\left(\mathbf{u}\left(t_0\right)^T \mathbf{v}\left(t_0\right)^T\right)^T$.

Appendix B

Equation for the Linear Stability of the Steady State

We write the characteristic equation for the eigenvalue, λ, of the constant velocity mushy region model, discussed in section 3.3.4. Using the ansatz for the variables $x_d(t)$, $x_u(t)$, and $H(t)$,

$$x_d(t) = x_{d0} + x_{\lambda,d1}\epsilon e^{-\lambda t}, \tag{B.1a}$$

$$x_u(t) = x_{u0} + x_{\lambda,u1}\epsilon e^{-\lambda t}, \tag{B.1b}$$

$$H(t) = H_0 + H_{\lambda,1}\epsilon e^{-\lambda t}, \tag{B.1c}$$

$$\theta(x,t) = \theta_{\lambda,0}\left(x\right) + \theta_{\lambda,1}\left(x\right)\epsilon e^{-\lambda t}, \tag{B.1d}$$

where x_{d0}, x_{u0}, and H_0 are the solutions to the steady state problem in section 3.3.3. The system of equations may now be written simply in the form

$$\begin{bmatrix} f_{11} & 0 & f_{13} \\ f_{21} & f_{22} & f_{23} \\ f_{31} & f_{32} & f_{33} \end{bmatrix} \begin{bmatrix} x_{\lambda,u1} \\ x_{\lambda,d1} \\ H_{\lambda,1} \end{bmatrix} = \begin{bmatrix} 0 \\ 0 \\ 0 \end{bmatrix}. \tag{B.2}$$

Setting the determinate of (B.2) to zero, we derive the characteristic equation for λ,

$$\begin{aligned} &(f_{21} - f_{31}) + (-f_{11}f_{22} + f_{11}f_{23} + f_{11}f_{32} - f_{11}f_{33} - f_{13}f_{21} + f_{13}f_{31} - f_{21}f_{32} + f_{22}f_{31}) \\ &(f_{11}f_{22}f_{33} - f_{11}f_{23}f_{32} + f_{13}f_{21}f_{32} - f_{13}f_{22}f_{31}) = 0, \end{aligned} \tag{B.3}$$

where $f_{m,n}$, $[m,n] \in [1,2,3]$ have the form

$$f_{1,1} = \frac{3U_0}{4}\left(-\frac{3x_{u0}\left(2\tan^{-1}\left(\frac{x_{u0}}{\sqrt{2H_0}}\right)+\pi\right)}{\sqrt{2H_0^5}} - \frac{6}{H_0^2} + \frac{4}{H_0\left(2H_0+x_{u0}^2\right)} + \frac{16}{\left(2H_0+x_{u0}^2\right)^2}\right), \tag{B.4}$$

$$\begin{aligned} f_{1,3} &= \lambda\left(\frac{3\left(3x_{u0}^2+4H_0\right)}{H_0^2\left(2H_0+x_{u0}^2\right)} + \frac{9H_0x_{u0}\left(\pi+2\tan^{-1}\left(\frac{x_{u0}}{\sqrt{2H_0}}\right)\right)}{2\sqrt{2H_0^3}}\right) \\ &+ \frac{3U_0x_{u0}\left(12H_0^2+44H_0x_{u0}^2+15x_{u0}^4\right)}{8H_0^3\left(2H_0+x_{u0}^2\right)^2} - \frac{9U_0\left(2H_0-5x_{u0}^2\right)\left(\pi-2\tan^{-1}\left(\frac{x_{u0}}{\sqrt{2H_0}}\right)\right)}{16\sqrt{2H_0^7}}, \\ f_{2,1} &= \frac{3U_0x_{u0}}{8H_0^{5/2}}\left(\frac{-4\sqrt{H_0}x_{d0}\left(10H_0+3x_{d0}^2\right)}{\left(2H_0+x_{d0}^2\right)^2} + 3\sqrt{2}\left(\pi-2\tan^{-1}\left(\frac{x_{d0}}{\sqrt{2H_0}}\right)\right)e^{\frac{2\lambda(x_{d0}-x_{u0})}{U_0}}\right), \end{aligned} \tag{B.5}$$

$$f_{2,2} = 3(x_{u0}-x_{d0})(x_{u0}+x_{d0})\left(\frac{3\lambda(\pi-2\tan^{-1}\left(\frac{x_{d0}}{\sqrt{2H_0}}\right)}{4\sqrt{2H_0^5}} - \frac{\lambda x_{d0}\left(10H_0+3x_{d0}\right)}{2H_0^2\left(2H_0+x_{d0}^2\right)^2} - \frac{8U_0}{\left(2H_0+x_{d0}^2\right)^3}\right), \tag{B.6}$$

$$\begin{aligned} f_{2,3} &= 3\lambda\left(\frac{3}{H_0^2} - \frac{2}{H_0\left(2H_0+x_{d0}^2\right)} - \frac{3x_{d0}\left(\pi-2\tan^{-1}\left(\frac{x_{d0}}{\sqrt{2H_0}}\right)\right)}{2\sqrt{2H_0^5}}\right) \\ &+ \frac{3U_0x_{d0}\left(4H_0^2\left(26H_0+33x_{u0}^2\right)+3x_{d0}^4\left(2H_0+5x_{u0}^2\right)+16H_0x_{d0}^2\left(2H_0+5x_{u0}^2\right)\right)}{8H_0^3\left(2H_0+x_{d0}^2\right)^3} \\ &- \frac{9U_0}{8\sqrt{2H_0^5}\left(2H_0+x_{d0}^2\right)^3}\left[\pi+2\tan^{-1}\left(\frac{x_{d0}}{\sqrt{2}\sqrt{H_0}}\right)\right]\left(\left(4e^{\frac{2\lambda(x_{d0}-x_{u0})}{U_0}}-2\right)-5x_{u0}^2\right), \end{aligned} \tag{B.7}$$

$$\begin{aligned} f_{3,1} &= \frac{3U_0x_{u0}\left(2\sqrt{H_0}\left(4H_0+3x_{d0}^2\right)-3\sqrt{2}x_{d0}\left(2H_0+x_{d0}^2\right)\cot^{-1}\left(\frac{x_{d0}}{\sqrt{2H_0}}\right)\right)e^{\frac{2\lambda(x_{d0}-x_{u0})}{U_0}}}{4H_0^{5/2}\left(2H_0+x_{d0}^2\right)} \\ &- \frac{3U_0x_{u0}\left(10H_0+9x_{u0}^2\right)}{4H_0^2\left(2H_0+x_{u0}^2\right)} + \frac{3U_0\left(2H_0-9x_{u0}^2\right)}{8\sqrt{2H_0^5}}\left(\pi+2\tan^{-1}\left(\frac{x_{u0}}{\sqrt{2H_0}}\right)\right)+1, \end{aligned} \tag{B.8}$$

$$\begin{aligned} f_{3,2} &= \frac{3U_0x_{d0}\left(4H_0^2+10H_0x_{u0}^2-2H_0x_{d0}^2+3x_{u0}^2x_{d0}^2\right)}{4H_0^2\left(2H_0+x_{d0}^2\right)^2} + \frac{3U_0\left(2H_0-3x_{u0}^2\right)\cot^{-1}\left(\frac{x_{d0}}{\sqrt{2}\sqrt{H_0}}\right)}{4\sqrt{2H_0^2}} \\ & 3\lambda(x_{u0}-x_{d0})(x_{u0}+x_{d0})\left(\frac{\left(4H_0+3x_{d0}^2\right)}{2H_0^2\left(2H_0+x_{d0}^2\right)} - \frac{3x_{d0}}{2\sqrt{2H_0^2}}\cot^{-1}\left(\frac{x_{d0}}{\sqrt{2}\sqrt{H_0}}\right)\right), \end{aligned} \tag{B.9}$$

$$
\begin{aligned}
f_{3,3} = {} & \frac{6\lambda\left(\left(2H_0+3x_{u0}^2\right)\left[\pi+2\tan^{-1}\left(\frac{x_{u0}}{\sqrt{2H_0}}\right)\right]+\left(2H_0+3x_{d0}^2\right)\cot^{-1}\left(\frac{x_{d0}}{\sqrt{2H_0}}\right)+6\sqrt{H_0}(x_{u0}-x_{d0})\right)}{2\sqrt{2H_0^5}} \\
& + \frac{9U_0x_{d0}\left(H_0\left(2-4e^{\frac{2\lambda(x_{d0}-x_{u0})}{U_0}}\right)+5x_{u0}^2\right)\cot^{-1}\left(\frac{x_{d0}}{\sqrt{2H_0}}\right)}{8\sqrt{2H_0^7}} \\
& + \frac{9U_0x_{u0}\left(5x_{u0}^2-2H_0\right)}{8\sqrt{2H_0^7}}\left(\pi+2\tan^{-1}\left(\frac{x_{u0}}{\sqrt{2H_0}}\right)\right)+8H_0^{3/2}\left(4H_0+3x_{d0}^2\right)e^{\frac{2\lambda(x_{d0}-x_{u0})}{U_0}} \\
& + \frac{8H_0^{3/2}\left(-32H_0^3-4H_0^2x_{u0}^2-52H_0^2x_{d0}^2+14H_0x_{u0}^4-32H_0x_{u0}^2x_{d0}^2-14H_0x_{d0}^4+5x_{u0}^4x_{d0}^2-11x_{u0}^2x_{d0}^4\right)}{\left(2H_0+x_{u0}^2\right)\left(2H_0+x_{d0}^2\right)^2}.
\end{aligned}
\tag{B.10}
$$

Appendix C

Closing Mushy Region Model Differential Equations

This appendix shows the differential equations for the derivatives dH/dt, dx_L/dt, and dx_R/dt, that describe the mushy region model in the various sections of the numerical computation, as the mushy region is closing as the velocity of the bottom surface decreases to zero with the form

$$U_0 = \hat{U}_0 \left(1 - 2\alpha t\right). \tag{C.1}$$

Equations used to derive these equations are listed in (3.11)-(3.16) and (3.75). We start where the characteristics leave the right hand boundary, and thus solve for the derivatives H and x_R, which are stated below:

$$\frac{dH}{dt} = -\frac{U_0 \left(D_1 E_3 - D_2 E_2\right) - D_1 - E_2}{D_1 E_1 - D_3 E_2}, \tag{C.2}$$

$$\frac{dx_d}{dt} = -\frac{U_0 \left(D_3 E_3 - D_2 E_1\right) - D_3 - E_1}{D_3 E_2 - D_1 E_1}, \tag{C.3}$$

where

$$D_1 = 3(\theta_d - 1)\left(\frac{2x_d}{H\left(2H + x_d^2\right)} + \frac{3x_d}{2H^2} - \frac{3\left(2H + x_d^2\right)\left(\pi - 2\tan^{-1}\left(\frac{x_d}{\sqrt{2H}}\right)\right)}{4\sqrt{2H^5}}\right), \tag{C.4}$$

$$D_2 = -\frac{3(\theta_d - 2)x_d}{H\left(2H + x_d^2\right)} - \frac{9\theta_d x_d}{4H^2} + \frac{3(3\theta_d - 4)\left(\pi - 2\tan^{-1}\left(\frac{x_d}{\sqrt{2H}}\right)\right)}{4\sqrt{2H^3}} + \frac{9\theta_d x_d^2\left(\pi - 2\tan^{-1}\left(\frac{x_d}{\sqrt{2H}}\right)\right)}{8\sqrt{2H^5}}, \tag{C.5}$$

$$D_3 = -\frac{3\left(3x_d^2 + 4H\right)}{H^2\left(2H + x_d^2\right)} + \frac{9x_d\left(\pi - 2\tan^{-1}\left(\frac{x_d}{\sqrt{2H}}\right)\right)}{2\sqrt{2H^5}}, \tag{C.6}$$

$$E_1 = -\frac{6}{H}\left(\frac{x_u}{2H + x_u^2} - \frac{x_d}{x_d^2 + 2H}\right) - \frac{6}{\sqrt{2H^3}}\left(\pi + \tan^{-1}\left(\frac{x_u}{\sqrt{2H}}\right) - \tan^{-1}\left(\frac{x_d}{\sqrt{2H}}\right)\right), \tag{C.7}$$

$$E_2 = \frac{12(1 - \theta_d)\left(2H + x_d^2\right)}{\left(2H + x_d^2\right)^2}, \tag{C.8}$$

$$E_3 = -\frac{6}{2H + x_u^2} - \frac{6(\theta_d - 2)}{2H + x_d^2}, \tag{C.9}$$

and

$$\theta_d = \theta\left(x_d(t), t\right), \tag{C.10}$$

and θ is solved using (3.30).

When the characteristics exit through both the left and right hand interfaces, we solve for the three derivatives H, x_d, and x_u, which have the form

$$\frac{dH}{dt} = -\frac{U_0\left(A_1B_1C_4 - A_1B_2C_3 - A_2B_1C_2\right) - A_1B_1 - A_1C_3 - B_1C_2}{A_1B_1C_1 - A_1B_3C_3 - A_3B_1C_2}, \tag{C.11}$$

$$\frac{dx_u}{dt} = -\frac{U_0\left(A_1B_2C_1 - A_1B_3C_4 + A_2B_3C_2 - A_3B_2C_2\right) + A_1B_3 + A_1C_1 - A_3C_2 + B_3C_2}{A_1B_1C_1 - A_1B_3C_3 - A_3B_1C_2}, \tag{C.12}$$

$$\frac{dx_d}{dt} = -\frac{U_0\left(A_2B_1C_1 - A_2A_2B_3C_3 - A_3B_1C_4 + A_3B_2C_3\right) + A_3B_1 + A_3C_3 + B_1C_1 - B_3C_3}{A_1B_1C_1 - A_1B_3C_3 - A_3B_1C_2} \tag{C.13}$$

where

$$A_1 = 3(\theta_d - 1)\left(\frac{2x_d}{H\left(2H + x_d^2\right)} + \frac{3x_d}{2H^2} - \frac{3\left(2H + x_d^2\right)\left(\pi - 2\tan^{-1}\left(\frac{x_d}{\sqrt{2H}}\right)\right)}{4\sqrt{2H^5}}\right), \tag{C.14}$$

$$A_2 = -\frac{3(\theta_d - 2)x_d}{H\left(2H + x_d^2\right)} - \frac{9\theta_d x_d}{4H^2} + \frac{3(3\theta_d - 4)\left(\pi - 2\tan^{-1}\left(\frac{x_d}{\sqrt{2H}}\right)\right)}{4\sqrt{2H^3}} + \frac{9\theta_d x_d^2\left(\pi - 2\tan^{-1}\left(\frac{x_d}{\sqrt{2H}}\right)\right)}{8\sqrt{2H^5}}, \tag{C.15}$$

$$A_3 = -\frac{3\left(3x_d^2 + 4H\right)}{H^2\left(2H + x_d^2\right)} + \frac{9x_d\left(\pi - 2\tan^{-1}\left(\frac{x_d}{\sqrt{2H}}\right)\right)}{2\sqrt{2H^5}}, \tag{C.16}$$

$$B_1 = \frac{6(\theta_u - 1)x_u}{H\left(2H + x_u^2\right)} + \frac{9(\theta_u - 1)x_u}{2H^2} + \frac{9(\theta_u - 1)\left(2H + x_u^2\right)\left(2\tan^{-1}\left(\frac{x_u}{\sqrt{2H}}\right) + \pi\right)}{4\sqrt{2H^5}}, \tag{C.17}$$

$$B_2 = -\frac{3x_u\left(2(5\theta_u - 4)H + 3\theta_u x_u^2\right)}{4H^2\left(2H + x_u^2\right)} + \frac{3\left((6\theta_u - 8)H + 3\theta_u x_u^2\right)\left(\pi + 2\tan^{-1}\left(\frac{x_u}{\sqrt{2H}}\right)\right)}{8\sqrt{2H^5}}, \tag{C.18}$$

$$B_3 = -\frac{3\left(3x_u^2 + 4H\right)}{H^2\left(2H + x_u^2\right)} - \frac{9x_u\left(\pi + 2\tan^{-1}\left(\frac{x_u}{\sqrt{2H}}\right)\right)}{2\sqrt{2H^5}}, \tag{C.19}$$

$$C_1 = -\frac{6}{H}\left(\frac{x_u}{2H + x_u^2} - \frac{x_d}{x_d^2 + 2H}\right) - \frac{6}{\sqrt{2H^3}}\left(\pi + \tan^{-1}\left(\frac{x_u}{\sqrt{2H}}\right) - \tan^{-1}\left(\frac{x_d}{\sqrt{2H}}\right)\right), \tag{C.20}$$

$$C_2 = \frac{12(1 - \theta_d)\left(2H + x_d^2\right)}{\left(2H + x_d^2\right)^2}, \tag{C.21}$$

$$C_3 = \frac{12(1 - \theta_u)\left(2H + x_u^2\right)}{\left(2H + x_u^2\right)^2}, \tag{C.22}$$

$$C_4 = 6\left(\frac{(\theta_u - 2)}{2H + x_u^2} - \frac{(\theta_d - 2)}{2H + x_d^2}\right), \tag{C.23}$$

and

$$\theta_u = \theta\left(x_u(t), t\right), \tag{C.24}$$

and θ is solved using (3.30).

Appendix D

Expansion of the Mushy Region Model when x_L Changes Causality

This appendix shows the expansion of the mushy region model when the velocity of the bottom surface slowly decreases, when the left hand boundary changes causility at time $t = t_I$. At this time, the numerator and denominator of the derivative dx_u/dt are both equal to zero. To initialize the system, we expand equations (3.11)-(3.16) and (3.75) with the expansion

$$t = t_I + \epsilon\hat{t}, \tag{D.1}$$

$$x_d = x_{d0}^* + \epsilon\hat{t}x_{d1}^*, \tag{D.2}$$

$$x_u = x_{u0}^* + \epsilon\hat{t}x_{u1}^*, \tag{D.3}$$

$$H = H_i + \epsilon\hat{t}H_{i1}, \tag{D.4}$$

$$P_d = P_{r0} + \epsilon P_{d1}^*\hat{t}, \tag{D.5}$$

$$P_u = P_{l0} + \epsilon P_{u1}^*\hat{t}, \tag{D.6}$$

$$F = F_0 + \epsilon F_1\hat{t}, \tag{D.7}$$

$$U_0 = \hat{U}_0\left(1 - 2\alpha t_I\right) - 2\alpha\hat{t}\hat{U}_0\epsilon, \tag{D.8}$$

where $x_{u0}^* = x_u(t_I)$, $x_{d0}^* = x_d(t_I)$ and $H_i = H(t_I)$. Using (3.30) and (3.31), the volume fraction, θ, evaluated on the boundaries x_u and x_R at $t = t_I$, have the asymptotic form

$$\theta\left(x_u(t_I+\epsilon), t_I+\epsilon\right) = 1 - \epsilon\theta_{u1}^* t_I, \tag{D.9}$$

$$\theta\left(x_d(t_I+\epsilon), t_I+\epsilon\right) = \theta_{d0}^* + \epsilon\theta_{d1}^* t_I, \tag{D.10}$$

where

$$\begin{aligned}
\theta^*_{d0} &= \frac{2H_i + {x^*_{u0}}^2}{2H_i + {x^*_{d0}}^2}, && \text{(D.11)}\\
\theta^*_{d1} &= \frac{(H_1 + x^*_{u1}x^*_{u0})\left(1 + \sqrt{\left(4\alpha^2 t_I^2 - 4\alpha t_I + 1 - \frac{8\alpha x^*_{u0} + 8\alpha x^*_{d0}}{\hat{U}_0(1-2\alpha t_I)}\right)}\right)}{\alpha\left(2H_i + {x^*_{d0}}^2\right)}\\
&\quad - \frac{4\left(2H_i + {x^*_{u0}}^2\right)(H_{i1}t_I + t_I x^*_{d1}x^*_{d0})}{\left(2H_i + {x^*_{d0}}^2\right)^2}, && \text{(D.12)}\\
\theta^*_{u1} &= \frac{2(2\alpha t_I - 1)(H_{i1} + x^*_{u1}x^*_{u0})}{\alpha\left(2H_i + {x^*_{u0}}^2\right)}. && \text{(D.13)}
\end{aligned}$$

The zeroth order expansion of the pressure boundary conditions, (3.15), and the force balance (3.16) have the form

$$P_{r0} = \hat{U}_0\left(1 - 2\alpha t_I\right)\left(\frac{3\tau_r\left(3{x^*_{u0}}^2 - 2H_i\right)}{8\sqrt{2H_i^5}} + \frac{3x^*_{d0}\left(2H_i - 3{x^*_{u0}}^2 - 12\theta^*_{d0}H_i x^*_{d0}\right)}{4H_i^2\left(2H_i + {x^*_{d0}}^2\right)}\right) = -1, \qquad \text{(D.14)}$$

$$P_{l0} = -\hat{U}_0\left(1 - 2\alpha t_I\right)\left(\frac{3x^*_{u0}\left(2H_i + 3{x^*_{u0}}^2\right)}{4H_i^2\left(2H_i + {x^*_{u0}}^2\right)} + \frac{3\left(2H_i - 3{x^*_{u0}}^2\right)\tau_l}{8\sqrt{2H_i^5}}\right) = -1, \qquad \text{(D.15)}$$

$$F_0 = 6\hat{U}_0\left(1 - 2\alpha t_I\right)\left(\frac{\theta^*_{d0}}{2H_i + {x^*_{d0}}^2} - \frac{2H_i + {x^*_{d0}}^2 - 2{x^*_{u0}}^2}{\left(2H_i + {x^*_{u0}}^2\right)\left(2H_i + {x^*_{d0}}^2\right)}\right) = 1, \qquad \text{(D.16)}$$

where

$$\tau_l = \pi + 2\tan^{-1}\left(\frac{x^*_{u0}}{\sqrt{2H_i}}\right), \quad \tau_r = \pi - 2\tan^{-1}\left(\frac{x^*_{d0}}{\sqrt{2H_i}}\right). \qquad \text{(D.17)}$$

and are satisfied identically. The first order expansions, which are written below, allows us to calculate the terms x^*_{u1}, x^*_{d1} and H_{i1},

$$\begin{aligned}
P^*_{d1} = &-3x^*_{d1}\left[\frac{\hat{U}_0\left(1 - 2\alpha t_I\right)\left(16H_i^2(\theta^*_{d0} - 1) + \left(10H_i + 3{x^*_{d0}}^2\right)\theta^*_{d0}{x^*_{d0}}^2\right)}{2H_i^2\left(2H_i + {x^*_{d0}}^2\right)^2} - \frac{(\theta^*_{d0} - 1)x^*_{d0}\left(10H_i + 3{x^*_{d0}}^2\right)}{2H_i^2\left(2H_i + {x^*_{d0}}^2\right)}\right.\\
&\left.+\frac{3\tau_r({x^*_{u0}}^2 - {x^*_{d0}}^2 - \theta^*_{d0}\hat{U}_0\left(1 - 2\alpha t_I\right))}{4\sqrt{2H_i^5}}\right] + 3\theta^*_{d1}\left[-\frac{x^*_{d0}\left(10H_i + 3{x^*_{d0}}^2\right)}{8H_i^3\left(2H_i + {x^*_{d0}}^2\right)} + \frac{3\left(H_i + {x^*_{d0}}^2\right)\tau_r}{8\sqrt{2H_i^7}}\right]\\
&+ \frac{3H_1}{\sqrt{H_i^7}}\left[\frac{H_i\left(4H_i + 3{x^*_{d0}}^2\right)}{4\left(2H_i + {x^*_{d0}}^2\right)} + \frac{3\tau_r\left(3\hat{U}_0\left(1 - 2\alpha t_I\right)\left({x^*_{u0}}^2 - 2H_i\right) - 8H_i x^*_{d0}\right)}{16\sqrt{2}}\right]\\
&+ 2\alpha t_I\hat{U}_0\left[\frac{\left(4H_i^2 t_I(20 - 23\theta^*_{d0})x^*_{d0} + 4H_i t_I(6 - 17\theta^*_{d0}){x^*_{d0}}^3 - 15t_I\theta^*_{d0}{x^*_{d0}}^5\right)}{32H_i^{7/2}\left(2H_i + {x^*_{d0}}^2\right)^2}\right] = 0, \qquad \text{(D.18)}
\end{aligned}$$

$$
\begin{aligned}
P^*_{u1} &= 3\theta^*_{u1} 2\alpha t_I \hat{U}_0 \left[\frac{x^*_{u0}\left(10H_i + 3{x^*_{u0}}^2\right)}{4H_i^2\left(2H_i + {x^*_{u0}}^2\right)} + \frac{3\left(2H_i + {x^*_{u0}}^2\right)\tau_l}{8\sqrt{2H_i^5}} \right] \\
&- 3x^*_{u1}x^*_{u0}U_0 t_I \left[\frac{x^*_{u0}\left(10H_i + 3{x^*_{u0}}^2\right)}{2H_i^2\left(2H_i + {x^*_{u0}}^2\right)^2} + \frac{3H_i\tau_l}{8\sqrt{2H_i^7}} \right] \\
&+ 3H_{i1}\left[\frac{-64H_i^3 + 4H_i^2 x^*_{u0}(3\hat{U}_0\left(1-2\alpha t_I\right) - 20x^*_{u0})}{8H_i^2\left(2H_i + {x^*_{u0}}^2\right)^2} - \frac{3\left(2H_i\hat{U}_0\left(1-2\alpha t_I\right) + 8H_i x^*_{u0} - 5t_I U_0 {x^*_{u0}}^2\right)\tau_l}{16\sqrt{2H_i^7}} \right] \\
&+ \frac{4H_i {x^*_{u0}}^3(11\hat{U}_0\left(1-2\alpha t_I\right) - 6x^*_{u0}) + 15{x^*_{u0}}^5}{8H_i^3\left(2H_i + {x^*_{u0}}^2\right)^2} = 0,
\end{aligned}
\tag{D.19}
$$

$$
\begin{aligned}
F_1 &= 3H_{i1}\left[\frac{2\tau_l - 2\tau_r + \pi}{\sqrt{2H_i^3}} + \frac{2x^*_{u0}}{H_i\left(2H_i + {x^*_{u0}}^2\right)} - \frac{2{x^*_{d0}}^3}{H_i\left(2H_i + {x^*_{d0}}^2\right)^2} \right] \\
&+ \frac{12t_I(\theta^*_{d0} - 2)U_0 x^*_{d1}x^*_{d0}}{\left(2H_i + {x^*_{d0}}^2\right)^2} + \frac{12t_I U_0 x^*_{u1}x^*_{u0}}{\left(2H_i + {x^*_{u0}}^2\right)^2} + \frac{32(\theta^*_{d0} - 1)x^*_{d1} - 2\theta^*_{d1}U_0}{2H_i + {x^*_{d0}}^2} + \frac{4(\theta^*_{d0} - 2)2\alpha t_I\hat{U}_0 - 4x^*_{d0}}{\left(2H_i + {x^*_{d0}}^2\right)^2} \\
&+ 2\alpha t_I\hat{U}_0\left[\frac{4{x^*_{u0}}^2}{\left(2H_i + {x^*_{u0}}^2\right)^3} + \frac{8H_i}{\left(2H_i + {x^*_{u0}}^2\right)^3} \right] \\
&+ 3\theta^*_{u1}\hat{U}_0\left(1 - 2\alpha t_I\right)\left[-\frac{2{x^*_{u0}}^2}{\left(2H_i + {x^*_{u0}}^2\right)^2} - \frac{4H_i}{\left(2H_i + {x^*_{u0}}^2\right)^2} \right] = 0.
\end{aligned}
\tag{D.20}
$$

Appendix E

Mushy Region Model Differential Equations

This appendix shows the differential equations for the derivatives dH/dt, dx_u/dt, and dx_d/dt, that describe the mushy region model in the various sections of the numerical computation. Equations used to derive these equations are listed in (3.89)-(3.91), (3.100)-(3.103), and (3.126)-(3.129). We start where the characteristics leave the right hand boundary, and thus solve for the derivatives of H and x_d, which are stated below:

$$\frac{dH}{dt} = F_{11}(x_u, x_d, H) = \frac{A_1G_1 - C_1D_1 + C_1 + G_1\frac{\delta}{\Omega}}{(E_1C_1 - B_1G_1)}, \tag{E.1}$$

$$\frac{dx_d}{dt} = F_{12}(x_u, x_d, H) = -\frac{E_1A_1 - B_1D_1 + B_1 + E_1\frac{\delta}{\Omega}}{(E_1C_1 - B_1G_1)}, \tag{E.2}$$

with

$$A_1 = -\frac{3ux_d\left(2(5\theta_d-4)H+3\theta_d x_d^2\right)}{4H^2\left(2H+x_d^2\right)} + \frac{3u\left(3\theta_d\left(2H+x_d^2\right)-8H\right)\left(\pi-2\tan^{-1}\left(\frac{x_d}{\sqrt{2H}}\right)\right)}{8\sqrt{2H^5}}, \tag{E.3}$$

$$B_1 = \frac{3\delta}{H^2}\left(\frac{2H}{2H+x_d^2}-3\right)+\frac{9\delta x_d}{2\sqrt{2H^5}}\left(\pi-2\tan^{-1}\left(\frac{x_d}{\sqrt{2H}}\right)\right), \tag{E.4}$$

$$C_1 = 3\delta(\theta_d-1)\left(\frac{x_d\left(10H+3x_d^2\right)}{2H^2\left(2H+x_d^2\right)}+\frac{3\left(2H+x_d^2\right)\left(\pi-2\tan^{-1}\left(\frac{x_d}{\sqrt{2H}}\right)\right)}{8\sqrt{2H^5}}\right), \tag{E.5}$$

$$D_1 = 6u\left(\frac{(\theta_d-2)}{2H+x_d^2}+\frac{1}{2H+x_u^2}\right), \tag{E.6}$$

$$E_1 = \frac{6\delta}{\sqrt{H}}\left(2H\left[\frac{x_u}{2H+x_u^2}-\frac{x_d}{2H+x_d^2}\right]+\sqrt{2H}\left[\tan^{-1}\left(\frac{x_u}{\sqrt{2H}}\right)-\tan^{-1}\left(\frac{x_d}{\sqrt{2H}}\right)+\pi\right]\right), \tag{E.7}$$

$$G_1 = \frac{12\delta(\theta_d-1)}{2H+x_d^2}, \tag{E.8}$$

where

$$\theta_d = \theta\left(x_d(t),t\right), \tag{E.9}$$

and θ is solved using (3.106) and (3.107).

When the characteristics exit through both the left and right hand interfaces, we solve for the three derivatives H, x_d, and x_u, which have the form

$$\frac{dH}{dt} = F_{21}(x_u,x_d,H) = -\frac{A_2G_2L_2+C_2D_2J_2-C_2G_2I_2+C_2G_2+(C_2J_2+G_2L_2)\frac{\delta}{\Omega}}{(B_2G_2L_2-C_2G_2H_2+E_2C_2J_2)} \tag{E.10}$$

$$\begin{aligned}\frac{dx_d}{dt} &= F_{22}(x_u,x_d,H)\\ &= -\frac{-A_2G_2H_2+E_2A_2J_2-B_2D_2J_2+B_2G_2I_2-B_2G_2+(E_2J_2-B_2H_2-G_2H_2)\frac{\delta}{\Omega}}{(B_2G_2L_2-C_2G_2H_2+E_2C_2J_2)}\end{aligned} \tag{E.11}$$

$$\begin{aligned}\frac{dx_u}{dt} &= F_{23}(x_u,x_d,H)\\ &= \frac{E_2A_2L_2-B_2D_2L_2+C_2D_2H_2-E_2C_2I_2+E_2C_2+(C_2H_2-B_2L_2+E_2L_2)\frac{\delta}{\Omega}}{(B_2G_2L_2-C_2G_2H_2+E_2C_2J_2)}\end{aligned} \tag{E.12}$$

with

$$A_2 = -\frac{3ux_u\left(2(5\theta_u-4)H+3\theta_u x_u^2\right)}{4H^2\left(2H+x_u^2\right)} - \frac{3u\left((6\theta_u-8)H+3\theta_u x_u^2\right)\left(\pi+2\tan^{-1}\left(\frac{x_u}{\sqrt{2H}}\right)\right)}{8\sqrt{2H^5}}, \tag{E.13}$$

$$B_2 = \frac{3\delta}{H^2}\left(\frac{2H}{2H+x_u^2}-3\right) - \frac{9\delta x_u}{2\sqrt{2H^5}}\left(2\tan^{-1}\left(\frac{x_u}{\sqrt{2H}}\right)+\pi\right), \tag{E.14}$$

$$C_2 = -3\delta(\theta_u-1)\left(\frac{x_u\left(10H+3x_u^2\right)}{2H^2\left(2H+x_u^2\right)} + \frac{3\left(2H+x_u^2\right)\left(\pi+2\tan^{-1}\left(\frac{x_u}{\sqrt{2H}}\right)\right)}{8\sqrt{2H^5}}\right), \tag{E.15}$$

$$D_2 = -\frac{3ux_d\left(2(5\theta_d-4)H+3\theta_d x_d^2\right)}{4H^2\left(2H+x_d^2\right)} + \frac{3u\left(3\theta_d\left(2H+x_d^2\right)-8H\right)\left(\pi-2\tan^{-1}\left(\frac{x_d}{\sqrt{2H}}\right)\right)}{8\sqrt{2H^5}}, \tag{E.16}$$

$$E_2 = \frac{3\delta}{H^2}\left(\frac{2H}{2H+x_d^2}-3\right) + \frac{9\delta x_d\left(\pi-2\tan^{-1}\left(\frac{x_d}{\sqrt{2H}}\right)\right)}{2\sqrt{2H^5}}, \tag{E.17}$$

$$G_2 = 3\delta(\theta_d-1)\left(\frac{x_d\left(10H+3x_d^2\right)}{2H^2\left(2H+x_d^2\right)} + \frac{3\left(2H+x_d^2\right)\left(\pi-2\tan^{-1}\left(\frac{x_d}{\sqrt{2H}}\right)\right)}{8\sqrt{2H^5}}\right), \tag{E.18}$$

$$I_2 = 6u\left(\frac{\theta_u-2}{2H+x_u^2} + \frac{2-\theta_d}{\theta_d 2H+x_d^2}\right), \tag{E.19}$$

$$H_2 = \frac{6\delta}{\sqrt{H}}\left(2H\left[\frac{x_u}{2H+x_u^2}-\frac{x_d}{2H+x_d^2}\right] + \sqrt{2H}\left[\tan^{-1}\left(\frac{x_u}{\sqrt{2H}}\right)-\tan^{-1}\left(\frac{x_d}{\sqrt{2H}}\right)+\pi\right]\right), \tag{E.20}$$

$$J_2 = \frac{12\delta(\theta_d-1)}{2H+x_d^2}, \tag{E.21}$$

$$L_2 = -\frac{12\delta(\theta_u-1)}{2H+x_u^2}, \tag{E.22}$$

where

$$\theta_u = \theta\left(x_u(t),t\right), \tag{E.23}$$

and θ is solved using (3.106) and (3.107).

Shortly after the velocity has changed sign, we have shown a second mushy region forms in the film. We note the new boundary conditions are x_{2u}, x_{2d}, x_{1u}, x_{1d}. Immediately after the mushy region forms, we assume the characteristics enter the second mushy region through both boundaries, x_{2u} and x_{2d}, and in the first mushy region exit through the both boundaries x_{1u} and x_{1d}. We solve for three derivatives: H, x_{1u}, and x_{1d}, which are

$$\frac{dH}{dt} = F_{31}(x_{2u}, x_{2d}, x_{1u}, x_{1d}, H) = -\frac{\Omega A_3 + \delta}{\Omega B_3}, \tag{E.24}$$

$$\frac{dx_{1d}}{dt} = F_{32}(x_{2u}, x_{2d}, x_{1u}, x_{1d}, H) = -\frac{-A_3 D_3 + B_3 C_3 + (B_3 - D_3)\frac{\delta}{\Omega}}{E_3 B_3}, \tag{E.25}$$

$$\frac{dx_{1u}}{dt} = F_{33}(x_{2u}, x_{2d}, x_{1u}, x_{1d}, H) = -\frac{-A_3 I_3 + B_3 G_3 - I_3\frac{\delta}{\Omega}}{B_3 H_3}, \tag{E.26}$$

with

$$A_3 = \frac{3u}{16H^3}\left(-\frac{4x_{2u}H\left(2H + 3x_{2u}^2\right)}{2H + x_{2u}^2} + \sqrt{2H}\left(2H - 3x_{2u}^2\right)\left(2\tan^{-1}\left(\frac{x_{2u}}{\sqrt{2H}}\right) + \pi\right)\right), \tag{E.27}$$

$$B_3 = \frac{3\delta}{H^2}\left(\frac{2H}{2H + x_{2u}^2} - 3\right) - \frac{9\delta x_{2u}}{2\sqrt{2H^5}}\left(2\tan^{-1}\left(\frac{x_{2u}}{\sqrt{2H}}\right) + \pi\right), \tag{E.28}$$

$$C_3 = -\frac{3ux_{1d}\left(2(5\theta_{1d} - 4)H + 3\theta_{1d}x_{1d}^2\right)}{4H^2\left(2H + x_{1d}^2\right)} + \frac{3u\left(3\theta_{1d}\left(2H + x_{1d}^2\right) - 8H\right)\left(\pi - 2\tan^{-1}\left(\frac{x_{1d}}{\sqrt{2H}}\right)\right)}{8\sqrt{2H^5}}, \tag{E.29}$$

$$D_3 = \frac{3\delta}{H^2}\left(\frac{2H}{2H + x_{1d}^2} - 3\right) + \frac{9\delta x_{1d}\left(\pi - 2\tan^{-1}\left(\frac{x_{1d}}{\sqrt{2H}}\right)\right)}{2\sqrt{2H^5}}, \tag{E.30}$$

$$E_3 = 3\delta(\theta_{1d} - 1)\left(\frac{x_{1d}\left(10H + 3x_{1d}^2\right)}{2H^2\left(2H + x_{1d}^2\right)} + \frac{3\left(2H + x_{1d}^2\right)\left(\pi - 2\tan^{-1}\left(\frac{x_{1d}}{\sqrt{2H}}\right)\right)}{8\sqrt{2H^5}}\right), \tag{E.31}$$

$$G_3 = -24u\left(2(\theta_{1u} - 1)H + \theta_{1u}x_{1u}^2 - x_{2d}^2\right), \tag{E.32}$$

$$I_3 = 96\delta(x_{2d} - x_{1u}), \tag{E.33}$$

$$H_3 = 48\delta(\theta_{1u} - 1)\left(2H + x_{1u}^2\right), \tag{E.34}$$

$$\tag{E.35}$$

where

$$\theta_{1u} = \theta_1\left(x_{1u}(t), t\right) \text{ and } \theta_{1d} = \theta_1\left(x_{1d}(t), t\right), \tag{E.36}$$

and θ_1 is solved using (3.106) and (3.107).

For some cases, the characteristics will start to exit through the left hand boundary of the second mushy region x_{2u} before the first mushy region has closed, requiring us to solve for four derivatives H, x_{1d}, x_{1u}, and x_{2u}, which are

$$\frac{dH}{dt} = F_{41}(x_{2u}, x_{2d}, x_{1u}, x_{1d}, H) = -\frac{J_4K_4 - I_4M_4}{J_4L_4 - H_4M_4}, \tag{E.37}$$

$$\frac{dx_{1u}}{dt} = F_{42}(x_{2u}, x_{2d}, x_{1u}, x_{1d}, H) = -\frac{I_4L_4 - H_4K_4}{J_4L_4 - H_4M_4}, \tag{E.38}$$

$$\begin{aligned}\frac{dx_{1d}}{dt} &= F_{43}(x_{2u}, x_{2d}, x_{1u}, x_{1d}, H) \\ &= -\frac{D_4J_4L_4 - D_4H_4M_4 + E_4I_4M_4 - E_4J_4K_4 + (J_4L_4 - H_4M_4)\,\frac{\delta}{\Omega}}{G_4(J_4L_4 - H_4M_4)},\end{aligned} \tag{E.39}$$

$$\begin{aligned}\frac{dx_{2u}}{dt} &= F_{44}(x_{2u}, x_{2d}, x_{1u}, x_{1d}, H) \\ &= -\frac{A_4J_4L_4 - A_4H_4M_4 + B_4I_4M_4 - B_4J_4K_4 + (J_4L_4 - H_4M_4)\,\frac{\delta}{\Omega}}{C_4(J_4L_4 - H_4M_4)},\end{aligned} \tag{E.40}$$

with

$$A_4 = \frac{3u}{16H^3}\left(-\frac{4x_{2u}H\left(2H+3x_{2u}^2\right)}{2H+x_{2u}^2} + \sqrt{2H}\left(2H-3x_{2u}^2\right)\left(2\tan^{-1}\left(\frac{x_{2u}}{\sqrt{2H}}\right)+\pi\right)\right), \tag{E.41}$$

$$B_4 = \frac{3\delta}{H^2}\left(\frac{2H}{2H+x_{2u}^2}-3\right) - \frac{9\delta x_{2u}}{2\sqrt{2H^5}}\left(2\tan^{-1}\left(\frac{x_{2u}}{\sqrt{2H}}\right)+\pi\right), \tag{E.42}$$

$$C_4 = -3\delta(\theta_{2u}-1)\left(\frac{x_{2u}\left(10H+3x_{2u}^2\right)}{2H^2\left(2H+x_{2u}^2\right)} + \frac{3\left(2H+x_{2u}^2\right)\left(\pi+2\tan^{-1}\left(\frac{x_{2u}}{\sqrt{2H}}\right)\right)}{8\sqrt{2H^5}}\right), \tag{E.43}$$

$$D_4 = -\frac{3ux_{1d}\left(2(5\theta_{1d}-4)H+3\theta_{1d}x_{1d}^2\right)}{4H^2\left(2H+x_{1d}^2\right)} + \frac{3u\left(3\theta_{1d}\left(2H+x_{1d}^2\right)-8H\right)\left(\pi-2\tan^{-1}\left(\frac{x_{1d}}{\sqrt{2H}}\right)\right)}{8\sqrt{2H^5}}, \tag{E.44}$$

$$E_4 = \frac{3\delta}{H^2}\left(\frac{2H}{2H+x_{1d}^2}-3\right) + \frac{9\delta x_{1d}\left(\pi-2\tan^{-1}\left(\frac{x_{1d}}{\sqrt{2H}}\right)\right)}{2\sqrt{2H^5}}, \tag{E.45}$$

$$G_4 = 3\delta(\theta_{1d}-1)\left(\frac{x_{1d}\left(10H+3x_{1d}^2\right)}{2H^2\left(2H+x_{1d}^2\right)} + \frac{3\left(2H+x_{1d}^2\right)\left(\pi-2\tan^{-1}\left(\frac{x_{1d}}{\sqrt{2H}}\right)\right)}{8\sqrt{2H^5}}\right), \tag{E.46}$$

$$I_4 = -24u\left(2(\theta_{1u}-1)H+\theta_{1u}x_{1u}^2-x_{2d}^2\right), \tag{E.47}$$

$$H_4 = 96\delta(x_{2d}-x_{1u}), \tag{E.48}$$

$$J_4 = 48\delta(\theta_{1u}-1)\left(2H+x_{1u}^2\right), \tag{E.49}$$

$$\begin{aligned} K_4 = {} & \frac{6u}{H}\left(\frac{x_{1u}^3}{\left(2H+x_{1u}^2\right)^2} - \frac{x_{2d}^3}{\left(2H+x_{2d}^2\right)^2}\right) + \frac{12ux_{2d}}{\left(2H+x_{2d}^2\right)^2} \\ & + 3\theta_{1u}u\left(H+\frac{x_{1u}^2}{2}\right)x_{2d}\left(\frac{10H+3x_{2d}^2}{2H^2\left(2H+x_{2d}^2\right)^2} - \frac{10H+3x_{1u}^2}{2H^2\left(2H+x_{1u}^2\right)^2}\right) \\ & + \frac{9\theta_{1u}u\left(H+\frac{x_{1u}^2}{2}\right)-6uH}{2\sqrt{2H^5}}\left(\tan^{-1}\left(\frac{x_{2d}}{\sqrt{2H}}\right)-\tan^{-1}\left(\frac{x_{1u}}{\sqrt{2H}}\right)\right), \end{aligned} \tag{E.50}$$

$$\begin{aligned} L_4 = {} & -24\left(\frac{1}{\left(2H+x_{1u}^2\right)^2}+\frac{1}{\left(2H+x_{2d}^2\right)^2}\right) + 6\delta x_{1u}x_{2d}\left(\frac{10H+3x_{2d}^2}{2H^2\left(2H+x_{2d}^2\right)^2} - \frac{10H+3x_{1u}^2}{2H^2\left(2H+x_{1u}^2\right)^2}\right), \\ & + \frac{9\delta x_{1u}}{\sqrt{2H^5}}\left(\tan^{-1}\left(\frac{x_{2d}}{\sqrt{2H}}\right)-\tan^{-1}\left(\frac{x_{1u}}{\sqrt{2H}}\right)\right) \end{aligned} \tag{E.51}$$

$$\begin{aligned} M_4 = {} & 3\left(2\delta(1-\theta_{1u})\left(H+\frac{x_{1u}^2}{2}\right)\right)x_{2d}\left(\frac{10H+3x_{2d}^2}{2H^2\left(2H+x_{2d}^2\right)^2} - \frac{10H+3x_{1u}^2}{2H^2\left(2H+x_{1u}^2\right)^2}\right) \\ & + \frac{9\delta(1-\theta_{1u})\left(H+\frac{x_{1u}^2}{2}\right)}{\sqrt{2H^5}}\left(\tan^{-1}\left(\frac{x_{2d}}{\sqrt{2H}}\right)-\tan^{-1}\left(\frac{x_{1u}}{\sqrt{2H}}\right)\right), \end{aligned} \tag{E.52}$$

where

$$\theta_{1,u} = \theta_1\left(x_{1u}(t),t\right), \quad \theta_{1d} = \theta_1\left(x_{1d}(t),t\right), \text{ and } \theta_{2u} = \theta_2\left(x_{2u}(t),t\right). \tag{E.53}$$

and $\theta_{1,2}$ are solved using (3.106) and (3.107).

Bibliography

P. Andersson, J. Tamminen, and C. Sandström. *Piston Ring Tribology.* VTT Tiedotteita, Helsinki, 2002.

J. Ashmore, C. Pino, and T. Mullin. Cavitation in a lubrication flow between a moving sphere and a boundary. *Physical Review Letters*, 94:124501–124510, 2005.

P. Atkins and J. De Paula. *Elements of Physical Chemistry.* Oxford University Press, 2013.

G. Batchelor. *An Introduction to Fluid Mechanics.* Cambridge University Press, Cambridge, 1st edition, 1967.

D. Berthe and P. Vergne. High pressure rheology for high pressure lubrication: a review. *Journal of Rheology*, 34(8):1387–1414, 1990.

G. Birkhoff and D. Hays. Free boundaries in partial lubrication. *Journal of Mathematics and Physics*, 42(1):126–138, 1963.

S. Boedo and J. Booker. Cavitation in normal separation of square and circular plates. *International Journal of Multiphase Flow*, 22(1001):149–149, 1996.

J. Booker. Classic cavitation models for finite element analysis. *Current Research in Cavitating Fluid Films*, 15(7):39–40, 1990.

J. Booker and K. Huebner. Application of finite element methods to lubrication: an engineering approach. *Journal of Lubrication Technology*, 94(4):313–323, 1972.

M. Braun and W. Hannon. Cavitation formation and modelling for fluid film bearings: a review. *Proceedings of the Institution of Mechanical Engineers, Part J: Journal of Engineering Tribology*, 224(9):839–863, 2010.

M. Braun and R. Hendricks. An experimental investigation of the vaporous/gaseous cavity characteristics of an eccentric journal bearing. *ASLE Transactions*, 27(1):1–14, 1984.

C. Brennen. *Cavitation and Bubble Dynamics.* Oxford University Press, 1st edition, 1995.

F. Bretherton. The motion of long bubbles in tubes. *Journal of Fluid Mechanics*, 10(2): 166–188, 1961.

D. Brewe. Theoretical modeling of the vapor cavitation in dynamically loaded journal bearings. *Journal of Tribology*, 108(4):628–637, 1986.

D. Brewe, J. Ball, and M. Khonsari. Introduction, Part 2: Current research in cavitating fluid films. *Proceedings of the Cavitation Symposium, STLE Annual Meeting, NASA TM-103184*, 5(4):25–26, 1988.

W. Cope. The hydrodynamical theory of film lubrication. *Proceedings of the Royal Society of London. Series A. Mathematical and Physical Sciences*, 197(1049):201–217, 1949.

J. Coyne and H. Elrod Jr. Conditions for the rupture of a lubricating film. Part I: Theoretical model. *Journal of Lubrication Technology*, 92(3):451–456, 1970.

J. Coyne and H. Elrod Jr. Conditions for the rupture of a lubricating film. Part II: New boundary conditions for Reynolds equation. *Journal of Lubrication Technology*, 93(1): 156–167, 1971.

D. Dowson and C. Taylor. Cavitation in bearings. *Annual Review of Fluid Mechanics*, 11: 35–66, 1979.

H. Elrod. A cavitation algorithm. *Journal of Lubrication Technology*, 103(3):350–354, 1981.

H. Elrod and M. Adams. A computer program for cavitation and starvation problems. *1st Leeds-Lyon Symposium on Tribology, Cavitation and Related Phenomena in Lubrication*, 1:37–41, 1974.

I. Etsion and L. Ludwig. Observation of pressure variation in the cavitation region of submerged journal bearings. *Journal of Lubrication Technology*, 104(2):157–163, 1982.

J. Fisher. The fracture of liquids. *Journal of Applied Physics*, 19(11):1062–1067, 1948.

L. Floberg. Boundary conditions of cavitation regions in journal bearings. *ASLE Transactions*, 4(2):282–286, 1961.

L. Floberg. On hydrodynamic lubrication with special reference to sub-cavity pressures and number of streamers in cavitation regions (hydrodynamic bearing lubrication of rotating cylinder with reference to sub-cavity pressure and cavitation regions). *ASLE Transactions*, 37:467–493, 1965.

L. Floberg. Sub-cavity pressures and number of oil streamers in cavitation regions with special reference to infinite journal bearing. *ACTA Polytechnica Scandinavica-Mechanical Engineerings Series*, 37:3–15, 1968.

L. Floberg. *On the Tensile Strength of Liquids.* Lund Tekniska Högskola Universitet, Lund, 1973.

L. Floberg. Cavitation boundary conditions with regard to the number of streamers and tensile strength of the liquid. *1st Leeds-Lyon Symposium on Tribology, Cavitation and Related Phenomena in Lubrication*, 1:31–36, 1974.

J. Frenkel. *Kinetic Theory of Liquids.* Oxford University Press, 1st edition, 1955.

R. Fusaro. Mechanisms of lubrication and wear of a bonded solid-lubricant film. *ASLE Transactions*, 24(2):191–204, 1981.

T. Gilles. *Automotive Engines: Diagnosis, Repair, Rebuilding.* Delmar Publishers, New York, NY, 1996.

A. Goldman, R. Cox, and H. Brenner. Slow viscous motion of a sphere parallel to a plane walli motion through a quiescent fluid. *Chemical Engineering Science*, 22(4):637–651, 1967a.

A. Goldman, R. Cox, and H. Brenner. Slow viscous motion of a sphere parallel to a plane wall couette flow. *Chemical Engineering Science*, 22(4):653–660, 1967b.

M. Groper and I. Etsion. The effect of shear flow and dissolved gas diffusion on the cavitation in a submerged journal bearing. *Journal of Tribology*, 123(3):494–500, 2001.

M. Groper and I. Etsion. Reverse flow as a possible mechanism for cavitation pressure build-up in a submerged journal bearing. *Journal of Tribology*, 124(2):320–326, 2002.

L. Gumbel. Vergleich der ergebnisse der rechnerischen behandlung des lagerschmierungsproblem mit neuren versuchergebnissen. *Monatsbild Berlin Bezirk VDI*, 506:125–128, 1921.

S. Haber and I. Etsion. Analysis of an oscillatory oil squeeze film containing a central gas bubble. *ASLE Transactions*, 28(2):253–260, 1985.

B. Hamrock, S. Schmid, and B. Jacobson. *Fundamentals of Fluid Film Lubrication.* CRC Press, New York, NY, 2004.

D. Hays and J. Feiten. *Cavities Between Moving Parallel Plates.* Elsevier Publishing Company, New York, NY, 1964.

R. Hendricks, R. Braun, and Mullen E. Analogy between cavitation and fracture mechanics. *Journal of Tribology*, 83071:26–35, 1983.

H. Heshmat. *Tribology of Interface Layers.* CRC Press, Boca Ratn (FL), 2010.

M. Hopkins. Viscous flow between rotating cylinders and a sheet moving between them. *British Journal of Applied Physics*, 8(11):442–450, 1957.

S. Hsu. Boundary lubrication of materials. *MRS Bulletin*, 16(10):54–58, 1991.

S. Hsu and R. Gates. Boundary lubricating films: formation and lubrication mechanism. *Tribology International*, 38(3):305–312, 2005.

S. Hsu, E. Klaus, and H. Cheng. A mechano-chemical descriptive model for wear under mixed lubrication conditions. *Wear*, 128(3):307–323, 1988.

S. Hsu, M. Shen, and A. Ruff. Wear prediction for metals. *Tribology International*, 30(5): 377–383, 1997.

B. Jacobson and B. Hamrock. High-speed motion picture camera experiments of cavitation in dynamically loaded journal bearings. *Journal of Lubrication Technology*, 105(3):446–452, 1983a.

B. Jacobson and B. Hamrock. Vapor cavitation in dynamically loaded journal bearings. *Journal of Lubrication Technology*, 65(2):256–272, 1983b.

B. Jakobsson and L. Floberg. The finite journal bearing, considering vaporization. *Journal of Lubrication Technology*, 6(4):116–134, 1957.

M. Khonsari. A review of thermal effects in hydrodynamic bearings. Part II: Journal bearings. *ASLE Transactions*, 30(1):26–33, 1986.

V. Krotov and A. Rusanov. Effect of surfactants on vapor-pressure of solvent in capillary systems, Part 2. changes in vapor-pressure during the adsorption of a surfactant in a closed system. *Colloid Journal of the USSR*, 44(1):19–28, 1982.

A. Kumar and J. Booker. A finite element cavitation algorithm: application/validation. *Journal of Tribology*, 113(2):276–284, 1991a.

A. Kumar and J. Booker. A finite element cavitation algorithm. *Journal of Tribology*, 113 (2):255–260, 1991b.

A. Lacey and M. Shillor. The existence and stability of regions with superheating in the classical two-phase one-dimensional stefan problem with heat sources. *IMA Journal of Applied Mathematics*, 30:215–230, 1983.

E. Lauga and M. Brenner. Dynamic mechanisms for apparent slip on hydrophobic surfaces. *Physical Review E*, 70:26311–26318, 2004.

B. Leach. Private communication, 2016.

L. Leal. *Advanced Transport Phenomena: Fluid Mechanics and Convective Transport Processes*. Cambridge University Press, 2007.

G. Lundholm. Circumferential groove journal bearing considering cavitation and dynamic statibility. *Acta Polytechnica Scandinavica.*, 42:3–12, 1969.

T. Mang and W. Dresel. *Lubricants and Lubrication*. John Wiley & Sons, 2007.

H. Mori, H. Yabe, and Y. Fujita. On the separation boundary condition for fluid lubrication theories of journal bearings. *ASLE Transactions*, 11(3):196–203, 1968.

T. Myers, R. Hall, M. Savage, and P. Gaskell. The transition region of elastohydrodynamic lubrication. *Proceedings of the Royal Society of London A: Mathematical, Physical and Engineering Sciences*, 432(1886):467–479, 1991.

J. Nouri. Private communication, 2016.

J. Ockendon, S. Howison, and A. Lacey. Mushy regions in negative squeeze films. *Quarterly Journal of Mechanics and Applied Mathematics*, 56(3):361–379, 2003.

K. Olsson. *Cavitation in Dynamically Loaded Bearings*. Scandinavian University Books, Stockholm, 1965.

R. Pit, H. Hervet, and L. Leger. Direct experimental evidence of slip in hexadecane: solid interfaces. *Physical Review Letters*, 85(5):980–983, 2000.

R. Pletcher, J. Tannehill, and D. Anderson. *Computational Fluid Mechanics and Heat Transfer.* CRC Press, Boca Ratn (FL), 2012.

M. Priest, D. Dowson, and C. Taylor. Theoretical modelling of cavitation in piston ring lubrication. *Proceedings of the Institution of Mechanical Engineers*, 214:435–447, 2000.

O. Reynolds. On the theory of lubrication and its application to Mr. Beauchamp Tower's experiments, including and experimental determination of the viscosity of olive oil. *Proceedings of the Royal Society*, 40:191–203, 1886.

P. Saffman. Selection mechanisms and stability of fingers and bubbles in hele-shaw cells. *IMA Journal of Applied Mathematics*, 46:137–145, 1991.

C. Sang-Myung. A study on oil consumption related with the piston ring pack with thinner ring width and lower ring tension. *Journal of the Korean Society of Tribologists and Lubrication Engineers*, 25:311–317, 2009.

M. Savage. Cavity instability. *1st Leeds-Lyon Symposium on Tribology, Cavitation and Related Phenomena in Lubrication*, 1:53–54, 1974.

M. Savage. Cavitation in lubrication. Part I. on boundary conditions and cavity fluid interfaces. *Journal of Fluid Mechanics*, 80(04):743–755, 1977.

W. Sawyer, K. Diaz, M. Hamilton, and B. Micklos. Evaluation of a model for the evolution of wear in a scotch-yoke mechanism. *Wear*, 2(2):678–682, 2003.

L. Shampine, M. Reichelt, and J. Kierzenka. Solving index-1 DAE's in MATLAB and Simulink. *SIAM Review*, 41(3):538–552, 1999.

A. Sommerfeld. The hydrodynamic theory of lubrication friction. *Communications in Mathematical Physics*, 50:97–155, 1904.

G. Stachowiak and A. Batchelor. *Engineering tribology.* Butterworth-Heinemann, 2013.

W. Stieber. *Des Schwimmlager: hydrodinamische Theorie des Gleitlagers.* VDI-Verlag, GmbH., Berlin, 1933.

D. Sun and D. Brewe. A high speed photography study of cavitation in a dynamically loaded journal bearing. *Journal of Tribology*, 113(2):287–292, 1991a.

D. Sun and D. Brewe. Two reference time scales for studying the dynamic cavitation of liquid films. *Journal of Tribology*, 114(3):612–615, 1991b.

D. Sun, D. Brewe, and P. Abel. Simultaneous pressure measurement and high-speed photography study of cavitation in a dynamically loaded journal bearing. *Journal of Tribology*, 115(1):88–95, 1993.

P. Swales. A review of cavitation phenomena in engineering situations. *1st Leeds-Lyon Symposium on Tribology, Cavitation and Related Phenomena in Lubrication*, 1:3–9, 1974.

H. Swift. The stability of lubricating films in journal bearings. *Proceedings of the Institution of Civil Engineers*, 233(1932):267–288, 1932.

C. Taylor. In the study of steady-state film rupture boundary conditions. *1st Leeds-Lyon Symposium on Tribology, Cavitation and Related Phenomena in Lubrication*, 1:59–65, 1974.

G. I. Taylor. Deposition of a viscous fluid on the wall of a tube. *Journal of Fluid Mechanics*, 10(2):161–165, 1961.

G. I. Taylor. Cavitation of a viscous fluid in narrow passages. *Journal of Fluid Mechanics*, 16(4):595–619, 1963.

G. I. Taylor. Cavitation in hydrodynamic lubrication. *Cavitation in Real Liquids*, 154(25): 80–101, 1964.

H. Temperley. The behaviour of water under hydrostatic tension: Part II. *Proceedings of the Physical Society*, 58(4):436–449, 1946.

H. Temperley and L. Chambers. The behaviour of water under hydrostatic tension: Part I. *Proceedings of the Physical Society*, 58(4):420–424, 1946.

D. Tretheway and C. Meinhart. A generating mechanism for apparent fluid slip in hydrophobic microchannels. *Physics of Fluids*, 16(5):1509–1515, 2004.

D. Vijayaraghavan and T. Keith Jr. Development and evaluation of a cavitation algorithm. *Tribology Transactions*, 32(2):225–233, 1989.

D. Vijayaraghavan and T. Keith Jr. An efficient, robust, and time accurate numerical scheme applied to a cavitation algorithm. *Journal of Tribology*, 112(1):44–51, 1990.

O. Vinogradova. Drainage of a thin liquid film confined between hydrophobic surfaces. *Langmuir*, 11:2213–2220, 1995.

M. Volmer. *Kinetic Analysis of Typical Special Cases with Experimental Verification: Kinetics of Phase Formation (Kinetik der Phasenbildung).* Steinkopff, Dresden, 1939.

C. Woods and D. Brewe. The solution of the Elrod algorithm for a dynamically loaded journal bearing using multigrid techniques. *Journal of Tribology*, 111(2):302–308, 1989.

Y. Zhu and S. Granick. Rate-dependent slip of Newtonian liquid at smooth surfaces. *Physical Review Letters*, 87:96105–96109, 2001.

Y. Zhu and S. Granick. Limits of the hydrodynamic no-slip boundary condition. *Physical Review Letters*, 88:106102–106106, 2002a.

Y. Zhu and S. Granick. Apparent slip of Newtonian fluids past adsorbed polymer layers. *Macromolecules*, 35(12):4658–4663, 2002b.

Y. Zhu and S. Granick. No-Slip boundary condition switches to partial slip when fluid contains surfactant. *Langmuir*, 18(26):10058–10063, 2002c.